Univerzita Palackého v Olomouci
Přírodovědecká fakulta

In-situ experimenty jaderného dopředného rozptylu

Habilitační práce

Vít Procházka

Olomouc, září 2018

Děkuji prof. Ing. Marcelovi Miglierinimu, Dr.Sc, prof. RNDr. Miroslavu Mašláňovi, CSc, doc. RNDr. Liboru Machalovi ,Ph.D., doc. RNDr. Jiřímu Pechouškovi, Ph.D., Mgr. Petru Novákovi, Ph.D. a Mgr. Vlastimilu Vrbovi za cenné rady a diskuze nad tématem této práce. Dále pak děkuji své ženě Pavle za podporu.

Prohlašuji, že jsem tuto práci vypracoval sám s uvedením všech použitých pramenů a spoluautorství.

V Olomouci 1. 9. 2018 Vít Procházka

Obsah

Úvod

Jedním z cílů materiálového výzkumu je popsání fázových transformací a porozumění dynamice těchto procesů. Těmito fázovými transformacemi mohou být například skupenská změna, změna vnitřního uspořádání spojená se změnou struktury nebo také chemické reakce. Detailní pochopení kinetiky a dynamiky například chemických reakcí v pevné fázi může vést například k využití těchto reakcí při syntéze nejrůznějších funkčních materiálů. Na druhou stranu některé procesy v pevných látkách mohou zhoršovat vlastnosti daných materiálů a díky porozumění mechanizmům a příčinám těchto transformací můžeme zachovat vhodné vlastnosti takových materiálů.

Abychom byli schopni detailně popsat a vysvětlit průběh a příčiny těchto procesů, je nutné pozorovat děje až na atomární úrovni. Navíc toto pozorování musí být dostatečně rychlé ve srovnání s dobou transformace. Řada experimentálních technik sice umožňuje pozorování fázových procesů, ale zpravidla sledují pouze makroskopické vlastnosti (magnetizační měření, diferenciální skenovací kalorimetrie a další). Na druhou stranu "mikroskopické" techniky (rentgenová difrakce [1], Mössbauerova spektroskopie [2], transmisní elektronová mikroskopie nebo mionová spinová rezonance [3]) jsou schopny poskytnout informace o atomárním uspořádání, nicméně jsou často příliš pomalé a poskytují informace jen o stacionárních stavech zkoumané látky. Důvodem je zpravidla nízká intenzita zdroje záření, které je použito ke zkoumání látky.

S použitím synchrotronu jako zdroje záření je možné provádět některá měření v kratším časovém intervalu. Jednou z takových metod, která navíc současně poskytuje informace o uspořádání na atomární úrovni, je jaderný dopředný rozptyl [4]. Tato práce je věnována právě využití jaderného dopředného rozptylu (NFS - nuclear forward scattering) ke studiu fázových transformací. V rámci této práce jsou popsány tzv. *in-situ* experimenty, tedy měření prováděná během sledovaného děje.

Experimenty jaderného dopředného rozptylu poskytují informace ve formě časového interferogramu vzorkem rozptýleného záření. Informace o lokálním elektronovém nebo atomárním uspořádání je nutné získat dodatečným vyhodnocením. To však není úplně jednoduché a je komplikováno řadou faktorů, které jsou v této práci diskutovány. V rámci jednoho *in-situ* měření je zpravidla načteno více než sto těchto záznamů. Proto pro vyhodnocení časových interferogramů bylo nutno vyvinout speciální software, který zjednodušuje a zefektivňuje práci s takto velkým množstvím dat.

První oblastí, ve které bylo využito jaderného dopředného rozptylu za tímto účelem, je krystalizace amorfních kovových slitin. Jedná se o materiály, které vykazují unikátní magnetické vlastnosti, a jsou proto využívány jako magnetické stínění nebo také v jádrech transformátorů. Aplikace *in-situ* experimentů jaderného dopředného rozptylu umožnila de-

tailní sledování kinetiky krystalizace v různých teplotách a poskytla cenné informace o vlivu magnetického pole na krystalizační proces.

Další aplikací NFS *in-situ* experimentů, která je v této práci popsána, je studium termální dekompozice ferátů. Jedná se o sloučeniny, ve kterých je železo přítomné ve vysokovalenčním stavu, například Fe(V) nebo Fe(VI). Tyto materiály mají velký potenciál pro využití v řadě aplikací jako je čistění vod nebo konstrukce vysokokapacitních a ekologicky nezávadných baterií. Díky NFS experimentům byla pozorována závislost dekompozičního procesu na teplotě a formování meziproduktů.

Poznámka: V celé práci je používaná jako desetinná značka tečka.

Kapitola 1

Jaderný rezonanční rozptyl

Elektromagnetické záření při dopadu na látku interaguje s elektrony a jádry [5, 6]. Jestliže má záření vhodnou energii, může dojít k excitaci jádra ze základního do některého excitovaného stavu za současné absorpce fotonu. Následně dochází k opětovné relaxaci jádra do základního stavu a vyzáření přebytečné energie ve formě γ-fotonu. Jevu, kdy je elektromagnetické záření rozptylováno jádry schopnými toto záření absorbovat, říkáme jaderný rezonanční rozptyl [4, 7, 8].

Při popisu této interakce sledujeme, zda a jakým způsobem došlo ke změně v systému jader a také zda došlo ke změně stavu jádra obklopující mřížky. Následně pak můžeme rozptylový proces charakterizovat jako koherentní nebo nekoherentní a také jako elastický nebo neelastický [9, 10]. Z experimentálního hlediska mají největší význam neelastický rozptyl, který zahrnuje i koherentní i nekoherentní proces [7, 9], a koherentní elastický rozptyl [11–14].

Neelastický rozptyl (NIS, nuclear inelastic scattering) je důležitou experimentální metodou umožňující studovat hustotu stavů fononů [12, 15]. Tato technika hraje důležitou roli například ve zkoumání vlastností zemského pláště [16]. NIS sice poskytuje cenné informace i o amorfních kovových slitinách studovaných v této práci [17, 18], nicméně tuto techniku doposud nelze využít pro měření *in-situ*, neboť doba měření jednoho fononového spektra je zpravidla několik hodin. Druhý případ, tedy koherentí elastický rozptyl, je možné využít ke studiu hyperjemných interakcí a fázového složení materiálu [19] a může být využit i pro *in-situ* měření.

1.1 Mössbauerův jev

U koherentního elastického rozptylu na systému jader nedochází ke změně jaderného systému. Tedy jádra se vrací do původního stavu, ve kterém se nacházela před rozptylem. Systém jader před rozptylem a po rozptylu můžeme popsat stejnou vlnovou funkcí a nemůžeme tedy určit, které jádro se interakce zúčastnilo [11]. Rozptýlené záření je pak koherentní se zářením dopadajícím. Při uvažovaném procesu nedochází ani ke změně krystalové mřížky, přesněji řečeno nedochází ke změně vibračního stavu krystalové mříže, tedy absorpci nebo emisi fononu [12, 20, 21].

Jev, kdy je jádrem vyzářen nebo pohlcen foton, aniž by došlo ke zpětnému rázu, tedy změně vibračního stavu mřížky, byl poprvé popsán a vysvětlen R. L. Mössbauerem, po

kterém nese název Mössbauerův jev [22]. Jedná se o bezodrazovou absorpci nebo emisi fotonu jádrem. V tomto případě změnu hybnosti při absorpci nebo emisi fotonu nese krystal jako celek a nedochází ke změně energie záření vlivem Dopplerova jevu. Z toho je také zřejmé, že ke koherentnímu rozptylu dochází pouze v pevných látkách. V plynech nebo kapalinách vždy dojde ke zpětnému rázu a tady proces není elastický.

Na pozorování tohoto jevu je založena Mössbauerova spektroskopie [19, 21, 23]. Tato technika je provozována v mnoha geometrických uspořádáních, transmisním [21], emisním [24–35], v uspořádání časově rozlišené Mössbauerovy spektroskopie [36–43], Mössbauerova spektroskopie konverzních rentgenů a elektronů [44,45] nebo také polarizované Mössbauerovy spektroskopie [46–49].

Jako zdroj záření pro Mössbauerovu spektroskopii je zpravidla využíván radioaktivní zářič s vhodnými energetickými přechody [50]. Asi nejčastěji je Mössbaerova spektroskopie aplikována ke studiu železa, kdy je jako zářič použit izotop ^{57}Co [51]. Tyto zářiče jsou komerčně dostupné [52]. Záření z těchto zdrojů je nekoherentní a nepolarizované, září uniformě do všech směrů a typická aktivita těchto zdrojů je 1-2 GBq. Již krátce po popsání Mössbauerova jevu bylo navrženo k excitaci jaderných přechodů využít synchrotronové záření [10, 53, 54]. V roce 1985 byly publikovány první úspěšné experimenty Mössbauerovy spektroskopie se synchrotronovým zářením [55].

Využití synchrotronového záření pro studium interakce jádra se svým okolím má oproti konvenčním (radioaktivním) zdrojům několik specifik, která budou diskutována později.

1.2 Synchrotronové záření

Jako zdroj synchrotronového záření slouží synchrotrony [56–58], případně lasery na volných elektronech [59], tedy urychlovače částic, které jsou konstruovány tak, aby nabité částice (nejčastěji elektrony) při průchodu speciálními zařízeními, wigglery a undulátory, emitovaly fotony. Záření ze synchrotronu je nutné před použitím pro experimenty jaderného dopředného rozptylu monochromatizovat na energie řádově desítek keV s energetickým rozlišením (šířkou pásma) 1-10 meV. Takto upravené záření je koherentní [60]. V dopředném směru je jeho koherence několik desítek metrů, v příčném směru pak je koherence podstatně nižší a pohybuje se někde kolem 1-100 μm [61, 62]. Záření je navíc lineárně polarizované [63], což umožňuje měřit stáčení roviny polarizace, takzvaný jaderný dichroizmus [64]. Výhodou synchrotronového záření je především jeho obrovská intenzita, která o několik řádů převyšuje konvenční zdroje, a právě díky ní je možné provádět *in-situ* experimenty [60]. Synchrotronové záření má často pulzní charakter, čehož se s výhodou využívá v experimentech jaderného rezonančního rozptylu k separaci dopadajících a rozptýlených fotonů [4]. Monochromatizací synchrotronového záření je možné získat fotony o energii vhodné k excitaci jader, pro která neexistuje vhodný radioaktivní izotop jako zdroj záření [65].

1.3 Interakce jader s okolím

U atomových jader můžeme určit celou řadu fyzikálních vlastností, například hmotnost, počet protonů, počet neutronů, elektrický náboj, paritu a další. Z pohledu jaderného rezo-

nančního rozptylu jsou nejdůležitější spin, magnetický moment a kvadrupolový moment. Všechny tři tyto vlastnosti jsou důsledkem aktuálního vnitřního uspořádání nukleonů v jádře. Proto jsou tyto vlastnosti vždy charakteristické pro daný stav. Jádra v základním stavu mají zpravidla jiný spin, magnetický moment i kvadrupólové štěpení než jádra v excitovaném stavu [50, 66]. Například jádro železa ^{57}Fe má v základním stavu spin 1/2 a v excitovaném 3/2. Parametry některých jader vhodných pro NFS experimenty jsou uvedeny v Tabulce 1.1.

Jádra mohou prostřednictvím náboje, magnetického a kvadrupólového momentu interagovat s magnetickým a elektrickým polem, které může být externí, nebo může mít svůj původ ve vnitřním rozložení atomů v látce. Interakce jádra s vlastním elektronovým obalem nebo elektrony, jejichž vlnová funkce má nenulový překryv s vlnovou funkcí jádra, označujeme jako hyperjemnou interakci [66].

Interakce magnetického pole s jádrem štěpí jaderné hladiny, na obr. 1.1 je uveden případ tohoto štěpení pro základní a excitovaný stav jádra ^{57}Fe. Interakce jádra s elektrickým polem mění energetický rozdíl mezi základním a excitovaným stavem a štěpí jaderné hladiny, jak je ukázáno na obr. 1.2 pro případ ^{57}Fe.

Pomocí experimentů Mössbauerovy spektroskopie a jaderného rezonančního rozptylu můžeme měřit toto energetické štěpení a jejich prostřednictvím pak získáváme informace o lokálním uspořádání látky v okolí daného jádra, magnetickém uspořádání a valenčním stavu atomu.

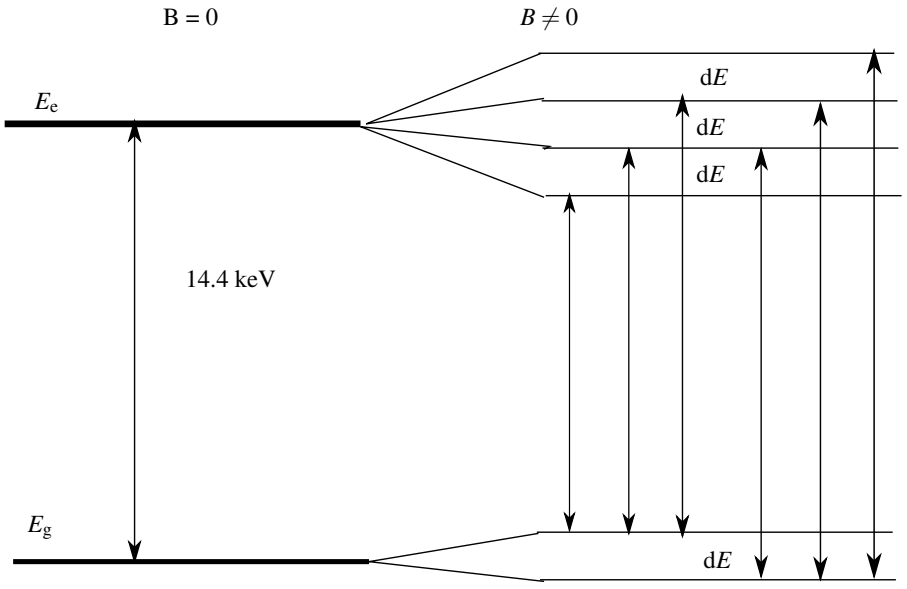

Obrázek 1.1: Štěpení energetických hladin základního a excitovaného stavu jádra ^{57}Fe v magnetickém poli.

Základní a excitovaný stav jádra spolu interagují prostřednictvím absorbovaného nebo emitovaného fotonu, a proto tyto stavy nejsou samostatné a musíme je chápat jako celek. Spin takové soustavy stanovíme pomocí pravidel pro skládání momentu hybnosti [67]. Pravděpodobnosti přechodu mezi jednotlivými jadernými hladinami jsou dány Clebschovými–Gordanovými koeficienty [68–72].

Z	Izotop	E_0 (keV)	τ_0	Γ_0	a(%)	I_g	I_e	Multipola.	$\mu_g(\mu_N)$	$\mu_e(\mu_N)$	Q_g barn	Q_e barn	α
19	40 K	29.834	5.96 ns	0.11 μeV	0.012	4−	3−	(M1)	−1.298	−1.29	−0.061	N.N	6.6
21	45 Sc	12.4	458.78 ms	1.4 aeV	100	7/2−	3/2+	(M2)	4.756	N.N	−0.22	N.N	632
26	57 Fe	14.4125	141.11 ns	4.66 neV	2.14	1/2−	3/2−	M1+E2	0.0906	−0.1553	0	0.16	8.56
28	61 Ni	67.408	7.6 ns	86.57 neV	1.19	3/2−	5/2−	M1+E2	0.75	0.48	0.162	−0.2	0.139
30	67 Zn	93.312	13.22 μs	49.8 peV	4.11	5/2−	1/2−	E2	0.8756	0.587	0.15	N.N	0.873
50	119 Sn	23.871	25.61 ns	25.7 neV	8.58	1/2+	3/2+	M1+E2	−1.0473	0.633	0	0.094	5.22
51	121 Sb	37.133	4.99 ns	0.13 μeV	57.25	5/2+	7/2+	M1	3.3634	2.518	−0.36	−0.48	11.11
52	125 Te	35.4919	2.14 ns	0.31 μeV	6.99	1/2+	3/2+	M1+E2	−0.8885	0.605	0	−0.31	14
53	127 I	57.606	2.76 ns	0.24 μeV	100	5/2+	7/2+	M1+E2	2.8133	2.54	−0.79	−0.71	3.77
55	133 Cs	80.997	9.05 ns	72.77 neV	100	7/2+	5/2+	M1+E2	2.582	3.45	−0.0037	−0.33	1.72
57	138 La	72.57	167.35 ns	3.93 neV	0.09	5+	3+	E2	3.7136	2.886	0.45	N.N	6.41
60	145 Nd	67.25	42.42 ns	15.52 neV	8.3	7/2−	3/2−	E2	−0.654	N.N	−0.254	N.N	9.61
60	145 Nd	72.5	1.04 ns	0.63 μeV	8.3	7/2−	5/2−	M1	−0.656	−0.320	−0.33	N.N	3.64
62	149 Sm	22.494	10.27 ns	64.08 neV	13.83	7/2−	5/2−	M1+E2	−0.672	−0.624	0.075	1.01	29.2
62	154 Sm	81.976	4.36 ns	0.15 μeV	22.7	0+	2+	E2	0	0.784	0	−1.87	4.94
63	151 Eu	21.532	13.99 ns	47.03 neV	47.82	5/2+	7/2+	M1+E2	3.472	2.591	0.903	1.28	28
63	153 Eu	83.3671	1.14 ns	0.58 μeV	52.18	5/2+	7/2+	M1+E2	1.533	1.81	2.41	0.44	3.82
63	153 Eu	97.4297	285.6 ps	2.3 μeV	52.18	5/2+	5/2−	E1	1.533	3.22	2.41	N.N	0.307
68	166 Er	80.574	2.63 ns	0.25 μeV	33.6	0+	2+	E2	0	0.632	0	−1.9	6.88
68	168 Er	79.804	2.71 ns	0.24 μeV	26.8	0+	2+	E2	0	0.642	0	−2.17	7.14
68	167 Er	79.3219	165.9 ps	3.97 μeV	22.95	7/2+	9/2+	M1+E2	0.564	N.N	2.827	N.N	6.06
72	176 Hf	88.351	2.06 ns	0.32 μeV	5.21	0+	2+	E2	0	0.539	0	−2.10	5.86
77	191 Ir	82.407	5.89 ns	0.11 μeV	37.3	3/2+	1/2+	M1+E2	0.1507	0.6	0.816	0	10.9
78	195 Pt	98.85	245.2 ps	2.68 μeV	33.8	1/2−	3/2−	M1+E2	0.60952	−0.62	0	N.N	7.12
79	197 Au	77.351	2.76 ns	0.24 μeV	100	3/2+	1/2+	M1+E2	0.1457	0.42	0.547	0	4.36
80	201 Hg	1.556	144.27 ns	4.56 neV	13.2	3/2−	1/2−	M1+E2	−0.56022	N.N	0.385	N.N	4.7E4
80	201 Hg	32.138	288.5 ps	2.28 μeV	13.2	3/2−	3/2−	M1+E2	−0.56022	N.N	0.385	0.3	41.9
80	201 Hg	26.269	865.6 ps	0.76 μeV	13.2	3/2−	1/2−	M1+E2	−0.56022	N.N	0.385	N.N	76.7
92	238 U	44.915	324.6 ps	2.03 μeV	99.27	0+	2+	E2	0	N.N	0	−3.23	618

Tabulka 1.1: Izotopy umožnující experimenty založené na Mössbauerovu jevu. Z-protonové číslo, E_0-energie jaderného přechodu, τ_0-doba života, Γ_0-vlastní šířka čáry, a-zastoupení v přirozené izotopové směsi, I_g-spin základního stavu, I_e-spin exitovaného stavu, μ_g-magnetický moment základního stavu, μ_e-magnetický moment excitovaného stavu, Q_g-kvadrupólový moment základního stavu, Q_e-kvadrupólový moment excitovaného stavu, α-konverzní faktor.Převzato z [10].

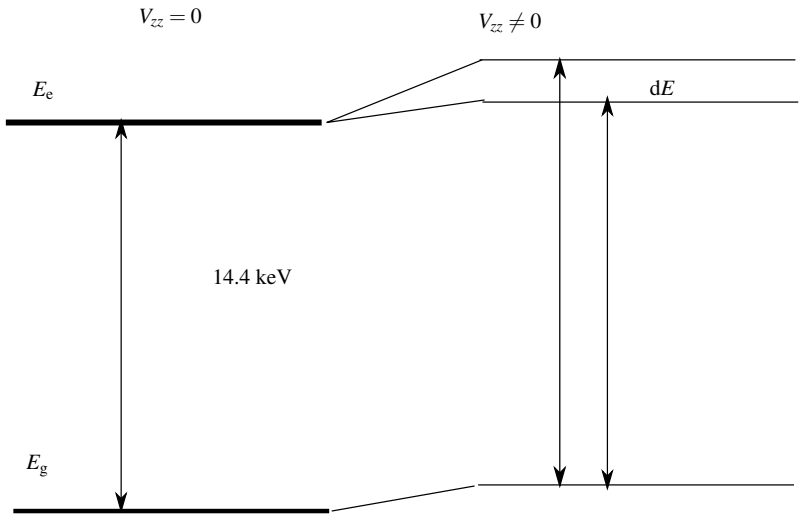

Obrázek 1.2: Štěpení energetických hladin základního a excitovaného stavu jádra ^{57}Fe v elektrickém poli.

1.4 Jaderný dopředný rozptyl

Impulz synchrotronového záření s vhodnou šířkou pásma dopadá na vzorek a rozptýlené záření je detekováno pomocí vhodného detektoru. Některé fotony dopadajícího pulzu jsou při průchodu látkou rezonančně absorbovány jádry, následně jsou s určitým zpožděním, které je dané dobou života excitovaného stavu, opět vyzářeny. Fotony, které neinteragovaly s látkou vůbec nebo byly rozptýleny elektrony, jsou zpožděny jen velice málo (na úrovni jednotek piko sekund až jednotek nanosekund) nebo vůbec a tvoří takzvaný prompt pík, viz obr. 1.3.

Během experimentů pak fotony detekujeme pouze v čase mezi jednotlivými pulzy a ne během trvání pulzů nebo krátce po nich. Proto jsme schopni zaznamenat pouze rozptýlené fotony. To nám přináší velkou výhodu v tom, že detekujeme pouze ty fotony, které interagovaly se studovanou látkou, a tedy nesou informaci o štěpení jaderných hladin. Díky tomu měříme s větším poměrem signálu a šumu než v konvenční Mössbauerově spektroskopii. Závislost počtu rozptýlených fotonů na čase zpoždění t za excitačním pulzem je zpravidla označována jako spektrum jaderného dopředného rozptylu (označení spektrum není zcela přesné, skutečně se jedná o interferogram). Na obr. 1.4 je znázorněn příklad NFS spektra hematitu v lineární a logaritmické škále..

Uspořádání experimentu jaderného dopředného rozptylu je znázorněno na obr. 1.5. Paprsek synchrotronového záření prochází monochromátorem a dopadá na vzorek Rozptýlené záření je následně detekováno lavinovou fotodiodou.

Teoretický popis jaderného koherentního rozptylu byl vypracován v šedesátých letech dvacátého století [73–77]. Navazuje na dřívější popis absorpce γ-záření jádrem [78]. K popisu interakce gamma záření je zpravidla použit semikvantový přístup [79–81], kdy záření je popisováno klasicky a jaderný systém kvantově mechanicky [82, 83]. Při odvozování se vychází z Maxwelových rovnic [84], kde lze na základě kvantové mechaniky a pravděpodobností přechodů mezi jadernými hladinami určit index lomu, který reprezentuje jaderný systém.

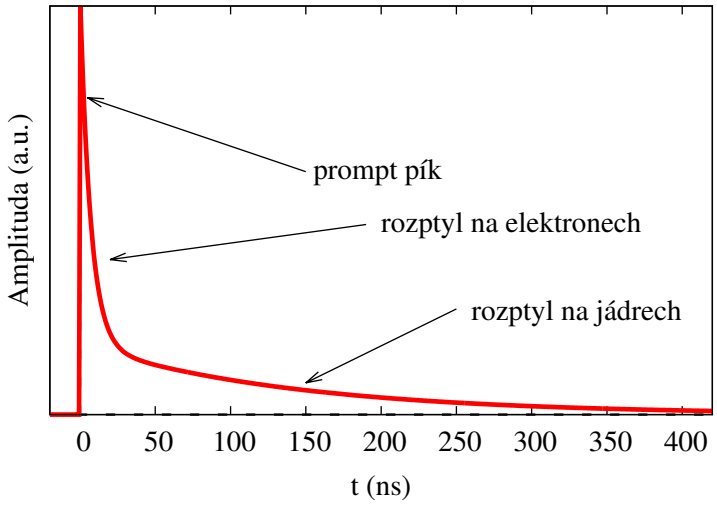

Obrázek 1.3: Prompt pík, nerezonančně rozptýlené záření a elasticky rozptýlené záření.

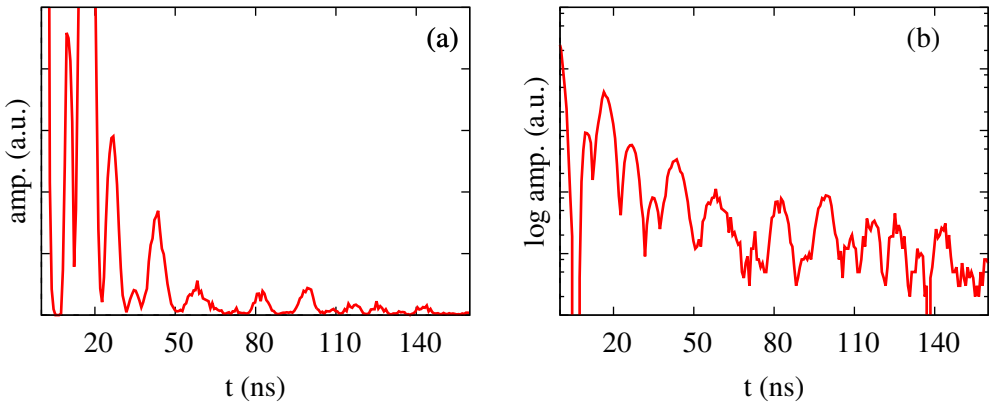

Obrázek 1.4: Příklad spektra NFS vykazující magnetické štěpení v lineární (a) a logaritmické (b) škále.

Dopadající záření popisujeme rovinnou vlnou $A_{\mathrm{in}}(x,t)$, kde x je poloha v prostoru a t je čas zpoždění za excitačním pulzem. Rozptýlenou vlnu $A_{\mathrm{sc}}(x,t)$ pak získáme pomocí rozptylové matice S [85] vztahem

$$A_{\mathrm{sc}}(x,t) = S\,A_{\mathrm{in}}(x,t). \tag{1.1}$$

Rozptylovou matici můžeme podle dynamické teorie difrakce [86] vyjádřit pomocí komplexního indexu lomu n vztahem

$$S = \mathrm{e}^{inz}, \tag{1.2}$$

kde z je tloušťka vzorku. Prošlé (transmitované) záření A_{tr} je součtem dopadající a rozptýlené vlny [85], tedy

$$A_{\mathrm{tr}}(x,t) = A_{\mathrm{in}}(x,t) + A_{\mathrm{sc}}(x,t). \tag{1.3}$$

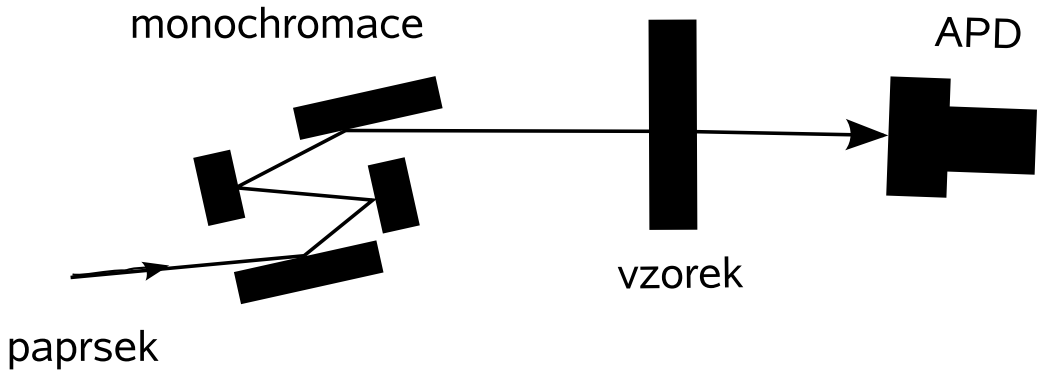

Obrázek 1.5: Schéma experimentálního uspořádání pro měření jaderného dopředného rozptylu. APD je lavinová fotodioda (*angl.* avalanche photodiode), která je v experimentech jaderného rezonančního rozptylu zpravidla využívána jako detektor záření. Záření ze synchrotronu je před dopadem na vzorek monochromatizováno.

Transmitovaná (prošlá) vlna v sobě obsahuje koherentní součet dopadlé a rozptýlené vlny. Jedná se tedy o záření, které je detekováno v případě experimentů transmisní Mössbauerovy spektroskopie. V případě jaderného dopředného rozptylu je detekována pouze rozptýlená vlna $A_{\mathrm{sc}}(x,t)$ a to díky pulznímu charakteru synchrotronového záření.

Výpočet indexu lomu n je představen v mnoha publikacích [8, 13, 14, 86, 87]. Pro popis polarizační závislosti [46, 78] je výhodné využít formalismu Stokesových matic [10, 88, 89] a pak pro prvky matice komplexního indexu lomu $N_{\mu\nu}$ dostáváme [83]

$$N_{\mu\nu} = \frac{4\pi}{k} \sum_{M'=-1}^{1} \sum_{M=-1}^{1} \left[\varepsilon_{\nu}^{*} \cdot Y_{M'}\right] \left[Y_{M}^{*} \cdot \varepsilon_{\mu}\right] F_{M'M}, \tag{1.4}$$

kde Y_M jsou vektorové sférické harmonické funkce, které závisí na vlnovém vektoru záření k a μ, ν jsou indexy maticových elementů ve zvolené $\varepsilon_{\mu,\nu}$ polarizační bázi. Funkce $F_{M'M}$ závislá na energii obsahuje informaci o hyperjemném štěpení a závisí na hyperjemném magnetickém poli, gradientu elektrického pole a jejich směrech. Γ_0 je vlastní šířka absorpce a je svázána s dobou života excitovaného stavu vztahem

$$\Gamma_0 = \hbar/\tau. \tag{1.5}$$

Štěpení jaderných hladin v důsledku hyperjemné interakce a externího pole je mnohem menší než šířka pásma excitačního pulzu, proto jsou jedním pulzem excitovány všechny jaderné přechody současně. V rozptýleném záření jsou obsaženy fotony emitované při přechodech mezi různými stavy, a tedy o různých energiích (frekvencích). Pro ^{57}Fe je obvyklý rozsah energií okolo 500 neV. Jak již bylo uvedeno, rozptýlené záření je koherentní [11, 14, 61, 62, 90], tudíž tyto fotony interferují a v čase se skládají do výsledného interferogramu, který nese informaci o energiích jednotlivých přechodů. Takto interferující záření je detekováno detektorem s velkým časovým rozlišením [82, 91] a díky interferenci se v časovém spektru tvoří výrazná minima a maxima, kvantové zázněje (viz obr. 1.4) [14, 92]. Ty nesou charakteristické znaky interakcí, které štěpí jaderné hladiny. Na obr. 1.4 je časové spektrum hematitu, tedy materiálu vykazujícího magnetické štěpení jaderných hladin.

Záření je rozptylováno do všech směrů a podle Braggova zákona [93] v určitých směrech dochází ke konstruktivní interferenci [1]. Tento proces je označován jako jaderný Braggovský rozptyl [55, 94–97]. Rezonančně rozptýlené záření pak nese informaci i o uspořádání na dlouhou vzdálenost (Braggovské úhly) i o uspořádání na krátkou vzdálenost (kvantové zázněje). Ve speciálním případě, kdy jedna Braggovská reflexe je realizována rozptylem atomů pouze jedné podmřížky, pak v Braggovsky rozptýleném záření máme informace pouze o hyperjemných polích ve vybrané krystalografické pozici.

Jedním z důležitých aspektů jaderného dopředného rozptylu je efekt zrychlení (angl. speed up effect) [7, 36, 38, 87]. Jedná se o zrychlování rozpadu excitovaného stavu v důsledku mnohonásobného rozptylu. Tedy procesu, kdy již jednou rozptýlené záření dále interaguje s látkou. Tento jev je nutné zahrnout do výpočtu jaderného dopředného rozptylu. Mnohonásobný rozptyl způsobuje změnu charakteru spekter. V energetické doméně se objevuje pokles intenzity v místě rezonance. Se vzrůstající tloušťkou vzorku se tento pokles zvětšuje a pro tlustý vzorek dochází k tomu, že se původně jedna čára jeví jako dublet, viz. obr. 1.6. Tento tvar je v energetické oblasti označován jako "Double hump profile". V časové doméně se tento efekt projeví jako dynamické zázněje [92]. Ty se skládají s kvantovými zázněji do hybridních záznějů a jejich přítomnost komplikuje následnou analýzu dat.

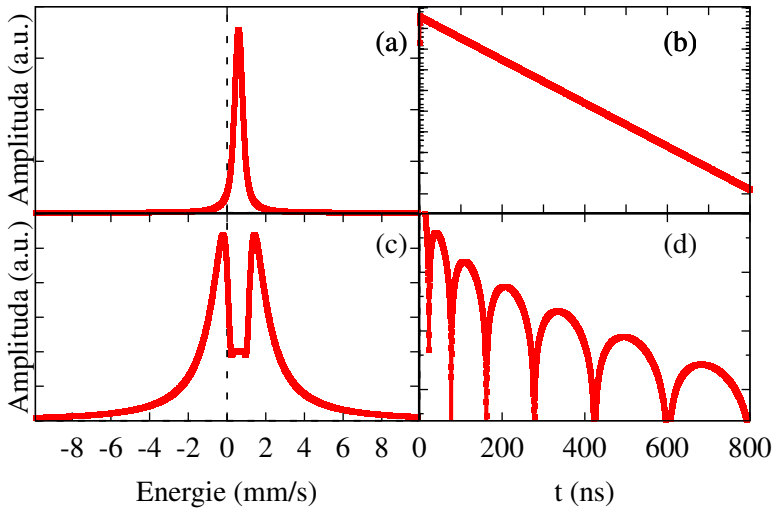

Obrázek 1.6: Spektra NFS tenkého (a) a (b) a tlustého (c) a (d) vzorku v energetické a časové doméně.

V experimentech jaderného dopředného rozptylu je detekována amplituda rozptýleného záření v závislosti na zpoždění za excitačním impulzem synchrotronového záření. Proto je nutné pro detekci použít detektor, který umožňuje přesné určení doby příletu fotonu do detektoru. Požadovaná přesnost určení musí být lepší než 0.5 ns. Nejčastěji jsou používány lavinové fotodiody [82, 91].

Detektory nejsou schopné zaznamenat fázi rozptýlených fotonů, ale pouze jejich amplitudu. Skutečnost, že při měření je detekována pouze amplituda a je ztracena informace o fázi, do jisté míry komplikuje získání informace o energiích jednotlivých přechodů [98–101]. Jedná se o situaci obdobnou fázovému problému v experimentech rentgenové difrakce,

kde chybějící informace o fázi difraktovaných paprsků znemožňuje přímé převedení výsledků měření z reciprokého do přímého prostoru [102, 103].

Většina fotonů neinteraguje s jádry a prochází přes vzorek buď nerozptýlena, nebo je rozptýlena elektrony. Toto záření je zformováno ve velmi krátkém, ale velice intenzivním pulzu, "prompt píku", jehož trvání je maximálně několik nanosekund. Takto intenzivní paprsek by způsobil zničení citlivého APD detektoru, proto je nutné pro ochranu použít lockovací systém, který ochrání detektor po dobu dopadu prompt píku (obr. 1.3).

Z experimentů NFS nejčastěji získáváme tři tzv. hyperjemné parametry, hyperjemné magnetické pole, které nám poskytuje informaci o magnetickém uspořádání ve studovaném vzorku, kvadrupolové štěpení (případně gradient elektrického pole) reflektující symetrii rozložení náboje kolem jádra a izomerní posuv, který je silně závislý na valenčním stavu atomu.

V následujících kapitolách budou podrobně popsány nejdůležitější aspekty realizace a vyhodnocení *in-situ* experimentů jaderného dopředného rozptylu. A dále pak její aplikace na dva rozdílné typy procesů, na výzkum krystalizace amorfních železoobsahujících slitin a na reakce v pevné fázi, konkrétně na dekompoziční proces sloučenin s vysokovalenčním železem.

Kapitola 2

In-situ experimenty

Jaderný dopředný rozptyl doposud nebyl pro studium kinetiky fázových přeměn používán. Jedním z důvodů je zřejmě experimentální náročnost a také komplikované vyhodnocení takových experimentů.

Doposud bylo touto technikou sledováno pouze několik procesů, krystalizace amorfních slitin na bázi železa [104–106], dekompozice sloučenin s vysokovalenčním železem [107] a reakce železa v pevné fázi. V této kapitole budou podrobně popsány experimentální aspekty těchto experimentů.

Při plánování *in-situ* experimentů je nutné uvažovat charakteristický čas měření a podle toho rozhodnout, zda je možné studovaný proces pozorovat určitou technikou *in-situ*, tedy přímo během procesu. Pro to je rozhodující čas potřebný pro jedno měření. Ten musí být mnohem kratší než doba trvání pozorovaného jevu (fázové transformace). Čas nutný pro načtení jednoho časového spektra je dán mnoha faktory. Těmi jsou počet fotonů v jednom excitačním pulzu, frekvence opakování těchto pulzů tloušťka studovaného vzorku, míra obohacení mössbauerovským izotopem, Lamb-Mössbauerův faktor a účinnost detektoru. Tyto faktory určují počet fotonů ve spektru. Aby bylo možné získat patřičné informace o studovaném vzorku je nutné, aby spektra měla dostatečnou intenzitu, tedy je nutné určitou dobu data akumulovat. V současnosti při použití obohaceného vzorku je možné načíst jedno spektrum s dostatečnou intenzitou již za dobu několika minut. Z toho plyne omezení na procesy, které je možné v současné době touto technikou sledovat. Tedy procesy s charakteristickou dobou průběhu v řádu desítek minut.

S dalším rozvojem techniky a především v souvislosti se stavbou laserů na volných elektronech dochází k dalšímu nárůstu intenzity synchrotronových zdrojů a to až o několik řádů. Čili v následujících letech je možné očekávat zkrácení doby měření až pod jednotky vteřin.

S růstem intenzity záření však přichází nebezpečí na radiační ohřev vzorku. Například na synchrotronu ESRF v Grenoblu pro měření na železe se využívá záření o energii 14.413 keV, se spektrální šířkou 3 meV a tokem 10^9 fotonů/s. Odhadnutý výkon dopadajícího záření je asi 1 μW v závislosti na elektronové absorpci vzoru.

Druhým omezujícím faktorem s ohledem na možnosti provádění *in-situ* experimentů je samotná doba života jádra v excitovaném stavu. Principiálně je možné touto technikou studovat i procesy svou rychlostí srovnatelné s dobou života excitovaného stavu (obdobně jako u experimentů Mössbauerovy spektroskopie s časovým rozlišením (TDMS - time differen-

tial Mössbauer spectroscopy) [36, 38, 39], nicméně tato skutečnost by výrazným způsobem komplikovala vyhodnocení takových experimentů a to proto, že hamiltonian hyperjemné interakce by již nebyl nezávislý na čase a tuto skutečnost by bylo nutné zahrnout do výpočtu časového spektra. Při výpočtu by bylo nutné řešit nestacionární Schrödingerovu rovnici a i následná analýza experimentálních dat by byla výrazně komplikovanější.

Fázové transformace jako chemické reakce nebo krystalizace kovových skel jsou ireverzibilní procesy při kterých dochází k ustavení energeticky výhodnějšího uspořádání. Aktuální stav studovaného vzorku je pak složitou funkcí aktuální teploty, času a dalších podmínek, při kterých proces probíhá. Například amorfní slitiny jsou v metastabilním stavu a během následné krystalizace relaxují do energeticky výhodnějšího stavu. Abychom zajistili dostatečnou intenzitu načtených spekter bylo by možné *in-situ* experimenty provést opakovaně a výsledná spektra postupně načítat, kdy transformace by pokaždé proběhla s novým kusem vstupního materiálu a bylo by současně nutné zajistit stejné podmínky při každém průběhu. Tento postup (pokud je autorovy známo) nebyl doposud prováděn. Zřejmě také proto, že při každém průběhu žíhání je nutno vyměnit vstupní materiál v žíhací peci, což zpravidla trvá nějakou dobu a proto je takové měření nepraktické. Pro provedení takového experimentu by bylo nutné zkonstruovat vhodný automatický výměník vzorku v peci a navíc zajistit dostatečně rychlé chlazení pece na původní teplotu.

2.1 Tloušťka vzorku

Jedním z důležitých aspektů *in-situ* experimentů je vhodné nastavení efektivní tloušťky vzorku. Při provádění *in-situ* experimentů je nutné vždy volit optimum mezi rychlostí sběru dat a deformací časového spektra v podobě dynamických záznějů. U tenkého vzorku sice nedochází k deformaci časového spektra dynamickými zázněji, na druhou stranu intenzita rozptýleného záření je nízká a enormně se prodlužuje doba načítání spektra.

Pro experimenty jaderného dopředného rozptylu je možné používat vzorky o větší efektivní tloušťce než pro transmisní experimenty. Optimální tloušťka je samozřejmě ovlivněna také elektronovou absorpcí ve vzorku. Protože v experimentech NFS není detekováno záření v oblasti prompt píku a těsně za ním může být počet detekovaných fotonů ovlivněn i tvarem spektra, kdy v případě širokých spekter dochází k rychlejší deexcitaci vzbuzených jaderných hladin a tedy větší část rozptýleného záření je v oblasti prompt píku a tedy není detekováno.

Na obr. 2.1 je znázorněna závislost počtu rozptýlených fotonů na tloušťce vzorku pro 100 % obohacený vzorek hematitu. Z této závislosti je patrné, že existuje optimální tloušťka vzorku. Současně jsou na obr. 2.2 znázorněna spektra NFS v časové a energetické doméně pro několik tlouštěk ze závislosti na obr 2.2. Je zřejmé, že pro větší tloušťky je již spektrum značně modifikováno efektem samoabsorpce projevujícím se štěpením hladin. Podstatný vliv na optimální tloušťku vzorku během měření má také elektronová absorpce záření.

2.2 Uchycení vzorku

Svazek monochromatizovaného synchrotronového záření má typicky oválný průřez s rozměrem přibližně $2\,\text{mm} \times 1\,\text{mm}$. Pro hledání svazku před měřením se zpravidla používá foto-

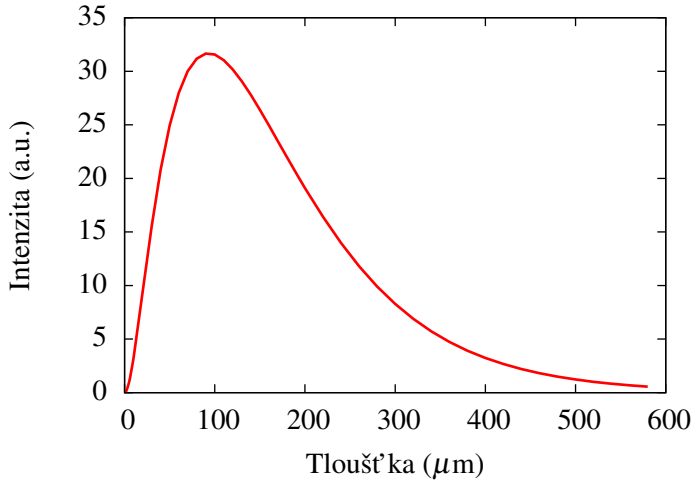

Obrázek 2.1: Intenzita rozptýleného záření v závislosti na tloušťce vzorku.

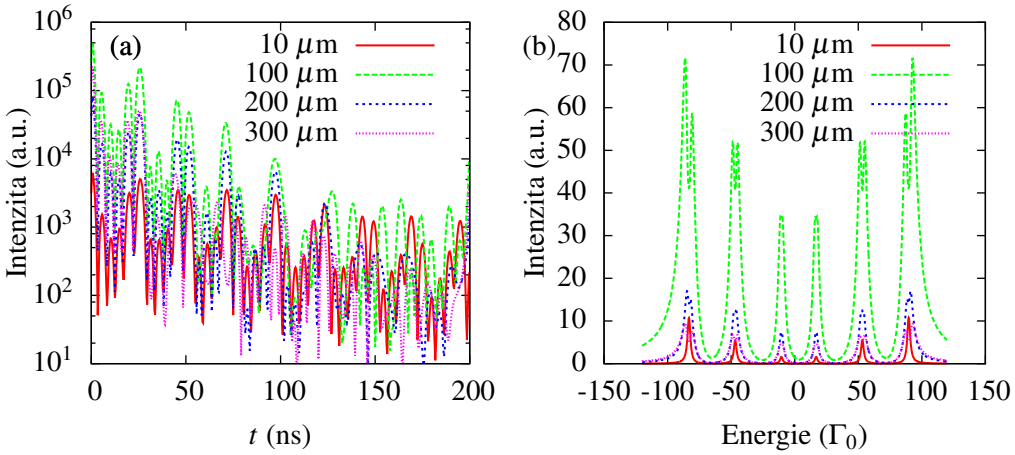

Obrázek 2.2: NFS spektrum v časové (a) a energetické (b) doméně. Závislost na tloušťce vzorku.

papír. Svazek při dopadu na fotopapír způsobí expozici, papír v oblasti expozice zčerná a je možné přibližně pozorovat tvar a rozměr paprsku, viz obr. 2.3.

Synchrotrony poskytují zpravidla svazek horizontální, tedy směr šíření je rovnoběžný s podlahou laboratoře. To přináší řadu úskalí při přípravě vzorku a celé aparatury. Například pro měření práškových vzorků je nutné zajistit, aby při celém průběhu experimentu nedocházelo k sesypávání vzorku. Tento problém samozřejmě odpadá pro vzorky kompaktní, mezi něž patří například v této práci studované amorfní slitiny.

Vzorek tedy musí být v ideálním případě homogenně rozložen na plochu o rozměrech svazku, tedy 1 mmx2 mm. Pro *in-situ* měření se zpravidla používají obohacené vzorky. Jejich příprava, kvůli nutnosti použít izotop ^{57}Fe, je poměrně nákladná, proto je vzorek připravován tak, aby tuto plochu právě pokrýval.

Pro umístění práškových vzorků ve vertikální poloze byly pro *in-situ* experiemnty vy-

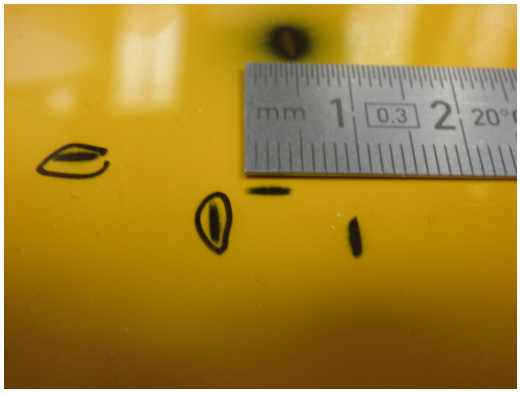

Obrázek 2.3: Velikost svazku zaznamenaná fotopapírem.

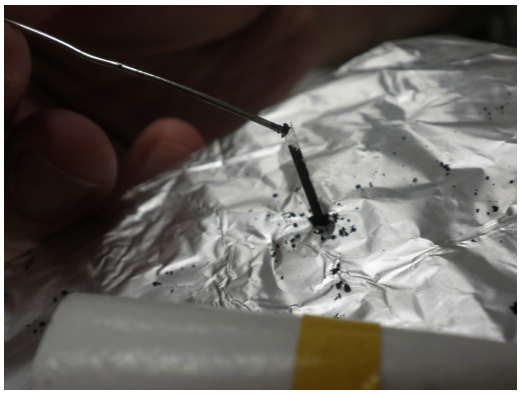

Obrázek 2.4: Práškový vzorek K_2FeO_4 v kapiláře.

užity dvě různé uchycovací metody a to vždy podle typu a konstrukce pece, která byla pro experimenty použita. V jednom případě byl vzorek umístěn v tenkostěnné kapiláře s průměrem 1 mm (obr. 2.4). Tato kapilára byla vložena do žíhací pece (obr. 2.5). Výhodou umístění vzorku v kapiláře je snadná manipulace a také to, že vzorek z kapiláry neuniká. Nevýhodou tohoto umístění je, že vzorek nemá ve všech místech stejnou tloušťku. Tuto skutečnost je nutné při analýze výsledků zahrnout do fitovacího modelu. Druhou nevýhodou tohoto uchycení je větší absorpce záření ve stěnách kapiláry a také omezení teplotního oboru do asi 700 °C, aby nedocházelo k tavení skla. Na obr. 2.5 je ukázáno umístění kapiláry v peci a umístění pece v experimentální místnosti.

Ve druhém případě byl použit k uchycení prášku ve vertikální poloze sendvičový systém, kdy prášek byl umístěn do díry v tenkém plechu, díra byla z obou stran uzavřena tenkou vrstvou slídy, viz obr. 2.6. Tento sendvič byl následně umístěn do pece (obr. 2.7). Výhodou tohoto uchycení vzorku je homogenní tloušťka vzorku. Nevýhodou komplikovanější skládání jednotlivých vzorku a obtížnější manipulace a to zvláště v případě, kdy jsou vzorky kompletovány v rukavicovém boxu kvůli omezení kontaktu se vzdušnou vlhkostí.

V případě amorfních slitin je uchycení vzorku snazší, neboť není riziko sesypání vzorku,

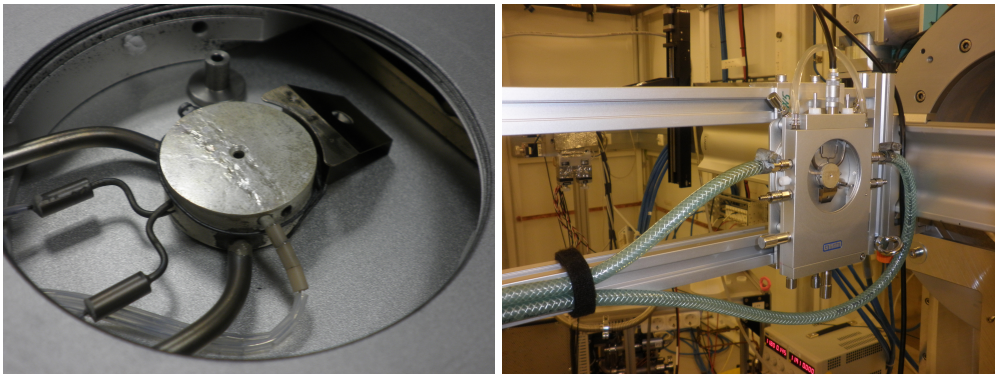

Obrázek 2.5: Pec pro žíhání. Vlevo otevřená pec s kovovým blokem zajišťující stabilitu, vpravo žíhací pec umístěná ve svazku teploty.

Obrázek 2.6: Sendvičový systém pro uchycení prášku ve vertikální poloze.

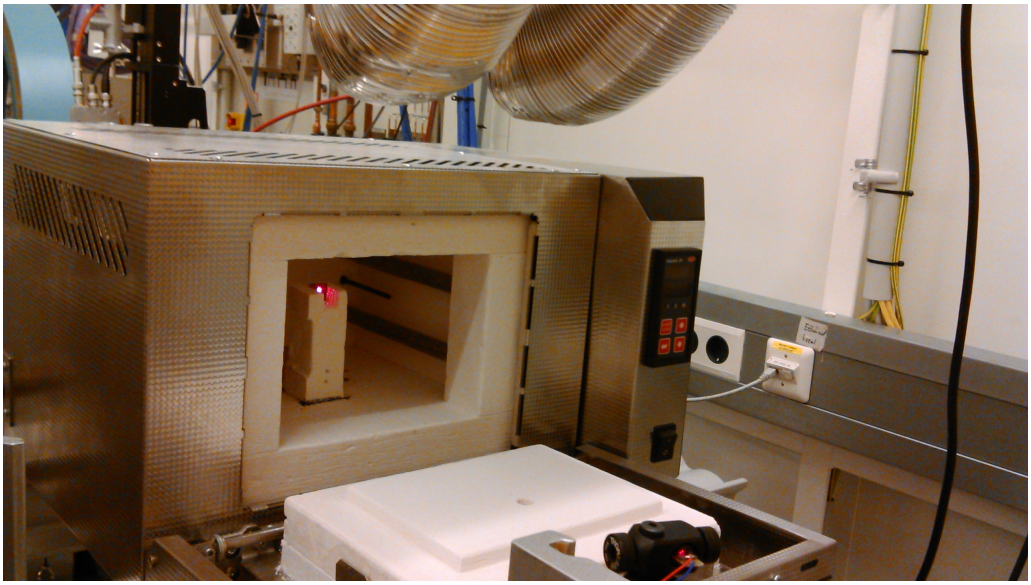

Obrázek 2.7: Sendvičový vzorek v peci.

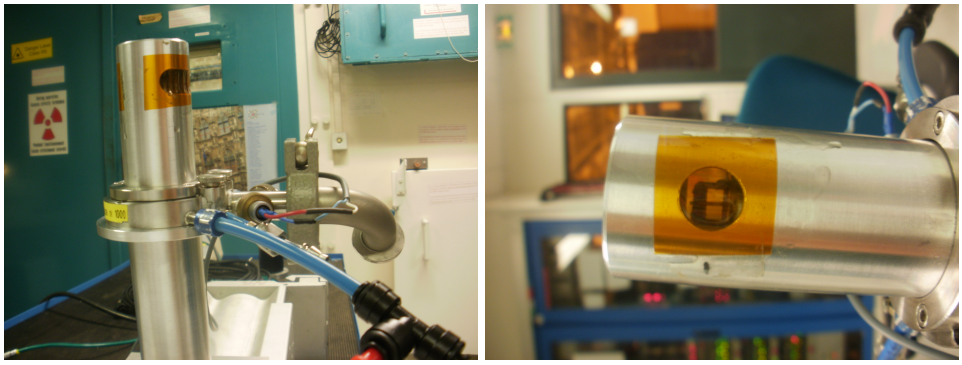

Obrázek 2.8: Pec pro měření amorfních slitin.

neboť se jedná o pásky o šířce přibližně 2 mm a tloušťce 20 μm. Při experimentech s amorfními slitinami byla použita pícka umožňující měření v ochranné atmosféře inertních plynů a ve vakuu. Tato pec je znázorněna na obr. 2.8.

2.3 Koherentní vs. nekoherentní sumace

Časové spektrum vzniká koherentním sečtením rozptýlených fotonů. Jedná se o interferenci fotonů o různé energii, které jsou emitovány vzorkem excitovaným pulzem synchrotronového záření. Základní předpoklad vzniku časového spektra s charakteristickými kvantovými zázněji je současná přítomnost jader vykazující charakteristické štěpení hladin.

V případě *in-situ* experimentů se některé fáze ve vzorku objevují jen na omezenou dobu nebo některé hyperjemné parametry se velice rychle mění (například s teplotou). Tedy během akumulace jednoho spektra dochází k výraznějším změnám hyperjemných interakcí. V tomto případě dochází k nekoherentnímu sečtení více spekter což může významně negativním způsobem ovlivnit vyhodnocení experimentu. V experimentech jaderného dopředného rozptylu neplatí, že součet spekter dvou materiálů by odpovídal spektru směsi těchto materiálů. Tuto vlastnost časových spekter je při vyhodnocení *in-situ* experimentů nutné brát v úvahu.

Příkladem, kde takové chování je možné pozorovat je magnetický přechod z feromagnetického do paramagnetického stavu při dynamicky rostoucí teplotě. V oblasti těsně pod Curieho bodem je změna hyperjemného magnetického pole s teplotou poměrně prudká a v případě rychlosti změny teploty 10 °C/min. dochází právě k nekoherentímu sečtení spekter odpovídajích různým hodnotám hyperjemného pole.

Dostupné programy pro vyhodnocení NFS experimentů však neumožňují vyhodnocování spekter vykazující tento jev. V současné době je na katedře experimentální fyziky vyvíjen software, který by již tuto možnost zahrnoval. Takový nástroj by mohl pomoci v případech, kdy nebylo možné spektra rozumným způsobem vyhodnotit. Příkladem je dekompozice K_2FeO_4 za podmínek kontrolované vlhkosti, viz kapitola 5.2.

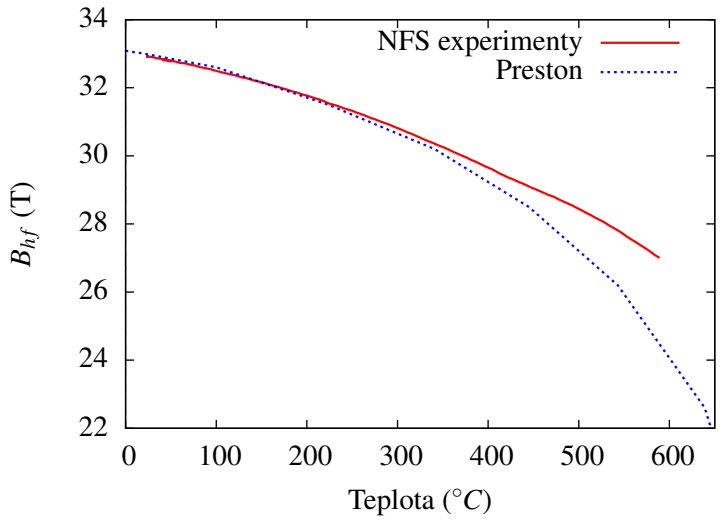

Obrázek 2.9: Kalibrační křivky teploty. Hupe - výsledky podle [108], NFS experimenty - výsledky získané pomocí měření NFS v kalibrované peci.

2.4 Kalibrace teploty

Příklady, které jsou v této práci představeny, jsou fázové transformace za zvýšené teploty, a to v izotermických podmínkách (izotermické experimenty), nebo za konstantního nárůstu teploty (dynamické experimenty).

Důležitým aspektem provádění experimentů za zvýšené teploty je měření teploty. Ta je zaznamenávána průběžně během celého měření a to i v případě izotermických experimentů. Nejlépe je, když může teplotní článek sloužící ke snímání teploty, být co nejblíže studovaného vzorku. Nicméně vždy se poloha termočlánku mírně liší, a je tedy nutné prověřit, zda teplotní gradient mezi vzorkem a termočlánkem není příliš velký. Tento gradient se zvlášť výrazně může projevit při měření s konstantním nárůstem teploty, kdy rozdíl teploty mezi vzorkem a termočlánkem je u těchto experimentů zpravidla větší než u izotermických experimentů. Navíc rozdíl teplot mezi vzorkem a termočlánkem s teplotou roste.

Abychom dosáhli požadované přesnosti měření teploty vzorku, je nutné provést kalibraci teploty v dostatečně širokém oboru teplot. K tomu je možné využít teplotní závislosti některého hyperjemného parametru vhodného kalibračního vzorku. Tím je například teplotní závislost hyperjemného magnetického pole B_{hf} α-Fe [108–113]. Před experimenty je vhodné změřit v požadovaném teplotním rozsahu NFS časová spektra při různých teplotách. Vyhodnocené hyperjemné pole pak srovnat s hodnotami z literatury [108].

V některých případech se rozdíl teplot může lišit až o desítky stupňů Celsia. Příklady těchto kalibračních křivek jsou uvedeny na obr. 2.9, ze kterého jsou patrné poměrně velké odchylky teploty na termočlánku od skutečné teploty na vzorku.

Kapitola 3

Vyhodnocení experimentů

Interakce jader se svým okolím nám poskytují cenné informace o lokálním uspořádání látky a jsou tím, co potřebujeme z experimentu získat. Vyhodnocení experimentů NFS probíhá v několika krocích. Prvním je vytvoření fyzikálního modelu. Ten obsahuje sadu pozic rezonujících (mössbauerovských) jader, kdy každá tato sada je popsána charakteristickými hodnotami hyperjemných parametrů. Každá pozice reprezentuje jádra s nějakým charakteristickým lokálním uspořádáním kolem rezonujícího atomu.

Výběr/sestavení správného fyzikálního modelu je poměrně obtížný úkol. Vždy je vhodné mít co možná nejvíce informací o studovaném materiálu. Na základě fyzikálního modelu je vypočteno časové spektrum, které je následně srovnáno s experimentálními výsledky, a určena hodnota odezvová funkce χ^2 podle vztahu

$$\chi^2 = \sum_i^n \frac{(f_{\mathtt{t}i} - f_{ei})^2}{\sigma_i^2}, \tag{3.1}$$

kde $f_{\mathtt{t}}$ a $t_{\mathtt{e}}$ jsou teoretické a experimentální hodnoty časového spektra a σ je střední kvadratická odchylka měření jednoho bodu spektra. Následně jsou pomocí lokální optimalizační procedury nalezeny hodnoty hyperjemných parametrů tak, aby χ^2 bylo minimální. Tento proces je realizován některým z vyhodnocovacích softwarů [114–117].

Každý program má určité výhody a nevýhody. Program FitSuite [116] umožňuje současné fitování NFS časového spektra a spektra transmisní Mössbauerovy spektroskopie. Jeho použití je však poměrně složité, fitovací procedura je pomalá a není doplněn podrobným manuálem pro uživatele. Program Motif [114,115] má jednoduché ovládání, ovšem neumožňuje práci s distribucemi hyperjemných parametrů. V této práci byl pro vyhodnocení použit program CONUSS [86, 117], který je dostatečně rychlý a současně umožňuje využití distribucí hyperjemných parametrů. Mimo to umožňuje výpočet časového spektra pro případ jaderné Braggovské difrakce. Během let vyhodnocování *in-situ* experimentů NFS se ukázalo, že i tento program má jistá omezení, a proto byl na katedře experimentální fyziky zahájen vývoj nového vyhodnocovacího softwaru, který by umožňoval nekoherentní sčítání spekter, práci s vrstevnatými vzorky a využíval nelokální optimalizační metody pro určování hyperjemných parametrů. Poslední zmíněný bod může být velice užitečný při hledání vhodného fyzikálního modelu.

3.1 Fyzikální model

Fyzikálním modelem rozumíme sadu pozic jader vykazujících různé hyperjemné parametry (různé interakce). Je sestavován tak, aby co nejlépe reflektoval skutečné rozložení jader a jejich interakci s okolím. Tento bod je obdobný s vyhodnocením transmisních Mössbauerovských spekter v energetické doméně. Hledání optimálního modelu pro vyhodnocení NFS experimentů je problematičtější než v případě transmisních měření v energetické doméně, neboť ze tvaru časového spektra není snadné odhadnout, z jakých spektrálních komponent se bude model skládat. Přímý převod spektra do energetické domény není možný, neboť detekujeme pouze amplitudu rozptýleného záření a nikoli fázi [102, 103]. V energetické doméně je zpravidla nafitována do spektra jedna spektrální komponenta modelu a následně částečně na základě sledování spektrálních reziduí (rozdílu fitované křivky a spektra) jsou přidávány další komponenty do fyzikálního modelu. Tuto možnost v případě vyhodnocování NFS experimentů nemáme, neboť ze sledování reziduí není možné odhadnout jaká komponenta ve spektru chybí nebo naopak přebývá.

Pro hledání parametrů modelu, tedy hyperjemných parametrů popisujících materiál, jsou zpravidla využity lokální optimalizační metody. Abychom nalezli správné hyperjemné parametry, je nutné jako vstupní parametry použít hodnoty poměrně blízké optimu. V opačném případě metoda selhává a optimální parametry nejsou algoritmem nalezeny.

V uplynulých letech bylo testováno využití genetických algoritmů pro vyhodnocování NFS. Snahou je vytvořit metodiku schopnou najít správný fitovací model automaticky, bez znalosti materiálu. To by bylo užitečné především při řešení přechodových stavů během fázových transformací, kde není možné zjistit parametry některého z přechodových stavů pomocí *ex-situ* technik ve stacionárním stavu. Nicméně kvůli složitosti odezvové funkce (odezvovou funkcí rozumíme závislost $\chi^2(p_1, p_2, ...p_n)$ na parametrech modelu) tyto techniky selhávají, není tedy možné je rutinně používat.

3.2 Sekvenční fitování

Vyhodnocení *in-situ* experimentů jaderného dopředného rozptylu má řadu specifik. Především se jedná o poměrně velký počet časových spekter změřených při jednom experimentu. Fitační model musí správně popisovat studovaný materiál v poměrně široké oblasti. Aby bylo možné efektivně takové experimenty vyhodnocovat, byl vyvinut software Hubert [118, 119]. Tento program slouží jako nadstavbový program pro výpočty pomocí softwaru CONUSS [117], navíc ale umožňuje sekvenční fitování [120].

Metoda sekvenčního fitování vychází z předpokladu, že hyperjemné parametry po sobě jdoucích spekter se příliš neliší. Výsledné hodnoty fitování jednoho spektra jsou brány jako vstupní hodnoty fitování spektra následujícího. Takto je možné vyhodnotit *in-situ* experiment obsahující kolem sta časových spekter během několika minut.

Celé vyhodnocení probíhá v krocích, které jsou schématicky znázorněny na obr. 3.1. Nejdříve je nafitováno první spektrum ve vyhodnocované sekvenci (ne nutně počátek experimentu). Toto fitování probíhá běžným způsobem pomocí vyhodnocovacího programu Hubert (CONUSS). Pro nalezení optimálních parametrů je použita minimalizace. Po vyhodnocení jsou výstupní parametry programem Hubert přeneseny do vstupního souboru

pro vyhodnocení pro následující spektrum a spuštěna optimalizační procedura. To se opakuje v celé vyhodnocované oblasti. Program současně přehledně vypisuje získané hodnoty do výstupního souboru.

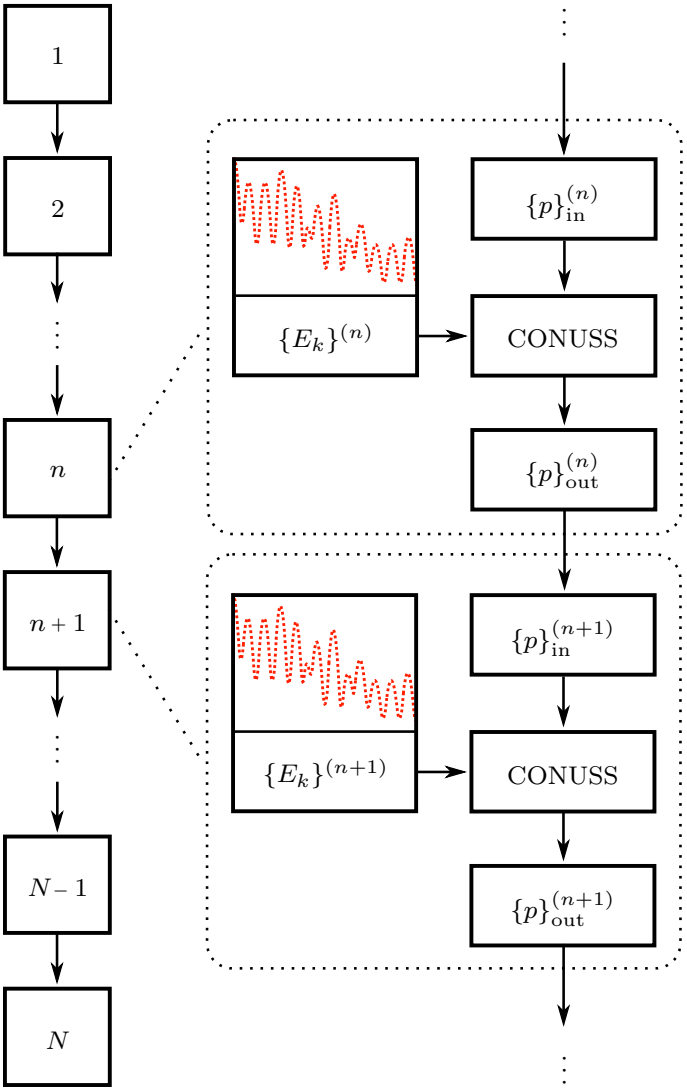

Obrázek 3.1: Schematické znázornění sekvenčního fitování. $1 - -n - -N$ označuje číslo NFS spektra, $\{E_k\}^{(n)}$ Experimentání data časového spektra, k index bodu ve spektru, $\{p\}_{\text{in}}^{(n)}$ sadu vstupních a $\{p\}_{\text{out}}^{(n)}$ výstupních parametrů.

Již z principu sekvenčního fitování je zřejmé, že nezbytnou podmínkou pro úspěšný průběh automatického vyhodnocení je malý rozdíl mezi jednotlivými spektry. Tedy že se hyperjemné parametry příliš nemění. Příkladem, kdy selhává, je přechod z feromagnetického do paramagnetického stavu. Těsně pod Curieho bodem hyperjemné magnetické pole klesá příliš rychle. Změna tohoto pole mezi jednotlivými spektry je příliš velká a lokální

optimalizační procedura není schopná najít optimální parametry, obr. 3.2. V tomto případě je nutný vnější zásah a je nezbytné nastavit vhodnější výchozí parametry pro fit. Takto je možné dosáhnout správného fitu a nalezení správné hodnoty hyperjemného pole.

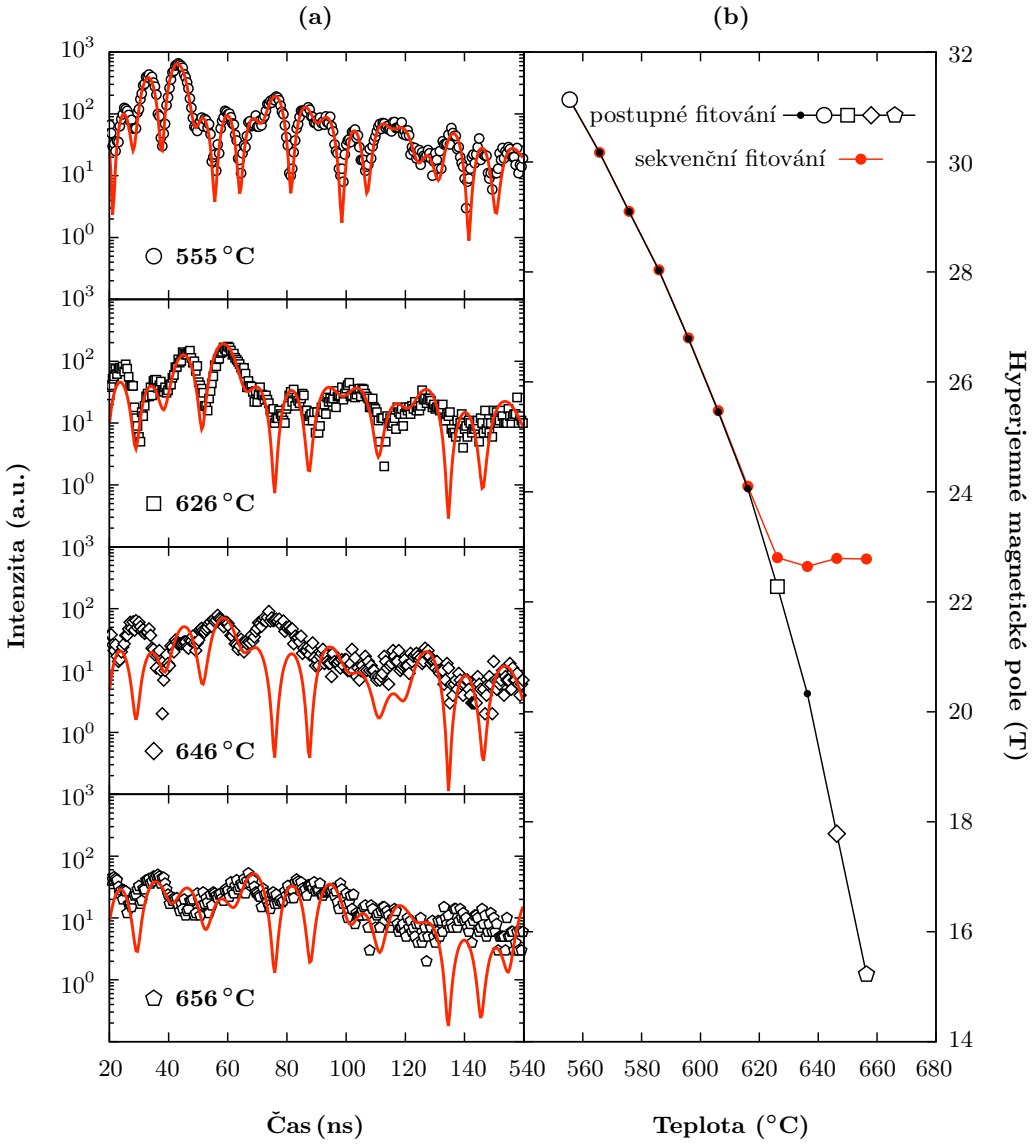

Obrázek 3.2: Průběh fitu přechodu z magnetického do paramagnetického stavu.

Sekvenční způsob vyhodnocení s sebou nese několik aspektů, které budou popsány v následujících podkapitolách. Některé umožňují například optimalizaci použitého vyhodnocovacího modelu.

3.3 Korelace parametrů

Jedním z úskalí vyhodnocení je korelace fitovaných parametrů. K tomu dochází, když fitované parametry mají obdobný vliv na tvar časového spektra. V takovém případě snížení hodnoty jednoho parametru způsobuje zvýšení hodnoty druhého parametru. Tento jev je v případě *in-situ* experimentů možné do jisté míry eliminovat nebo alespoň odhadnout jeho míru.

Celý průběh experimenentu (všechna relevantní časová spektra) je nafitován několikrát, kdy jsou jednotlivé parametry postupně fixovány na různé hodnotě a po fitu jsou hodnoty zbývajících hyperjemných parametrů porovnány. Na obr. 3.3 je znázorněn příklad takového chování pro případ vyhodnocení amorfní slitiny. V grafu jsou vykresleny hodnoty množství jedné (krystalické) komponenty a jejího hyperjemného magnetického pole pro tři různé šířky distribuce hyperjemného magnetického pole. Ve spodním grafu je pak vykreslen parametr χ^2. Z grafu je zřejmé, že vyhodnocení je zatíženo mírnou korelací parametrů a tuto skutečnost je třeba zahrnout do interpretace získaných výsledků.

3.4 Hystereze hyperjemných parametrů

Při sekvenčním fitování jsou pro fitování jednoho spektra použity výsledky vyhodnocení předchozího spektra. Nicméně toto pořadí nemusí nutně odpovídat časové posloupnosti, v jakém byla spektra změřena. Fitovat můžeme ve směru času i opačně, přičemž výsledné hodnoty hyperjemných parametrů by měly být stejné a nezávislé na směru vyhodnocení. V některých případech se však stane, že pro různé směry fitování pozorujeme hysterezi získaných parametrů.

Příklad takové hystereze je znázorněn na obr. 3.4. Jedná se o měření teplotního rozkladu K_2FeO_4. Na obr. 3.4 a je znázorněno množství šestimocného železa na čase žíhání, kdy bylo pro vyhodnocení použito dvoukomponentového modelu. V grafu je zřejmé, že při směru fitování v kladném směru času jsou hodnoty jiné než při fitování proti směru času. To je zpravidla způsobeno nedokonalostí použitého fyzikálního modelu. Poté, co byly do modelu přidány komponenty popisující meziprodukty rozkladu, hystereze ze zmiňované závislosti zmizela, viz obr. 3.4 b. Na obrázcích jsou pro doilustrování situace vykresleny odpovídající průběhy parametru χ^2. I na nich je zřejmé, že při použití pěti komponent dochází k lepší shodě fitu s experimentem.

Samotné pozorování hystereze nám sice nedává žádný návod na to, jaká komponenta ve vyhodnocovacím modelu chybí nebo přebývá a jak model přiblížit reálné situaci ve vzorku, nicméně díky pozorování hysterezí je možné odhalit nedokonalost použitého fyzikálního modelu.

3.5 Izomerní posuv

Jak již bylo zmíněno v úvodu, prostřednictvím experimentů NFS je možné, stejně jako pomocí Mössbauerovy spektroskopie, získat informace o valenčním stavu mössbauerovských atomů prostřednictvím izomerního posuvu. Izomerní posuv je určován vždy relativně ke zvolenému standardu. V Mössbauerově spektroskopii je jako standard voleno α-železo

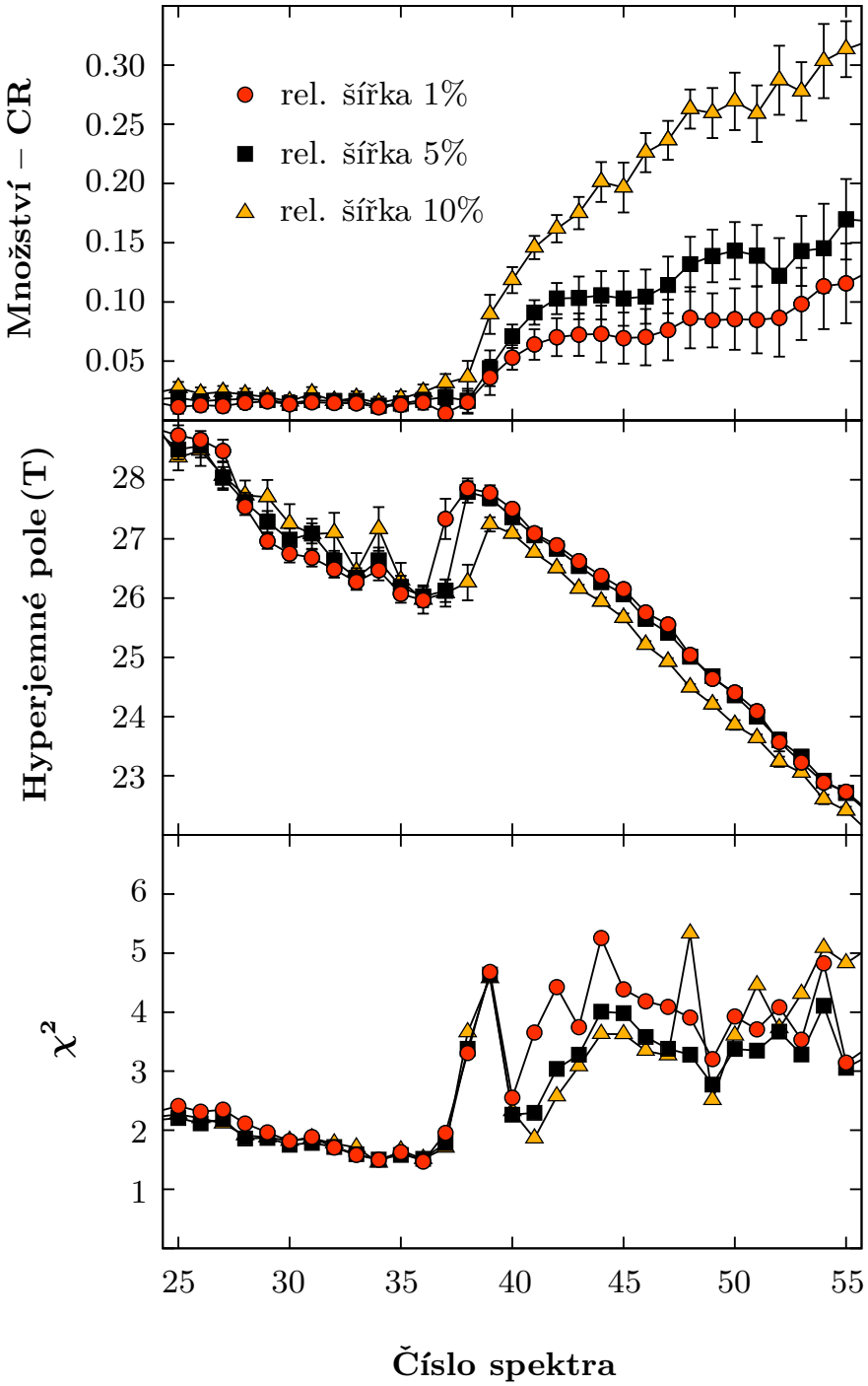

Obrázek 3.3: Korelace parametru. Množství krystalické fáze v amorfní slitině $Fe_{81}Mo_8Cu_1B_{10}$ (nahoře), hyperjemné magnetické pole krystalické komponenty (uprostřed), parametr χ^2 (dole).

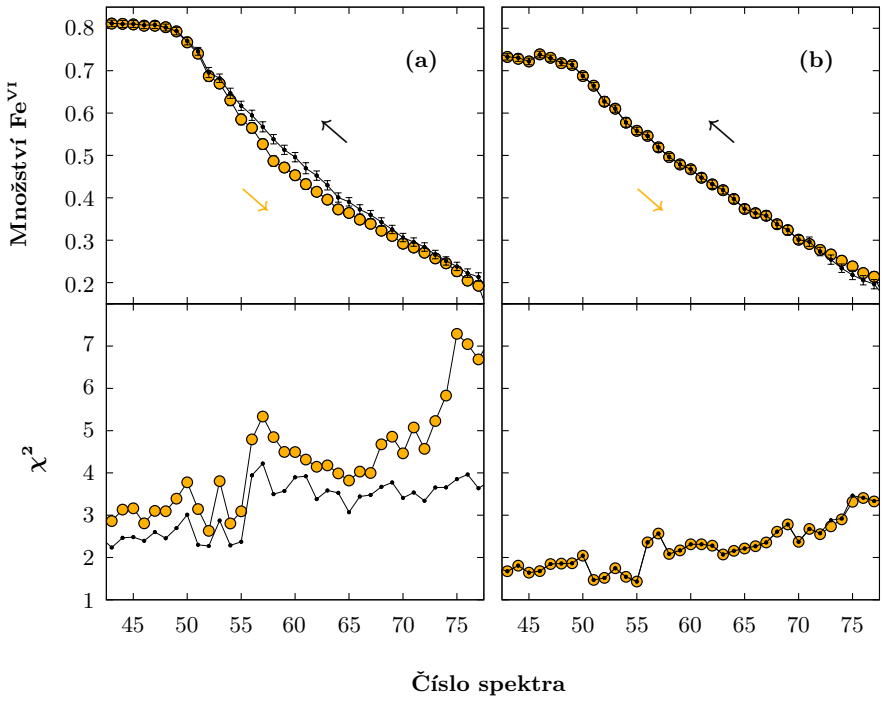

Obrázek 3.4: Hystereze hyperjemných parametrů při vyhodnocení tepelného rozkladu K_2FeO_4.

nebo nitroprusid sodný, které jsou použity i ke kalibraci rychlostní osy spektrometru. Máme změřený posun čar α-železa vůči zářiči a následně při měření studovaných vzorků máme změřený posun spektra vůči zářiči. Tedy vždy můžeme určit izomerní posuv vůči kalibračnímu vzorku.

U experimentů NFS je určení izomerního posuvu poněkud složitější. Pulzy synchrotronového záření použité pro měření NFS jsou z energetického pohledu širokopásmové. Zahrnují fotony v celém oboru energií měřeného spektra (typicky 1-5 meV). Všechny přechody jsou excitovány současně a rozptýlené fotony interferují do výsledného časového spektra. Takto změřené spektrum není možné vztáhnout k žádnému standardu izomerního posuvu. Izomerní posuvy jednotlivých komponent obsažených ve spektru pak můžeme určovat jen relativně vůči sobě.

K získání spektra NFS vztaženého vůči nějakému referenčnímu materiálu (např. α-železa) je možné využít dlouhé (řádově desítky metrů) koherence synchrotronového záření v přímém směru. Do dráhy svazku, buď za vzorek nebo před vzorek, je vložen ještě referenční vzorek. Ten koherentně přispívá ke změřenému spektru. Při vyhodnocení zahrneme do fitovacího modelu také referenční vzorek a izomerní posuvy ve vzorku vztáhneme právě k hodnotě izomerního posuvu tohoto referenčního materiálu.

Tento materiál je volen tak, aby co nejméně ovlivňoval výsledné spektrum, aby překryv spektrálních čar referenčního materiálu a vzorku byl minimální a současně efektivní tloušťka byla přibližně třikrát až desetkrát menší než u studovaného vzorku.

Kapitola 4

Krystalizace amorfních slitin

Porozumění vztahu mezi strukturou materiálu a jeho vlastnostmi je jednou ze základních otázek materiálového výzkumu. Chápání strukturního uspořádání v neuspořádaných systémech, jako jsou například amorfní kovové slitiny, je klíčem pro zlepšení a využití jejich vlastností v konkrétních aplikacích. Tyto technologicky slibné materiály jsou kvůli jejich amorfní struktuře zpravidla označovány jako kovová skla. Chemické složení těchto materiálů umožňuje růst nanokrystalických zrn v amorfní matrici. K tomuto procesu dochází při zvýšení teploty nad určitou kritickou mez a současně dochází ke změně vlastností těchto materiálů. V některých případech dokonce vede ke zlepšení vlastností.

Kovová skla jsou připravena zpravidla rychlým chlazením taveniny o vhodném složení. Při schlazení je v materiálu "zamrazen"neuspořádaný stav taveniny. Při zvýšení teploty nad tzv. teplotu krystalizace u nich dochází k uspořádání atomů do pravidelné krystalové mříže. Volbou vhodného složení těchto materiálu je možné dosáhnout toho, že v materiálu sice vzniknou krystalová zrna, ale jejich velikost je omezena a nedosahují rozměrů větších než několik nm. Volbou složení a žíháním je pak možné připravovat nanokrystalické materiály o vhodných vlastnostech. U takto vytvořených materiálů je pak nižší riziko zhoršení vlastností při zahřátí [121].

I přes to, že jsou tyto materiály studovány již řadu let, jejich výzkum není u konce a stále přitahují pozornost díky svým unikátním vlastnostem [122]. Přechod mezi amorfním a nanokrystalickým stavem je obvykle studován v ustáleném stavu, kdy žíháním za určitých podmínek je získáno jedno určité uspořádání a to je pak korelováno s výslednými vlastnostmi. Méně pozornosti je věnováno přechodovým stavům, které se objevují po krátkou dobu během samotné nanokrystalizace, zvláště pak kinetice formování nanozrn v amorfní matrici.

Feromagnetická kovová skla s amorfní strukturou na bázi železa vykazují aplikačně zajímavější vlastnosti než jejich krystalický protějšek. To je způsobeno především chybějícím uspořádáním na dlouhou vzdálenost, což se projeví především v jejich magnetických vlastnostech [123, 124]. Tyto materiály našly své uplatnění například jako magnetické stínění, jádra transformátorů, senzory a záznamová média [125, 126].

Změny ve struktuře a především formování naokrystalických zrn mění především magnetické vlastnosti těchto materiálů. K tomu dochází především díky feromagnetické výměnné interakci mezi zrny v amorfní matrici. K porozumění krystalizačních procesů je vhodné použít *in-situ* techniku umožňující studium uspořádání atomů na krátkou vzdále-

nost a tou je bezesporu jaderný dopředný rozptyl.

Doposud bylo pro studování fenoménu nanokrystalizace použito řady technik [127–129]. Většina těchto technik ale poskytuje informace *ex-situ* a získání dostatečně kvalitních výsledků vyžaduje dlouhé měření. Proto tyto metody neposkytují žádné relevantní informace o kinetice krystalizace. Metody jako diferenciální skenovací kalorimetrie nebo magnetizační měření umožňují *in-situ* experimenty, nicméně poskytují informace o makroskopických vlastnostech. *In-situ* experimenty poskytující informace na atomární úrovni se zatím omezují pouze na difrakční experimenty s využitím synchrotronového záření. [130–132].

Výhodou NFS experimentů je, že poskytují informace o lokálním uspořádání materiálu tedy i o amorfních slitinách, i když jim chybí uspořádání na dlouhou vzdálenost.

4.1 Popis experimentů

Experimenty jaderného rozptylu byly provedeny na experimentální stanici ID18 a ID22N synchrotronu ESRF v Grenoblu [16,133]. Pro excitaci jader ^{57}Fe bylo použito záření o energii 14.413 keV, spektrální šířce 3 meV a toku 10^9 fotonů/s. Stopa svazku byla 0.7 ± 0.3 mm^2. Odhadnutý výkon dopadajícího záření je asi 2 μW. Vzorek byl umístěn v laboratorní peci (obr. 2.8) a měření probíhala v mírném přetlaku dusíku, přibližně 10 mbar .

Nanokrystalizace byla studována u vzorků amorfních slitin se složením $Fe_{90}Zr_7B_3$, $Fe_{81}Mo_8Cu_1B_{10}$ a $(Fe_{2.85}Co_1)_{77}Mo_8Cu_1B_{14}$. Vzorky byly připraveny metodou rychlého chlazení na rotujícím válci. Vybraná složení zajišťují tvorbu nanokrystalických zrn během prvního stupně krystalizace. Studované amorfní slitiny byly připraveny ve formě pásků o šířce 1-2 mm a tloušťce asi 20 μm. Pro zvýšení rychlosti sběru dat byly připraveny vzorky obohacené izotopem ^{57}Fe na 50 %. V přirozené izotopické směsi je ^{57}Fe zastoupeno pouze 2.17 %.

Experimenty byly provedeny ve dvou režimech, izotermickém a dynamickém. Při izotermickém byla po počátečním nárůstu (40 °C/min) teplota držena konstantní na stanovené hodnotě (obr. 4.1 a). Dynamický experiment znamená měření během konstantního ohřevu z pokojové teploty až po 700 °C (obr. 4.1 b). V obou případech byla NFS časová spektra zaznamenávána v časových intervalech jedné minuty. Experiment byl proveden v transmisní geometrii, a tedy výsledná spektra nesou informace o celém objemu studovaných vzorků.

Pro kvalitativní analýzu *in-situ* experimentů a přehlednou demonstraci výsledků jsou vhodné konturové grafy (např. obr. 4.3), kde na x-ové ose je vyneseno časové zpoždění za excitačním pulzem, na y-ose je pak buď čas žíhání nebo teplota žíhání a intenzita rozptýleného záření je znázorněna v barevné škále. Konkrétně je barevnou škálou znázorněn logaritmus intenzity. Konturové grafy umožňují snadnou orientaci v experimentu. Pro přesné vyhodnocení je nicméně nutná analýza pomocí softwaru CONUSS [86,117] s využitím nadstavbového softwaru Hubert [118]. K této analýze je nutné vytvořit vhodný fyzikální model co nejlépe reflektující specifika vzorku.

Sledované materiály ve stavu po přípravě (as-quenched stav) jsou amorfní a v závislosti na svém složení mohou za pokojové teploty být paramagnetické nebo slabě magnetické, proto je tento neuspořádaný paramagnetický nebo slabě feromagnetický stav reprezentován komponentou vykazující velkou distribuci kvadrupólového štěpení nebo distribucí nízkého magnetického pole. Sledovaná složení vykazují Curiovu teplotu v blízkosti pokojové teploty

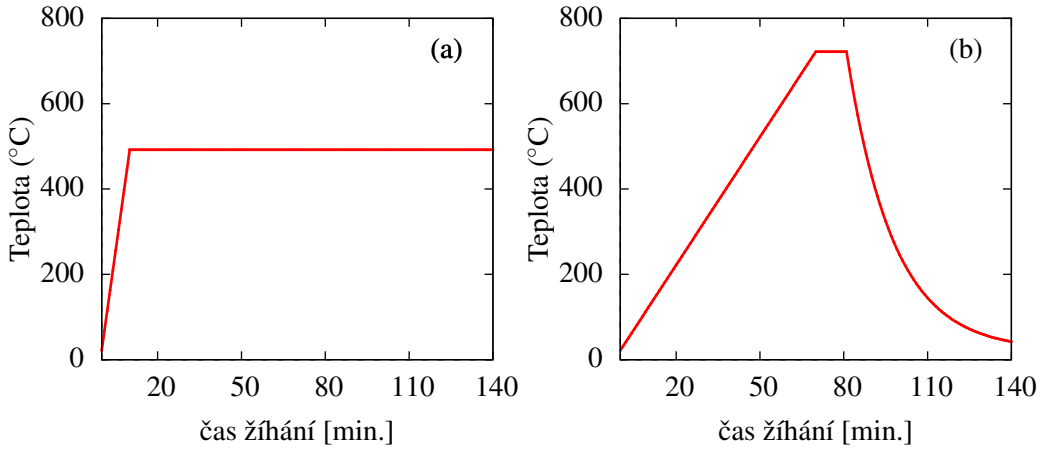

Obrázek 4.1: Teplotní průběh při izotermickém (a) a dynamickém experimentu (b).

nebo mírně nad ní (do 200 °C). Slabě magnetické materiály se vzrůstem teploty přechází do paramagnetického stavu a magnetická interakce mizí.

Při dalším ohřevu po překročení teploty prvotní krystalizace T_{x1} dochází k formování nanozrn v amorfní matrici. Díky složení tato zrna zpravidla vytváří bcc strukturu nanokrystalů. Pro tuto strukturu je typické magnetické uspořádání s hyperjemným polem nad 30 T (při pokojové teplotě). To se v časových spektrech jaderného dopředného rozptylu projeví prostřednictvím kvantových záznějů o vyšší frekvenci (viz obr. 1.4). V případě vytváření bcc struktury α-železa je možné tato zrna popsat pomocí komponenty s dobře definovaným magnetickým polem, která reprezentuje atomy uvnitř těchto zrn, kde atomy vykazují úplnou periodicitu krystalové mříže. U materiálů, kde se nevytváří struktura α-železa, ale například slitina železa a kobaltu, je situace složitější. V takovém materiálu mají zpravidla železa s různým počtem sousedních kobaltů různá hyperjemná pole a krystalová zrna je vhodnější popisovat několika komponentami danými binomickým rozdělením podle počtu sousedních atomů (např. kobaltu).

Atomy přítomné na rozhraní mezi amorfním materiálem a krystalickými zrny vykazují narušenou symetrii a jsou zpravidla označovány jako interfaciální oblasti [104], nicméně jsou stále magneticky uspořádané. Hodnota hyperjemného pole na jádrech z této oblasti je ale nižší než u krystalických zrn. A pole je také hůře definované. Proto tyto oblasti jsou popisovány pomocí distribuce hyperjemného magnetického pole. Přítomnost takových oblastí byla potvrzena také transmisními mössbauerovskými experimenty [134].

Zvolený fyzikální model tedy rozlišuje různá okolí jader železa, neuspořádané (amorfní, AM), částečně uspořádané na hranicích mezi uspořádaným a neuspořádaným stavem (interfaciální - IF) a pravidelně uspořádaná krystalová zrna (CR). Toto rozdělení je schematicky znázorněno na obr. 4.2.

Hyperjemné parametry všech tří komponent vykazují během krystalizace závislost na teplotě a času. Eventuelně se u nich kvalitativně mění typ hyperjemné interakce, jak se děje například při přechodu přes Curiovu teplotu. Fyzikální model musí být schopný všechny tyto změny správně reflektovat a to včetně správného tvaru distribuce hyperjemných parametrů. K jeho určení může být s výhodou využit program Hubert [118].

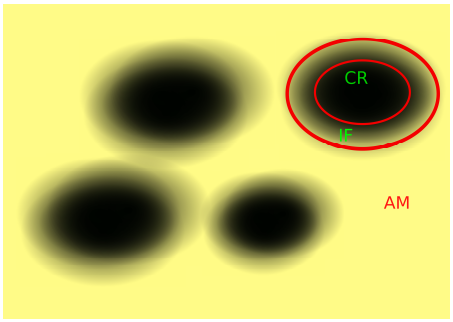

Obrázek 4.2: Schematická znázornění nanokrystalického materiálu. Reziduální amorfní materiál – AM, vnitřní, korová, část nanokrystalických zrn – CR, a interfaciální oblast – IF.

4.2 Vliv teploty, $(Fe_{2.85}Co_1)_{77}Mo_8Cu_1B_{14}$

Prvním příkladem dynamických experimentů je studium kinetiky krystalizace v amorfní slitině o složení $(Fe_{2.85}Co_1)_{77}Mo_8Cu_1B_{14}$. Tento příklad byl vybrán proto, že vhodně demonstruje možnosti *in-situ* experimentů. Tato amorfní slitina vykazuje dva fázové přechody. Jeden přechod prvního druhu a jeden přechod druhého druhu.

$(Fe_{2.85}Co_1)_{77}Mo_8Cu_1B_{14}$ je svým složením atypický oproti ostatním amorfním slitinám použitým v této práci, neboť obsahuje dva magnetické prvky, železo a kobalt. Díky svému složení vykazuje za pokojové teploty magnetické uspořádání. To je patrné z vysokofrekvenčních kvantových záznějů v příslušných časových spektrech, jak lze vidět na obr. 4.3.

Je vhodné zdůraznit, že data zobrazená na obr. 4.3 jsou data získaná přímo z experimentálního zařízení. Bez jakékoli analýzy jsou v grafu patrné dvě zásadní změny charakteru časových spekter, a sice při teplotách 247 °C a 435 °C. Tyto změny souvisí s magnetickým a strukturním přechodem. První přechod je z feromagnetického do paramagnetického stavu a druhá změna charakteru je způsobena nástupem prvotní krystalizace. Tyto body pak rozdělují celý teplotní rozsah na tři oblasti, ve kterých studovaný materiál je amorfní magnetický, amorfní paramagnetický a nanokrystalický magnetický. Rozdílný charakter v časových spektrech v těchto oblastech je znázorněn na obr. 4.4, kde jsou vykresleny příklady spekter ze všech tří oblastí.

Časové spektrum vykazuje relativně vysokou frekvenci kvantových záznějů, která je typická pro magneticky uspořádaný materiál s hyperjemným polem nad 20 T. Současně na tvar tohoto spektra má vliv také efektivní tloušťka, která se ve spektrech projevuje dynamickými zázněji. Celkově pak v tomto případě pozorujeme hybridní zázněje, tedy kombinaci kvantových a dynamických záznějů [135].

Se vzrůstající teplotou se maxima kvantových záznějů posouvají k delším časům a mění se jejich frekvence a současně klesá jejich intenzita. To je dáno poklesem hyperjemného magnetického pole s teplotou. Magnetické kvantové zázněje vymizí, když teplota dosáhne Curiovy teploty. V paramagnetickém stavu pak v energetické doméně namísto sextetu pozorujeme pouze jednu širokou spektrální čáru. Výsledná interference pak vykazuje velice rychlý pokles a příslušné časové spektrum téměř vymizí. Tento jev je znázorněn na obr 4.5 a,

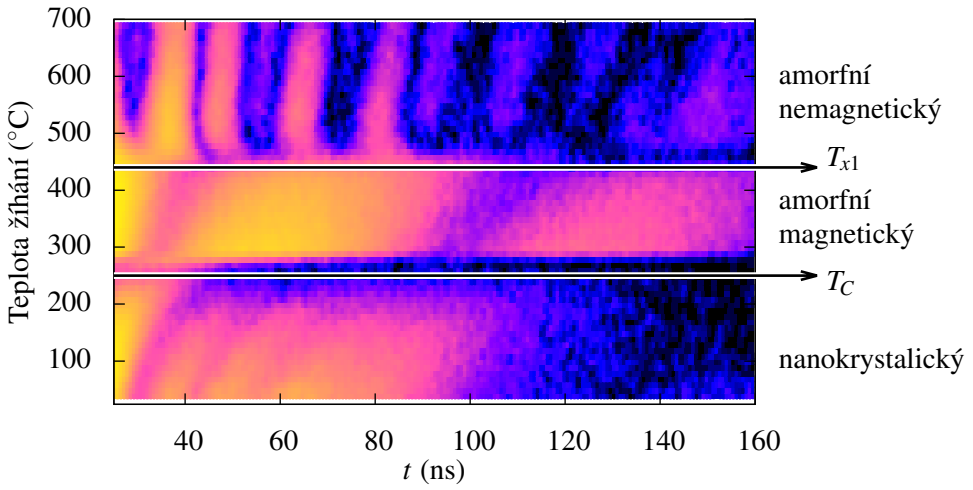

Obrázek 4.3: Konturový graf *in-situ* experimentu NFS amorfního slitiny o složení $(Fe_{2.85}Co_1)_{77}Mo_8Cu_1B_{14}$, dynamické podmínky, teplotní rozsah měření 300 až 1000 K. Teplotní nárůst 10 K/min

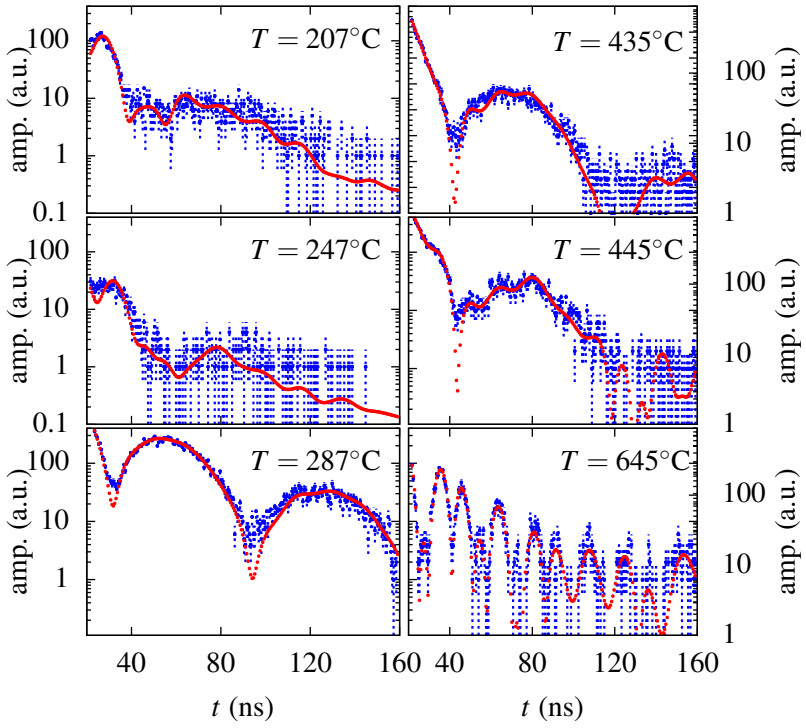

Obrázek 4.4: Časová spektra v různých oblastech (207,°C a 247,°C amorfní magnetická oblast, 287,°C a 435,°C amorfní paramagnetická oblast a 445,°C a 645,°C nanokrystalická magnetická oblast) pro amorfní slitinu $(Fe_{2.85}Co_1)_{77}Mo_8Cu_1B_{14}$.

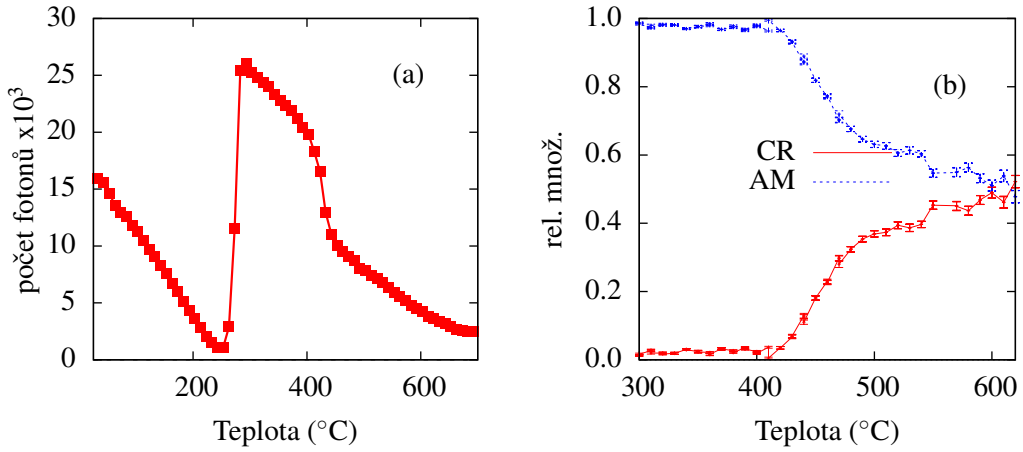

Obrázek 4.5: Celková intenzita záření (a) a relativní poměr spektrálních komponent AM a CR (b) $(Fe_{2.85}Co_1)_{77}Mo_8Cu_1B_{14}$, teploty přechodu jsou vyznačeny šipkou.

kde je vykreslena suma všech detekovaných fotonů v rozsahu 20-160 ns v závislosti na teplotě žíhání.

V grafu jsou patrné výrazné skoky. První odpovídá právě přechodu do paramagnetického stavu a druhý pak nástupu krystalizace. Při nástupu krystalizace, kdy jsou formovány magnetické interakce, zřejmě dochází k částečné polarizaci amorfní matrice vlivem okolních magnetických krystalických zrn. U takto zpolarizovaného amorfního materiálu dochází k rozšíření spektrální čáry, a tedy k rychlejšímu poklesu intenzity v čase. Z toho důvodu pak část fotonů přechází do oblasti pod 20 ns, ve které fotony detekovány nejsou, a proto v grafu pozorujeme pokles celkové intenzity.

Formování nanokrystalických zrn bcc-(Fe,Co) během prvotní krystalizace se projeví objevením se příslušných kvantových záznějů ve spektrech, jak je patrné z obr. 4.4 a. Pro srovnání byla vybrána časová spektra příslušející teplotám 435 °C, 445 °C a 645 °C. Pro 430 °C je vzorek stále amorfní a paramagnetický, to znamená, že na všechna jádra působí pouze elektrická kvadrupólová interakce. S nástupem krystalizace se v oblasti 43–83 ns objevují slabé, ale rychlejší zázněje. Pro teplotu 450 °C jsou tyto zázněje již dobře patrné. Časová spektra při teplotě 640 °C vykazují již zřetelně vyvinuté magnetické oblasti ve vzorku.

Teplotu krystalizace T_{x1} je možné určit ze změny relativního množství amorfní komponenty (AM) a krystalické komponenty (CR) po nafitování všech spekter. Teplotu krystalizace a také Curieově teplotě je možné určit z teplotní závislosti celkové intenzity ve spektru. Tato závislost je vykreslena na obr. 4.4. Zde lokální minimum při 247 °C odpovídá Curiově teplotě amorfního materiálu. Následný rychlý nárůst odpovídá nástupu krystalizace. Další pokles v intenzitě rozptýleného záření je dán poklesem Lamb-Mössbauerova faktoru f s teplotou. Teplota nástupu krystalizace byla určena jako $T_{x1} = 435$ °C. Stejná hodnota byla určena ze závislosti jednotlivých spektrálních komponent na teplotě, obr. 4.5 b.

Na obr. 4.6 je vykreslena teplotní závislost hyperjemného magnetického pole a kvadrupólového štěpení amorfní komponenty. Toto magnetické pole klesá až do chvíle, kdy je srov-

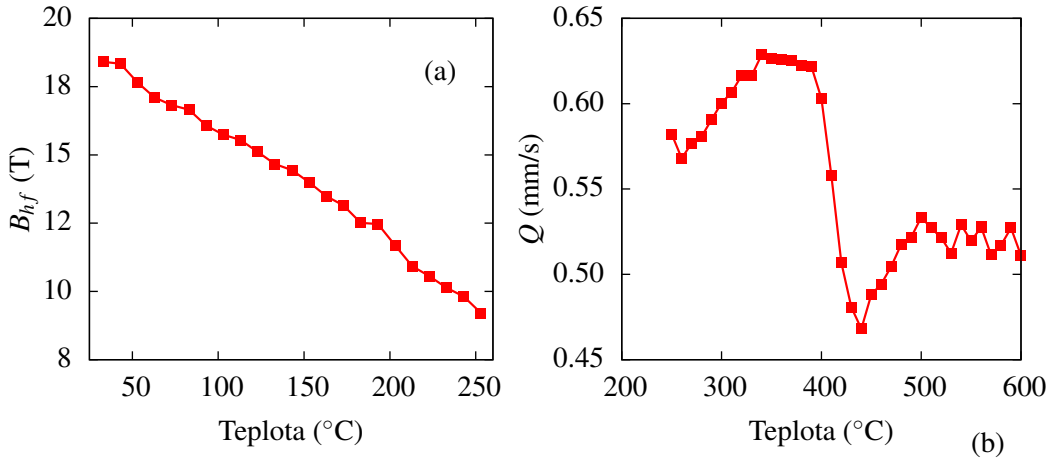

Obrázek 4.6: Teplotní závislost (a) hyperjemného magnetického pole a (b) kvadrupólového štěpení amorfní komponenty

natelné s kvadrupólovým štěpením.

Teplotní vývoj kvadrupólového štěpení poskytuje informaci o lokální symetrii okolí železa v amorfní části materiálu. Vykazuje zřetelné lokální minimum, jak je patrné na obr 4.6 b. Inflexní bod odpovídá nástupu krystalizace.

Tento příklad byl vybrán proto, že na něm lze demonstrovat možnosti sledování strukturních a fázových přeměn pomocí NFS. Při tomto dynamickém experimentu bylo možné sledovat průběh nanokrystalizace během zvyšování teploty a kinetiku krystalizace.

4.3 Vliv magnetického pole, $Fe_{81}Mo_8Cu_1B_{10}$

Pro zlepšení magnetických vlastností nanokrystalických materiálů je někdy nanokrystalizace prováděna za současné aplikace magnetického pole [136]. Výsledkem je indukovaná magnetická anizotropie. Nicméně všechny studie byly prováděny *ex-situ*, tedy až po magnetickém žíhání. Zásadní otázkou je, jaký vliv má aplikované magnetické pole na průběh nanokrystalizace.

Obdobně jako v předchozím případě byly provedeny dynamické experimenty, jednou bez aplikovaného magnetického pole a jednou s aplikovaným polem o velikosti 0.625 T. V tomto případě byl studován vzorek amorfní slitiny o složení $Fe_{81}Mo_8Cu_1B_{10}$. Tento materiál je v as-quenched stavu amorfní a za pokojové teploty velice slabě magnetický. Pomocí Mössbauerovy spektroskopie konverzních elektronů (CEMS) bylo detekováno nepatrné množství krystalických zrn na povrchu vzorku [137] a to na obou stranách pásku.

Konturový graf časových spekter měřených během nárůstu teploty v magnetickém poli a bez něho jsou znázorněny na obr. 4.7. I když aplikované pole je poměrně nízké, jeho vliv je na obr. 4.7 zřetelný. Vliv pole je patrný především ze změny charakteru časových spekter.

Za pokojové teploty je kovové sklo se složením $Fe_{81}Mo_8Cu_1B_{10}$ amorfní a bez magnetického pole vykazuje především kvadrupólovou interakci s malým příspěvkem magnetické interakce. Ta však nad Curieho bodem zcela vymizí. S nástupem krystalizace se objevuje

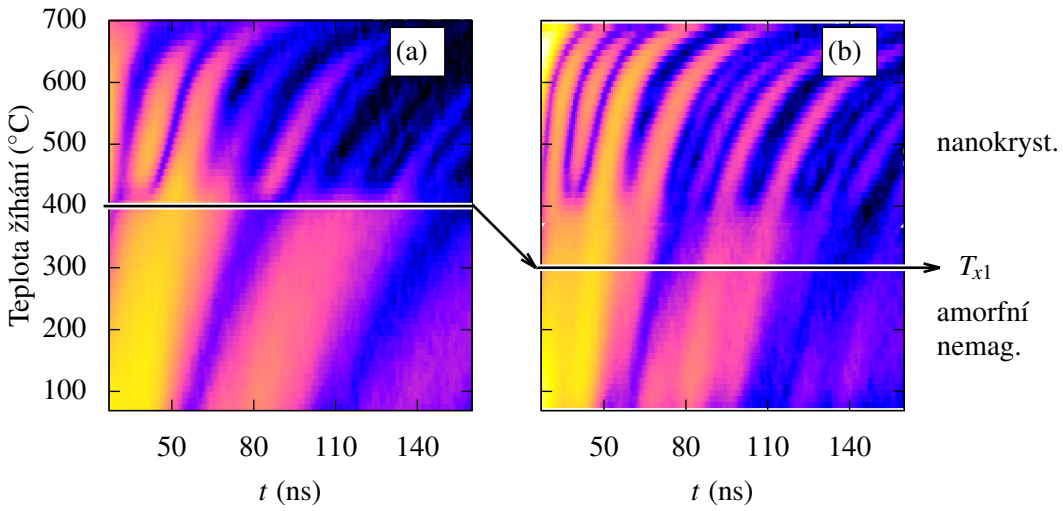

Obrázek 4.7: Contourový graf NFS časových spekter měřených bez magnetickýho pole (a) a s polem 0.652 T (b).

příspěvek magnetické interakce, k čemuž dochází přibližně při teplotě $\sim 400\,^{\circ}$C. Nárůst magnetické interakce je výraznější v případě aplikovaného hyperjemného pole. Spektra obdobného charakteru se objevují již při teplotě o přibližně $100\,^{\circ}$C nižší.

Výsledky analýzy časových spekter jsou ukázány na obr. 4.8, kde jsou vykreslena množství amorfní (AM) a krystalické (CR+IF) fáze v závislosti na teplotě.

Je zřejmé, že nástup krystalizace je vhodnější určovat z obr. 4.8 než z konturového grafu, obr. 4.7. To je mimo jiné také způsobeno tím, že v konturovém grafu je vykreslen logaritmus intenzity, což může způsobovat určité zkreslení.

V závislostech na obr. 4.8 je patrný příspěvek malého množství krystalických zrn, která vznikla již při přípravě. Ve vyhodnocovacím modelu jsou reprezentovány komponentou s ostrou hodnotou magnetického pole. Na obr. 4.9 je znázorněno hyperjemné magnetické pole interfaciální a krystalické komponenty. Pro srovnání je graf doplněn průběhem hyperjemného magnetického pole bcc-železa [108]. Velikost hyperjemného pole bcc železa je mírně větší než u amorfní slitiny.

Při určité teplotě žíhaní se objevují další krystalová zrna a všechna zrna pak dále rostou. Nástup krystalizace je také zřejmý z prudkého nárůstu hyperjemného magnetického pole obou komponent. Z obr. 4.9 je také patrný posun nástupu krystalizace k nižším teplotám v případě aplikace magnetického pole. Teplota nástupu krystalizace poklesla ze $400\,^{\circ}$C na $300\,^{\circ}$C. Nižší hyperjemné magnetické pole s ohledem na bcc-železo je zřejmě způsobeno malým rozměrem nanokrystalů a také možnými příměsemi ostatních prvků (Cu, Mo, B). S rostoucí teplotou pak dále hyperjemné pole klesá s tím, jak se teplota přibližuje Curieho bodu.

V této kapitole bylo ukázáno, jak NFS *in-situ* experimenty umožňují sledovat krystalizační procesy. Pomocí *in-situ* experimentů byl také pozorován vliv magnetického pole na krystalizaci. Hlavním rozdílem mezi krystalizací v poli a bez pole je teplota nástupu krystalizace a samotná kinetika krystalizace. Zatímco na výsledném materiálu se přítomnost pole během krystalizace výrazně neprojeví.

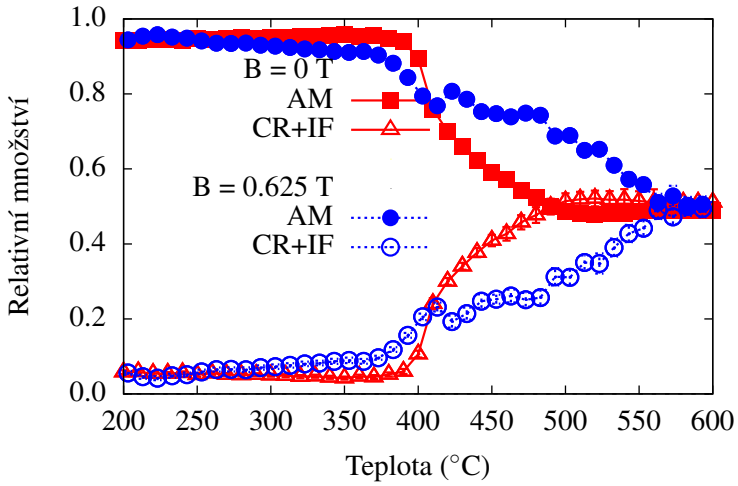

Obrázek 4.8: Relativní množství amorfní (AM) a nanokrystalické (IF+CR) komponenty v závislosti na teplotě pro $Fe_{81}Mo_8Cu_1B_{10}$, žíháno bez pole a v poli.

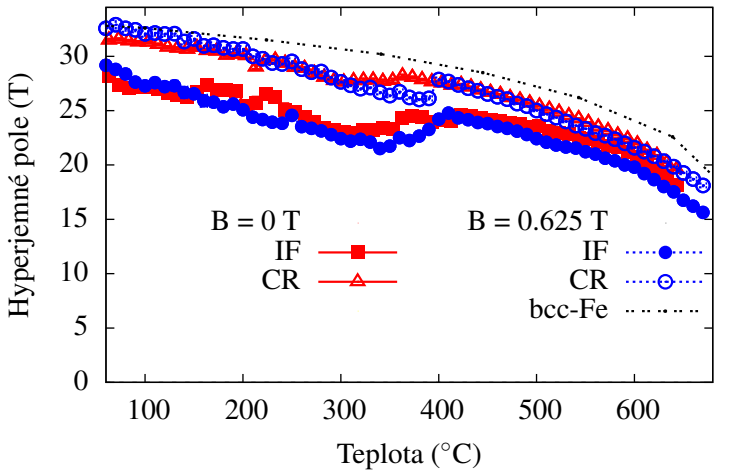

Obrázek 4.9: Hyperjemné magnetické pole interfacialní a krystalické komponenty pro krystalizaci $Fe_{81}Mo_8Cu_1B_{10}$ v poli a bez pole. Pro srovnání je vykresleno hyperjemné magnetické pole bcc-železa [108].

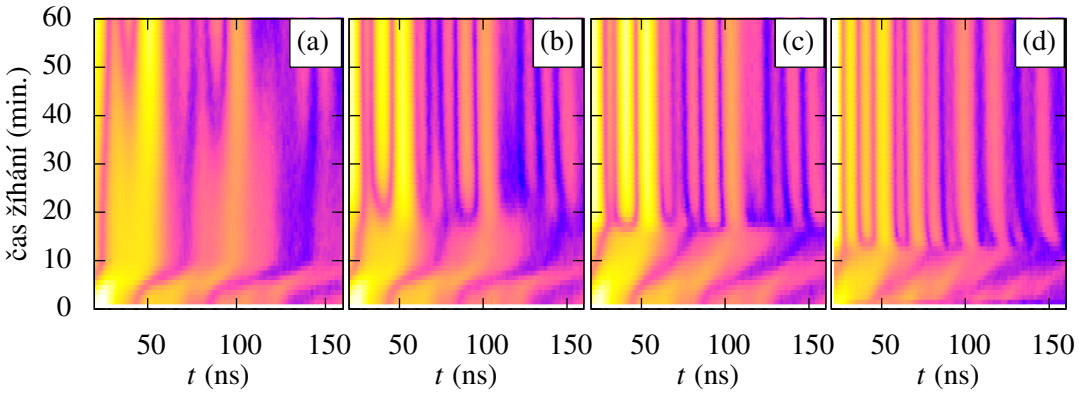

Obrázek 4.10: Konturový graf izotermického NFS experimentu na amorfním $Fe_{90}Zr_7B_3$ za teploty 470 °C (a), 480 °C (b) a 510 °C bez magnetického pole (c) a v magnetickém poli 0.652 T při teplotě 480 °C (d).

4.4 Izotermické experimenty, $Fe_{90}Zr_7B_3$

V předchozích dvou případech byly experimenty prováděny během nárůstu teploty a tedy systém byl vystaven změně podmínek během krystalizace a na krystalizaci měl vliv ubíhající čas a také narůstající teplota. Nyní se zaměříme na studium kinetiky krystalizace za konstantních podmínek.

V tomto případě byly studovány vzorky amorfního $Fe_{90}Zr_7B_3$, které byly připraveny stejnou technikou jako předcházející dva systémy, tedy rychlým chlazením taveniny na rotujícím válci. Rozměry vzorků byly také stejné. Po počátečním rychlém nárůstu (40 °C/min) byla teplota držena na konstantní hodnotě. Spektra jaderného dopředného rozptylu byla detekována vždy po dobu jedné minuty. Pro experimenty byly zvoleny teploty 470 °C, 480 °C a 510 °C. Experiment ve 480 °C byl navíc proveden ještě i s aplikací magnetického pole 0.652 T [138].

Na obr. 4.10 jsou znázorněny konturové grafy. V as-quenched stavu je studovaný materiál paramagnetický a vykazuje typické spektrum materiálu s kvarupólovou interakcí. V závislosti na teplotě žíhání se objevují v rozmezí 10-30 minut od začátku žíhání první náznaky krystalizace. Vznikající nanokrystaly jsou identifikovány pomocí hyperjemné magnetické interakce, neboť u krystalických zrn působí na jádra hyperjemné pole s velikostí nad 20 T. To se projeví kvantovými zázněji o vyšší frekvenci. Protože se během experimentu teplota nemění, nemění se zásadně ani poloha kvantových záznějů.

Časový vývoj jednotlivých komponent (AM, CR, a IF) je vykreslen na obr. 4.11. Všimněme si, že na začátku krystalizace je ve studovaných vzorcích vyšší zastoupení interfaciální fáze než krystalické. To indikuje, že zrna jsou poměrně malá, a proto většina atomů tvoří povrchovou část vzorku. Následně zrna rostou a proto množství CR fáze převyšuje fázi IF. Množství IF se ustaluje na určité hodnotě.

Nárůst teploty žíhání z 470 °C na 480 °C zrychluje formování nanozrn. Při 480 °C k dosažení 60 % z celkového množství nanozrn stačí třikrát nižší čas než při 470 °C (x-ové osy mají jiný rozsah). Další nárůst teploty na 510 °C ještě krystalizaci zrychluje (obr. 4.11c). Stejného efektu je však dosaženo, když je na vzorek žíhaný při teplotě 480 °C aplikováno magnetické pole o velikosti 0.652 T.(obr. 4.11d). Čas potřebný ke krystalizaci je asi třikrát

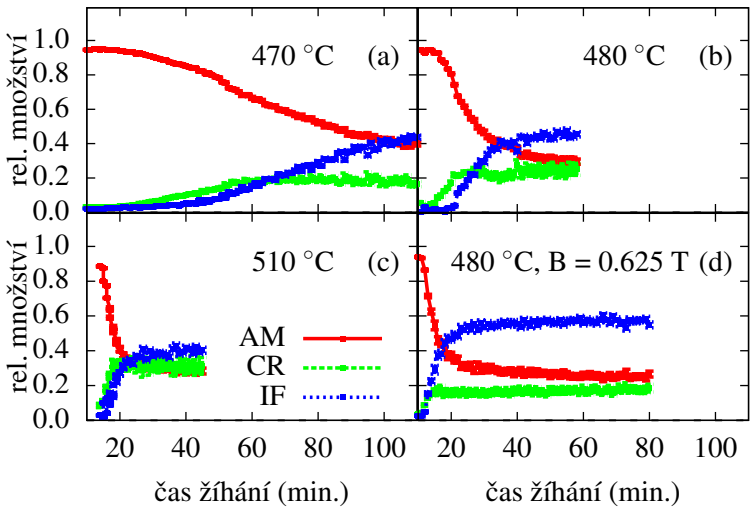

Obrázek 4.11: Relativní množství jednotlivých spektrálních komponent, amorfní (AM) - zelené čtverce, krystalická zrna (CR) - modrá kolečka a interfaciální oblast (I) fialové trojúhelníky) na čase při teplotách 470 °C (a), 480 °C (b), 510 °C (c) a 480 °C v externím poli 0.652 T (d).

kratší než v případě nulového pole.

Relativní množství krystalické a interfacialní komponenty v závislosti na čase je ukázáno na obr. 4.12. Jak již bylo zmíněno, poměrně malá změna v teplotě žíhání má zásadní vliv na rychlost krystalizace. Se změnou teploty na 510 °C již tak výrazná změna rychlosti krystalizace spojena není. Je zajímavé, že při žíhání při 480 °C se vytvoří podobné množství krystalových zrn.

Obr. 4.12 srovnává množství AM, CR a IF [105]. Z tohoto grafu je zřejmé, že ve všech třech případech probíhá krystalizace obdobným způsobem. Nicméně obr. 4.12 b odhaluje zásadní rozdíl mezi jednotlivými průběhy krystalizace. V něm je vykresleno množství krystalické a interfaciální složky dohromady, tedy CR+IF v porovnání s experimentem při nejnižší teplotě (470 °C).

Hyperjemné magnetické pole B_{hf} krystalické a interfaciální komponenty je s ohledem na čas žíhání znázorněno na obr. 4.13. Hyperjemné pole nejdříve roste a pak saturuje na určité hodnotě. Nižší hodnota na začátku krystalizace je způsobena neuspořádaností nových zárodků zrn. Saturační pole závisí na teplotě žíhání. Toto pole je přibližně o 1.5 T menší než pro bcc-železo [108], ke snížení pole dochází v důsledku malých rozměrů nanozrn.

V této kapitole byly experimenty NFS aplikovány na studium nanokrystalizace při izotermickém žíhání. Díky této technice bylo možné sledovat detailní vývoj nanokrystalických zrn v amorfní matrici. Tato technika umožnila porovnat kinetiku krystalizace v závislosti na teplotě a aplikovaném magnetickém poli. Zajímavým zjištěním je, že zatímco charakter krystalizace je ve všech případech stejný, rychlost krystalizace se rapidně mění s teplotou a také aplikovaným magnetickým polem.

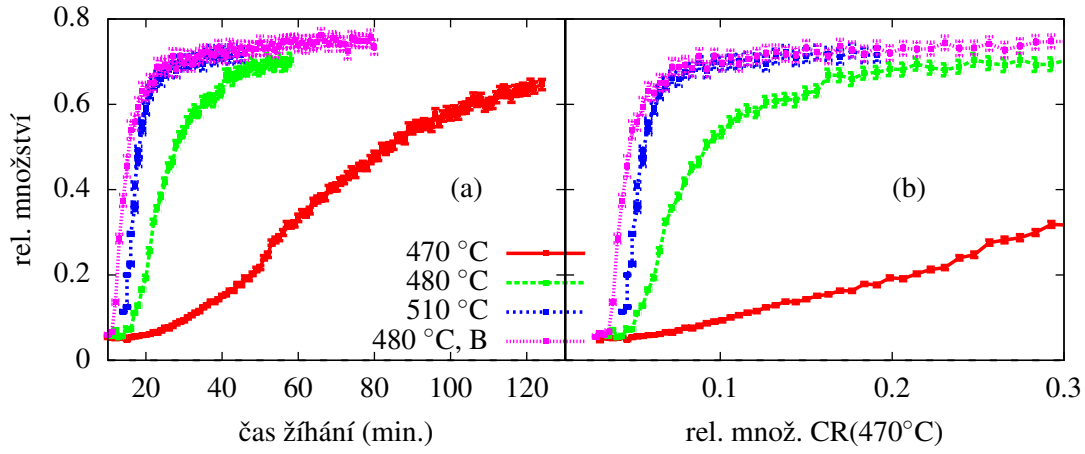

Obrázek 4.12: Relativní množství krystalické a interfaciální složky (CR+IF) v závislosti na teplotě žíhání (a), relativní množství krystalické a interfaciální složky (CR+IF) v závislosti na množství krystalické fáze při teplotě 470 °C (b) .

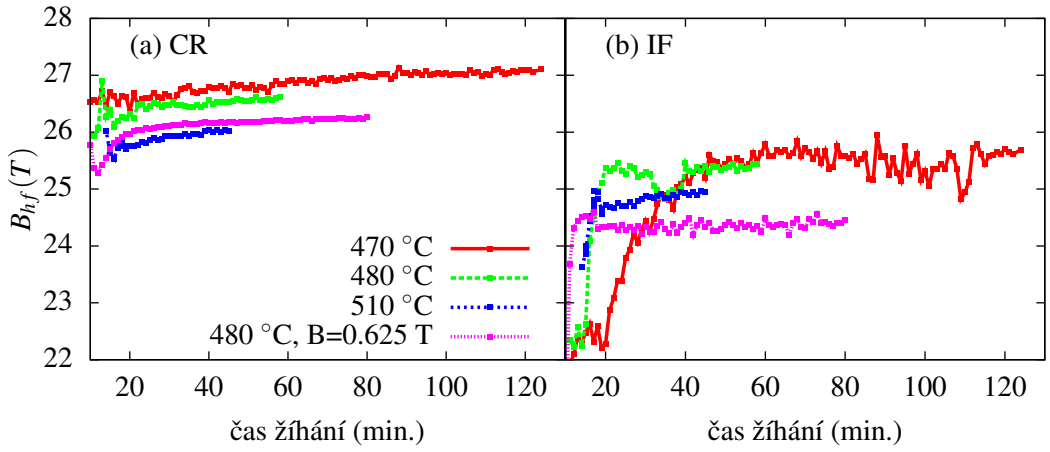

Obrázek 4.13: Hyperjemné magnetické pole CR (a) a IF (b) komponenty v závislosti na čase žíhání amorfní kovové slitiny $Fe_{90}Zr_7B_3$.

Kapitola 5

Dekompozice K_2FeO_4

Sloučeniny železa ve vysokovalentním stavu mají díky svým oxidačním vlastnostem velký potenciál pro různé aplikace [139]. Mohou být využity k čištění vod [140] a nebo výrobu vysokokapacitních, pro životní prostředí šetrných baterií. Aby jejich potenciál mohl být plně využit, je užitečné porozumět procesům, které jsou zodpovědné za jejich vznik i rozklad. Toho je možné docílit například s pomocí lokální *in-situ* techniky jakou je jaderný dopředný rozptyl. Sloučenina K_2FeO_4 [141] obsahuje železo ve stavu 6+. Nicméně je nestabilní a za přítomnosti vlhkosti nebo za vyšší teploty se rozkládá na K_2FeO_4 [142].

5.1 Dekompozice vlivem teploty

V této části budou popsány výsledky *in-situ* studie teplotního rozkladu K_2FeO_4 [107] pomocí jaderného dopředného rozptylu [143]. Během tohoto rozkladu je železo ve stavu 6+ redukováno do stavu 3+. V obou případech je železo v tetraedrální koordinaci, tedy obklopeno čtyřmi kyslíky.

Experimenty jaderného dopředného rozptylu byly provedeny na vzorku K_2FeO_4 mírou obohacení nuklidem ^{57}Fe asi 90 %. Vzorek vykazoval poměrně velkou disperzi velikosti částic, od desítek nanometrů až po desítky mikrometrů [143]. Prášek studovaného vzorku byl nasypán do kapiláry (obr. 2.4) a umístěn do pece. Následně byl žíhán při teplotách 200 °C, 220 °C, 235 °C a 250 °C. Rychlost ohřevu na stanovenou teplotu byla 50 °C/min.

Časová spektra byla akumulována během ohřevu i následného žíhání na konstantní teplotě vždy po dobu jedné minuty a následně zapsána do souborů. Celková doba trvání jednoho experimentu byla mezi 150 a 220 minutami. Všechny experimenty byly provedeny na experimentálním stanovišti P01 ve výzkumném centru DESY v Hamburku. Pro měření byl použit monochromatizovaný svazek polarizovaného záření s velikostí stopy 1 mm×2 mm. Šířka energetického pásma použitého záření byla 5 meV a energie 14.41 keV. Tato energie odpovídá jadernému přechodu ^{57}Fe.

Výsledky pozorování dekompozice za výše zmíněných teplot jsou znázorněny ve formě konturových grafů na obr. 5.1. Proces dekompozice můžeme kvalitativně sledovat podle změn v charakteru kvantových záznějů. Začátek dekompozice je možné určit jako místo, kde se objeví kvantové zázněje o vyšší ferekvenci. To je spojeno s formováním magneticky uspořádaného $KFeO_2$, což je produkt dekompozice. Z konturových grafů, obr 5.1, je patrné, že rychlost dekompozice roste se stoupající teplotou žíhání. Nicméně pro podrobnější

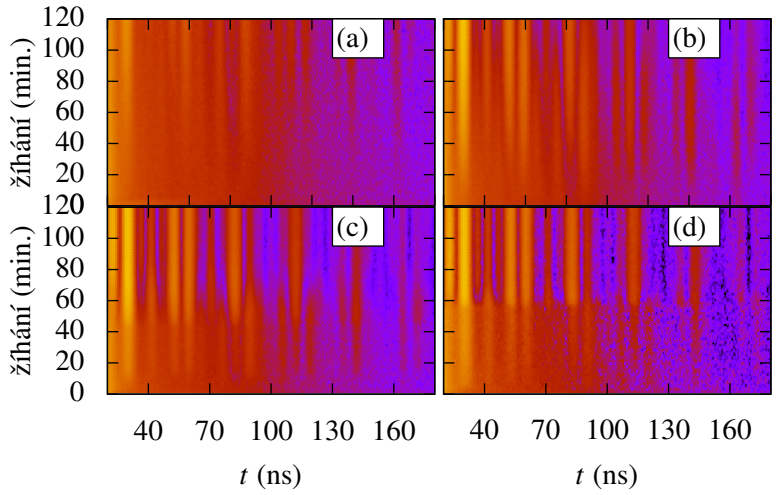

Obrázek 5.1: Konturový graf NFS spekter z experimentu teplotního rozkladu K_2FeO_4 při teplotách 200 °C, 220 °C, 235 °C a 250 °C.

popis dekompozičního procesu je nutné provést vyhodnocení celého experimentu pomocí softwaru Hubert [120].

Použitý fyzikální model obsahuje pět spektrálních komponent [143]. První reprezentuje původní materiál, tedy K_2FeO_4. Kvadrupólový moment tohoto materiálu byl určen jako Q_I=0 mm/s a izomerní posun IS_I=-0.9 mm/s [107]. Druhá komponenta popisuje produkt dekompozice $KFeO_2$. Tato komponenta vykazuje ve shodě s [107] hypejemné pole B_{II}=45.8 T, kvadrupólové štěpení $Q_{II} = 0.5$ mm/s a izomerní posuv IS_{II}=0.3 mm/s. Zbývající tři komponenty byly přisouzeny meziproduktům dekompozičního procesu [143] s ruzným lokálním okolí železa. Během fitování byly zpřesňovány následující parametry: relativní zastoupení jednotlivých komponent W_I, W_{II}, W_{III}, W_{IV}, W_V, jejich izomerní posun IS_I, IS_{II}, IS_{III}, IS_{IV}, IS_V, hyperjemné magnetické pole komponenty II a III, tedy B_{II} a B_{III}, a tloušťka vzorku T_h. Izomerní posun IS_I byl fixován na hodnotě určené z transmisních měření, neboť NFS umožňuje určit pouze rozdíl izomerních posuvů, ne jejich absolutní hodnotu. K tomu by bylo nutné provádět experimenty s externím standardem. To je však experimentálně poměrně komplikované a navíc vyhodnocení takových experimentů je poměrně složité.

Na obr. 5.2 je znázorněn úbytek relativního množství K_2FeO_4 na čase pro všechny teploty žíhání. V tomto obrázku je možné pozorovat kinetiku dekompozičního procesu. Zatímco křivky pro teploty 200 °C a 220 °C vykazují spíše rovnoměrný pokles, u křivek pro teploty 235 °C a 250 °C je možné pozorovat rychlý pokles a saturaci následovanou rychlým poklesem.

Množství všech pěti komponent pro teploty žíhání 200 °C, 220 °C, 235 °C, 250 °C jsou znázorněny na obr. 5.3–5.6. Komponenty III a V jsou patrné pro všechny teploty, zatímco komponenta IV se objevuje pouze pro teploty 220 °C a 235 °C.

Proces formování a růstu zrn $KFeO_2$ může být sledován prostřednictvím hyperjemného magnetického pole, kdy rozměrově malá zrna vykazují nižší hyperjemné pole než zrna větší. Podobné chování je možné pozorovat například u zrn α-železa [104]. Pro zdůraznění korelace mezi množstvím $KFeO_2$ a hyperjemným polem jsou v obr. 5.7 vykresleny mimo hyperjemného magnetického pole druhé komponenty B_{II} také její množství. V případě teplot 200 °C a 220 °C hyperjemné magnetické pole saturuje spíše na začátku dekompozice,

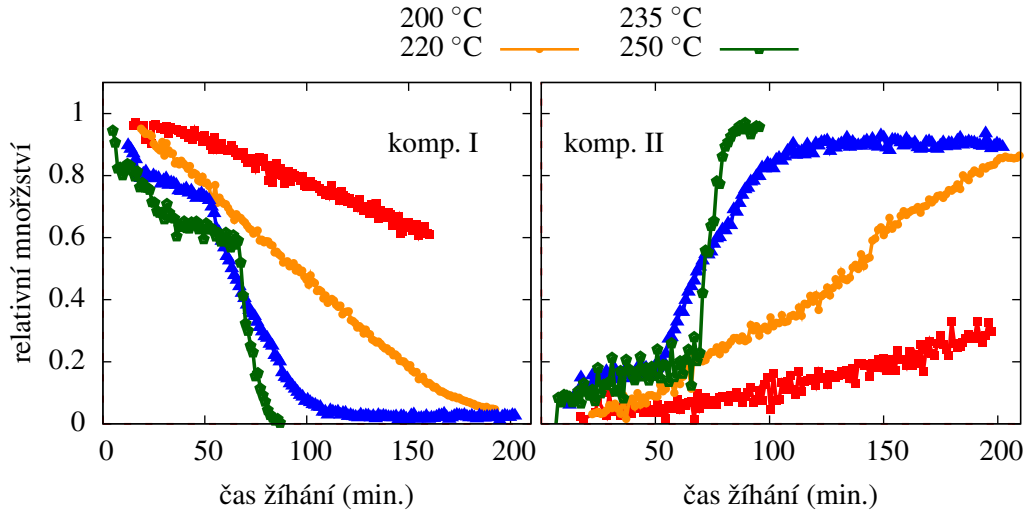

Obrázek 5.2: Množství (a) K_2FeO_4 and (b) $KFeO_2$ během dekompozičního procesu K_2FeO_4 při teplotách 200 °C, 220 °C, 235 °C a 250 °C.

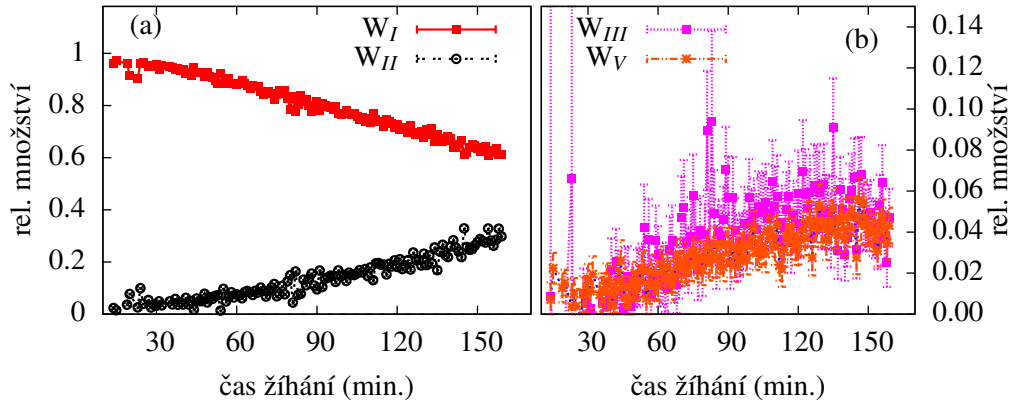

Obrázek 5.3: Závislost množství jednotlivých komponent dekompozice na čase žíhání pro teplotu 200 °C.

zatímco při teplotách 235 °C a 250 °C dochází k saturaci až souběžně se schodem v dekompozici.

Jaderný dopředný rozptyl je lokálně citlivou metodou. Na atomy se stejným okolím působí stejné nebo velice podobné hyperjemné interakce, proto je popisujeme jednou spektrální komponentou. Na počátku experimentu vzorek obsahuje pouze K_2FeO_4 ve formě zrn. Všechny atomy s výjimkou těch na povrchu (kterých je zanedbatelné množství) mají stejné okolí, a tedy i stejné hyperjemné pole. Lokální okolí se v průběhu dekompozice mění a jádra jsou vystavena jinému působení okolí. Proto množství komponenty I přímo odráží rozklad prekurzoru (původního materiálu). Analýza této křivky nám přímo poskytuje informaci o rozkladu K_2FeO_4. Nicméně formování produktu celého procesu může probíhat více cestami. Může vznikat celá řada meziproduktů, kdy každý takový meziprodukt je charakterizován určitou sadou hyperjemných parametrů. Nicméně během přechodových procesů, například v průběhu chemických reakcí, dekompozičních procesů nebo fázových přeměn

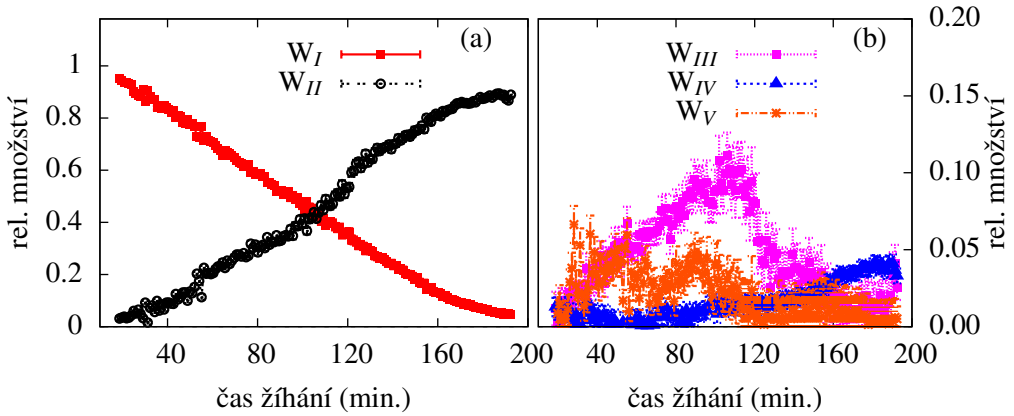

Obrázek 5.4: Závislost množství jednotlivých komponent dekompozice na čase žíhání pro teplotu 220 °C.

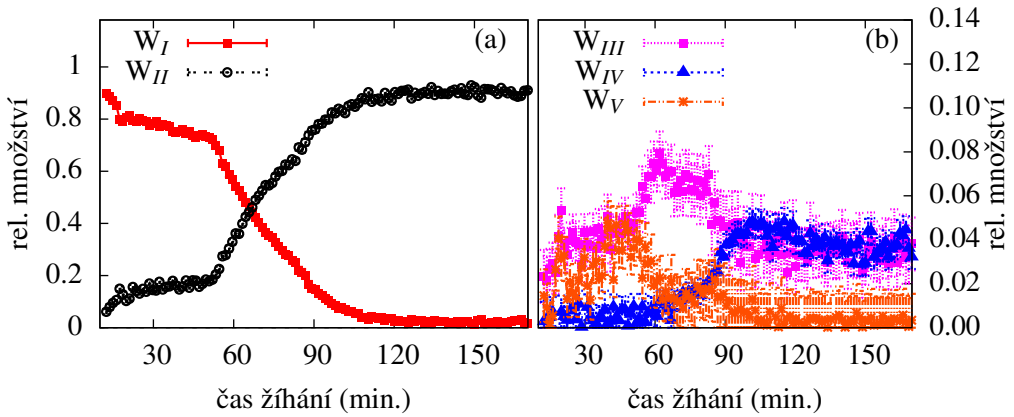

Obrázek 5.5: Závislost množství jednotlivých komponent dekompozice na čase žíhání pro teplotu 235 °C.

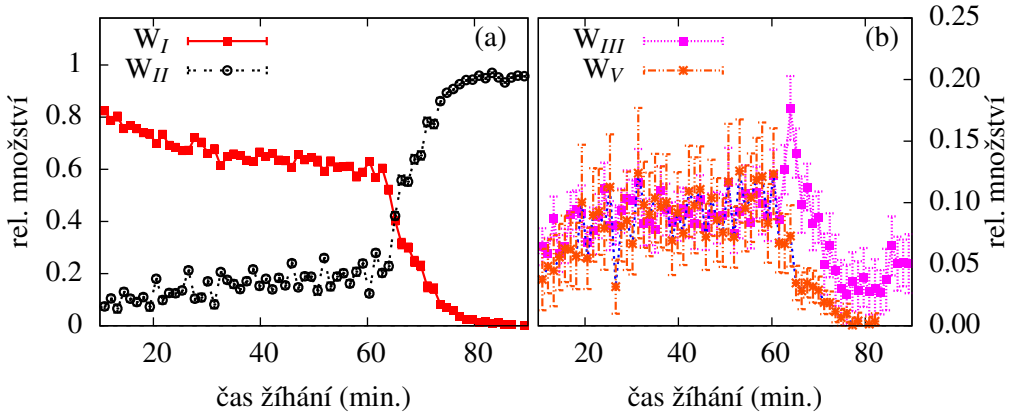

Obrázek 5.6: Závislost množství jednotlivých komponent dekompozice na čase žíhání pro teplotu 250 °C.

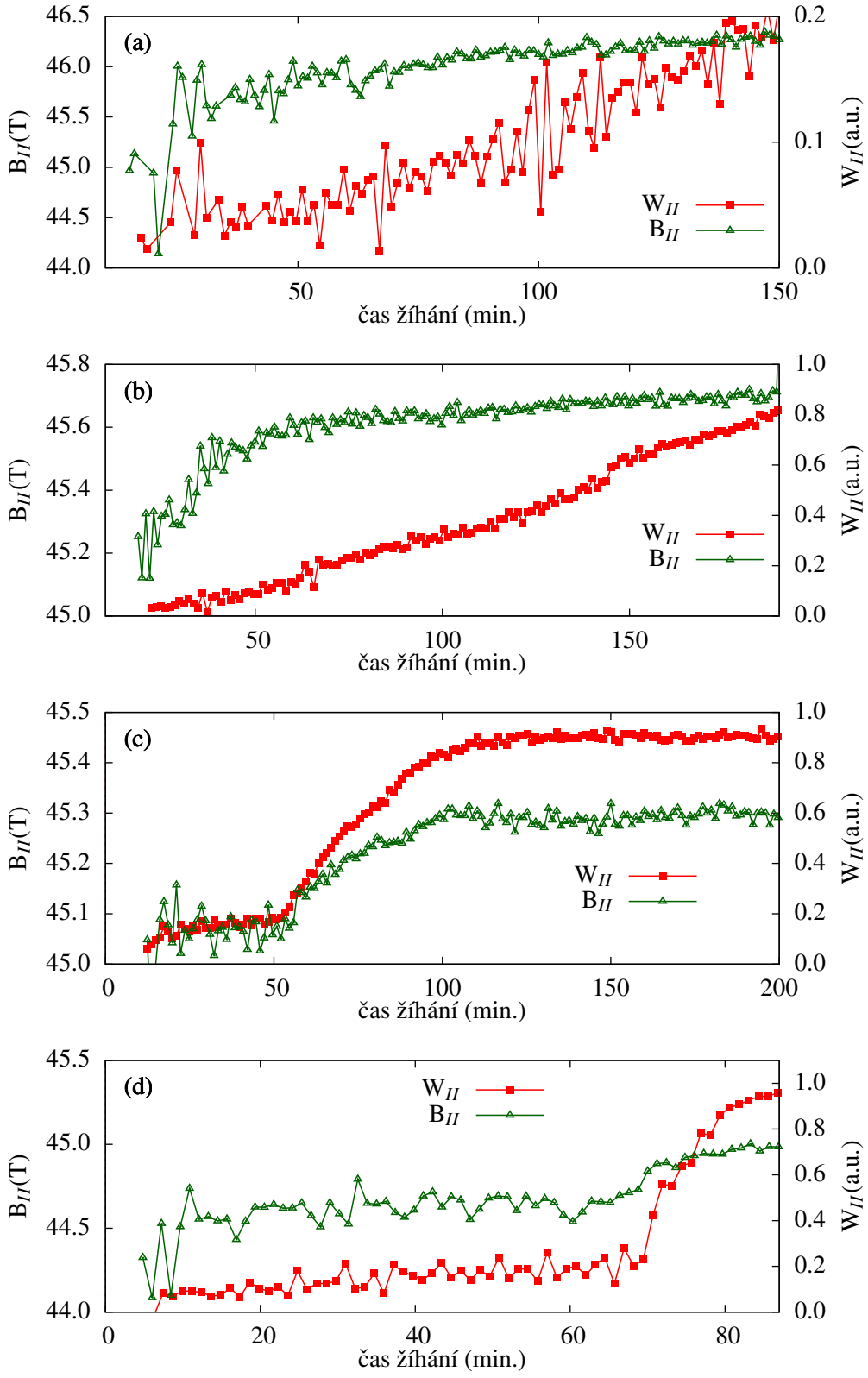

Obrázek 5.7: Hyperjemné magnetické pole (zelené trojúhelníky) korelované s množstvím $KFeO_2$ (červené čtverce) pro teploty 200 °C (a), 220 °C (b), 235 °C (c) and 250 °C (d).

se atomy ocitají v určitém nedefinovaném stavu, který může vykazovat různé hyperjemné interakce. To se může dít například kvůli ne úplně uspořádanému okolí.

U zde popisovaných experimentů, kdy dochází k přechodovým stavům, je třeba zohledňovat také časové okno experimentu. Pro tyto experimenty je časové okno 1min. Rychlejší procesy jsou nepozorovatelné, neboť jsou v rámci jednoho spektra zprůměrovány.

Dynamika studovaného dekompozičního procesu může být ovlivněna řadou faktorů, termodynamickými potenciály přítomných sloučenin, teplotou, rozměrem zrn apod. U procesů v pevné fázi je omezen pohyb atomů na větší vzdálenost, a proto je potřebné tento aspekt zohledňovat. V případech, kdy transformace není isostrukturální, například když je formována chemicky odlišná látka, difúze atomů musí hrát zásadní roli. Navíc při těchto změnách může docházet k uvolňování plynů a také ke změnám hustoty materiálů. Tyto změny budou způsobovat vznik prasklin v materiálu. Ty pak usnadňují transport atomů a také odchod plynů během transformace.

U studovaného procesu dekompozice K_2FeO_4 na $KFeO_2$ dochází právě ke změně hustoty a uvolnění plynů. Jak je znázorněno v následující rovnici

$$4K_2FeO_4 \rightarrow 2K_2O + 4KFeO_2 + 3O_2. \tag{5.1}$$

Během rozkladu dochází k transportu atomů K, Fe a O. Hustoty jednotlivých materiálů jsou $\rho(K_2FeO_4)$=2.355 kg/m^3, $\rho(KFeO_2)$=5454 kg/m^3 a $\rho(K_2O)$=2350 kg/m^3, průměrná hustota produktu je ρ($2K_2O$ + 4 $KFeO_2$) = 5454 kg/m^3. Navíc při této transformaci dochází k zásadní změně struktury. V K_2FeO_4 je jeden atom železa obklopen čtyřmi kyslíkovými atomy v tetraedrálním uspořádání [144]. V druhém nejbližším okolí se nachází osm draslíkových iontů. Ve struktuře $KFeO_2$ železa obsazují dvě různé krystalografické pozice, obě jsou tetraedrální, tvořené kyslíky. Druhé nejbližší okolí je u jedné pozice tvořeno třemi draslíky a čtyřmi železy a u druhé pak čtyřmi draslíky a čtyřmi železy [142]. Při formování $KFeO_2$ je pak část draslíků nahrazena železy a draslíky jsou ze struktury vyloučeny a přebytečná energie je uvolněna ve formě tepla.

Dokud je rychlost difuze dostatečná na to, aby umožnila transport dostatečného množství atomů z nitra zrn na povrch, může dekompozice probíhat podle obr. 5.7a a 5.7b. Nicméně se vzrůstem teploty vzniká větší počet nukleačních center, difuze již není schopná zajistit dostatečný transport atomů. Proto se v materiálu v důsledku napětí způsobeného rozdílem hustoty původního a nového materiálu mohou objevovat praskliny. To vede ke snazšímu uvolňování plynů a dalšímu postupu dekompozičního procesu. V průběhu dekompozice se pak objeví výrazný skok, obr. 5.7c a 5.7d. Takový závěr je podpořen tím, že skoky v rychlosti dekompozice dochází pro teploty 235 °C a 250 °C při stejném množství produktu ve vzorku, a sice asi 20 %. Meziprodukty III, IV, a V mohou být interpretovány jako ionty železa s různým počtem železa ve svém okolí. Tyto atomy pak podle počtu železa v druhém nejbližším okolí vykazují různý izomerní posuv.

Prudký nárůst množství komponenty III je silně korelován s průběhem dekompozice. V oblasti, kde dekompozice probíhá rychle, se dá očekávat vznik velkého počtu malých zrn. U malých zrn je pak na povrchu relativně větší počet zrn. Protože současně tato komponenta má asi o 2 T nižší hyperjemné pole než komponenta II, můžeme atomy , které popisuje komponenta III, připsat atomům na povrchu krystalových zrn. Podobná situace byla pozorována i u krystalizace amorfních slitin,

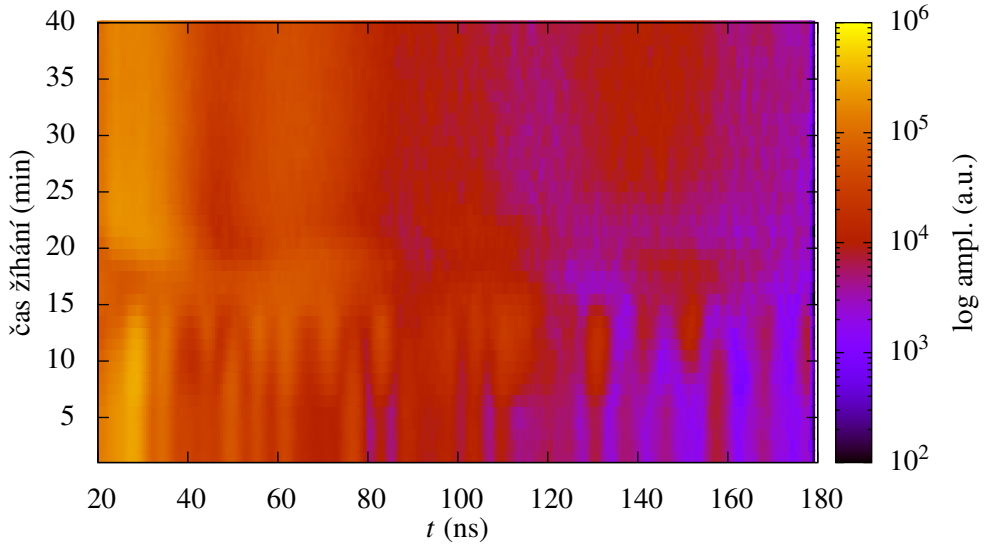

Obrázek 5.8: Dekompozice K_2FeO_4 na pokojové teplotě za řízené vlhkosti.

Komponenta IV může být podle jejího izomerního posuvu připsána železu ve stavu 4+. Dá se očekávat, že tato komponenta je nestabilní a bude se dále rozkládat. Proto zřejmě tato komponenta nebyla pozorována v konvenčních mössbauerovských experimentech.

Experimenty jaderného rozptylu umožnily pozorovat kinetiku dekompozičního procesu v závislosti na teplotě. Výsledky byly popsány mechanistickým modelem. Kinetika dekompozice je zřejmě výrazně ovlivněna difuzí.

5.2 Dekompozice za přístupu vlhkosti

Během experimentů v Hamburku byly provedeny také experimenty s řízenou vlhkostí. Jestliže je K_2FeO_4 v kontaktu se vzdušnou vlhkostí, dochází u něho k rozkladu na $KFeO_2$ obdobně jak při zvýšené teplotě. Na obr. 5.8 je konturový graf, který ukazuje průběh rozkladu. Z grafu je patrné, že dochází k zásadním změnám ve struktuře kvantových záznějů. I přes velkou snahu se doposud nepodařilo výsledky tohoto experimentu uspokojivě interpretovat.

Jedním z důvodů neúspěchu může být skutečnost, že transformace probíhá příliš rychle a z toho důvodu jsou některá spektra zatížena tím, že došlo k nekoherentnímu součtu různých stavů materiálu. Tato možnost doposud nebyla v žádném vyhodnocovacím softwaru zakomponována. Nicméně zohlednění této možnosti je plánované zakomponovat do nového softwaru, který je v současnosti vyvíjen na katedře experimentální fyziky.

Závěr

V této práci byla ukázána celá řada aspektů *in-situ* experimentů jaderného dopředného rozptylu, kdy byly sledovány ireverzibilní fázové přechody. Představené výsledky ukazují, že jaderný dopředný rozptyl je technikou vhodnou pro studium kinetiky fázových transformací na atomární úrovni.

U amorfních slitin bylo možné sledovat vývoj krystalizace za různých podmínek. Tyto experimenty ukázaly také na vliv magnetického pole na kinetiku krystalizace, kdy byl pozorován vliv na rychlost krystalizace nikoli však na charakter krystalizace.

Na příkladu studia dekompozice sloučenin s vysokovalenčním stavem železa bylo ukázáno, že *in-situ* experimenty NFS umožňují studium kinetiky chemických reakcí. V průběhu dekompozičního procesu byly pozorovány intermediální stavy, které jsou s využitím konvenčních technik nezaznamenatelné.

S dalším zvýšením intenzity synchrotronového záření, například na nově budovaných laserech na volných elektronech můžeme očekávat snížení času potřebného pro zaznamenání jednoho spektra s dostatečnou statistikou a tím bude také umožněno sledování procesů podstatně rychlejších než u představených příkladů.

Literatura

[1] V. Valvoda, M. Polcarová, a P. Lukáč. *Základy strukturní analýzy*. Karolinum, Praha, 1992.

[2] P. Gütlich, E. Bill, a A. X. Trautwein. *Mössbauer Spectroscopy and Transition Metal Chemistry*. Springer-Verlag Berlin Heidelberg New York, 2011.

[3] J.S. Lord. Muon spin resonance in ferromagnets. *J. Magn. Magn. Mater.*, 177-181:1470–1471, 1998.

[4] W. Sturhahn, E.E. Alp, T.S. Toellner, P. Hession, M. Hu, a J. Sutter. Introduction to nuclear resonant scattering with synchrotron radiation. *Hyperfine Interact.*, 113:47–58, 1998.

[5] T. A. Littlefield a N. Thorley. *Atomic and Nuclear Physics-An Introduction*. D. van Nostrand company ltd, London, 1963.

[6] W. N. Cottingham a D. A. Greenwood. *An Introduction to Nuclear Physics*. Cambridge University Press, Cambridge, Second edition 2001.

[7] G. V. Smirnov. General properties of nuclear resonant scattering. *Hyperfine Interact.*, 123/124:31–77, 1999.

[8] G. R. Hoy. Quantum mechanical model for nuclear-resonant scattering of Fe^{57} gamma gamma radiation. *J. Phys.: Cond. Matt.*, 9:8749–8765, 1997.

[9] W. Sturhahn a V. G. Kohn. Theoretical aspects of incoherent nuclear resonance scattering. *Hyperfine Interact.*, 123/124:367–399, 1999.

[10] R. Röhlsberger. *Nuclear Condensed Matter Physics with Synchrotron Radiation*. Springer-Verlag Berlin Heidelberg New York, 2004.

[11] Yuri Kagan. Theory of coherent phenomena and fundamentals in neuclear resonant scattering. *Hyperfine Interact.*, 123/124:83–126, 1999.

[12] W. Sturhahn, T. S. Toellner, E. E. Alp, X. Zhang, M. Ando, Y.Yoda, S Kikuta, M. Seto, C. W. Kimball, a B. Dabrowski. Phonon density of states measured by inelastic nuclear resonant scattering. *Phys. Rev. Lett.*, 74:3832, 1995.

[13] Y. V. Shvyd'ko. Nuclear resonance forward scattering of x rays: Time and space picture. *Phys. Rev. B*, 59:9132, 1999.

[14] Y. V. Shvyd'ko. Coherent nuclear resnant scattering of x-rays: Time and space picture. *Hyperfine Interact.*, 123/124:275–299, 1999.

[15] H. J. Lipkin. Mössbauer sum rules for use with synchrotron sources. *Hyperfine Interact.*, 123/124:349–366, 1999.

[16] V. Potapkin, A. I. Chumakov, G. V. Smirnov, J.-P. Celse, R. Rüffer, C. McCammon, a L. Dubrovinsky. The ^{57}Fe synchrotron mössbauer source at the ESRF. *J. Synchrotron Radiat.*, 19(4):559–569, May 2012.

[17] S. Stankov, Y. Z. Yue, M. Miglierini, B. Sepiol, I. Sergueev, A. I. Chumakov, L. Hu, P. Svec, a R. Rüffer. Vibrational properties of nanograins and interfaces in nanocrystalline materials. *Phys. Rev. Lett.*, 100(23):235503, Jun 2008.

[18] S. Stankov, M. Miglierini, A. I. Chumakov, I. Sergueev, Y. Z. Yue, B. Sepiol, P. Svec, L. Hu, a R. Rüffer. Vibrational thermodynamics of $Fe_{90}Zr_7B_3$ nanocrystalline alloy from nuclear inelastic scattering. *Phys. Rev. B*, 82(14):144301, Oct 2010.

[19] N. N. Greenwood a T. C. Gibb. *Mössbauer spectroscopy*. Chapman and Hall Ltd, London, 1971.

[20] N. W. Ashcroft a N. David Mermin. *Solid State Physics*. Brooks/Cole, Belmond, 1976.

[21] U. Gonser. *Mössbauer Spectroscopy*. Springer-Verlag Berlin Heidelberg New York, 1975.

[22] L. Mössbauer. zakladni clanek. *Nevim*.

[23] B. Sedlák a R. N. Kuz'min. *Jaderné resonanční metody ve fyzice pevných látek*. Státní pedagogické nakladatelství, Praha, 1978.

[24] L. D. Nagy. Trends in mössbauer emission spectroscopy. *Hyperfine Interact.*, 83:3–19, 1994.

[25] S. Ambe a F. Ambe. 119-Sn-emission Mössbauer studies on 119-Te and 119-Sb in S, Se and Te. *Bull. Chem. Soc. Jpn.*, 63:3260–3263, 1990.

[26] T. Becze-Deák, L. Bottyán, G. Corradi, L. Korecz, D. L. Nagy, K. Polgár, S. Sayed, a H. Spiering. ^{57}Co mössbauer emission study of $LiNbO_3$, Fe:$LiNbO_3$ and Mg:$LiNbO_3$ in various thermochemical reduction states. *J. Radioanal. Nucl. Chem.*, 246:33–37, 2000.

[27] Alexander A. Kamnev. Application of emission (^{57}Co) Mössbauer spectroscopy in bioscience. *J. Mol. Struct.*, 744-747:161–167, 2005.

[28] A. A. Kamnev, A. V. Tugarova, K. Kovács, E. Kuzmann, B. Biró, P. A. Tarantilis, a Z. Homonnay. ^{57}(Co) emission Mössbauer spectroscopy as a tool for probing speciation and metabolic transformations of cobalt(II) in bacterial cells. *Anal. Bioanal. Chem.*, 405:1921–1927, 2013.

[29] V. V. Popov. Emission Mössbauer spectroscopy of grain boundaries of polycrystalline copper. *Structure, Phase Transformations and Diffusion*, 113:883–887, 2012.

[30] K. Ruebenbauer a U.D. Wdowik. Nucleogenic iron studied by emission Mössbauer spectroscopy in Co-metal. *J. Phys. Chem. Solids*, 66:716–721, 2005.

[31] I. Yu. Kantor, L. S. Dubrovinsky, a C. A. McCammon. Spin crossover in (Mg, Fe)O: A Mössbauer effect study with an alternative interpretation of x-ray emission spectroscopy data. *Phys. Rev. B*, 73:100101, 2006.

[32] K. Ruebenbauer a U. D. Wdowik. Nucleogenic iron charge states in CoO studied by Mössbauer spectroscopy. *J. Phys. Chem. Solids*, 65:2004, 2004.

[33] Yu. D. Perfiliev. Prospects for emission Mössbauer spectroscopy in chemical investigations. *Bulletin of the Russian Academy of Sciences: Physics,*, 74:321–325, 2010.

[34] Z. Homonnay, K. Nomura, G. Juhász, E. Kuzmann, S. Hamakawa, T. Hayakawa, a A. Vértes. Microstructure and CO_2-absorption in $Sr_{0.95}Ca_{0.05}Co_{0.5}Fe_{0.5}O_3$ and $Sr_{0.5}Ca_{0.5}Co_{0.5}Fe_{0.5}O_3$ as studied by emission Mössbauer spectroscopy. *J. Radioanal. Nucl. Chem.*, 255:425–429, 2003.

[35] O. Schneeweiss, J. Čermák, I. Turek, a P. Lejček. Investigations of grain boundaries in copper using emission Mössbauer spectroscopy. *Hyperfine Interact.*, 126:215–218, 2000.

[36] F. J. Lynch, R. E. Holland, a M. Hamermesh. Time dependence of resonantly filtered gamma ray from Fe^{57}. *Phys. Rev.*, 120:513, 1960.

[37] H. Drost, K. Palow, a G. Weyer. Time distribution of Mössbauer scattered radiation. *J. Phys. Colloques*, 35:C6–679–C6–681, 1974.

[38] R. E. Holland, F. J. Lynch, G. J. Perlow, a S. S. Hanna. Time spectra of filtered resonance radiation of Fe^{57}. *Phys. Rev. Lett.*, 4:181, 1960.

[39] R. Albrecht, M. Alflen, P. Gütlich, Zs. Kajcos, R. Schulze, H. Spiering, a F. Tuczek. A new spectrometer for time-differential Mössbauer emission spectroscopy (TDMES). *Nucl. Instr. Meth. Phys. Res. A*, 257:209–214, 1987.

[40] D. W. Hamill a G. R. Hoy. Coincidence-Mössbauer spectroscopy. *Phys. Rev. Lett.*, 21:724, 1968.

[41] M. Alflen, H. Spiering, Zs. Kajcsos, a W. Meyer. Evaluation of accidental coincidences for time-differential Mössbauer-spectroscopy. *Nucl. Instr. Meth. Phys. Res. A*, 356:356–361, 1995.

[42] D. L. Balabanski, A. Proyokova, a P. S. Kamenov. The time-dependence of resonantly filtered recoilless gamma-radiation: An approach to the numerical problem. *Nucl. Instr. Meth. Phys. Res. B*, 16:434–438, 1986.

[43] Zs. Kajcos, M. Alflen, H. Spiering, P. Gütlich, R. Albrecht, R. Schulze, a R. Kreuz. A time-differential Mössbauer emission spectrometer with high efficiency and high time resolution. *Hyperfine Interact.*, 29:1551–1554, 1986.

[44] P. Schaaf, A. Krämer, L. Blaes, G. Wagner, F. Aubertin, a U. Gonser. Simultaneous conversion electron, conversion X-ray and transmission Mössbauer spectroscopy. *Nuclear Instruments and Methods in Physics Research Section B: Beam Interactions with Materials and Atoms*, 53(2):184–186, Feb 1991.

[45] J. A. Sawicki a B. D. Sawicka. Experimental techniques for conversion electron Mössbauer spectroscopy. *Hyperfine Interactions*, 13(1-3):199–219, Jan 1983.

[46] K. Szymanski. Explicit expression for the intensity tensor for 3/2-1/2 transitions and solution of the ambiguity problem in Mössbauer spectroscopy. *J. Phys.: Condens. Matter*, 12:7495–7507, 2000.

[47] Krzysztof Szymański. Polarized radiation in Mössbauer spectroscopy. *Phys. Rep.*, 423(6):295–338, Feb 2006.

[48] D. Satuła, K. Szymański, a L. Dobrzyński. A single line linearly polarized source for Mössbauer spectroscopy. *Nucl. Instr. Meth. Phys. Res. B*, 269(21):2504–2508, Nov 2011.

[49] K. Szymański. Theory of the resonant filter for polarized radiation. *Nucl. Instr. Meth. Phys. Res. B*, 243(2):429–434, Feb 2006.

[50] M.-M. Bé, V. Chisté, C. Dulieu, E. Browne, V. Chechev, N. Kuzmenko, R. Helmer, A. Nichols, E. Schönfeld, a R. Dersch. *Table of Radionuclides*. Bureau International Des Poids et Mesures, 2004.

[51] *http://www.nucleide.org/DDEP_WG/Nuclides/Co-57_tables.pdf*.

[52] *http://www.ritverc.com/products/detail.php?ID=1686*.

[53] S. L. Ruby. Mossbauer experiments without conventional sources. *J. phys. Colloques*, 35:C6–209 – C6–211, 1974.

[54] Yu Kagan, A M Afanas'ev, a V G Kohn. On excitation of isomeric nuclear states in a crystal by synchrotron radiation. *J. Phys. Condens. Matter*, 12:615, 1979.

[55] E. Gerdau, R. Rüffer, H. Winkler, W. Tolksdorf, C. P. Klages, a J. P. Hannon. Nuclear Bragg diffraction of synchrotron radiation in yttrium iron garnet. *Phys. Rev. Lett.*, 54:835–838, 1985.

[56] D.H. Bilderback, P. Elleaume, a E. Weckert. Review of third and next generation synchrotron light sources. *J.Phys. B At. Mol. Opt. Phys.*, 38:S773–S797, 2005.

[57] M. Eriksson. Synchrotron radiation. *Lect. Notes Phys.*, 697:59–70, 2006.

[58] C. Kunz. Synchrotron radiation: third generation sources. *J. Phys. Condens. Matter*, 13:7499–7510, 2001.

[59] H. Schlenvoigt, K. Haupt, A. Debus, F. Budde, O. Jäckel, S. Pfotenhauer, J. G. Gallacher, E. Brunetti, R. P. Shanks, S. M. Wiggins, D. A. Jaroszynski, E Rohwer, a H. Schwoerer. Synchrotron radiation from laser-accelerated monoenergetic electrons. *IEEE Trans. Plasma Sci.*, 36:1773, 2008.

[60] G. Mulhaupt a R. Rüffer. Properties of synchrotron radiation. *Hyperfine Interact.*, 123/124:13–30, 1999.

[61] A. Q. R. Baron, A. I. Chumakov, H. F. Grünsteudel, H. Grünsteudel, L. Niesen, a R. Rüffer. Transverse X-ray coherence in nuclear scattering of synchrotron radiation. *Phys. Rev. Lett.*, 77(23):4808–4811, Dec 1996.

[62] A. Q. R. Baron. Transverse coherence in nuclear resonant scattering of synchrotron radiation. *Hyperfine Interact.*, 123/124:667–680, 1999.

[63] J. C. Lang, G. Srajer, a R. J. Dejus. A comparison of an elliptical multipole wiggler and crystal optics for the production of circularly polarized x-rays. *Rev. Sci. Instrum.*, 67:62, 1996.

[64] D. P. Siddons, U. Bergmann, a J. B. Hastings. Polarization effects in resonant nuclea scattering. *Hyperfine Interact.*, 123/124:681–719, 1999.

[65] O. Leupold, A.I. Chumakov, E.E. Alp, W. Sturhahn, a A.Q.R. Baron. Noniron isotopes. *Hyperfine Interaction*, 123/124:611–631, 1999.

[66] A. Abragam. *The Principles of Nuclear Magnetism*. Clarendon Press, Oxford, 1961.

[67] M. E. Rose. *Elementary Theory of Angular Momentum*. John Wiley and Sons, Inc, New York, Chapman and Hall Ltd, London, 1957.

[68] R. E. Raab a O. L. De Lange. *Multipole Theory in Electromagnetism*. Clarendon Press, Oxford, 2005.

[69] Arne Alex, Matthias Kalus, Alan Huckleberry, a Jan von Delft. A numerical algorithm for the explicit calculation of su(n) and SL($n,\mathbb{C}$)sl(n,c) Clebsch–Gordan coefficients. *J. Math. Phys.*, 52(2):23507, Feb 2011.

[70] C. J. Voyer a D. H. Ryan. A complete solution to the Mössbauer problem all in one place. *Hyperfine Interact.*, 170:91–104, 2006.

[71] E. Kreber a U. Gosner. Evaluation of relative line intensities in Mössbauer spectroscopy. *Nucl. Instr. Meth.*, 121:17–23, 1974.

[72] W. Kündig. Evaluation of Mössbauer spectra for ^{57}Fe. *Nucl. Instr. Meth.*, 48:219–228, 1967.

[73] J. P. Hannon a G. T. Trammell. Mössbauer diffraction. I. Quantum theory of gamma-ray and X-ray optics. *Phys. Rev. B*, 169:315, 1968.

[74] J. P. Hannon a G. T. Trammell. Mössbauer diffraction. II. Quantum theory of gamma-ray and X-ray optics. *Phys. Rev. B*, 186:306, 1969.

[75] J. P. Hannon, N. J. Carron, a G. T. Trammell. Mossbauer diffraction III. Emission of Mössbauer y rays from crystals. B. Dynamical solutions. *Phys. Rev. B*, 9:2810–2831, 1974.

[76] J. P. Hannon, N. J. Carron, a G. T. Trammell. Mössbauer diffraction. III. Emission of Mössbauer x-rays from crystals. A. general theory. *Phys. Rev. B*, 9:2791–2809, 1974.

[77] G. T. Trammell a J. P. Hannon. Quantum beats nuclei excited by synchrotron pulses. *Phys. Rev. B*, 18:165, 1978.

[78] H. Frauenfelder, D. E. Nagle, R. D. Taylor, D. R. F. Cochran, a W. M. Visscher. Elliptical polarization of Fe^{57} gamma rays. *Phys. Rev.*, 126(3):1065–1075, May 1962.

[79] J. Klíma a B. Velický. *Kvantová mechanika I.* Karolinum, 2016.

[80] J. Klíma a B. Velický. *Kvantová mechanika II*. Karolinum, 2018.

[81] J. J. Sakurai. *Modern quantum mechanics; rev. ed.* Addison-Wesley, Reading, MA, 1994.

[82] A. Q. R. Baron. *Resonant Nuclear Scattering of Synchrotron Radiation: Detector Development and Specular Scattering From a thin layer of* ^{57}Fe. Stanford Linear Accelerator Center, 1995.

[83] D. E. Brown. *Nuclear Dynamic Diffraction Using Synchrotron Radiation*. Stanford Linear Accelerator Center, 1993.

[84] B. Sedlák a I. Štoll. *Elektřina a magnetismus*. Academia, 2002.

[85] C. L'Abbé, R. Callens, a J. Odeurs. Time-integrated synchrotron Mössbauer spectroscopy. *Hyperfine Interact.*, 135:275–294, 2001.

[86] W. Sturhahn a E. Gerdau. Evaluation of time-differential measurements of nuclear-resonance scatterin of x rays. *Phys. Rev. B*, 49:9285, 1994.

[87] G. R. Hoy. Time-domain, nuclear-resonant, forward scattering: the classical approach. *Hyperfine Interact.*, 107:381–399, 1997.

[88] R. M. Housley a U. Gonser. Mössbauer Faraday effect. *Phys. Rev.*, 171:480–484, Jul 1968.

[89] R. M. Housley, R. W. Grant, a U. Gonser. Coherence and polarization effects in Mössbauer absorption by single crystals. *Phys. Rev.*, 178:514–522, Feb 1969.

[90] S. Gordienko, A. Pukhov, O. Shorokhov, a T. Baeva. Coherent focusing of high harmonics: A new way towards the extreme indtensities. *Phys. Rev. Lett.*, 94:103903, 2005.

[91] A. Q.R. Baron. Detectors for nuclear resonant scattering experiments. *Hyperfine Interact.*, 125:29–42, 2000.

[92] Y. V. Shvyd'ko, U. van Brück, W. Potzel, P. Schindelmann, E. Gerdau, O. Leupold, J. Metge, H. D. Rüter, a G. V. Smirnov. Hybrid beat in nuclear forward scattering of synchrotron radiation. *Phys. Rev. B*, 57:3552, 1998.

[93] Charles Kittel. *Introduction to Solid State Physics*. John Wiley and Sons, Inc, New York, Chapman and Hall Ltd, London, 2005.

[94] R. Rüffer, H.D. R üter, a E. Gerdau. Hyperfine spectroscopy in diffraction geometry. *Hyperfine Interact.*, 123/124:405–426, 1999.

[95] R. Rüffer, E. Gerdau, M. Grote, R. Hollatz, R. Röhlsberger, H.D. Rüter, a W. Sturhahn. Nuclear bragg diffraction using synchrotron radiation: A new method for hyperfine spectroscopy. *Nucl. Instr. Meth. Phys. Res. A*, 303(3):495–502, Jun 1991.

[96] D.P. Siddons, J.B. Hastings, a G. Faigel. A new apparatus for the study of nuclear Bragg scattering. *Nucl. Instr. Meth. Phys. Res. A*, 266(1–3):329–335, Apr 1988.

[97] U. van Bürck, R. L. Mössbauer, E. Gerdau, R. Rüffer, R. Hollatz, G. V. Smirnov, a J. P. Hannon. Nuclear bragg scattering of synchrotron radiation with strong speedup of coherent decay, measured on antiferromagnetic ^{57}febo$_3$. *Phys. Rev. Lett.*, 59:355–358, Jul 1987.

[98] W. Sturhahn. Phase problem in synchrotron Mössbauer spectroscopy. *Phys. Rev. B*, 63(9), Jan 2001.

[99] R. Callens, C. L'abbé, J. Meersschaut, I. Serdons, W. Sturhahn, a T. S. Toellner. Phase determination in nuclear resonant scattering using a velocity drive as an interferometer and phase shifter. *Phys. Rev. B*, 72(8):081402(R), Aug 2005.

[100] R. Callens, R. Coussement, C. L'abbé, S. Nasu, K. Vyvey, T. Yamada, Y. Yoda, a J. Odeurs. Stroboscopic detection of nuclear forward-scattered synchrotron radiation. *Phys. Rev. B*, 65(18):180404(R), Apr 2002.

[101] A. I. Rykov, I. A. Rykov, K. Nomura, a X. Zhang. Frequency spectra of quantum beats in nuclear forward scattering of ^{57}fe: The Mössbauer spectroscopy with superior energy resolution. *Hyperfine Interact.*, 163(1–4):29–56, May 2006.

[102] D. Sayre. X-ray crystallography: The past and present of the phase problem. *Struct. Chem.*, 13:81–96, 2002.

[103] Q. Shen. Solving the phase problem using reference-beam x-ray diffraction. *Phys. Rev. Lett.*, 80:3268–3271, Apr 1998.

[104] M. Miglierini, V. Prochazka, S. Stankov, P. Svec, M. Zajac, J. Kohout, A. Lancok, D. Janickovic, a P. Svec. Crystallization kinetics of nanocrystalline alloys revealed byin situnuclear forward scattering of synchrotron radiation. *Phys. Rev. B*, 86(2):020202(R), Jul 2012.

[105] M. Miglierini, V. Procházka, R. Rüffer, a R. Zbořil. In situ crystallization of metallic glasses during magnetic field annealing. *Acta Mater.*, 91:50–56, Jun 2015.

[106] V. Procházka, V. Vrba, D. Smrčka, R. Rüffer, P. Matúš, M. Mašláň, a M.B. Miglierini. Structural transformation of NANOPERM-type metallic glasses followed in situ by synchrotron radiation during thermal annealing in external magnetic field. *J. Alloys Compd.*, 638:398–404, Jul 2015.

[107] L. Machala, R. Zboril, V. K. Sharma, J. Filip, O. Schneeweiss, a Z. Homonnay. Mössbauer characterization and in situ monitoring of thermal decomposition of potassium ferrate(vi), K_2FeO_4 in static air conditions. *J. Phys. Chem. B*, 111(16):4280–4286, Apr 2007.

[108] R. S. Preston, S. S. Hanna, a J. Heberle. Mössbauer effect in metallic iron. *Phys. Rev.*, 128:2207–2218, Dec 1962.

[109] S. S. Hanna a R. S. Preston. Mössbauer cross section of fe^{57} in iron. *Phys. Rev.*, 139:A722–A725, Aug 1965.

[110] G. J. Perlow, S. S. Hanna, M. Hamermesh, C. Littlejohn, D. H. Vincent, R. S. Preston, a J. Heberle. Polarization of nuclear resonance radiation in ferromagnetic fe^{57}. *Phys. Rev. Lett.*, 4:74–75, Jan 1960.

[111] S. S. Hanna, J. Heberle, C. Littlejohn, G. J. Perlow, R. S. Preston, a D. H. Vincent. Polarized spectra and hyperfine structure in fe^{57}. *Phys. Rev. Lett.*, 4:177–180, Feb 1960.

[112] S. S. Hanna, J. Heberle, C. Littlejohn, G. J. Perlow, R. S. Preston, a D. H. Vincent. Observations on the mössbauer effect in fe^{57}. *Phys. Rev. Lett.*, 4:28–29, Jan 1960.

[113] S. S. Hanna, J. Heberle, G. J. Perlow, R. S. Preston, a D. H. Vincent. Direction of the effective magnetic field at the nucleus in ferromagnetic iron. *Phys. Rev. Lett.*, 4:513–515, May 1960.

[114] Y. V. Shvyd'ko. MOTIF: Evaluation of time spectra for nuclear forward scattering. *Hyperfine Interact.*, 125:173–188, 2000.

[115] Yuri Shvyd'ko. *Motif. A program for fitting Mössbauer time spectra of neuclear forward scattering, User's Guide, 1999.*

[116] *http://www.fs.kfki.hu/.*

[117] W. Sturhahn. CONUSS and PHOENIX: Evaluation of nuclear resonance scattering data. *Hyperfine Interact.*, 125:149–172, 2000.

[118] Vít Procházka. *Hubert: User Guide*. http://atmilab.upol.cz/texty.html.

[119] V. Vrba, V. Procházka, D. Smrčka, a M. Miglierini. Hubert: Software for efficient analysis of in-situ nuclear forward scattering experiments. *AIP Conference Proceedings*, 1781:020013, 2016.

[120] V. Vrba, V. Procházka, D. Smrčka, a M. Miglierini. Advanced approach to the analysis of a series of in-situ nuclear forward scattering experiments. *Nucl. Instr. Meth. Phys. Res. A*, 847:111–116, Mar 2017.

[121] A Hernando. Magnetic properties and spin disorder in nanocrystalline materials. *J. Phys.: Condens. Matter*, 11(48):9455–9482, Nov 1999.

[122] A. Inoue a A. Takeuchi. Recent development and application products of bulk glassy alloys. *Acta Mater.*, 59(6):2243–2267, Apr 2011.

[123] G. Herzer. Modern soft magnets: Amorphous and nanocrystalline materials. *Acta Mater.*, 61(3):718–734, Feb 2013.

[124] M. E. McHenry, M. A. Willard, a D. E. Laughlin. Amorphous and nanocrystalline materials for applications as soft magnets. *Prog. Mater Sci.*, 44(4):291–433, Oct 1999.

[125] M.E. McHenry a D.E. Laughlin. Nano-scale materials development for future magnetic applications. *Acta Mater.*, 48(1):223–238, Jan 2000.

[126] O. Gutfleisch, M. A. Willard, E. Brück, Ch. H. Chen, S. G. Sankar, a J. P. Liu. Magnetic materials and devices for the 21st century: Stronger, lighter, and more energy efficient. *Adv. Mater.*, 23(7):821–842, Dec 2010.

[127] M. Miglierini, M. Kopcewicz, B. Idzikowski, Z. E. Horváth, A. Grabias, I. Škorvánek, P. Duźewski, a Cs. S. Daróczi. Structure, hyperfine interactions, and magnetic behavior of amorphous and nanocrystalline $Fe_{80}M_7B_{12}Cu_1S$ (M=Mo, Nb, Ti) alloys. *J. Appl. Phys.*, 85(2):1014–1025, Jan 1999.

[128] M. Pavuk, M. Miglierini, M. Vujtek, M. Mashlan, R. Zboril, a Y. Jiraskova. Afm and mössbauer spectrometry investigation of the nanocrystallization process in Fe–Mo–Cu–B rapidly quenched alloy. *J. Phys. Condens. Matter*, 19(21):216219, May 2007.

[129] M. Miglierini, A. Lančok, a J. Kohout. Hyperfine fields in nanocrystalline Fe–Zr–B probed by ^{57}Fe nuclear magnetic resonance spectroscopy. *Appl. Phys. Lett.*, 96(21):211902, May 2010.

[130] N. Mattern, M. Stoica, G. Vaughan, a J. Eckert. Thermal behaviour of $Pd_{40}Cu_{30}Ni_{10}P_{20}$ bulk metallic glass. *Acta Mater.*, 60(2):517–524, Jan 2012.

[131] G. Wang, N. Mattern, J. Bednarčík, R. Li, B. Zhang, a J. Eckert. Correlation between elastic structural behavior and yield strength of metallic glasses. *Acta Mater.*, 60(6–7):3074–3083, Apr 2012.

[132] T. Egami, Y. Tong, a W. Dmowski. Deformation in metallic glasses studied by synchrotron x-ray diffraction. *Metals*, 6(1):22, Jan 2016.

[133] https://www.esrf.eu/usersandscience/experiments/mex/id18.

[134] M. Miglierini a J.-M. Greneche. Mössbauer spectrometry of fe(cu)mb-type nanocrystalline alloys: I. the fitting model for the mössbauer spectra. *J. Phys. Condens. Matter*, 9(10):2303–2319, Mar 1997.

[135] Yu.V. Shvyd'ko a U. van Brück. Hybrid forms of beat phenomena in nuclear forward scattering of synchrotron radiation. *Hyperfine Interact.*, 123/124:511–527, 1999.

[136] I. Škorvánek, J. Marcin, J. Turčanová, J. Kováč, a P. Švec. Improvement of soft magnetic properties in $Fe_{38}Co_{38}Mo_8B_{15}Cu$ amorphous and nanocrystalline alloys by heat treatment in external magnetic field. *J. Alloys Compd.*, 504:S135–S138, Aug 2010.

[137] M. Miglierini, T. Hatala, a M. Bujdoš. Depth-selective study of surface crystallization in NANOPERM-type alloys. *Acta Phys. Pol. A*, 126(1):56–57, Jul 2014.

[138] M. Miglierini, M. Pavlovič, V. Procházka, T. Hatala, G. Schumacher, a R. Rüffer. Evolution of structure and local magnetic fields during crystallization of HITPERM glassy alloys studied by in situ diffraction and nuclear forward scattering of synchrotron radiation. *Physical Chemistry Chemical Physics*, 17(42):28239–28249, 2015.

[139] J. D. Rush a B. H. J. Bielski. Pulse radiolytic studies of the reaction of perhydroxyl/superoxide O_2- with iron(ii)/iron(iii) ions. the reactivity of HO_2/O_2- with ferric ions and its implication on the occurrence of the Haber-Weiss reaction. *J. Phys. Chem.*, 89(23):5062–5066, Nov 1985.

[140] B. J. Yates, R. Zboril, a V. K. Sharma. Engineering aspects of ferrate in water and wastewater treatment – a review. *J. Environ. Sci. Health C*, 49(14):1603–1614, Oct 2014.

[141] Z. Tomkowicz a A. Szytuła. Crystal and magnetic structure of $KFeO_2$. *J. Phys. Chem. Solids*, 38(10):1117–1123, 1977.

[142] N. Z. Ali, J. Nuss, D. Sheptyakov, a M. Jansen. The $AFeO_2$ (A=K, Rb and Cs) family: A comparative study of structures and structural phase transitions. *J. Solid State Chem.*, 183(3):752–759, Mar 2010.

[143] L. Machala, V. Procházka, M. Miglierini, V. K. Sharma, Z. Marušák, H.-Ch. Wille, a R. Zbořil. Direct evidence of Fe(v) and Fe(iv) intermediates during reduction of Fe(vi) to Fe(iii): a nuclear forward scattering of synchrotron radiation approach. *Phys. Chem. Chem. Phys.*, 17(34):21787–21790, 2015.

[144] R. J. Audette, J. W. Quail, W. H. Black, a B. E. Robertson. Crystal structures of M_2FeO_4 (M=K,Rb,Cs). *J. Solid State Chem.*, 8:43–49, 1973.

Vybrané publikace

PHYSICAL REVIEW B **86**, 020202(R) (2012)

Crystallization kinetics of nanocrystalline alloys revealed by *in situ* nuclear forward scattering of synchrotron radiation

M. Miglierini,[1,2,*] V. Prochazka,[2] S. Stankov,[3,4] P. Svec, Sr.,[5] M. Zajac,[6] J. Kohout,[7] A. Lancok,[8] D. Janickovic,[5] and P. Svec[5]

[1]*Institute of Nuclear and Physical Engineering, Slovak University of Technology, 812 19 Bratislava, Slovakia*

[2]*Regional Centre of Advanced Technologies and Materials, Palacky University, 771 46 Olomouc, Czech Republic*

[3]*Institute for Synchrotron Radiation, Karlsruhe Institute of Technology, Campus Nord, 76344 Eggenstein-Leopoldshafen, Germany*

[4]*Laboratory for Applications of Synchrotron Radiation, Karlsruhe Institute of Technology, Campus South, 76131 Karlsruhe, Germany*

[5]*Institute of Physics, Slovak Academy of Sciences, 845 11 Bratislava, Slovakia*

[6]*European Synchrotron Radiation Facility, BP 220, 38043 Grenoble, France*

[7]*Faculty of Mathematics and Physics, Charles University, 180 00 Prague, Czech Republic*

[8]*Institute of Inorganic Chemistry of the AS CR, v.v.i., 250 68 Husinec-Řež, Czech Republic*

(Received 30 August 2011; revised manuscript received 4 June 2012; published 31 July 2012)

The nanocrystallization kinetics of $Fe_{90}Zr_7B_3$ is investigated by *in situ* nuclear forward scattering of synchrotron radiation upon isothermal annealing. The nucleation and growth processes are accessed separately for the nanograins, their interfaces, and the residual amorphous matrix by monitoring the time evolution of the corresponding hyperfine parameters. This approach discloses the structural transformations taking place in this class of technologically important materials.

DOI: 10.1103/PhysRevB.86.020202 PACS number(s): 75.50.Tt, 61.46.Hk, 64.70.dg, 71.70.Jp

A central problem in nanotechnology is the understanding of the structure-to-properties relationship of the nanocrystalline interfaces that is essential for tailoring the functionalities, efficiency, and performance of near-future nanodevices consisting of subnanometer sized layers of material. The investigation of such buried layers, however, is a demanding experimental task. Direct methods used for imaging the interfaces, such as cross-sectional transmission electron microscopy, are destructive and do not allow for the observation of the structural changes that are taking place during nanograin growth and the formation of the interfaces. On the other hand, the information obtained by *in situ* techniques used for the investigation of the nanocrystallization kinetics is either averaged over the entire sample (differential scanning calorimetry) or over the distribution of electron densities (x-ray diffraction) and does not provide site-specific information.

The use of local probe techniques such as Mössbauer spectroscopy has offered unique opportunities to access the magnetic properties of the interfaces and nanograins separately.[1,2] Exploiting the fact that the hyperfine interactions instantly reflect the structural arrangement of the probe ^{57}Fe atom, it became possible to investigate the structural modifications of the sample by examining the hyperfine parameters that correspond to the Fe atoms located inside the nanograins, at their surfaces, or forming the interfaces.[3] Changes in microstructure, crystallization behavior, and the magnetic states of nanocrystalline alloys suggested that the interface regions play a significant role in the propagation of ferromagnetic exchange interactions between the nanograins through the amorphous matrix.[2,4–6] The relatively long acquisition times of a conventional Mössbauer spectrum (up to several hours), however, limited the application of this technique only to samples in equilibrium conditions having a well-defined crystallization state and prohibited the monitoring of the crystallization process itself.

Nanocrystalline alloys prepared by a controlled heat treatment of metallic glasses exhibit unique magnetic properties[7] that are caused by the size, amount, and chemical composition of the nanocrystallites embedded in a residual amorphous matrix.[8] Structural changes, related to crystallization, that occur in these materials, once exposed to elevated temperatures for prolonged operational times (sensors, transformer cores, recording devices, magnetic shielding, etc.[9]), deteriorate their performance. Therefore, a comprehensive understanding of the evolution of nanograins, interfaces, and the amorphous matrix during nanocrystallization is essential in order to understand, optimize, and conserve the unique magnetic properties exhibited by the nanocrystalline alloys. Among this class of materials the pioneering $Fe_{90}Zr_7B_3$ Nanoperm[10] still attracts considerable attention and was established as a model system for studying the structural,[11] dynamic,[12,13] and magnetic[14] properties of ternary nanocrystalline alloys.

In this Rapid Communication we report on the investigation of the nanocrystallization kinetics in $Fe_{90}Zr_7B_3$ separately for the nanograins, interface layers, and residual amorphous matrix by nuclear forward scattering of synchrotron radiation. The outstanding brilliance of the x-ray beams produced by third generation synchrotrons ensures rapid recording of time spectra, allowing for a direct *in situ* observation of dynamical processes that are taking place during heat treatment. Employing the fact that hyperfine interactions instantly reflect the state of the structural arrangement by examination of the corresponding hyperfine parameters during nanocrystallization, it is now possible to follow separately the structural evolution of different sites of the ^{57}Fe probe atoms. The obtained results are used to thoroughly assess the available models for nucleation and nanograin growth upon an isothermal annealing of this class of technologically important materials.

A $Fe_{90}Zr_7B_3$ amorphous alloy enriched to 63% in ^{57}Fe was prepared by a melt-spinning technique in a form of 2 mm wide and 20 μm thick ribbons. The as-quenched alloy contained bcc Fe nanocrystals that were identified in the surface regions of the ribbon by conversion electron Mössbauer spectrometry.[13] As

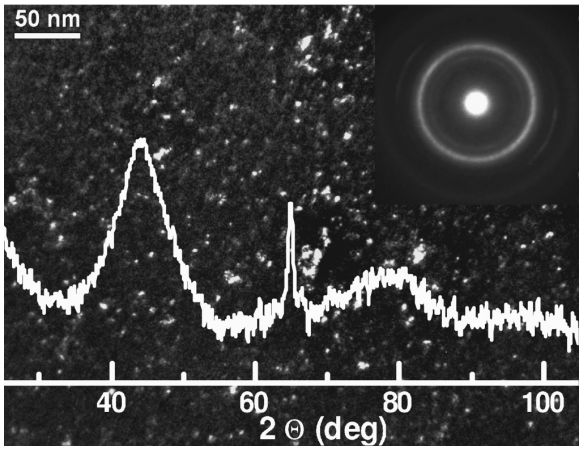

FIG. 1. Transmission electron micrograph (dark field) of the as-quenched $Fe_{90}Zr_7B_3$ alloy. Electron and x-ray diffraction patterns are also included.

demonstrated in Fig. 1, they were found also in the bulk of the ribbon, amounting to approximately 2.5% with sizes of about 2 nm determined by x-ray diffraction, electron diffraction, and transmission electron microscopy. The narrow [002] reflection at 65° indicates a strong preferential orientation of the quenched-in nanocrystals, which is confirmed also by an intensity variation of some electron diffraction rings. In addition, a Zr content of about 0.2% was identified inside the bcc Fe nanograins.[14] Nuclear forward scattering experiments were carried out at the Nuclear Resonance end station ID22N of the European Synchrotron Radiation Facility. We used photons with an energy of 14.413 keV and an energy resolution of about 3 meV. The sample was placed inside a vacuum furnace and heated up to a temperature of 743 K with a ramp of 40 K/min. An isothermal experiment at this temperature was performed for up to 130 min. The temperature of the experiment was chosen close to the onset of crystallization at 783 K determined from differential scanning calorimetry.[13] The time spectra of nuclear forward scattering were continuously recorded with an acquisition time of 1 min.

A contour plot obtained from a three-dimensional (3D) image of all 130 spectra is illustrated in Fig. 2(a). The elapsed decay time of the nuclear resonant level and the time of annealing are displayed on the x and y axes, respectively. The measured intensities are color coded in a logarithmic scale. Selected time spectra obtained after annealing for 15, 40, and 120 min are shown in Fig. 2(b). All spectra were consistently analyzed with the CONUSS code.[15] The amorphous matrix was reconstructed by a distribution of electric quadrupole interactions (quadrupole splitting) corresponding to its paramagnetic state above the Curie point at a given temperature. The nanocrystalline phase of bcc Fe formed upon annealing was associated with a spectral component featuring magnetic dipole interactions with a unique value of the hyperfine magnetic field [open circles in Fig. 3(a)]. The third component is ascribed to iron atoms that are localized at the surfaces of nanocrystalline grains buried inside the amorphous phase. These atoms exhibit symmetry different from those in the nanograins. They belong to the interface regions and were refined from the spectra using a distribution of magnetic hyperfine fields with average values plotted as open triangles in Fig. 3(a). The presence of this spectral component was revealed by conventional Mössbauer effect experiments[1,2,16,17] performed under static conditions.

The relative contents of amorphous, nanograin, and interface components, isomer shifts of the amorphous and interface fractions determined relative to that of the nanocrystalline phase, quadrupole splitting of the amorphous and interface fractions, hyperfine magnetic fields of the nanograins and interfaces, as well as the Debye temperature, an intensity scaling factor, and shift along the time scale were free

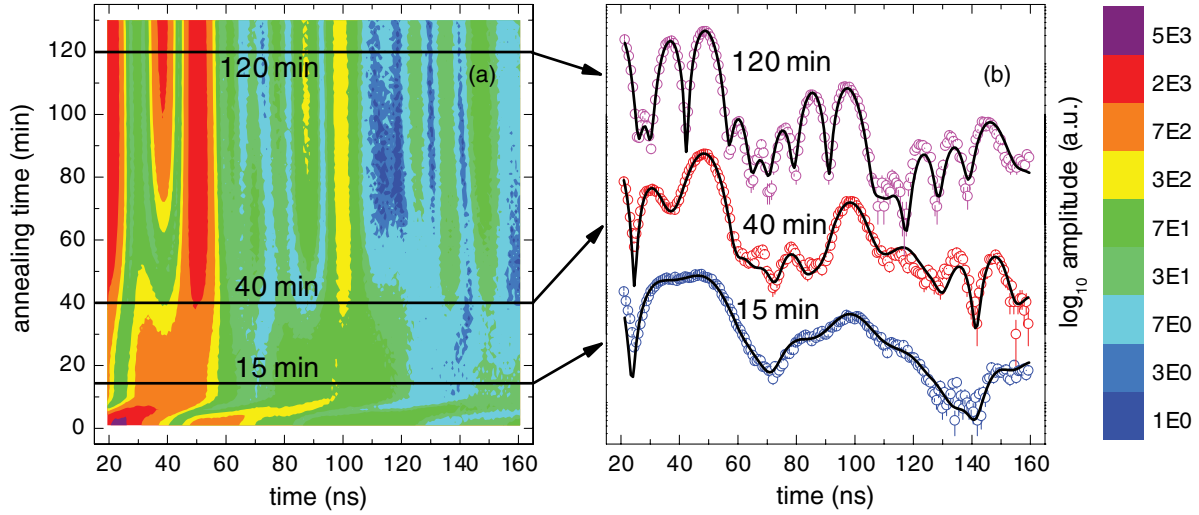

FIG. 2. (Color online) Contour plot of 3D nuclear forward scattering spectra of $Fe_{90}Zr_7B_3$ annealed at 743 K (a) and selected records (open symbols) with fits (solid lines) for 15, 40, and 120 min of annealing (b).

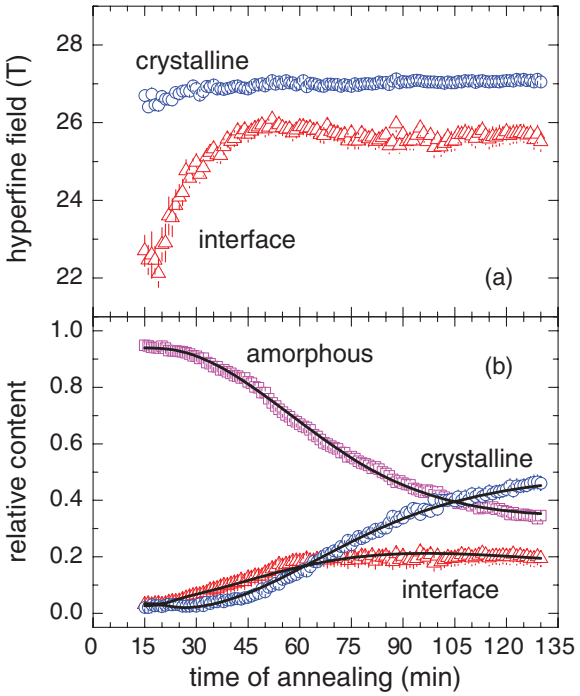

FIG. 3. (Color online) Time evolution of the hyperfine magnetic fields (a) and relative content of spectral components (b) derived from the analysis of nuclear forward scattering spectra recorded at 743 K (open symbols). Solid lines in (b) represent fits between theoretically calculated (according to the model described in the text) and experimentally obtained data.

parameters during analysis. The quadrupole splitting and isomer shift of the nanograin component were set to zero and fixed.

The time dependencies of hyperfine fields and relative fractions of the components derived from the consistent analysis of the time spectra from Fig. 2 are shown in Figs. 3(a) and 3(b), respectively. After reaching the temperature of isothermal annealing at the 15th minute, the relative contents are almost constant for about 5 min up to the 20th minute of annealing. The values of the hyperfine magnetic fields at 743 K are reduced due to superparamagnetic behavior at this elevated temperature. Within the following 15 min (up to the 35th min) new grains with subnanometer sizes are formed around the existing nucleation centers. This is revealed by an increase of interfacial regions (when nearly all atoms constitute predominantly the nanograin surface) while the amount of Fe atoms located inside the nanograins remains unaffected [Fig. 3(b)]. The enhanced contribution of the interfaces is also indirectly confirmed by a significant increase of the corresponding values of the hyperfine field, as depicted in Fig. 3(a). Simultaneously the amount of iron located inside the amorphous residual matrix gradually diminishes.

The nanograin content steadily rises after about 40 min of heat treatment, together with the interface component, while the depletion of Fe in the residual material continues. At this moment the growing nanograins reach their size and density that correspond to the final values of the hyperfine fields for the nanograins and interfaces [Fig. 3(a)]. After about 60 min of annealing the relative fraction of interfaces seemingly saturates and only the nanograin fraction continues to rise on account of the residual amorphous matrix. This behavior clearly indicates a nanograin growth process. The amount of Fe in the bulk of nanocrystals increases more rapidly compared to that at their surfaces. The increased number and density of nanograins eventually leads to the formation of agglomerates which effectively suppresses the contribution of the interface fraction while the number of Fe atoms positioned within the nanograins rises. At this stage, the average grain size reached a final value of 12 ± 3 nm, as derived from x-ray diffraction patterns.[12]

The hyperfine field corresponding to the nanograins coincides with the value reported from Mössbauer effect experiments for bcc Fe at a particular temperature of the experiment.[18] The interfaces are characterized with systematically lower (by 1–2 T) values of the hyperfine fields when their relative content is stabilized. This is in agreement with the results from high-temperature Mössbauer effect experiments performed upon the same nanocrystalline alloy.[6] The relative atomic fraction of the interface component increases only up to a certain value determined by the size and the amount of the nanograins. The hyperfine fields of the interfaces are low at the onset of crystallization due to a significant influence of the surrounding paramagnetic amorphous matrix, and they reach their final values when the first and second coordinations of iron atoms are completed and stabilized. The values of the hyperfine fields are also governed by the broken translational symmetry experienced by the ^{57}Fe atoms positioned at the surface of the nanograins. From one side they are surrounded by the perfect long-range ordered atoms of the nanograin interior. The amorphous matrix, which is positioned from the other side of the interface atoms, implies lower values of the hyperfine fields because it contains an effectively higher concentration of nonmagnetic elements. They are accumulated namely in close proximity to the newly developed Fe nanograins, as demonstrated by atom probe field ion microscopy,[19] which might further contribute to the observed decrease of the magnetic fields. This effect is more pronounced than a possible contribution of nonmagnetic atoms positioned in the nanocrystalline lattice itself, which was estimated to be about 0.2% Zr.[14]

The unique possibility to investigate the time evolution of the nanograins, interfaces, and the residual amorphous matrix separately upon isothermal annealing allowed for assessing the crystallization kinetics in this nanocrystalline alloy. We have considered crystallization according to the Johnson-Mehl-Avrami nucleation (site saturation nucleation), grain growth, and impingement[20] extended by a simplified model that assumes two types of spherelike grains: quenched-in grains (Q) and newly formed grains (F). We have assumed that the grains consist of a surface layer and a core. The thickness of the former was kept constant with annealing time during simulation. The experimentally obtained time dependencies of the spectral components [symbols in Fig. 3(b)] were reproduced by taking into account the contributions from the surface layers and the bulk of the grains.[20] The time evolution of the relative weights of the amorphous residual

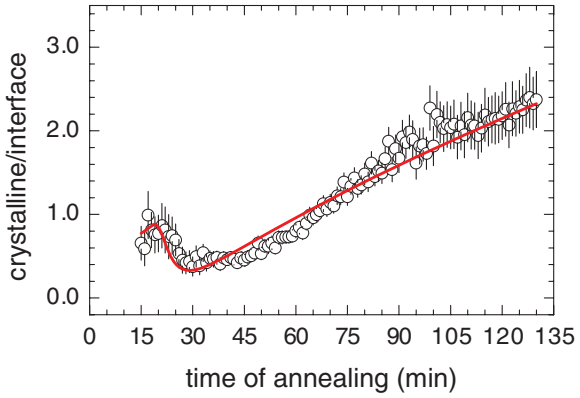

FIG. 4. (Color online) Ratio of the relative contents of crystalline and interface components as a function of annealing time at 743 K: Open symbols, experimental data; solid line, ratio of fits from theoretical calculations.

matrix (W_{AM}), interface regions (W_{IF}), and nanocrystals (W_{NC}) are expressed as

$$W_{AM} = (1 - C_0) + (C_0 - C_\infty) \cdot \left[1 - \exp\left(-\frac{4}{3}\pi \int_0^{t-t_0} N(\tau) \cdot [(t-\tau)\cdot v]^w d\tau\right)\right], \quad (1)$$

where τ is the time for formation of $N(\tau)d\tau$ new grains which grow with speed v, w describes the grain growth process, C_0 and C_∞ represent the amount of phase before and after the transformation, respectively,

$$W_{IF} = (1 - W_{AM})\frac{RQ_{IF} + (1-R)F_{IF}}{Q+F}, \quad (2)$$

$$W_{NC} = (1 - W_{AM})\frac{RQ_{NC} + (1-R)F_{NC}}{Q+F}, \quad (3)$$

with Q and F being integral volumes of all quenched-in and newly formed grains at time t, respectively, subscripts IF and NC denote contributions from interfaces (surface layer) and interiors of the grains (core), and R stands for the ratio of the number of quenched-in and newly formed grains.

This model assumes that all nucleation centers are formed at the beginning of the crystallization and that the rate of grain growth is governed by the Avrami exponent $n = 2.0 \pm 0.2$. Using Eqs. (1)–(3), the time dependencies of the relative contents of all three components were fitted to the experimentally obtained data. The solid curves in Fig. 3(b) represent the resulting fits. This figure reveals a very good agreement between the experimentally obtained and theoretically calculated data for all three components along the duration of the entire experiment.

In Fig. 4, the evolution of the experimentally obtained ratio of the relative contents of the crystalline and interface components (symbols) is plotted as a function of annealing time. It is superimposed with a solid line obtained from the fits from Fig. 3(b). It should be noted that in this representation all possible deviations between the experimental and theoretical time dependencies for crystalline and interface components that are hardly seen in Fig. 3(b) now become visible. This comparison reveals that the experimental results are fully consistent with the calculated time dependencies even for tiny details seen at an early stage of the annealing process.

The quenched-in nanocrystallites manifest themselves at the very beginning with a certain bulk-to-surface (i.e., crystalline/interface) ratio. After the 20th minute of annealing, new nanograins are formed. Their small dimensions favor a higher contribution of the interface component because the majority of atoms form the grain surfaces. This is indicated by a decrease of the crystalline/interface ratio. Finally, from about the 35th minute, the grain grow process starts and the ratio steadily increases due to a higher contribution of the bulk of the grains.

The deviations between the experimentally measured and theoretically calculated data which are seen between the 45th and the 65th minute of annealing arise most likely from the fact that in our model we have calculated the evolution of an individual grain without taking into account the presence of the neighboring grains. In reality, however, the growth of grains is constrained due to impingement. This means that the grain growth is limited when the grains approach each other or when they are in very close proximity to the neighboring grains and surrounded by an increased concentration of Zr and B atoms.[19,21] Consequently, the contribution of the surface layers shows a tendency to saturate whereas the bulk of the grains still rises. The interface layer thickness towards the end of annealing is about 0.7 nm, which is in agreement with 0.6 nm reported in Ref. 1.

In conclusion, by applying nuclear forward scattering of synchrotron radiation *in situ* in the course of isothermal heating of $Fe_{90}Zr_7B_3$ Nanoperm, we were able to follow the time evolution of hyperfine interactions for the nanograins, interfaces, and the residual amorphous matrix separately. The obtained results were employed to thoroughly assess the available models for nucleation and grain growth upon an isothermal annealing of the amorphous precursor to fine details.

Even though the overall formation of nanocrystals can be deduced also from other analytical techniques, the approach proposed here provides the possibility to study separately the contributions of Fe atoms positioned at different locations within the interior or at the surface of the nanograins comprising also their hyperfine interactions. Furthermore, applied at different annealing temperatures and to alloys with various compositions, this method can provide information about the crystallization kinetics of the technologically important family of nanocrystalline materials prepared by controlled crystallization of an amorphous precursor.

This work was supported by Grants No. VEGA 1/0286/12, No. APVV-0492-11, No. MSM0021620834, and No. P204/10/0035, and by the Operational Program Research and Development for Innovations European Regional Development Fund (CZ.1.05/2.1.00/03.0058) and the Operational Program Education for Competitiveness European Social Fund (Project No. CZ.1.07/2.3.00/20.0017). S.S. acknowledges support by the Helmholtz Association (VH-NG-625).

*marcel.miglierini@stuba.sk

[1]A. Slawska-Waniewska and J. M. Greneche, Phys. Rev. B **56**, 8491 (1997).
[2]M. Miglierini and J. M. Greneche, J. Phys.: Condens. Matter **9**, 2321 (1997).
[3]M. Miglierini and J. M. Greneche, J. Phys.: Condens. Matter **9**, 2303 (1997).
[4]K. Suzuki and J. M. Cadogan, Phys. Rev. B **58**, 2730 (1998).
[5]J. M. Greneche, N. Randrianantoandro, A. Slawska-Waniewska, and M. Miglierini, Hyperfine Interact. **113**, 279 (1998).
[6]S. Stankov, B. Sepiol, T. Kanuch, D. Scherjau, R. Würschum, and M. Miglierini, J. Phys.: Condens. Matter **17**, 3183 (2005).
[7]K. Suzuki, A. Makino, A. Inoue, and T. Masumoto, J. Appl. Phys. **70**, 6232 (1991).
[8]G. Herzer, Phys. Scr., T **49A**, 307 (1993).
[9]M. E. McHenry and D. E. Laughlin, Acta Mater. **48**, 223 (2000).
[10]K. Suzuki, N. Kataoka, A. Inoue, A. Makino, and T. Masumoto, Mater. Trans., JIM **31**, 743 (1990).
[11]T. Ohkubo, H. Kai, A. Makino, and Y. Hirotsu, Mater. Sci. Eng., A **312**, 274 (2001).
[12]S. Stankov, Y. Z. Yue, M. Miglierini, B. Sepiol, I. Sergueev, A. I. Chumakov, L. Hu, P. Svec, and R. Rüffer, Phys. Rev. Lett. **100**, 235503 (2008).
[13]S. Stankov, M. Miglierini, A. I. Chumakov, I. Sergueev, Y. Z. Yue, B. Sepiol, P. Svec, L. Hu, and R. Rüffer, Phys. Rev. B **82**, 144301 (2010).
[14]M. Miglierini, A. Lancok, and J. Kohout, Appl. Phys. Lett. **96**, 211902 (2010).
[15]W. Sturhahn and E. Gerdau, Phys. Rev. B **49**, 9285 (1994).
[16]T. Kemény, D. Kaptás, J. Balogh, L. F. Kiss, T. Pusztai, and I. Vincze, J. Phys.: Condens. Matter **11**, 2841 (1999).
[17]J. Balogh, L. Bujdosó, D. Kaptás, T. Kemény, I. Vincze, S. Szabó, and D. L. Beke, Phys. Rev. B **61**, 4109 (2000).
[18]R. S. Preston, S. S. Hanna, and J. Heberle, Phys. Rev. **168**, 2207 (1962).
[19]K. Hono, Y. Zhang, A. Inoue, and T. Sakurai, Mater. Sci. Eng., A **226–228**, 498 (1997).
[20]F. Liu, F. Sommer, and E. J. Mittemeijer, J. Mater. Sci. **39**, 1621 (2004).
[21]E. Pineda and D. Crespo, Phys. Rev. B **60**, 3104 (1999).

Nuclear Instruments and Methods in Physics Research A 847 (2017) 111–116

Contents lists available at ScienceDirect

Nuclear Instruments and Methods in Physics Research A

journal homepage: www.elsevier.com/locate/nima

Advanced approach to the analysis of a series of *in-situ* nuclear forward scattering experiments

Vlastimil Vrba[a,*], Vít Procházka[a], David Smrčka[a], Marcel Miglierini[b,c]

[a] *Department of Experimental Physics, Faculty of Science, Palacký University Olomouc, 17. listopadu 12, 771 46 Olomouc, Czechia*
[b] *Slovak University of Technology in Bratislava, Faculty of Electrical Engineering and Information Technology, Institute of Nuclear and Physical Engineering, Ilkovicova 3, 812 19 Bratislava, Slovakia*
[c] *Department of Nuclear Reactors, Faculty of Nuclear Science and Physical Engineering, Czech Technical University in Prague, V Holešovičkách 2, 180 00 Prague, Czechia*

ARTICLE INFO

Keywords:
Nuclear forward scattering
Data evaluation
In-situ experiments
Crystallization
Chemical reaction

ABSTRACT

This study introduces a sequential fitting procedure as a specific approach to nuclear forward scattering (NFS) data evaluation. Principles and usage of this advanced evaluation method are described in details and its utilization is demonstrated on NFS *in-situ* investigations of fast processes. Such experiments frequently consist of hundreds of time spectra which need to be evaluated. The introduced procedure allows the analysis of these experiments and significantly decreases the time needed for the data evaluation. The key contributions of the study are the sequential use of the output fitting parameters of a previous data set as the input parameters for the next data set and the model suitability crosscheck option of applying the procedure in ascending and descending directions of the data sets. Described fitting methodology is beneficial for checking of model validity and reliability of obtained results.

1. Introduction

With current high brilliance synchrotron radiation sources nuclear forward scattering (NFS) [1–4] has become a suitable experimental technique for investigation of various types of processes in a solid state such as chemical and phase transformations or a system development with a dynamic change of conditions [5,6]. Information on the studied processes is contained in a sequence of measured NFS time spectra. This is accompanied by a new demand on the evaluation procedures. However, physical reliability of results and conclusion should be ensured.

NFS gives a unique information on fast processes in studied systems, but the evaluation of measured time spectra can be difficult. NFS data evaluation is usually realized by fitting calculated time spectra to experimental data. Parameters describing the theoretical curve are refined during the fitting process. For evaluation of individual time spectra several programs have been developed including CONUSS [7,8], MOTIF [9] or FitSuite [10]. Crucial task of NFS data evaluation is to find an appropriate model describing the studied system. All nuclei in specific conditions, i.e. different chemical, structural and magnetic surroundings, contribute to one model component. Each component in the model is described by a set of parameters including relative amount of corresponding resonant nuclei, hyperfine parameters, their distributions and texture. During the investigated process some components might disappear and new components might appear in the system as the latter might undergo magnetic or structural transformations. Many parameters may also be significantly changing during the process. Consequently, the physical model applied in the fitting should be modified. Therefore evaluation is even more complicated when observing the whole process via a sequence of measured time spectra.

For samples enriched by ^{57}Fe the achievable accumulation time of one time spectrum is approximately one minute. For the processes which last from several minutes to hours the total number of time spectra which need to be evaluated rises up to hundreds [6]. Therefore automation of the evaluation procedure would bring significant increase of efficiency of NFS data analysis. In [11] an approach using artificial neural network (ANN) for the analysis of nuclear resonant scattering experiments was introduced. By using this method time requirement for time spectra evaluation was significantly decreased. However, sufficient time for neural network initial training is still needed and there are limitations in a range of relevant parameters describing the time spectra for ANN analysis to be efficient.

In this paper we introduce sequential fitting procedure (SFP) which is based on a conventional fitting method and connects neighbouring time spectra through their input and output values of fitted parameters. After manual evaluation of one time spectrum SFP is initiated and the

* Corresponding author.
E-mail addresses: vlastimil.vrba01@upol.cz (V. Vrba), v.prochazka@upol.cz (V. Procházka), david.smrcka@upol.cz (D. Smrčka), marcel.miglierini@stuba.sk (M. Miglierini).

http://dx.doi.org/10.1016/j.nima.2016.11.050
Received 27 September 2016; Received in revised form 9 November 2016; Accepted 21 November 2016
Available online 23 November 2016
0168-9002/

rest of time spectra is evaluated automatically. This is not a new idea, however, the aim of this paper is to describe in detail a wide range of different aspects connected with SFP and show several advantages of SFP used for analysis of NFS experiments with a high number of acquired data. Several features connected with evaluation of a sequence of NFS time spectra are discussed, including checking of a validity of selected model by monitoring an agreement of theory with experimental data, checking hysteresis phenomena and correlations between fitted parameters.

Utilization of SFP is demonstrated using examples of three different physical processes. The first example shows temperature evolution of magnetic hyperfine field during the heating of hematite in the range close to its Néel temperature. The second process is crystallization in amorphous metals. It is a temperature induced process of formation of nanocrystalline grains in amorphous matrix [12,13]. Using the SFP method crystallization process was investigated *in-situ* under isothermal and dynamic temperature conditions and influence of an external magnetic field on the crystallization was studied [14,15]. The last application is an investigation of chemical reactions in a solid state, where thermal decomposition of potassium ferrates (transformation among K-Fe-O compounds with different Fe valent states) was observed [16].

2. Sequential fitting procedure using hubert

Evaluation of NFS experimental data is based on calculation of the time spectrum according to a selected model and its comparison with the measured experimental data. Theoretical and experimental data, described by the set of values $\{T_k\}$ and $\{E_k\}$ respectively, are compared with respect to their statistical agreement quantified by χ^2 parameter

$$\chi^2 = \sum_k \frac{(E_k - T_k)^2}{\sigma_k^2}. \quad (1)$$

The sum runs over $k = 1, 2, \ldots, K$ where index k describes the corresponding delay times $\{t_k\}$ after the excitation synchrotron radiation pulse. The measurement standard deviation σ_k is usually estimated as $\sqrt{E_k}$. During the evaluation the values of model parameters are iteratively changed and χ^2 value is monitored. This iterative process is stopped after χ^2 reaches selected stopping condition and fitted parameters describing the model are obtained. The evaluation is influenced by the initial values of fitted parameters. The fitting process converges if the initial values are close enough to the real ones.

A sequence of NFS time spectra is accumulated during a process. In order to extract relevant information on the process each time spectrum should be evaluated properly. Moreover, not only values of the parameters corresponding to the individual time spectra should be determined correctly, but also their evolution over the whole time interval of the process should be “reasonable”. That means the time spectra should be analyzed properly as the whole sequence. SFP can be used for more efficient analysis of NFS data sequences.

SFP proceeds in several steps. First, the initial values of fitted parameters for evaluation of the first time spectrum are set as close as possible to correct values. Then the fitting process runs and the resulting values of fitted parameters are obtained. In the next step connection between the first and the second time spectrum is made. This is done by setting the output values from the first time spectrum fitting as starting values for the second time spectrum fitting. After evaluation of the second time spectrum the connection between the second and the third time spectrum is made. This mechanism is applied for the whole sequence of the time spectra. Fig. 1 shows principles of SFP where $n = 1, 2, \ldots, N-1$ is index of the time spectra, $\{E_k\}^{(n)}$ is corresponding experimental data set, $\{p\}_{\text{in}}^{(n)}$ is a set of initial values of fitted parameters and $\{p\}_{\text{out}}^{(n)}$ is set of output values of fitted parameters.

In order to handle the iterative fitting procedure the Hubert software has been created. Hubert is a free software developed by C++ programming language in QtCreator environment [17]. It uses SFP and the CONUSS software which runs at the background for fitting the individual time spectra.

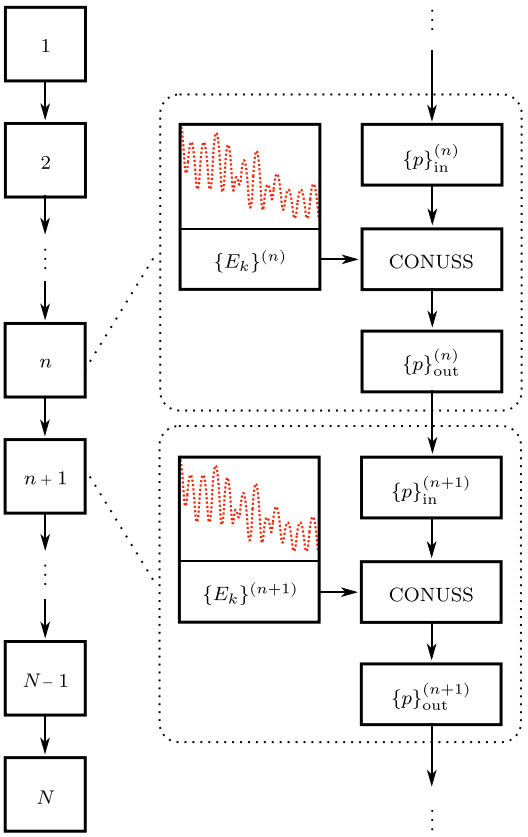

Fig. 1. Schematic illustration of the SFP principle implemented in Hubert.

3. Fitting methodology

Strong and weak points of the sequential analysis approach are described on three examples: the temperature evolution of magnetic hyperfine field in hematite, the crystallization process in amorphous metals and the solid state reaction. Closer information on the conducted experiments, used fitting models and reliability of fitted time spectra for the latter two examples can be found elsewhere [5,6,14–16].

The essential condition for successful SFP is sufficiently small difference between fitted parameters of the neighbouring time spectra. SFP usually fails and the fitting procedure doesn't converge in the range where some fitting parameters change too rapidly or even stepwise. This might occur, for example, for very fast chemical reactions, structural transformations or magnetic transformations, where SFP fails due to a large change in hyperfine magnetic field. The last mentioned case is demonstrated by a set of time spectra acquired during the heating of hematite [18]. The sample was heated up with constant heating rate of 10 °C/min in a wide range of temperatures to approximately 1000 °C. One time spectrum corresponds to one minute of measurement. Fig. 2 shows selected time spectra in the temperature range from 550 °C to 660 °C and compares resulted values of magnetic hyperfine field obtained by fitting the corresponding time spectra manually (each time spectrum was fitted separately one by one) and by using the SFP approach. The results from SFP evaluation are in

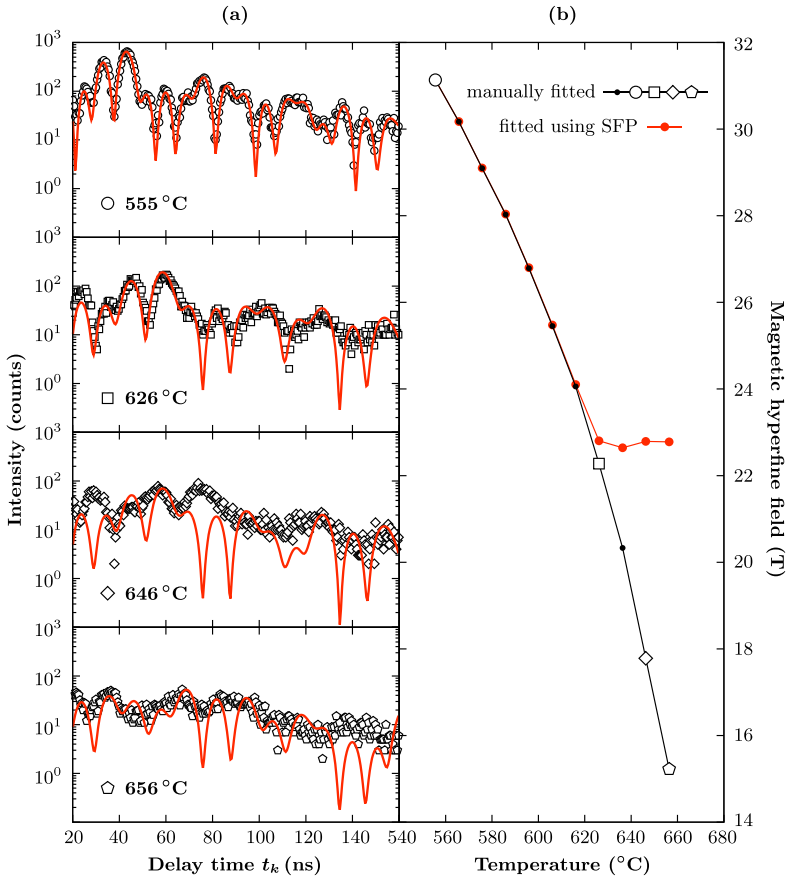

Fig. 2. (a) Examples of NFS time spectra of hematite for different temperatures in the temperature range close to the Néel temperature. The red curves represent fit of the time spectra obtained using SFP. The misfit is clearly visible. (b) comparison of magnetic hyperfine field values obtained by manual fit and SFP fit of the time spectra sequence.

agreement with the results from manual fitting up to 620 °C. After that the change of the magnetic hyperfine field starts to be too high (more than 1 T) as the temperature gets close to the Néel temperature of the hematite [19] and SFP starts to give incorrect results.

In a real case of fast chemical or structural transformation in a time domain the process might start slowly, reach some fast transformation range and then continue slowly again. In that case the SFP can still be used. However, in the fast transformation range time spectra should be fitted manually (bigger manual change in initial values is needed) and the rest can be fitted sequentially again.

In [14] the crystallization process of $Fe_{81}Mo_8Cu_1B_{10}$ amorphous metals under dynamic temperature conditions was observed by NFS experiments. Samples in the form of thin ribbons with thickness about 20 μm were enriched by ^{57}Fe to approximately 50% and measured in an evacuated furnace. By placing the furnace between two electromagnets influence of an external magnetic field of magnitude 0.652 T on the crystallization process was studied. A model with three components was used for analysis of measured time spectra. One component corresponds to the amorphous matrix described by the isomer shift and the quadrupole splitting with a broad distribution. The amorphous component is paramagnetic in a studied temperature range. The second and third components correspond to the inner and surface part of the crystalline grains. Both components are ferromagnetic. The surface part is characterized by broad magnetic hyperfine field distribution.

During the measurement the samples were heated up from the room temperature with constant temperature rate 10 °C/min. NFS time spectra were measured continuously during the heating and each time spectrum was accumulated during one minute. Analysis of the time spectra showed that the model is sufficient in a temperature range approximately up to 600 °C. After the proper manual fitting of one time spectrum the SFP was successfully applied for the whole considered temperature range.

The validity of the model and reliability of fitted parameters was tested. The interpretation of the results was performed in agreement with the described methodology and despite the uncertainty of some of the fitted parameters the formation of crystalline grains was clearly observed.

Crucial task in SFP as well as for correct analysis of NFS experiments is to create a correct model for analysis of NFS experiments. The selected model should be ideally valid for the whole analyzed time spectra sequence. In cases where one physical model can't cover the whole experiment more models need to be used. However, an overlap between the models is appropriate. The basic way of checking the model validity is to follow the χ^2 parameter and identify a range of the model validity by watching noticeable increases in χ^2.

When interpreting the χ^2 dependence one should check possible correlation of χ^2 with the total number of counts in given time spectrum. In ideal case the χ^2 should be close to one. However, there are often minor discrepancies between experimental data and used fitting model, frequently caused by slightly different line shape. Although these discrepancies have no influence on the interpretation of model components the χ^2 is consequently higher than one. Moreover, in this case the χ^2 may increase with increasing data statistics as the relative errors of the experimental points decrease. In NFS the statistics of measured time spectra depends on the incoming

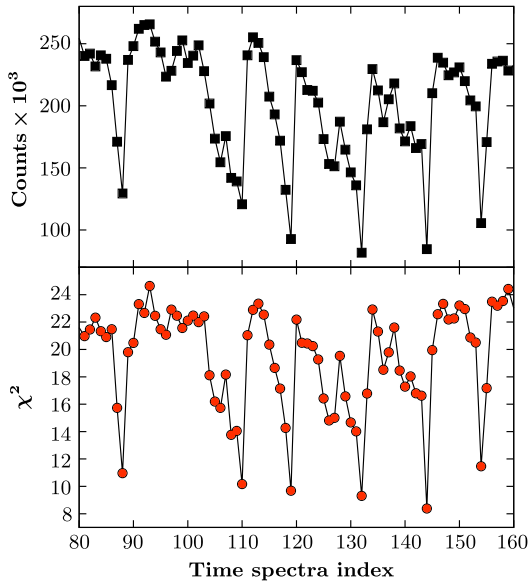

Fig. 3. Correlation between χ^2 and total number of counts in NFS time spectra.

radiation intensity which might exhibit fluctuations due to instabilities of high resolution monochromators (Fig. 3). This could result in observable changes in the χ^2 that are not connected with the quality of the used model.

However, if the correlation between the total number of counts and χ^2 is not observed, the noticeable changes in χ^2 may indicate that the used model fails and some spectral components might be incorrect or missing. Therefore the indication of using insufficient model can be even easier for a sequence of time spectra than for a separate experiment.

Another aspect of the data analysis especially using SFP is a correlation between different parameters. The correlation may occur in cases where two or more fitting parameters have similar influence on the time spectra. For example Lamb-Mössbauer factor and quadrupole splitting may cause similar effect on the shape of hybrid beats [20]. Possible correlation between two parameters for a sequence of time spectra can be checked by fixing one of the parameters, keeping the other parameters fitted and then comparing the obtained dependencies. Behaviour of fitted parameters can be also checked with setting several different values for the fixed parameter and comparing the results including the χ^2 dependences. Using this approach one can exclude correlation between parameters and thus reliability of fitted dependencies can be approved.

All discussed features are connected to the problem of multiple solutions where different sets of fitted values sometimes even with comparable χ^2 values can be obtained. In that case validity of a chosen model should be checked for each set of values independently. For a given set the model might work just for the time spectra in a small range and fails for the rest of them. Physical interpretation of obtained values and exclusion of the unphysical dependencies is also required. However, identification of the correct set of values is not always possible. Occurrence of multiple solutions can therefore considerably raise the uncertainty of fitted parameter values and consequently complicate the analysis of the whole experiment and its interpretation.

It is shown that for obtaining at least partial information from fitted sets of values one can follow “trends” of the fitted dependencies. By trends we mean typical characteristics of corresponding dependencies which are same for all the fitted sets. These trends can be therefore interpreted independently on the knowledge of the real values of parameters. Fig. 4 shows resulting relative amount of the inner part

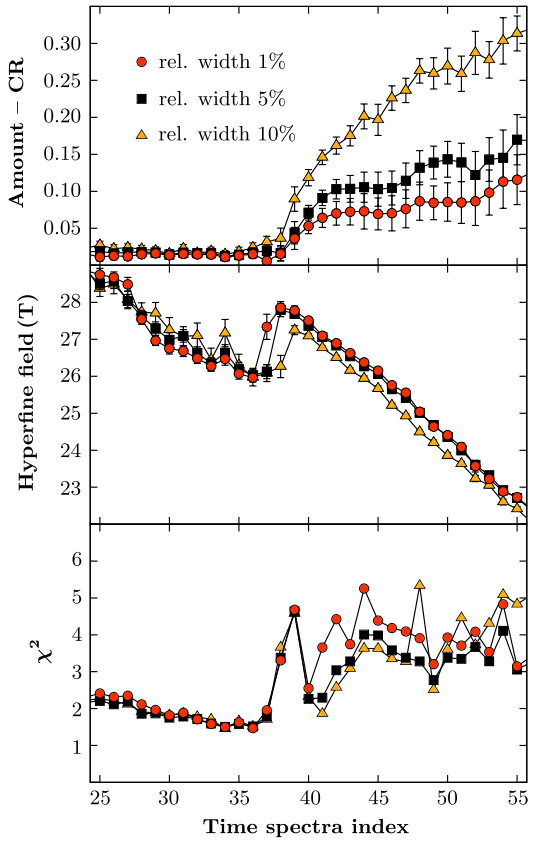

Fig. 4. Example of three fitted dependencies of relative amount of the crystalline component (CR), crystalline component magnetic hyperfine field and χ^2 obtained for different relative width (FWHM) of the magnetic hyperfine field distribution.

of crystalline grains (denoted as CR), corresponding hyperfine magnetic field and χ^2. Three dependences were obtained by using magnetic hyperfine field distribution with different relative width (FWHM) during the fitting procedure. The relative distribution width is given as percentages of the corresponding hyperfine field values. Despite the significant differences between the results the characteristics of all the dependencies are the same. The beginning of the transformation can be identified from the trends in relative amounts of individual spectral components and magnetic hyperfine fields. The temperature of the transformation beginning is the same for all three sets of values.

Using the example of crystallization in amorphous metals, we have discussed several problems of NFS data analysis using SFP. The last discussed feature will be demonstrated on an example of solid state chemical reactions.

In [16] thermally induced chemical reaction in potassium ferrate samples was studied. Decomposition in powder samples was observed under isothermal conditions. One NFS time spectrum was accumulated during one minute. K_2FeO_4 containing iron ions in valent state 6+ decomposed at temperatures above 200 °C to KFeO with iron in the valent state 3+. Except the initial and final compound intermediate states undetectable by *ex-situ* methods were also observed. The experimental data were successfully fitted by a model consisting of five components where iron in different valent states was represented by one component for each valent state.

Along with following the χ^2 parameter the model imperfections can be also verified by reversing of SFP where a “hysteresis” effect can be observed. It means that SFP gives different results when it starts from one or from the another side of the data sequence (viz. ascending vs.

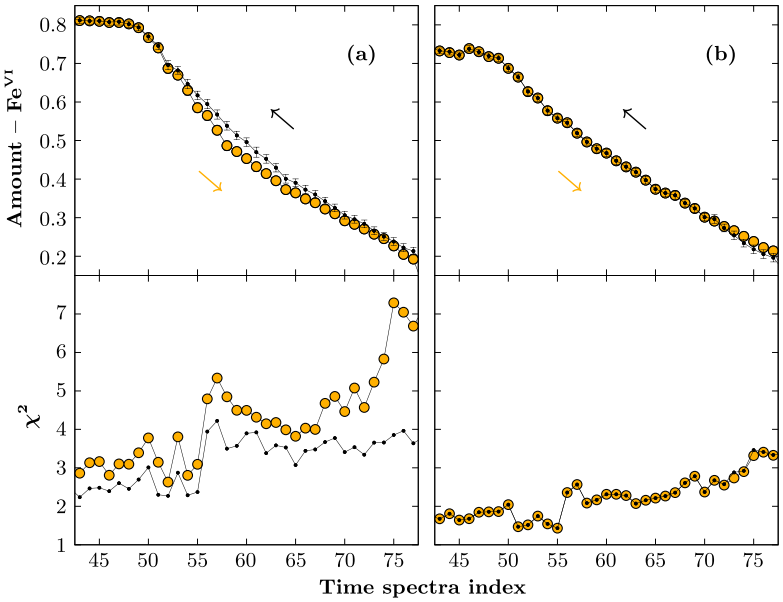

Fig. 5. Example of the hysteresis effect. Results were obtained using (a) incomplete model with two components corresponding to $K_2Fe^{VI}O_4$ and $KFe^{III}O$ and (b) improved model including intermediate components with Fe^{III}, Fe^{IV} and Fe^{VI}.

descending time of in-situ NFS experiments). Fig. 5 shows comparison of two models used for analysis of the potassium ferrate decomposition. The model with two components corresponding to K_2FeO_4 transforming to KFeO is shown in 5(a). The hysteresis effect can be seen clearly. In 5(b) the improved model including other three intermediate compounds evolving during the transformation is shown. The use of the improved model results in lowering of χ^2 as well as disappearance of the hysteresis.

Although the mentioned features are helpful in checking the model validity χ^2 increase or hysteresis observation itself doesn't provide any clue how to improve the model. In case of Mössbauer spectroscopy some missing or misinterpreted components in the model can be checked by analyzing positions and characters of spectral lines in the energy domain. In NFS checking of the model validity from analysis of the time domain dependencies is extremely difficult. Nevertheless, NFS may give us a unique information regarding, for example, specific evolution of hyperfine parameters or new components occurring during the process. This might not be obtainable by other experimental techniques. Therefore observation of hysteresis could be a clue for indication of unknown physical phenomena. It should be noted that identification of new fitting components is possible only when sufficiently high number of NFS data is evaluated using, for example, this advanced SFP approach.

4. Conclusions

It was shown that a sequence of NFS time spectra can be effectively evaluated using the SFP approach. Its use is especially helpful for *in-situ* studies of processes where up to hundreds of accumulated time spectra are evaluated. In such cases usage of SFP can decrease the time needed for data evaluation significantly. Although *in-situ* NFS is not a routine experimental technique its importance grows up as the current photon sources develop. Considerable increase in the synchrotron radiation brilliance in free electron lasers can be expected in the future. Consequently much faster chemical processes will become observable by this technique.

The metallic glasses crystallization study and thermal decomposition in potassium ferrate samples have been successfully analyzed by the Hubert program with SFP implemented. The analysis included checking of the model validity and reliability of the values of fitted parameters. Despite the problems connected with the time spectra evaluation such as correlations and equivalent multiple solutions the sequential fitting offers a possibility of extracting relevant information on studied processes by following the trends of fitted parameters.

Acknowledgements

The authors gratefully acknowledge the support by the internal IGA grant of Palacký University (IGA_PrF_2016_022), the project GACR 14-12449S, and the Project VEGA 1/0182/16. The authors would also like to thank Helena Sedláčková (Palacký University Olomouc, Czech Republic) for her help with this paper.

References

[1] W. Sturhahn, Nuclear resonant spectroscopy, J. Phys: Condens. Matter 16 (2004) S497–S530. http://dx.doi.org/10.1088/0953-8984/16/5/009.
[2] R. Rüffer, Nuclear resonant scattering into the new millennium, Hyperfine Interact. 141–142 (2002) 83–97. http://dx.doi.org/10.1023/A:1021249902719.
[3] G.K. Shenoy, R. Röhlsberger, Scientific opportunities in nuclear resonance spectroscopy from source-driven revolution, Hyperfine Interact. 182 (2008) 157–172. http://dx.doi.org/10.1007/s10751-008-9720-y.
[4] R. Rüffer, A.I. Chumakov, Nuclear resonance beamline at ESRF, Hyperfine Interact. 97–98 (1996) 589–604. http://dx.doi.org/10.1007/BF02150199.
[5] M. Miglierini, V. Procházka, S. Stankov, P. Svec Sr., M. Zajac, J. Kohout, A. Lancok, D. Janickovic, P. Svec, Crystallization kinetics of nanocrystalline alloys revealed by in situ nuclear forward scattering of synchrotron radiation, Phys. Rev. B 86 (2012) 020202. http://dx.doi.org/10.1103/PhysRevB.86.020202.
[6] M. Miglierini, V. Procházka, R. Rüffer, R. Zbořil, In situ crystallization of metallic glasses during magnetic field annealing, Acta Mater. 91 (2015) 50–56. http://dx.doi.org/10.1016/j.actamat.2015.03.012.
[7] W. Sturhahn, E. Gerdau, Evaluation of time-differential measurements of nuclear-resonance scattering of x rays, Phys. Rev. B 49 (1994) 9285–9294. http://dx.doi.org/10.1103/PhysRevB.49.9285.
[8] W. Sturhahn, CONUSS and PHOENIX: evaluation of nuclear resonant scattering data, Hyperfine Interact. 125 (2000) 149–172. http://dx.doi.org/10.1023/A:1012681503686.
[9] Y.V. Shvyd'ko, MOTIF: evaluation of time spectra for nuclear forward scattering, Hyperfine Interact. 125 (2000) 173–188. http://dx.doi.org/10.1023/A:1012633620524.
[10] S. Sajti, L. Deák, L. Bottyán, FitSuite a general program for simultaneous fitting (and simulation) of experimental data. arXiv:0907.2805
[11] N. Planckaert, J. Demeulemeester, B. Laenens, D. Smeets, J. Meersschaut,

C. L'abbé, K. Temst, A. Vantomme, Artificial neural networks applied to the analysis of synchrotron nuclear resonant scattering data, J. Synchrotron Radiat. 17 (2010) 86–92. http://dx.doi.org/10.1107/S0909049509042824.
[12] S.D. Kaloshkin, I.A. Tomilin, The crystallization kinetics of amorphous alloys, Thermochim. Acta 280–281 (1996) 303–317. http://dx.doi.org/10.1016/0040-6031(96)02926-7.
[13] X.-L. Wang, J. Almer, C.T. Liu, Y.D. Wang, J.K. Zhao, A.D. Stoica, D.R. Haeffner, W.H. Wang, In situ synchrotron study of phase transformation behaviors in bulk metallic glass by simultaneous diffraction and small angle scattering, Phys. Rev. Lett. 91 (2003) 26. http://dx.doi.org/10.1103/PhysRevLett.91.265501.
[14] V. Procházka, V. Vrba, D. Smrčka, R. Rüffer, M. Matúš, M. Mašláň, M. Miglierini, Structural transformation of NANOPERM-type metallic glasses followed in situ by synchrotron radiation during thermal annealing in external magnetic field, J. Alloy. Compd. 638 (2015) 394–404. http://dx.doi.org/10.1016/j.jallcom.2015.03.058.
[15] M. Miglierini, M. Pavlovič, V. Procházka, T. Hatala, G. Schumacher, R. Rüffer, Evolution of structure and local magnetic fields during crystallization of HITPERM glassy alloys studied by in situ diffraction and nuclear forward scattering of synchrotron radiation, Phys. Chem. Chem. Phys. 17 (2015) 28239–28249. http://dx.doi.org/10.1039/C5CP00245A.
[16] L. Machala, V. Procházka, M. Miglierini, V.K. Sharma, Z. Marušák, H.-C. Wille, R. Zbořil, Direct evidence of Fe(V) and Fe(IV) intermediates during reduction of Fe(VI) to Fe(III): a nuclear forward scattering of synchrotron radiation approach, Phys. Chem. Chem. Phys. 17 (2015) 21787–21790. http://dx.doi.org/10.1039/c5cp03784k.
[17] V. Procházka, V. Vrba, Hubert Software Package. ⟨http://fyzika.upol.cz/cs/vysledky-vyzkumu/software-hubert⟩, 2015.
[18] Unpublished Measurements.
[19] F. Bodker, M.F. Hansen, C.B. Koch, K. Lefmann, S. Morup, Magnetic properties of hematite nanoparticles, Phys. Rev. B 61 (2000) 6826–6838. http://dx.doi.org/10.1103/PhysRevB.61.6826.
[20] Y.V. Shvyd'ko, U. van Bürck, W. Potzel, P. Schindelmann, E. Gerdau, O. Leupold, J. Metge, H.D. Rüter, G.V. Smirnov, Hybrid beat in nuclear forward scattering of synchrotron radiation, Phys. Rev. B 57 (1998) 6. http://dx.doi.org/10.1103/PhysRevB.57.3552.

Available online at www.sciencedirect.com

ScienceDirect

Acta Materialia 91 (2015) 50–56

Acta MATERIALIA

www.elsevier.com/locate/actamat

In situ crystallization of metallic glasses during magnetic field annealing

M. Miglierini,[a,b,*] V. Procházka,[c] R. Rüffer[d] and R. Zbořil[b]

[a]*Institute of Nuclear and Physical Engineering, Slovak University of Technology, Ilkovičova 3, 812 19 Bratislava, Slovakia*
[b]*Regional Centre of Advanced Technologies and Materials, Palacky University, 17. listopadu 12, 771 46 Olomouc, Czech Republic*
[c]*Department of Experimental Physics, Faculty of Science, Palacky University, 17. listopadu 12, 771 46 Olomouc, Czech Republic*
[d]*ESRF-The European Synchrotron, CS40220, 38043 Grenoble Cedex 9, France*

Received 6 November 2014; revised 5 March 2015; accepted 5 March 2015

Abstract—The impact of an external magnetic field upon changes in the crystallization kinetics of $Fe_{90}Zr_7B_3$ metallic glass is studied by *in situ* nuclear forward scattering (NFS) of synchrotron radiation. Structural and magnetic information on the whole process of nanograin formation is monitored on fly in real time by means of time domain Mössbauer effect technique. Isothermal annealing performed at 753 K under weak magnetic field ($B_{ext} = 0.652$ T) exhibits more rapid crystallization in comparison with zero-field conditions. These surprising effects of an external magnetic field upon the process of phase transformation are attributed to energetic perturbations of magnetic interactions in comparison with the thermal energy. Consequently, the formation of nucleation centers is enhanced. Such accelerated crystallization was not reported so far for metallic glasses exposed to magnetic field *during* annealing. The influence of magnetic field on the resulting properties is usually assessed under static conditions *after* annealing. The use of NFS with rapid data acquisition has allowed *in situ* observation of the microstructure development throughout the fast annealing processes. In this way, not only the starting and the final stages of the structure can be characterized but also the intermediate transition period states of the transformation can be followed to fine details.

Keywords: Nuclear forward scattering; Structural transformation; Metallic glasses; Crystallization

1. Introduction

Physical properties of amorphous [1,2] and nanocrystalline alloys [3,4] comprising their magnetic [5] and mechanic performance [6] are governed by the size, amount, and chemical composition of the nanograins embedded in the surrounding amorphous matrix [7]. Due to their unique soft magnetic properties, namely Fe-based amorphous metallic glasses are often employed as magnetic shielding, transformer cores, sensors, and recording media [8]. Structural changes related mostly to crystallization that can occur in these materials when they are exposed to high enough temperatures for prolonged operational times degrade their working parameters. Therefore, a comprehensive understanding of the evolution of nanograins during nanocrystallization is essential [9] in order to understand, optimize, and conserve the unique magnetic properties exhibited by nanocrystalline alloys. In order to tailor specific properties of the nanograins, one has several possibilities how to control their formation including the grain size. For example, temperature, time profile of the annealing temperature, and applied pressure [10], belong among the most widely used. Special emphasis is put on the so-called magnetic annealing when the desired magnetic parameters are obtained *via* temperature annealing in an external magnetic field [5,6].

In some particular applications (e.g., transformer cores, magnetic shielding, magnetic circuits for resonant cavities), the metallic glasses can be affected by both an elevated temperature and, simultaneously, by a static and/or alternating magnetic field. Therefore, understanding the influence of magnetic fields upon the crystallization process is another important issue for the preparation of materials with specific properties and prevention of deterioration of their performance. Magnetic energy of an external magnetic field is one of the contributions to the total energy of the system, which is decisive for structural arrangement and thermal stability. Thermodynamic potentials are crucial for the kinetics of transition processes. Nevertheless, real influence of magnetic field on the thermodynamic potential is not fully understood and the impact of thermal annealing under magnetic field upon the resulting material properties is difficult to predict.

So far, the consequences of an impact of magnetic field upon structural transformations were investigated mostly in steels. Extensive review of solid–solid phase transformation (austenite to ferrite) in Fe-based alloys caused

* Corresponding author at: Institute of Nuclear and Physical Engineering, Slovak University of Technology, Ilkovičova 3, 812 19 Bratislava, Slovakia.

http://dx.doi.org/10.1016/j.actamat.2015.03.012
1359-6462/

by strong magnetic fields (up to 10 T) is presented by Ohtsuka [11]. The effects of magnetic fields on the transformation temperature and phase diagram are explained thermodynamically. Nevertheless, Enomoto [12] states in his review paper that the influence of magnetic field upon kinetics (e.g., influence on diffusion and grain boundary mobility) is least understood. Isothermal transformation kinetics of the austenite phase into the martensite phase in metastable austenitic maraging steel was recently reported by San Martin et al. [13] employing time-dependent magnetization measurements for temperatures from 4 to 298 K and continuous applied magnetic fields up to 30 T. The transformation kinetics was shown to be accelerated by several orders of magnitude when high magnetic fields are applied.

As far as metallic glasses and nanocrystalline alloys are concerned, the effect of magnetic field during heat treatment (eventually followed by nanocrystallization) was investigated only in connection with their macroscopic magnetic properties [5,14,19]. Annealing under static magnetic fields with different orientations and strength improved the induced anisotropies and the coercive field values in HITPERM-type materials that remained fairly stable at elevated temperatures [15–17]. Similar phenomena were reported for other soft magnetic Fe-based amorphous alloys and compared to advanced non-oriented silicon steels [18]. External magnetic fields as high as 17 T were also applied [19]. On the other hand, the soft magnetic properties of Fe-rich nanocrystalline soft magnetic alloys are dramatically improved by the use of a rotating field during nanocrystallization [14,20]. Nevertheless, all observations reported up to now were limited to the use of macroscopic characterization techniques including magnetic measurements. They provide integral information averaged over all structurally different components in the emerging nanocrystalline arrangement. The microstructure developed upon magnetic annealing was studied by transmission electron microscopy (TEM) and by X-ray diffraction (XRD). After field annealing, no significant changes in either the crystallization behavior or in the size and morphology of grains as compared to the zero-field-annealed reference samples was found [15]. Because these analyses were performed under static *ex situ* conditions only a comparison of the original and the final state of the sample was possible. That means that it is possible that from the morphological point of view the samples before and after magnetic annealing might look alike though their magnetic responses may vary. Here, we employ a method that offers unique possibility of obtaining simultaneous information from both microstructural arrangement and from the corresponding hyperfine interactions during *in situ* annealing.

In the elucidation of crystallization behavior of metallic glasses, along with conventional analytical tools also sophisticated and advanced techniques were employed. For example, solute clustering and partitioning behavior in the early crystallization stage of a $Fe_{73.5}Si_{13.5}B_9Nb_3Cu_1$ amorphous alloy were studied by employing a three-dimensional atom probe and a high resolution electron microscope [21]. Recently, rapid annealing (4–10 s) induced primary crystallization of soft magnetic Fe–Si nanocrystals in a $Fe_{73.5}Si_{15.5}Cu_1Nb_3B_7$ amorphous alloy has been systematically studied by atom probe tomography and compared with conventional annealing [22]. The use of on line *in situ* characterization techniques is, however still limited to diffraction of synchrotron radiation. For example, *in-situ* High Energy X-ray Diffraction (HEXRD) of synchrotron radiation was employed to follow the change of free volumes upon heating [23] and to measure plastic deformation mechanisms of metallic glasses [24]. Modifications of structural arrangement including relaxation processes were investigated in swift heavy-ion bombarded $Fe_{73}Cu_1Nb_3Si_{16}B_7$ metallic glass also by HEXRD [25]. A more sophisticated technique of real-time *in situ* synchrotron X-ray tomographic microscopy was used to describe the nucleation mechanism and growth kinetics of an aluminum alloy [26].

In this work we deal with the problem how an external magnetic field affects the progress of structural transformation in metallic glasses *during* isothermal heat treatment. In doing so, we have made use of nuclear forward scattering (NFS) of synchrotron radiation with ^{57}Fe nuclei [27,28]. More details on the NFS technique can be found also elsewhere [29]. Extremely brilliant X-rays produced by the third generation of synchrotron sources combined with precise monochromatization enable rapid data acquisition. Consequently, it is possible to monitor the crystallization process on fly which allows its direct study even during *in situ* annealing. Benefiting from the fact that hyperfine interactions are straightforwardly related to structural arrangement we have recently reported on the nucleation and growth processes that are taking place during isothermal annealing of a metallic glass [9]. Through time evolution of the identified hyperfine interactions we have followed the structural transformation separately for the nanograins, their interfaces, and the residual amorphous matrix. The obtained experimental results matched completely with theoretically calculated predictions according to the available crystallization models. Here, we extend the previous results toward studies performed under simultaneous action of the external magnetic field.

Our work was motivated by the fact that even though the effects of (strong) magnetic fields upon phase transformations were studied in ordered metallic alloys (steels), so far no evidence of any changes in the kinetics of crystallization were reported in disordered amorphous metallic alloys. The investigations performed up to now on metallic glasses aimed at characterization of the final static stages of the alloys after the thermal treatment under external magnetic field conditions and at the resulting macroscopic magnetic parameters. Nevertheless, using conventional analytical tools it was not possible to unveil the progress of crystallization during the influence of the magnetic field. We made use of NFS that enables rapid acquisition of experimental data sensitive to both structural arrangements as well as to magnetic states of the probe nuclei. Choosing the NANOPERM alloy as a typical representative of metallic glasses that exhibit nanocrystallization we have followed its phase transformation *during* isothermal heat treatment under the presence of a weak external magnetic field.

2. Experimental details

Ribbons of $Fe_{90}Zr_7B_3$ metallic glass were prepared by a melt spinning technique. They were about 2 mm wide and 20 μm thick. To ensure smooth and rapid data acquisition, the iron contents were enriched to about 63% in ^{57}Fe. We

have chosen this NANOPERM system because during primary crystallization it forms bcc-Fe nanocrystals [30]. The latter is a calibration material for Mössbauer spectrometry. Even more importantly, the corresponding Mössbauer spectrum as well as the nuclear resonant interferogram is relatively simple. In addition, structural [9], dynamic [31,32], and magnetic properties [33] of (physically) the same material were already thoroughly studied. The as-quenched alloy exhibits an amorphous character with slight surface crystallization of bcc-Fe [32,33]. A small amount of Zr (about 0.2%) was identified in the core of the bcc-Fe nanograins [33]. At the same time, because the NANOPERM metallic glass represents a whole group of alloys that exhibit advantageous magnetic properties achieved through nanocrystallization, we expect that the obtained results can be extended and generalized toward all nanocrystalline alloys.

Nuclear Forward Scattering (NFS) experiments were performed at the Nuclear Resonance beamline [34] (ID18) of the European Synchrotron Radiation Facility (ESRF). Excitation of the ^{57}Fe nuclear levels was accomplished by a photon beam with 14.4 keV energy and ca. 1 meV bandwidth. Samples were placed in a vacuum furnace and heated up to the annealing temperatures of $T_a = 753$ K and 783 K with a heating rate of 40 K/min. When the destination temperature was reached, an isothermal annealing continued for up to 120 min. The NFS interferograms were recorded every minute during the whole annealing process. The magnetic field of 0.652 T was oriented along the ribbon length of the sample in the furnace, perpendicular to the incident photon beam and collinear with its π polarization, i.e. in the horizontal plane. Samples were placed in a furnace in such a way that the magnetic field was directed along the ribbon length (longitudinal arrangement). Schematic layout of the experiment is shown in Fig. 1.

3. Results and discussion

Typical set of NFS interferograms is shown as an example in Fig. 2(a) in a form of a contour plot whose intensities are color coded in a logarithmic scale. The elapsed decay time of the nuclear resonant level and the time of annealing are displayed on the x and y axes, respectively. In order to demonstrate the feasibility of the theoretical fits from which the respective quantitative (relative area) as well as qualitative (hyperfine field values) parameters were derived three representative experimental NFS patterns with the resulting calculated curves are demonstrated in Fig. 2(b). They exhibit three principal categories of the observed structural arrangements within the investigated system: (i) almost completely amorphous material just at the onset of crystallization (annealing time 11 min), (ii) development of nanocrystallization (22 min), and final state (52 min) when the amount of nanocrystals in the samples is stabilized during the given annealing conditions. Experimental NFS data from all experiments (amounting more than 150 individual records) were consistently analyzed according to a theoretical model introduced in Ref. [9] using the CONUSS evaluation software package [35,36].

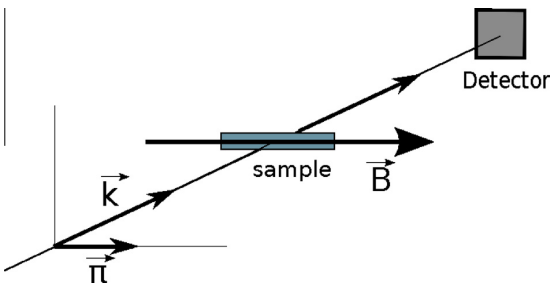

Fig. 1. Geometrical arrangement of the experiment. Ribbon length of the sample is parallel to the induction of the external magnetic field B and collinear with the synchrotron beam polarization π. The k-vector of photons is perpendicular to both.

At the beginning of thermal treatment, the investigated $Fe_{90}Zr_7B_3$ NANOPERM alloy exhibits an average bulk content of less than 3% of bcc-Fe nanograins [9]. They were formed during the quenching process and are preferentially located at both surfaces of the ribbon [32]. Few of them are situated also in the bulk. It took approximately 11–12 min from the beginning of the heating to stabilize the destination temperature of isothermal treatment. We assume that the incubation time of crystallization is included within this transition period during the temperature increase. Note that annealing temperatures of 753 K and 783 K are close and equal to the temperature of the onset of crystallization, respectively. The latter was determined to be of 783 K using differential scanning calorimetry [32]. Consequently, rather rapid crystallization kinetics is expected.

During annealing, the amount of nanocrystalline grains grows and after a certain time, which depends upon the heating conditions as discussed below, it saturates. Time evolutions of three structurally different positions of the ^{57}Fe atoms comprising amorphous (AM), interfacial (IF), and nanocrystalline (CR) regions are illustrated in Fig. 3. The partial components were obtained from the evaluation of the NFS interferograms that were acquired during isothermal annealing at 753 K without and with an external magnetic field, and at 783 K. Time dependences obtained from evaluation of experimental data (plotted by symbols) are overlaid by solid curves that represent results of the fits according to the crystallization model introduced recently [9]. Satisfactory agreement is reached for all three different annealing conditions.

In Fig. 3(a), formation of small nanograins is observed in the time region from 15 to 27 min. Higher IF values than the CR ones indicate that the majority of iron atoms experience broken symmetry of atoms located at the interface regions between the nanocrystals and the amorphous matrix. Consequently, the nanograins as such do not have well developed crystalline symmetry. This assumption is evidenced by a rapid increase of the IF component that is assigned to Fe atoms at the surfaces of the grains while the portion of iron atoms positioned in the core of nanograins possessing full bcc symmetry (CR) grows rather slowly.

The symmetry breaking at the surfaces of the nanograins that have been formed during the annealing at 753 K is documented by their hyperfine magnetic fields B_{IF}. They exhibit low values in Fig. 4(a) during the initial annealing up to about 22 min when they stabilize at a constant value of about 25.4 T. It is noteworthy that the B_{IF} values are by about 1 T smaller that those of the well ordered crystalline core of nanograins B_{CR} (26.5 T). These are almost constant over the whole inspected time interval which confirms their

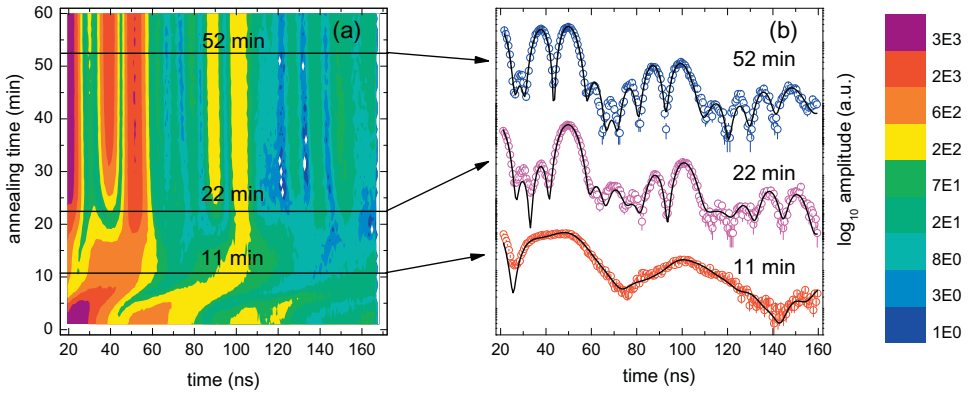

Fig. 2. Contour plot of 3D nuclear forward scattering spectra of $Fe_{90}Zr_7B_3$ annealed at 753 K (a) and selected records (open symbols) obtained after annealing for 11, 22, and 52 min of annealing (b). The calculated fitting curves are given by solid lines.

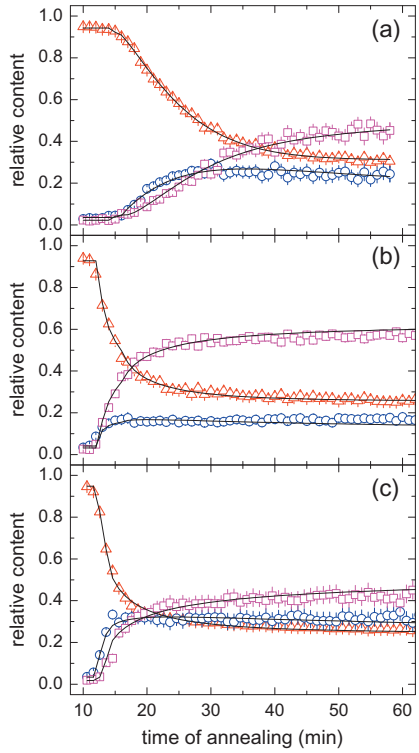

Fig. 3. Relative amounts of structural components including amorphous (AM, red triangles), interfacial (IF, blue circles), and crystalline (CR, magenta squares) regions plotted against annealing time at 753 K (a), at 753 K within the external magnetic field (0.652 T), and at 783 K (c). Solid curves represent fits according to the crystallization model introduced in Ref. [9]. (For interpretation of the references to color in this figure legend, the reader is referred to the web version of this article.)

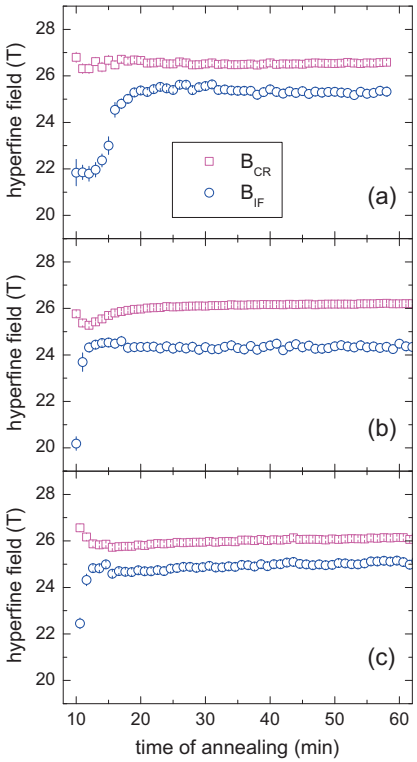

Fig. 4. Hyperfine magnetic field of crystalline (B_{CR} – magenta squares) and interfacial (B_{IF} – blue circles) components derived from the NFS interferograms recorded against time of annealing at 753 K (a), at 753 K in $B_{ext} = 0.652$ T (b), and at 783 K (c). (For interpretation of the references to colour in this figure legend, the reader is referred to the web version of this article.)

well developed structural arrangement. Small perturbations in B_{CR} at the beginning of the inspected time interval (10 min) are caused by stabilization of the temperature when it was reaching the set-up point.

From the viewpoint of hyperfine interactions, the bulk of bcc-Fe nanograins are stable during the isothermal annealing. As demonstrated by relative contents of the IF and CR components in Fig. 3(a), during the first 30 min of annealing the IF component dominates that of the CR one. This indicates that the grains are rather small and thus exhibit a higher contribution of the atoms located at their surfaces. Then, the grains grow in size which is documented by a higher fraction of the CR component. The grain-growth process saturates after the first hour of annealing.

Structural transformation during annealing at the same temperature of 753 K but in a weak magnetic field of 0.652 T proceeds much faster. Nanocrystals are well developed within the first 15 min after the beginning of annealing. This is demonstrated by saturated contribution of the IF component in Fig. 3(b) as well as by the associated B_{IF} in Fig. 4(b) which has significantly increased from about 20 T up to 24.4 T within this time period and then it is also stabilized. The grains are, however growing in size as seen from rising CR contribution that levels after about 25 min of annealing. The B_{CR} value is stabilized after 15 min of annealing to about 25.8 T. This is lower than in the zero-field annealed sample due to the applied magnetic field. From Fig. 4(a) and (b) it is also evident that Fe atoms in the interfacial regions exhibit a lower magnetic field which yields a difference of about 0.9 T with respect to zero-field annealing.

Magnetic field has a strong influence on the crystallization kinetics when the time needed for crystallization is by a factor of 3 less than that without the external magnetic field at the same temperature of annealing. The evolution of nanocrystals formation with time is shown in Fig. 5. The symbols represent combined contributions from the IF and CR components while the solid lines are results of the fits to the experimental data according to the crystallization model [9]. This observation introduces a new view at the energy balance of the crystallization process through the huge influence of small energetic perturbations of magnetic interactions in comparison with the thermal energy.

Temperature increase from 753 K to 783 K expectedly speeded-up the crystallization rate (compare also Fig. 3(a) and (c)). The same effect is reached, however by annealing at lower temperatures in an external magnetic field of 0.652 T (Fig. 3(b)). It is noteworthy that the formation of nanocrystals exhibits almost the same progress with time when the metallic glass was annealed under these two conditions.

The hyperfine field values of bcc-Fe crystallites B_{CR} that were obtained by averaging the data presented in Fig. 4 over the time interval from the 20th up to the 60th min, that is where B_{CR} are stabilized, are of 26.5 T, 25.7 T, and 25.8 T (error range $\pm$ 0.1 T) for annealing at 753 K, 783 K, and 753 K in $B_{ext} = 0.652$ T, respectively. They are consistent with those obtained from the conventional Mössbauer spectra of α-Fe foils taken *in situ* under the particular temperatures and averaged over the results reported by several research groups [37–41]. Small deviations (~1.4 T) between Mössbauer spectrometry and NFS data can be attributed to the fact that while in the former, foils with well developed crystals several micrometers in size were used, the NFS experiments were performed upon bcc-Fe nanograins embedded in a residual amorphous matrix of different compositions. Thus, contribution of small inclusions of other constituent elements in the newly formed bcc nanocrystals [33,40] as well as the influence of the surrounding amorphous matrix upon the resulting hyperfine magnetic field values cannot be completely ruled out.

From a qualitative point of view the time progress of crystallization is very alike for all three types of isothermal annealing. This phenomenon is illustrated with the help of two different time scales that are used in Fig. 6. The annealing time displayed on the bottom axis corresponds to the annealing temperature of 753 K whereas the top axis is used for annealing at 783 K and at 753 K in an external magnetic field. Though the top axis characterizes more rapid time evolution, all presented dependences are comparable within the range of experimental errors. In fact, the scaling of the top axis was obtained from a mutual comparison of decrease in relative AM contributions (Fig. 6(a)) as observed under different annealing conditions. The total relative amount of nanocrystals in Fig. 6(b) consists of contributions that stem from the sum of IF

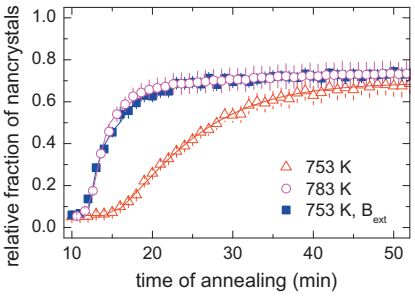

Fig. 5. Relative content of nanocrystals (including interfacial and crystalline components) plotted against annealing time at 753 K (red triangles), at 753 K within the external magnetic field $B_{ext} = 0.652$ T (blue squares), and at 783 K (magenta circles). Solid curves represent fits according to the crystallization model introduced in Ref. [9]. (For interpretation of the references to color in this figure legend, the reader is referred to the web version of this article.)

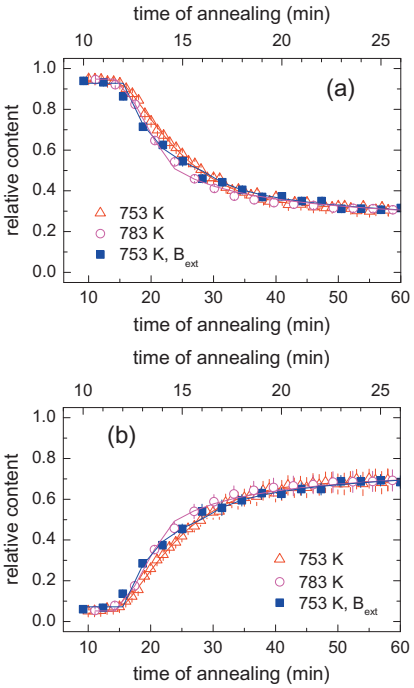

Fig. 6. Relative contents of amorphous residual phase (a) and nanocrystallites (IF + CR) (b) plotted against time of annealing. The bottom time axes refer to the lower annealing temperature (753 K). The top axes correspond to the annealing at 783 K and at 753 K in $B_{ext} = 0.652$ T. Solid curves represent fits according to the crystallization model introduced in Ref. [9].

and CR components similar as in Fig. 5. The solid lines correspond to the fits. Whatever annealing conditions were used the behavior of the curves exhibits the same trends that are in agreement with the assumed crystallization process based upon on-site nucleation and consequential growth of spherical grains [9]. Thus, in a reduced time scale, the mechanisms of the nanocrystal formation are the same irrespective of annealing conditions.

Though the magnetic field applied simultaneously with annealing presumably affects also the final state of the material after the crystallization is completed we have focused our attention on the transition period *during* the transformation. A higher annealing temperature has caused an anticipated increase of the crystallization rate (Fig. 5). Similar though unexpected behavior was unveiled when the weak magnetic field was applied at a lower annealing temperature. In addition, the formation of larger grains was observed in the latter case. In order to better understand differences in the crystallization kinetics between different types of annealing process, IF and CR components are plotted separately in Fig. 7(a) and (b), respectively.

The following assumptions can be made. In the case of a higher annealing temperature (e.g. 783 K), a lower energetic barrier for the formation of nucleation centers will result in a higher number of nanograins. This consequently leads to smaller nanograins due to space impeachment. Therefore, the relative contribution of interfacial regions (IF) that belong to Fe atoms with disturbed local surface symmetry would increase in comparison with those that

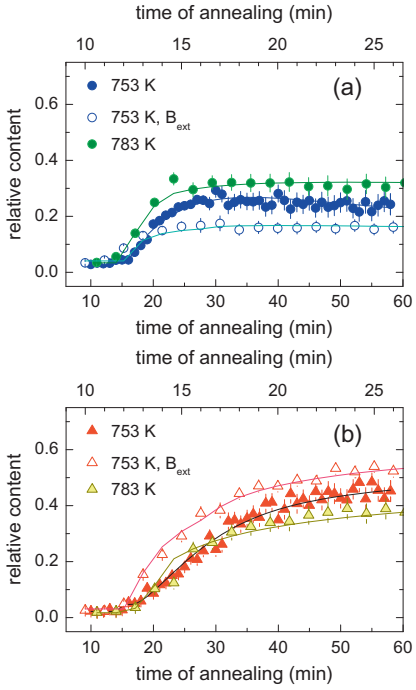

Fig. 7. Relative contents of interfacial IF (a) and nanocrystalline CR (b) components plotted against time of annealing. The bottom time axes refer to the lower annealing temperature (753 K). The top axes correspond to the annealing at 783 K and at 753 K in $B_{ext} = 0.652$ T. Solid curves represent fits according to the crystallization model introduced in Ref. [9].

are created by 753 K annealing. This effect is seen in Fig. 7(a). On the other hand, relative contribution of IF regions in the sample annealed at 753 K in an external magnetic field is the lowest. Thus, an increase in magnetically induced energy barriers for nucleation favors formation of a smaller number of larger grains which grow more rapidly than during a simple heat treatment in zero magnetic field. This observation is backed by the time dependences in Fig. 7(b) that represent relative contributions from the interior of bcc-Fe grains.

As far as field-induced changes in the kinetics of crystallization are concerned, we suggest the following explanation. Structural transformation from amorphous into nanocrystalline state is a non-equilibrium thermodynamic process during which the critical temperature and the crystallization rate are governed by the Gibbs potential profile, energetic barrier for a nucleation center formation [42] and by the diffusion rate [43]. The assessment of crystallization kinetics relays upon the difference between Gibbs potentials in amorphous and crystalline states as well as the height of the energetic barrier [44,45]. We can speculate that both these thermodynamic parameters are affected by the applied magnetic field. If the difference in the Gibbs potentials became smaller, the crystallization would start earlier, and, eventually with a higher crystallization rate.

4. Conclusions

Kinetics of crystallization of a NANOPERM $Fe_{90}Zr_7B_3$ alloy was investigated with the help of *in situ* nuclear forward scattering of synchrotron radiation. Isothermal annealing performed at the temperature slightly below the crystallization temperature (as derived from DSC) has led to the formation of nanocrystallites over a time span of about one hour. A rapid speed up effect on the crystallization process was observed when a weak magnetic field was applied even though the initially amorphous NANOPERM alloy was paramagnetic before transformation. The time needed for saturation of the nanocrystallites was factor of 3 shorter than in the previous case.

In order to reach the same crystallization rate without an external magnetic field an additional contribution of a thermal energy of 30 K is needed. Detailed analyses of nuclear forward scattered interferograms that were decomposed into contributions stemming from the amorphous residual phase and newly formed nanocrystallites provided an opportunity to study independently the role of structurally different regions. Moreover, using this approach it was possible to further differentiate between contributions from the surfaces and bulk of the nanograins. Different amounts of iron atoms located at the grains' surfaces and in their bulk were observed for different crystallization conditions, *i.e.* temperature and/or magnetic field. Even though from a qualitative point of view the time evolution of the crystallization process is the same irrespective of annealing conditions, the evaluation of these deviations unveiled some differences in the supposed spherical grain growth process. By 'a qualitative point' we mean that the crystallization kinetics is usually assessed by taking into consideration the formation of the nanograins as such without any separation of contributions from their surfaces and bulks.

Our results show that the use of a weak external magnetic field imposed upon the samples during their heat treatment favors formation of larger grains. Here, an effect

of an increased energy barrier caused by magnetic perturbations that subsequently prevent formation of new nucleation centers is considered. This is in contrast with zero-field annealing when presumably smaller grains are formed.

An accelerated crystallization of metallic glasses was followed to fine details that are completely hidden when conventional analytical tools are employed. Even though the influence of (strong) magnetic fields upon phase transformations was already studied in structurally ordered materials (steels), their impact on the progress of crystallization in metallic glasses was not reported so far. The most striking result of our observation is the fact that already weak magnetic fields have triggered a considerably high influence upon the crystallization kinetics of metallic glasses. On the other hand, we can conclude that the mechanisms of the nanocrystals formation are the same irrespective of annealing conditions. The application of *in situ* NFS experiments has a huge potential for observations of the evolution of phase transformations in real time performed on fly during short time intervals.

Acknowledgements

The authors gratefully acknowledge the support by the project LO1305 of the Ministry of Education, Youth and Sports of the Czech Republic and the projects SK-PL-0032-12, CZ.1.07/2.3.00/20.0155, and CZ.1.07/2.3.00/30.0041.

References

[1] M.F. Ashby, A.L. Greer, Scripta Mater. 54 (2006) 321.
[2] A. Inoue, A. Takeuchi, Acta Mater. 59 (2011) 2243.
[3] H. Gleiter, Acta Mater. 48 (2000) 1.
[4] K. Suzuki, A. Makino, A. Inoue, T. Masumoto, J. Appl. Phys. 70 (1991) 6232.
[5] G. Herzer, Acta Mater. 61 (2013) 718.
[6] A. Schuh, T.C. Hufnagel, U. Ramamurty, Acta Mater. 55 (2007) 4067.
[7] G. Herzer, Phys. Scr. T. 49A (1993) 307.
[8] M.E. McHenry, D.E. Laughlin, Acta Mater. 48 (2000) 223.
[9] M. Miglierini, V. Prochazka, S. Stankov, P. Svec Sr., M. Zajac, J. Kohout, A. Lancok, D. Janickovic, P. Svec, Phys. Rev. B 86 (2012) 020202(R).
[10] F. Ye, K. Lu, Phys. Rev. B 60 (1999) 7018.
[11] H. Ohtsuka, Sci. Technol. Adv. Mater. 9 (2008) 013004.
[12] M. Enomoto, Mater. Trans. 46 (2005) 1088.
[13] D. San Martin, N.H. van Dijk, E. Jiménez-Melero, E. Kampert, U. Zeitler, S. van der Zwaag, Mater. Sci. Eng., A 527 (2010) 5241.
[14] K. Suzuki, G. Herzer, Scripta Mater. 67 (2012) 548.
[15] I. Škorvánek, J. Marcin, T. Krenický, J. Kováč, P. Švec, D. Janičkovič, J. Magn. Magn. Mater. 304 (2006) 203.
[16] I. Škorvánek, J. Marcin, J. Turčanová, J. Kováč, P. Švec, Magnetohydrodynamics 45 (2009) 267.
[17] I. Škorvánek, J. Marcin, J. Turčanová, J. Kováč, P. Švec, J. Alloys Compd. 504S (2010) S135.
[18] I. Škorvánek, J. Marcin, M. Capik, M. Varga, J. Turčanová, J. Kováč, P. Švec, D. Janičkovič, F. Kováč, V. Stoyka, Magnetohydrodynamics 48 (2012) 371.
[19] F. Johnson, H. Garmestani, S.Y. Chu, M.E. McHenry, D.E. Laughlin, IEEE Trans. Magn. 40 (2004) 2697.
[20] K. Suzuki, N. Ito, J.S. Garitaonandia, J.D. Cashion, J. Appl. Phys. 99 (2006) 08F114.
[21] K. Hono, D.H. Ping, M. Ohnuma, H. Onodera, Acta Mater. 47 (1999) 997.
[22] K.G. Pradeep, G. Herzer, P. Choi, D. Raabe, Acta Mater. 68 (2014) 295.
[23] N. Mattern, M. Stoica, G. Vaughan, J. Eckert, Acta Mater. 60 (2012) 517.
[24] G. Wang, N. Mattern, J. Bednarčík, R. Li, B. Zhang, J. Eckert, Acta Mater. 60 (2012) 3074.
[25] S. Michalik, J. Michalikova, M. Pavlovic, P. Sovak, H.-P. Liermann, M. Miglierini, Acta Mater. 80 (2014) 309.
[26] C. Puncreobutr, A.B. Phillion, J.L. Fife, P. Rockett, A.P. Horsfield, P.D. Lee, Acta Mater. 79 (2014) 292.
[27] Y.V. Shvyd'ko, Phys. Rev. B 57 (1998) 3552.
[28] Y.V. Shvyd'ko, Phys. Rev. B 59 (1999) 9132.
[29] R. Röhlsberger, Nuclear Condensed Matter Physics with Synchrotron Radiation – Basic Principles, Methodology and Applications, Springer-Verlag, Berlin Heidelber, 2004.
[30] K. Suzuki, N. Kataoka, A. Inoue, A. Makino, T. Masumoto, Mater. Trans., JIM 31 (1990) 743.
[31] S. Stankov, Y.Z. Yue, M. Miglierini, B. Sepiol, I. Sergueev, A.I. Chumakov, L. Hu, P. Svec, R. Rüffer, Phys. Rev. Lett. 100 (2008) 235503.
[32] S. Stankov, M. Miglierini, A.I. Chumakov, I. Sergueev, Y.Z. Yue, B. Sepiol, P. Svec, L. Hu, R. Rüffer, Phys. Rev. B 82 (2010) 144301.
[33] M. Miglierini, A. Lancok, J. Kohout, Appl. Phys. Lett. 96 (2010) 211902.
[34] R. Rüffer, A.I. Chumakov, Hyperfine Interact. 97–98 (1996) 589.
[35] W. Sturhahn, E. Gerdau, Phys. Rev. B 49 (1994) 9285.
[36] W. Sturhahn, Hyperfine Interact. 125 (2000) 149.
[37] R.S. Preston, S.S. Hanna, J. Heberle, Phys. Rev. B 128 (1962) 2207.
[38] O. Hupe, M.A. Chuev, H. Bremers, J. Hesse, A.M. Afanas'ev, J. Phys.: Condens. Matter 11 (1999) 10545.
[39] O. Hupe, M.A. Chuev, H. Bremers, J. Hesse, A.M. Afanas'ev, K.G. Efthimiadis, E.K. Polychroniadis, Mössbauer effect in iron-based nanocrystalline alloys, in: M. Mashlan, M. Miglierini, P. Schaaf (Eds.), Materials Research in Atomic Scale by Mössbauer Spectroscopy, Kluwer, Dordrecht, 2003.
[40] M. Miglierini, J.-M. Grenèche, J. Phys.: Condens. Matter 15 (2003) 5637.
[41] S. Stankov, B. Sepiol, T. Kaňuch, D. Scherjau, R. Würschum, M. Miglierini, J. Phys.: Condens. Matter 17 (2005) 3183.
[42] V. Erukhimovitch, J. Baram, Phys. Rev. B 50 (1994) 5854.
[43] A.L. Greer, N. Karpe, J. Bottiger, J. Alloys Compd. 194 (1993) 199.
[44] F. Liu, F. Sommer, E.J. Mittemeijer, J. Mater. Sci. 39 (2004) 1621.
[45] J. Farjas, P. Roura, Acta Mater. 54 (2006) 5573.

Journal of Alloys and Compounds 638 (2015) 398–404

Contents lists available at ScienceDirect

Journal of Alloys and Compounds

journal homepage: www.elsevier.com/locate/jalcom

Structural transformation of NANOPERM-type metallic glasses followed *in situ* by synchrotron radiation during thermal annealing in external magnetic field

V. Procházka [a,*,1], V. Vrba [a], D. Smrčka [a], R. Rüffer [b], P. Matúš [c], M. Mašláň [a], M.B. Miglierini [d,e,1]

[a] Department of Experimental Physics, Faculty of Science, Palacký University, 17. listopadu 12, 771 46 Olomouc, Czech Republic
[b] ESRF-The European Synchrotron, CS40220, 38043 Grenoble Cedex 9, France
[c] Institute of Laboratory Research on Geomaterials, Faculty of Natural Sciences, Comenius University, Mlynská dolina, 842 15 Bratislava, Slovakia
[d] Institute of Nuclear and Physical Engineering, Slovak University of Technology, 812 19 Bratislava, Slovakia
[e] Regional Centre of Advanced Technologies and Materials, Palacký University, 17. listopadu 12, 771 46 Olomouc, Czech Republic

ARTICLE INFO

Article history:
Received 6 February 2015
Received in revised form 6 March 2015
Accepted 7 March 2015
Available online 17 March 2015

Keywords:
NANOPERM
Metallic glass
Nuclear resonant scattering
Crystallization kinetics

ABSTRACT

Kinetics of the crystallization process of Fe–Mo–Cu–B-type metallic glass is studied to fine details during heat treatment under weak external magnetic field (0.652 T). Structural arrangement as well as magnetic microstructure is followed on-fly using sophisticated method of *in situ* nuclear forward scattering (NFS) of synchrotron radiation. The latter provides both quantitative (relative fractions) and qualitative (hyperfine magnetic fields) temperature dependencies of all structurally different samples' components. They belong to the amorphous residual matrix, the newly formed nanocrystalline grains, and to their surfaces, respectively. The onset of crystallization during in-field magnetic annealing starts ~100 K earlier than that in zero field.

1. Introduction

Iron based amorphous [1,2] and nanocrystalline [3,4] alloys exhibit excellent magnetic properties which offer a number of possible application, e.g. magnetic shielding, transformer, and electromotor cores [5–7]. Their properties are strongly related to the structural arrangement [8] which is formed during the preparation process or by additional thermal treatment. The starting amorphous materials are usually prepared by the method of rapid quenching. During this process, a melt with the selected composition is rapidly quenched down which results in a disordered structure in a thermodynamically metastable state formation. After subsequent exposure to elevated temperature above some critical point the material relaxes into thermodynamically favourable state. In addition, the formation of nanograins occurs in the amorphous matrix when crystallization temperature is exceeded [8].

During this process the originally amorphous alloy transforms into partially crystalline state and the Gibbs potential falls to its minimum. Crystallization is an irreversible phase transformation. During this non-equilibrium thermodynamic process both the critical temperature and the crystallization rate are determined by the Gibbs potential profile, energetic barrier for a nucleation centre formation [9], and by diffusion rate [10] at the specific temperature [11]. The Gibbs potential is a function of thermodynamic parameters like temperature, composition, pressure an/or magnetic field.

In order to improve their magnetic parameters, the formation of nanocrystalline alloys from metallic glasses often takes place under the conditions when the temperature of annealing and external magnetic field act upon the originally amorphous alloy simultaneously. The response of various types of metallic glasses to the so-called magnetic annealing has been studied by several groups [12–16] resulting in appearance of induced magnetic anisotropy in the heat-treated soft magnetic alloys. The beneficial effects of heat treatment under magnetic field are discussed in terms of the improved magnetic softness and the possibility to tune the application oriented properties of Fe-based soft magnetic alloys by employing only magnetization measurements. The behaviour of microstructure was sometimes followed by X-ray diffraction and transmission electron microscopy after the annealing. Nevertheless, no significant changes in either the crystallization behaviour or in the size and morphology of grains as compared to the zero-field-annealed reference samples were found [14]. It should be noted that this is the only statement which relates to

* Corresponding author.
E-mail address: v.prochazka@upol.cz (V. Procházka).
[1] VP and MBM contributed equally to this work.

http://dx.doi.org/10.1016/j.jallcom.2015.03.058
0925-8388/

possible structural deviations imposed by magnetic annealing we have found in a literature. The experiments were performed upon $(Fe_{1-x}Co_x)_{81}Nb_7B_{12}$ HITPERM-type metallic glass exposed to field annealing inside transverse (640 kA/m ≃ 812 mT) and longitudinal (20 kA/m ≃ 25 mT) fields for 1 h at 773 K [14].

Regarding the previously reported results [12–16], detail knowledge and understanding of the materials behaviour under magnetic annealing is crucial to preserve its properties and functionality. This paper focuses on the impact of magnetic field on the crystallization kinetics and critical temperature of NANOPERM-type metallic glasses. Recently, an effect of magnetic field applied during crystallization of a metallic glass has been reported [17]. Nevertheless, the question whether the applied field affects the nucleation barrier rather than the energy difference between the amorphous and the crystalline states or both of them is still open. In contrast to [17] where the evolution of structural transformation took place under isothermal magnetic annealing, here we studied the effect of dynamically changing conditions (temperature).

The crystallization process is typically followed by macroscopic methods like Differential Scanning Calorimetry (DSC) [18,19] or magnetization measurements [20]. Microscopic methods like X-ray diffraction or Mössbauer spectroscopy [21,22] are usually employed *ex situ*, i.e. after the heating at a certain temperature is completed. However, such approach can be affected by the cooling process. Therefore, experimental methods that enable *in situ* observation during the annealing should be used in order to inspect the kinetics of crystallization. Magnetization measurements and DSC, which are generally applied for *in situ* investigations, provide only integral information that is averaged over all structurally different components comprising the emerging nanocrystalline grains as well as the residual amorphous matrix. That is why a local probe *in situ* experimental approach is necessary.

Recently, the method of nuclear forward scattering of synchrotron radiation (NFS) become suitable for *in situ* experiments. Extremely brilliant X-rays produced by the third generation of synchrotron sources combined with precise monochromatization of the photons energy enable rapid data acquisition. Consequently, it is possible to monitor the crystallization process within a sufficient time sampling of approximately one minute. This allows direct study even during the annealing. Advantaging from the fact that hyperfine interactions are straightforwardly related to structural arrangement we have recently reported on the nucleation and growth processes that are taking place during isothermal annealing of metallic glasses [11]. Through time evolution of hyperfine interactions we followed the structural transformation separately for the nanograins, their interfaces, and the residual amorphous matrix.

This paper aims at the investigation of crystallization process under applied external magnetic field. The impact of magnetic field has been studied mainly in ordered steels in case of austenite to martensite transformation [23–25]. Acceleration of crystallization in applied external magnetic field has been reported in the $Fe_{90}Zr_7B_3$ metallic glass [17] during isothermal annealing. Here we employ different approach that makes use of a dynamical temperature increase over wide range of temperatures. This provides relevant information on changes in the progress of crystallization with respect to the applied magnetic field. On the other hand, the evolution of hyperfine field values with temperature should be assumed in the evaluation procedure. Using sophisticated experimental approach we can obtain new insights into the thermodynamics of the amorphous alloys.

2. Experimental details

The studied metallic glass $Fe_{81}Mo_8Cu_1B_{10}$ was prepared by a melt-spinning technique in a form of ∼2 mm wide and ∼20 μm thick ribbons at the Institute of Physics, Slovak Academy of Sciences in Bratislava (courtesy of D. Janičkovič). Their chemical composition has been checked by optical emission spectrometry with inductively coupled plasma (Mo, B) and flame atomic absorption spectrometry (Fe, Cu). Though both methods provide accuracy far below 0.5 at.%, we will use the above mentioned formula (rounded to the units of at.%) for the identification of the samples composition. In order to increase the count rate of NFS experiments the samples were prepared from iron enriched to about 50% of the stable isotope ^{57}Fe.

The NFS experiments were performed at the Nuclear Resonance side-station (ID22N) in ESRF, Grenoble [26]. The synchrotron radiation features tuneable energy, high degree of polarization in the plane of the storage ring, small beam cross-section, negligible divergence of the beam, pulsed time structure, and above all extremely high brilliance (intensity). Excitation of the ^{57}Fe nuclear levels was accomplished by photons with 14.413 keV energy and ∼3 meV bandwidth.

The investigated ribbon-shaped samples about 5 mm in length were placed inside a furnace installed between two poles of an electromagnet. The latter provided external magnetic fields of 0.652 T. The incident linearly polarized beam entered the sample perpendicular to the sample plane and the applied magnetic field was oriented parallel to the polarization. Samples were heated in a vacuum from a room temperature up to ∼700 °C with the heating rate of 10 °C/min. NFS data were measured starting from the beginning of heating and stored in one minute intervals, which was sufficient to achieve satisfactory statistics. The annealing experiment was performed with and without the external magnetic field applied.

The data obtained have been evaluated by the software package CONUSS [27,28] which calculates and fits the theoretical model to the experimental points. The evaluation is based on the diagonalization of the hyperfine interaction Hamiltonian and the scattering amplitude calculation [29].

3. Results and discussion

The accumulated NFS time spectra are presented in a form of contour plots in Fig. 1. The horizontal axes represent the time delay elapsed between the excitation pulse and the detection of the

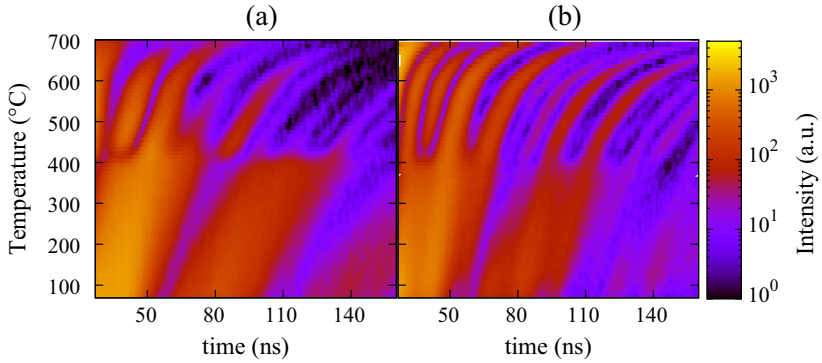

Fig. 1. Contour plots of NFS time records of the $Fe_{81}Mo_8Cu_1B_{10}$ metallic glass measured without (a) and with external magnetic field of 0.652 T (b).

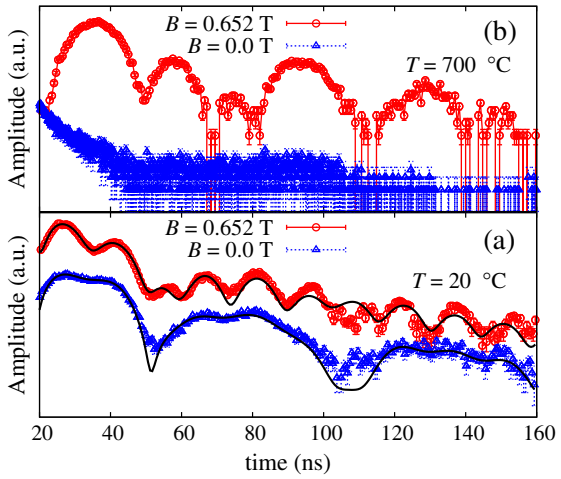

Fig. 2. Examples of selected NFS time spectra of the $Fe_{81}Mo_8Cu_1B_{10}$ alloy measured at 20 °C (a) and at 700 °C (b) in zero external magnetic field (blue triangles) and in $B = 0.652$ T (red circles). Solid lines are fits according to the theoretical model described in the text. (For interpretation of the references to colour in this figure legend, the reader is referred to the web version of this article.)

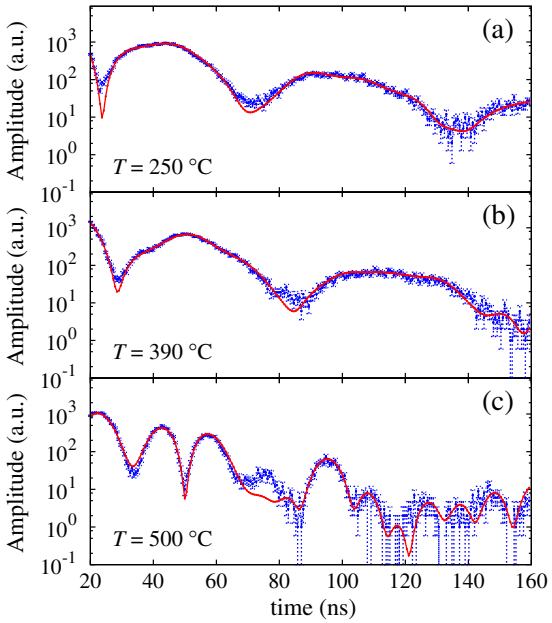

Fig. 3. Examples of selected NFS experimental data (full symbols) with the fitted curves (solid lines) of the $Fe_{81}Mo_8Cu_1B_{10}$ alloy measured in zero external magnetic field at the indicated temperatures: amorphous state before the crystallization (a), beginning of crystallization (b), well developed crystallization (c).

de-excited photons. The temperature at the sample is given on the vertical axes. Intensities of the recorded signals are colours coded in a logarithmic scale.

The investigated metallic glass exhibits at a room temperature an amorphous structure with prevailing electric quadrupole interactions. They are shown in Fig. 2a by well developed quantum beats for zero-field (ZF) experiment. Nevertheless, as unveiled by Conversion Electron Mössbauer Spectrometry (CEMS), traces of surface crystallization were identified on both sides of the studied ribbons [30]. On the wheel side, some nanocrystals were found by conversion X-rays (CXMS) even in more deep subsurface regions [30]. The surface nanocrystals demonstrate themselves by hardly visible beatings of magnetic origin in the ZF time spectrum in time intervals 60–90 ns and 140–160 ns. For the in-field experiment, however, the magnetic contribution becomes more clearly visible over the whole time span in Fig. 2a. The obtained NFS time spectra were appropriately described by distributions of quadrupole splitting that correspond to an ensemble of iron nuclei found in the amorphous part of the alloy (AM) and feel zero hyperfine magnetic fields. Presence of surface magnetic bcc-Fe nanocrystals was modelled by two interferometric components characterized by hyperfine magnetic fields. The resulting fits are plotted in Fig. 2a by solid lines. The shapes of NFS time spectra recorded at 700 °C that shown in Fig. 2b we will discuss below.

Selected examples of NFS time spectra measured without external magnetic field and fitted according to the model described above are shown in Fig. 3. A time spectrum in Fig. 3a corresponds to a paramagnetic amorphous state before the onset of crystallization. Note that at this elevated temperature the contribution of magnetic beatings that belong to the surface nanocrystals is drastically suppressed and almost no signs of them are seen in the time regions 60–80 ns and 140–160 ns as was the case of a room temperature measurement in Fig. 2a. This is a consequence of a small number and tiny sizes of the nanocrystals whose magnetic moments are highly relaxed at this relatively high temperature. As a result, rather simple features of quantum beats that represent almost pure electric quadrupole interactions can be observed.

At the beginning of (bulk) crystallization, presence of weak magnetic hyperfine interactions in the time interval 140–160 ns is unveiled in Fig. 3b. They were introduced by the newly formed ferromagnetic bcc-Fe nanograins. Contribution of magnetic dipole hyperfine interactions that correspond to hyperfine magnetic fields of bcc-Fe nanocrystals becomes fully visible in Fig. 3c which was recorded after sufficiently long time of annealing (at high enough temperature) when the first crystallization step is already well developed.

Taking into consideration the fitting model of conventional Mössbauer spectra of nanocrystalline alloys [31,32], the two magnetically split components that are assigned to the bcc-Fe nanograins can be interpreted as follows. One of them, denoted as CR, represents iron atoms that reside in the bulk of nanograins and exhibit well established crystalline symmetry. The second one, henceforth denoted as IF, is assigned to those iron atoms that are located at the surfaces of the nanograins and have more or less disturbed translation periodicity. Such atoms form an interfaceperiodicity. Such atoms form an between the residual amorphous matrix and the nanograins. Due to broken symmetry they are described by a broad Gaussian distribution of hyperfine magnetic field. The same approach was used to evaluate isothermal NFS time spectra in our recent work [11]. In the ZF experiment, the onset of crystallization can be determined as $T_{x1} = 390$ °C.

The situation when the NFS data were acquired at the same temperatures but under simultaneous effect of an external magnetic field $B_{ext} = 0.652$ T is shown in Fig. 4. In amorphous state, i.e. at moderately elevated temperature of 250 °C, quantum beats of quadrupole splitting that represent paramagnetic amorphous state of the sample dominate in Fig. 4a. Nevertheless, traces of dipole magnetic interactions which belong to surface nanocrystals are also observed. It is noteworthy that while the crystallization just starts at 390 °C in ZF annealing conditions, it has been quite well developed already when even weak external magnetic field (0.652 T) was applied. The corresponding NFS time spectrum in Fig. 4b shows already significant contribution of dipole magnetic

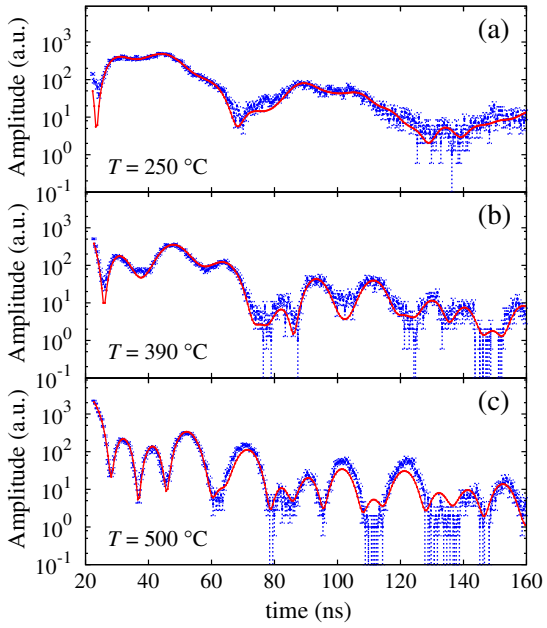

Fig. 4. Examples of selected NFS experimental data (full symbols) with the fitted curves (solid lines) of the $Fe_{81}Mo_8Cu_1B_{10}$ alloy measured in an external magnetic field of 0.652 T at the same temperatures as those in Fig. 3.

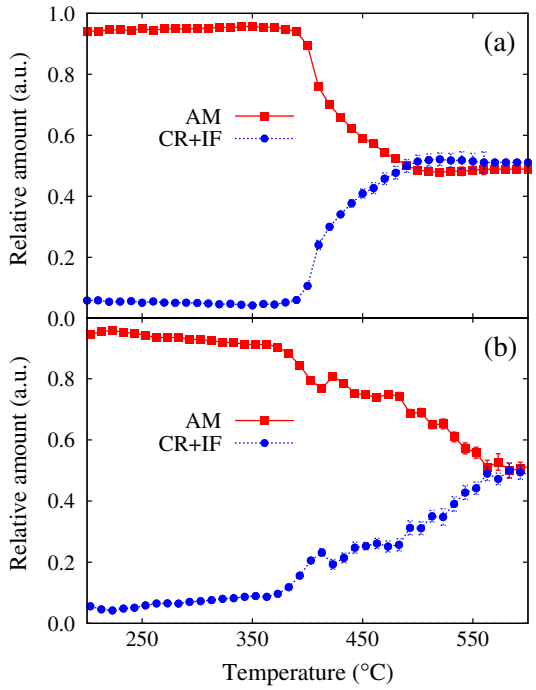

Fig. 5. Relative amounts of amorphous (AM) (red squares) and total nanocrystalline (CR + IF) (blue circles) components plotted against the temperature of annealing as obtained from NFS of the $Fe_{81}Mo_8Cu_1B_{10}$ alloy in zero magnetic field (a) and in the field of 0.652 T (b). (For interpretation of the references to colour in this figure legend, the reader is referred to the web version of this article.)

hyperfine interactions that stem from the presence of bcc-Fe nanocrystals.

The selected examples of NFS time spectra in Figs. 2a, 3, and 4 clearly demonstrate the feasibility of the physical model used to evaluate the experimentally acquired data. The significance of the fits was checked by χ^2 criterion. Using this approach, very satisfactory fits were achieved over broad temperature interval from the beginning of the annealing up to ~600 °C. Here, two effects, which significantly influence the fitting model used, start to exhibit themselves. They are illustrated in Fig. 2b where NFS time spectra taken at 700 °C are presented. They are even better seen in Fig. 1 where the peaks of quantum beats that correspond to high temperature (>600 °C) time spectra are evidently shifted towards higher delayed times.

The first effect rests with temperature evolution of hyperfine magnetic fields that tend to collapse in the vicinity of Curie temperature as demonstrated by the ZF NFS time spectrum in Fig. 2b. It is featureless because the signal from ferromagnetic bcc-Fe nanocrystals is ill-defined as their hyperfine magnetic fields fall down to values that are comparable in strength with those of quadrupole splitting of the paramagnetic residual amorphous phase. Consequently, the applied fitting model that consists of one distribution of quadrupole splitting (AM) and two hyperfine magnetic fields (CR, IF) is no longer valid.

The second effect is due to the new crystalline phases formation during the second step of crystallization. This situation is shown in Fig. 2b for the in-field experiment where the progress of crystallization is more developed than in the ZF one. Along with bcc-Fe, iron borides formation is expected [33]. Consequently, the current fitting model cannot be satisfactorily applied, either. In order to account for additional crystalline phases that are produced during the second crystallization step, the corresponding fitting model should be extended by additional components featuring hyperfine magnetic fields (and their temperature dependencies). This is, however, beyond the scope of the present study. That is why we shall follow to discuss the results obtained from the fits up to 600 °C, i.e. within the first step of structural transformation [33].

Temperature dependencies of the relative fractions of the amorphous residual phase (AM) and the entire crystalline component, i.e. CR + IF are plotted against the temperature of annealing in Fig. 5. Several observations are worth to be mentioned: (i) Surface crystallization that occurs in the as-quenched state contributes by ~6% up to ~250 °C regardless the presence of external magnetic field (the data for $T < 200$ °C exhibit no temperature evolution and that is why it is not given in Fig. 5). (ii) The onset of crystallization in ZF is determined as $T_{x1} = 390$ °C while for in-field experiment it starts by ~100 degrees earlier. (iii) The beginning of ZF crystallization (Fig. 5a) is quite abrupt and the formation of nanocrystallites is rapid while during in-field annealing in Fig. 5b a moderate increase in the crystalline fraction is observed. (iv) Saturation of crystalline content in the ZF experiment is observed at ~490 °C which is again by ~100 degrees earlier than under in-field conditions. (v) In both cases, however, the final crystalline content within the inspected interval of annealing temperatures ($T < 600$ °C) is almost the same (~50%) within the error margin. Namely this last point is worth to emphasize this might be the reason why the in-field annealed alloys do not need to exhibit any structural changes [14] when inspected only after (and not during) magnetic annealing.

While the relative contributions of the total crystalline and amorphous regions within the alloy subjected to annealing can be derived also for example by *in situ* diffraction of synchrotron radiation [34], the NFS experiments can go further. Making use of hyperfine interactions it is possible to assess the contributions from structurally different regions to fine details. The relative fractions of iron atoms that constitute an interior of the nanograins

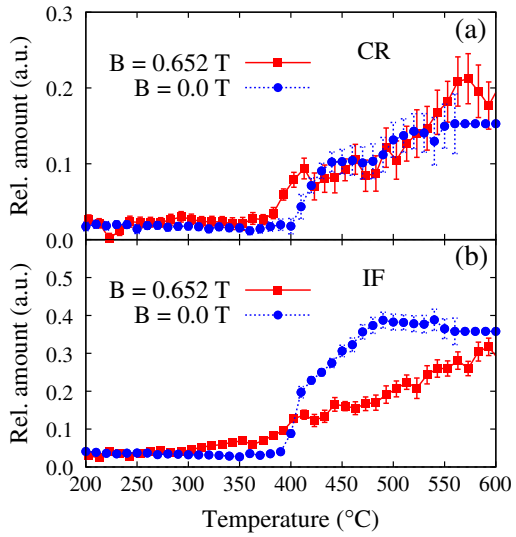

Fig. 6. Relative amounts of crystalline grains (CR) (a) and interface (IF) (b) components plotted against the temperature of annealing as obtained from NFS of the $Fe_{81}Mo_8Cu_1B_{10}$ alloy in zero magnetic field (blue circles) and in the field of 0.652 T (red squares). (For interpretation of the references to colour in this figure legend, the reader is referred to the web version of this article.)

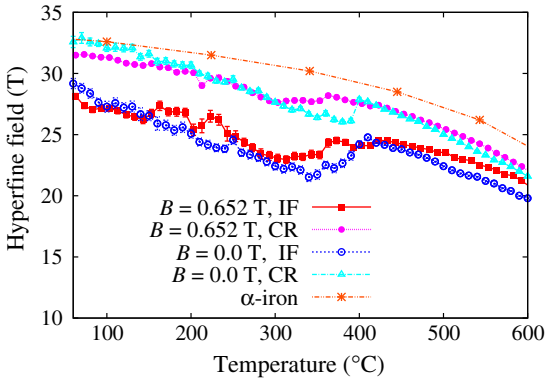

Fig. 7. Hyperfine magnetic fields of crystalline (CR) and interfacial (IF) components plotted against the temperature of annealing as obtained from NFS of the $Fe_{81}Mo_8Cu_1B_{10}$ alloy measured in zero and nonzero (0.652 T) external magnetic field. Values corresponding to α-Fe are given for comparison (see text).

(CR) as well as their surfaces (IF) were derived from the fitting of the experimental NFS time spectra to the model which was introduced above. The results are mutually compared in Fig. 6. It should be noted that the IF components appear at lower temperatures in both modes of annealing than the corresponding CR ones. This means that the newly formed crystallites are rather small as they consist almost exclusively of surface atoms with broken symmetry. As the grains grow in size, the CR components evolve also.

The CR and IF temperature dependencies tend to saturate for $T > 490$ °C when annealed in zero-field. On the other hand, during the in-field experiment both components exhibit rising tendency. At the final inspected temperature of ~600 °C, the IF:CR ratio is ~2.6 and ~1.5 for ZF and in-field experiment, respectively. This can be interpreted in terms of prevailing contribution of atoms located at the grains surfaces when no magnetic field is applied during temperature induced structural transformation from amorphous into nanocrystalline state. Givening the fact that the total crystalline contents (CR + IF) is almost the same for both modes of annealing, one can expect the formation of smaller number of larger grains favoured by magnetic annealing.

The beginning of crystallization can be also determined from the temperature dependencies of hyperfine fields in Fig. 7. In the precrystallization stage, the plotted hyperfine fields correspond to quenched-in nanograins that have been formed during the production of the samples. As discussed above, they are predominantly located in subsurface regions [30] and contribute only marginally to the NFS time spectra (see Fig. 5). Nevertheless, their hyperfine magnetic fields follow temperature evolution of those that correspond to bulk α-Fe crystallites. The latter values taken from conventional Mössbauer spectrometry temperature experiments performed by Preston et al. [35] are plotted in Fig. 7 for comparison. With rising temperature of annealing the hyperfine magnetic fields of the quenched-in nanograins decrease more rapidly than those of crystalline α-Fe. This is due to temperature induced relaxation of the magnetic moments as a result of small grain dimensions. The differences observed between hyperfine magnetic fields, which correspond to the CR and IF components, are of ~3.5 T. Note that the oscillations of field values in the temperature range 150–250 °C for the IF component obtained from in-field experiments are artefacts caused by the fitting procedure due to a small relative fraction (~6%) of the grains in this precrystallization stage.

With the onset of (bulk) crystallization, a sudden increase in hyperfine magnetic fields of both components by ~2.5 T is observed. This indicates the formation and growth of new nanograins which step by step acquire well developed structural arrangement with rising temperature of annealing. Their hyperfine magnetic fields closely follow the temperature dependence of α-Fe crystallites. Nevertheless, slightly lower hyperfine magnetic fields suggest that the established nanocrystals do not have a perfect bcc crystalline lattice that might contain some Mo inclusions [34]. In ZF experiment, an abrupt increase of CR hyperfine magnetic fields is observed at ~400 °C which acceptably coincides with the crystallization temperature $T_{x1} = 390$ °C determined from relative fractions of the fitted components (see Fig. 5).

4. Conclusions

The effect of weak external magnetic field (0.652 T), which was applied during dynamical annealing of the $Fe_{81}Mo_8Cu_1B_{10}$ metallic glass, upon its structural transformations from amorphous into nanocrystalline state was monitored *in situ* using nuclear forward scattering (NFS) of synchrotron radiation. Significant influence of the field oriented parallel to the polarization of the synchrotron radiation was revealed. The main conclusions can be summarised as follows:

- The external magnetic field causes earlier onset of crystallization than it was observed during annealing under zero-field (ZF) conditions. Difference of ~100 degrees in the crystallization temperatures was found between ZF and in-field experiments. Structural transformation proceeds quite rapidly during ZF annealing whereas the nanocrystalline contents increase rather slowly in an external magnetic field. At the same time, saturation of the amount of nanocrystals is found in the former case. During magnetic annealing, the total crystalline content rises progressively. In both annealing modes, however, the total crystalline fraction is almost identical towards the end of the first crystallization step.
- At high temperature of ZF annealing ($T \sim 700$ °C), the bcc crystalline phase undergoes a transition from ferromagnetic order into paramagnetic state. Note that magnetic interactions in

the amorphous residual phase collapse much earlier. When a magnetic field is applied, the newly formed crystalline phase is still ferromagnetic at this temperature. Possible explanation assumes that the external magnetic field triggers not only the first but also the second crystallization step at lower temperatures. Consequently, additional crystalline phases (except of bcc-Fe that is formed during the first crystallization step) appear. They are responsible for the observed dipole hyperfine magnetic interactions.

- The evolution of structural transformations is determined also from temperature development of hyperfine magnetic fields that correspond to the nanocrystals. According to their values, the grains are identified as bcc-Fe with minor inclusions of Mo in the crystalline lattice.
- Deconvolution of NFS time spectra into several components according to a suitably chosen physical model, which is thoroughly described in the text above, enables to follow separately the trends in temperature evolution of the particular quantitative (relative fractions) as well as qualitative (hyperfine magnetic fields) parameters for all structurally different elements contained within the investigated alloy, viz. the amorphous residual matrix, the crystalline grains, and the interfacial regions. Based on the results obtained, we can come to the conclusion that magnetic annealing encourage production of smaller number of larger nanograins in comparison with those obtained during ZF annealing.
- Acquisition of NFS experimental data in short time intervals of ~1 min and their consequent theoretical evaluation has enabled on fly inspection of the behaviour of the investigated metallic glass during dynamical changes of the temperature of annealing, i.e. during the process of structural transformation that was scanned *in situ*. Such approach is applicable also to other types of Fe-based metallic glasses and thus the obtained results can be straightforwardly generalized.

The crystallization rate is determined by the difference of the Gibbs potential in amorphous and crystalline states as well as by an energy barrier for formation of new nucleation centres [36,37]. Considering the present study, we can assume that both these conditions are affected by external magnetic field that is applied during annealing. If the energy barrier was decreased, the probability of new grains formation would increase and, consequently, the onset of crystallization would appear earlier, i.e. at lower T_{x1}. Indeed, this is what we have found by comparing the progress of structural transformation *in situ* during the process of annealing. It is noteworthy that we did not simply compare the original and the final states of the investigated metallic glass before and after annealing with and without external magnetic field but checked its evolution systematically during the heating itself. In this paper we demonstrate that the method of nuclear forward scattering of synchrotron radiation is a very effective tool for *in situ* studies of structural transformations. Time evolution of the latter can be investigated not only under isothermal conditions [11] but also when the temperature is dynamically changing.

Acknowledgements

This work was supported by the projects LO1305 of the Ministry of Education, Youth and Sports of the Czech Republic, POST-UP II. CZ.1.07/2.3.00/30.0041, and IGA_PrF_2015_017. The authors would like to thank M. Zajac, P. Švec, D. Janičkovič, J. Kohout, and A. Lančok for their technical assistance during measurements on the synchrotron.

References

[1] M. Ashby, A. Greer, Metallic glasses as structural materials, Scr. Mater. 54 (2006) 321–326, http://dx.doi.org/10.1016/j.scriptamat.2005.09.051.
[2] A. Inoue, A. Takeuchi, Recent development and application product of bulk glass alloys, Acta Mater. 59 (2011) 2243–2267, http://dx.doi.org/10.1016/j.actamat.2010.11.027.
[3] H. Gleiter, Nanostructured materials: basic concepts and microstructure, Acta Mater. 48 (2000) 1–29, http://dx.doi.org/10.1016/S1359-6454(99)00285-2.
[4] K. Suzuki, A. Makino, A. Inoue, T. Masumoto, Soft magnetic-properties of nanocrystalline bcc Fe–Zr–B and Fe–M–B–Cu (M = transition-metal) alloys with high saturation magnetization, J. Appl. Phys. 70 (1991) 6232–6237, http://dx.doi.org/10.1063/1.350006.
[5] G. Herzer, Modern soft magnets: amorphous and nanocrystalline materials, Acta Mater. 61 (2013) 718–734, http://dx.doi.org/10.1016/j.actamat.2012.10.040.
[6] C.A. Schuh, T.C. Hufnagel, U. Ramamurty, Overview no. 144 – mechanical behavior of amorphous alloys, Acta Mater. 55 (2007) 4067–4109, http://dx.doi.org/10.1016/j.actamat.2007.01.052.
[7] M. McHenry, D. Laughlin, Nano-scale materials development for future magnetic applications, Acta Mater. 48 (2000) 223–238, http://dx.doi.org/10.1016/S1359-6454(99)00296-7.
[8] G. Herzer, Nanocrystalline soft-magnetic materials, Phys. Scr. T49A (1993) 307–314, http://dx.doi.org/10.1088/0031-8949/1993/T49A/054.
[9] V. Erukhimovitch, J. Baram, Crystallization kinetics, Phys. Rev. B 50 (1994) 5854–5856, http://dx.doi.org/10.1103/PhysRevB.50.5854.
[10] A.L. Greer, N. Karpe, J. Bottiger, Diffusional aspects of the solid-state amorphization reaction, J. Alloys Comp. 194 (1993) 199–211, http://dx.doi.org/10.1016/0925-8388(93)90003-6.
[11] M. Miglierini, V. Prochazka, S. Stankov, S.P. Svec, M. Zajac, J. Kohout, A. Lancok, D. Janickovic, P. Svec, Crystallization kinetics of nanocrystalline alloys revealed by in situ nuclear forward scattering of synchrotron radiation, Phys. Rev. B 86 (2012) 020202, http://dx.doi.org/10.1103/PhysRevB.86.020202.
[12] F. Johnson, H. Garmestani, S.Y. Chu, M.E. McHenry, D.E. Laughlin, Induced anisotropy in FeCo-based nanocrystalline ferromagnetic alloys (HITPERM) by very high field annealing, IEEE Trans. Mag. 40 (2004) 2697–2699, http://dx.doi.org/10.1109/TMAG.2004.832278.
[13] K. Suzuki, N. Ito, J. Garitaonandia, J. Cashion, High saturation magnetization and soft magnetic properties of nanocrystalline $(Fe,Co)_{90}Zr_7B_3$, J. Appl. Phys. 99 (2006) 08F114, http://dx.doi.org/10.1063/1.2169503.
[14] I. Škorvánek, J. Marcin, T. Krenický, J. Kováč, P. Švec, D. Janičkovič, Improved soft magnetic behaviour in field-annealed nanocrystalline hitperm alloys, J. Magn. Magn. Mater. 304 (2006) 203–207, http://dx.doi.org/10.1016/j.jmmm.2006.02.120.
[15] I. Škorvánek, J. Marcin, J. Turčanová, J. Kováč, P. Švec, Improvement of soft magnetic properties in $Fe_{38}Co_{38}Mo_8B_{15}Cu$ amorphous and nanocrystalline alloys by heat treatment in external magnetic field, J. Alloys Comp. 504 (2010) S135–S138, http://dx.doi.org/10.1016/j.jallcom.2010.04.033.
[16] I. Škorvánek, J. Marcin, M. Capik, M. Varga, J. Turčanová, J. Kováč, P. Švec, D. Janičkovič, F. Kováč, V. Stoyka, Tailoring of functional properties in Fe-based soft magnetic alloys by thermal processing under magnetic field, Magnetohydrodynamics 48 (2012) 371–377.
[17] M. Miglierini, V. Procházka, R.Rüffer, R. Zbořil, Accelerated crystallization of metallic glasses in weak magnetic fields unveiled by in situ nuclear forward scattering of synchrotron radiation, Acta Mater. (2015), (in press), http://dx.doi.org/10.1016/j.actamat.2015.03.012.
[18] C. Conde, A. Conde, D. Janičkovič, P. Švec, Composition dependence of Curie temperature and microstructure in amorphous Fe–Co–Mo–Cu–B metallic glasses, J. Magn. Magn. Mater. 304 (2006) e739–e742, http://dx.doi.org/10.1016/j.jmmm.2006.02.208.
[19] D.R. Allen, J.C. Foley, J.H. Perepezko, Nanocrystal development during primary crystallization of amorphous alloys, Acta Mater. 46 (1998) 431–440, http://dx.doi.org/10.1016/S1359-6454(97)00279-6.
[20] Y. Jirásková, M. Maryško, R. Zbořil, Magnetic and structural features of amorphous FeMo-based alloys, J. Magn. Magn. Mater. 316 (2007) e16–e19, http://dx.doi.org/10.1016/j.jmmm.2007.02.012.
[21] J. Garitaonandia, D. Schmool, J. Barandiaran, Model of exchange field penetration in nanocrystalline $Fe_{87}Zr_6B_6Cu$ alloys from magnetic and Mössbauer studies, Phys. Rev. B 58 (1998) 12147–12158, http://dx.doi.org/10.1103/PhysRevB.58.12147.
[22] G. Hampel, A. Pundt, J. Hesse, Crystallization of $Fe_{73.5}C_1Nb_3Si_{13.5}B_9$ – structure and kinetics examined by X-ray diffraction and Mössbauer-effect spectroscopy, J. Phys.: Condens. Matter. 4 (1992) 3195–3214, http://dx.doi.org/10.1088/0953-8984/4/12/013.
[23] H. Ohtsuka, Structural control of Fe-based alloys through diffusional solid/solid phase transformations in a high magnetic field, Sci. Technol. Adv. Mater. 9 (2008) 013004, http://dx.doi.org/10.1088/1468-6996/9/1/013004.
[24] M. Enomoto, Enhanced phenomena in metals with electric and magnetic fields: II magnetic fields, Mater. Trans. 46 (2005) 1088–1092, http://dx.doi.org/10.2320/matertrans.46.1088.
[25] D. San Martin, N. van Dijk, E. Jimenez-Melero, E. Kempert, U. Zeitier, S. van der Zwaag, Real-time martensitic transformation kinetics in maraging steel under high magnetic fields, Mater. Sci. Eng. A 527 (2010) 5241–5245, http://dx.doi.org/10.1016/j.msea.2010.04.085.

[26] R. Rüffer, A. Chumakov, Nuclear resonance beamline at ESRF, Hyperfine Interact. 589 (1996) 97–98, http://dx.doi.org/10.1007/BF02150199.
[27] W. Sturhahn, E. Gerdau, Evaluation of time-differential measurements of nuclear-resonance scattering of X-rays, Phys. Rev. B 49 (1994) 9285, http://dx.doi.org/10.1103/PhysRevB.49.9285.
[28] W. Sturhahn, CONUSS and PHOENIX: evaluation of nuclear resonant scattering data, Hyperfine Interact. 125 (2000) 149–172, http://dx.doi.org/10.1023/A:1012681503686.
[29] G.T. Trammel, J.P. Hannon, Quantum beats from nuclei excited by synchrotron pulses, Phys. Rev. B 18 (1978) 165–172, http://dx.doi.org/10.1103/PhysRevB.18.165.
[30] M. Miglierini, T. Hatala, M. Bujdoš, Depth-selective study of surface crystallization in NANOPERM-type alloys, Acta Phys. Pol. A 126 (2014) 56–57.
[31] M. Miglierini, J.-M. Grenèche, Mössbauer spectrometry of Fe(Cu)MB-type nanocrystalline alloys: I. The fitting model for the Mössbauer spectra, J. Phys.: Condens. Matter 9 (1997) 2303–2319, http://dx.doi.org/10.1088/0953-8984/9/10/017.
[32] M. Miglierini, J.-M. Grenèche, Temperature behaviour of iron nanograins in NANOPERM-type alloys, J. Phys.: Condens. Matter 15 (2003) 5637–5648, http://dx.doi.org/10.1088/0953-8984/15/32/323.
[33] E. Illeková, D. Janičkovič, M. Miglierini, I. Škorvánek, P. Švec, Influence of Fe/B ratio on thermodynamic properties of amorphous Fe–Mo–Cu–B, J. Magn. Magn. Mater. 304 (2006) e636–e638, http://dx.doi.org/10.1016/j.jmmm.2006.02.212.
[34] M. Miglierini, M. Pavlovič, V. Procházka, T. Hatala, G. Schumacher, R. Rüffer, In-situ characterization of nanocrystalline alloys by synchrotron radiation, Phys. Chem. Chem. Phys., (in preparation).
[35] R.S. Preston, S.S. Hanna, J. Heberle, Mössbauer effect in metallic iron, Phys. Rev. B 128 (1962) 2207, http://dx.doi.org/10.1103/PhysRev.128.2207.
[36] F. Liu, F. Sommer, E.J. Mittemeijer, An analytical model for isothermal and isochronal transformation kinetics, J. Mater. Sci. 39 (2004) 1621–1634, http://dx.doi.org/10.1023/B:JMSC.0000016161.79365.69.
[37] J. Farjas, P. Roura, Modification of the Kolmogorov–Johnson–Mehl–Avrami rate equation for non-isothermal experiments and its analytical solution, Acta Mater. 54 (2006) 5573–5579, http://dx.doi.org/10.1016/j.actamat.2006.07.037.

PCCP

PAPER

View Article Online
View Journal

Cite this: DOI: 10.1039/c5cp00245a

Evolution of structure and local magnetic fields during crystallization of HITPERM glassy alloys studied by *in situ* diffraction and nuclear forward scattering of synchrotron radiation

Marcel Miglierini,*[ab] Márius Pavlovič,[a] Vít Procházka,[c] Tomáš Hatala,†[a] Gerhard Schumacher[d] and Rudolf Rüffer[e]

Received 15th January 2015,
Accepted 14th April 2015

DOI: 10.1039/c5cp00245a

www.rsc.org/pccp

Evolution of structure and local magnetic fields in $(Fe_{1-x}Co_x)_{76}Mo_8Cu_1B_{15}$ (HITPERM) metallic glass ribbons with various amounts of Co (x = 0, 0.25, 0.5) were studied *in situ* using diffraction and nuclear forward scattering of synchrotron radiation. It was found that crystallization of all three glasses proceeds in two stages. In the first stage, bcc (Fe,Co) nanocrystals are formed, while in the second stage additional crystalline phases evolve. For all three glasses, the crystallization temperatures at the wheel side were found to be lower than at the air side of the ribbon. The crystallization temperatures were found to decrease with increasing Co content. The lattice parameters of the bcc nanocrystals decrease up to about 550 °C and then increase pointing to squeezing Mo atoms out of the nanograins or to interface effects between the nanocrystals and the glassy matrix. Nuclear forward scattering enabled separate evaluation of the contributions that stem from structurally different regions within the investigated samples including the newly formed nanocrystals and the residual amorphous matrix. Even minor Co content (x = 0.25) has a substantial effect not only upon the magnetic behaviour of the alloy but also upon its structure. Making use of hyperfine magnetic fields, it was possible to unveil structurally diverse positions of Fe atoms that reside in a nanocrystalline lattice with different numbers of Co nearest neighbours.

1. Introduction

Nanocrystalline metallic alloys represent a new class of materials with unique physical properties that are suitable for a variety of practical applications.[1] There are three families of nanocrystalline alloys (NCAs), namely FINEMET,[2] NANOPERM,[3] and HITPERM.[4] They all can be prepared from metallic glasses (MGs) with a suitable chemical composition that are annealed under well defined conditions (temperature and time). Annealing induces partial crystallization that is characterized by formation of crystalline grains with typical sizes of up to several tens of nanometres. Physical properties of the NCAs can be tailored not only with the aid of their chemical composition, but also by varying the size of the nanocrystalline grains, their morphology, and composition. Thus, structural transformations obtained through crystallization considerably affect the macroscopic physical properties of these materials.

Crystallization is a one-way process of phase transformation that governs the structural order. In order to understand macroscopic properties of the NCAs, it is inevitable to understand their microstructure as well as the physical consequences of structural transformations. The latter are accompanied by changes in hyperfine interactions that, consequently, modify the overall magnetic properties. In contrast to MGs, the magnetic parameters of the NCAs do not substantially deteriorate at elevated temperatures,[5,6] which might occur in some practical applications.

In order to understand the correlation between structural arrangement and macroscopic magnetic properties, both amorphous MGs and NCAs are investigated by a broad arsenal of diagnostic techniques. In our earlier studies, we used differential scanning calorimetry (DSC), X-ray diffraction, transmission electron microscopy, high resolution electron microscopy, electron diffraction, scanning microscopy, Mössbauer spectrometry, nuclear magnetic resonance spectroscopy, atomic field microscopy and conventional magnetic measurements.[7–12] Nevertheless, the majority of these techniques can provide only

[a] *Institute of Nuclear and Physical Engineering, Slovak University of Technology, Ilkovičova 3, 812 19 Bratislava, Slovakia. E-mail: marcel.miglierini@stuba.sk*
[b] *Regional Centre of Advanced Technologies and Materials, Palacky University, 17. listopadu 12, 771 46 Olomouc, Czech Republic*
[c] *Department of Experimental Physics, Faculty of Science, Palacky University, 17. listopadu 12, 771 46 Olomouc, Czech Republic*
[d] *Helmholtz-Zentrum Berlin für Materialien und Energie GmbH, Hahn-Meitner Platz 1, D-14109 Berlin, Germany*
[e] *ESRF-The European Synchrotron, CS40220, 38043 Grenoble Cedex 9, France*
† Current address: Vacuumschmelze, s.r.o, Horná Streda 1325/14, 916 24 Horná Streda, Slovakia.

ex situ information as the time needed for acquisition of sufficiently good statistics of the experimental data frequently extends over several tens of minutes or even hours. Subsequently, *in situ* investigation of the induced structural transformations is not possible in real time using these techniques.

There are few methods suitable for *in situ* investigations. However, they usually scan the whole bulk of the investigated systems and provide information that is averaged over all structurally different regions. These comprise for example DSC and/or magnetic measurements. Thus, the *in situ* characterization of structural transformations during crystallization of MGs is an ambitious task. This is especially true when information on an atomic level is of interest. To ensure this, advanced *in situ* characterization analytical tools such as those using superior intense X-ray beams produced by the third generation of the synchrotron radiation sources should be employed.

Formation of ultrafine microstructure in a FINEMET-type alloy was followed by Köster *et al.*[13] using *in situ* time resolved diffraction of synchrotron radiation (DSR). Their findings emphasised the role of diffusion of impurities during the transformation. Kinetics of crystallization of FINEMET-type MGs[14,15] and the effect of Co upon the kinetics of crystallization[16] were also studied using *in situ* DSR. Structural relaxation processes in MGs studied by *in situ* DSR showed that microscopic structural changes can be correlated to macroscopic characteristics such as the thermal expansion coefficient.[17] Furthermore, Poulsen *et al.*[18] demonstrated that deformation tensor components can be extracted from MGs using high quality synchrotron diffraction data. As far as bulk MGs are concerned, differences in their glass-forming abilities were pointed out to be responsible for different icosahedral arrangements in short-range order.[19]

High Energy X-ray Diffraction (HEXRD) of synchrotron radiation was employed *in situ* to investigate the change of free volumes upon heating.[20] It was also engaged to measure plastic deformation mechanisms in MGs.[21] Recently, we have used *in situ* HEXRD (energy $\sim$60 keV) for the study of structural arrangements and relaxation processes induced in FINEMET-type MGs by swift heavy-ion bombardment.[22] Kinetics of crystallization was reported earlier in similar alloys using low energy ($\sim$7 keV) *in situ* DSR.[23]

As mentioned above, mostly FINEMET-type alloys have been studied by advanced *in situ* tools so far. In this work, we demonstrate the use of novel *in situ* characterization techniques based on synchrotron radiation in the investigation of (Fe,Co)–Mo–Cu–B nanocrystalline alloys with varying chemical composition. We have chosen this Mo-HITPERM system because of its interesting magnetic behaviour and also because it was thoroughly studied using conventional methods. Structural transformation, compositional dependence of Curie temperature, and magnetic behaviour of $(Fe_xCo_1)_{79}Mo_8Cu_1B_{12}$ (x = 1, 2, 3, 6, 9, 12) and $Fe_{79}Mo_8Cu_1B_{12}$ MGs were investigated by Conde *et al.*[24,25] Recently, changes in the magnetic properties provoked by the microstructural evolution were followed also by Mössbauer spectrometry.[26] Namely the latter technique enables mutual correlation between structural arrangement and magnetic order. Mössbauer spectrometry was extensively employed to examine hyperfine interactions of the as-quenched and annealed aforementioned MG as well as of the one with the same Fe/Co ratio but with higher amount of boron, that is $(Fe_{1-x}Co_1)_{76}Mo_8Cu_1B_{15}$.[27,28] Though both compositions behave very alike especially for higher Co contents, their original Co-free alloys are remarkably different from the magnetic order point of view. While the alloy with 12 at% of boron is paramagnetic at room temperature, weak magnetic interactions are observed for 15 at% of boron. That is why the latter system is better suited for the study of hyperfine magnetic interactions in the vicinity and above room temperature.

In this work, formation of nanocrystalline grains during structural transformation of a heat-treated original metallic glass is followed by *in situ* diffraction of synchrotron radiation. Extended information about changes in their magnetic states is obtained by nuclear forward scattering (NFS) of synchrotron radiation.[29] This method enables differentiation of the signal given by the amorphous residual matrix from the signal given by the newly formed nanocrystals. Because the experimental data are collected during a very short time (about one minute), on-fly inspection of both structural and magnetic aspects of the transformation is possible. Furthermore, NFS can distinguish between atoms positioned in the bulk and those on the surfaces of the nanograins.

2. Experimental details

2.1 Investigated materials

NANOPERM-type nanocrystalline alloys based on Fe–M–B–Cu, where M = Zr, Nb, Hf, Mo,... have been proposed by Suzuki.[3,30] These alloys show small magnetostrictive coefficients and, simultaneously, large permeability. Substitution of cobalt atoms at the expense of iron in the (Fe,Co)–M–Cu–B-type alloys called HITPERM[4] shows high permeability and high Curie temperatures. Cobalt with its soft magnetic properties is important for set of magnetic properties in the final alloys.

As-quenched MG alloys $(Fe_{1-x}Co_x)_{76}Mo_8Cu_1B_{15}$ with various amount of Co (x = 0, 0.25, 0.5) were prepared by the method of planar-flow casting on a rotating quenching wheel in the form of ribbons about 10 mm wide and 20 μm thick. In addition, about 1–2 mm wide ribbons that were enriched to about 50% in the ^{57}Fe isotope were prepared for x = 0 and 0.25. Because the content of the ^{57}Fe in natural iron is only $\sim$2%, these samples were used to facilitate the NFS experiments, *i.e.*, to increase the count rate and so to shorten the acquisition time.

The side of the ribbons that was in direct contact with the quenching wheel will be referred to as the wheel side. The opposite side, *i.e.*, the one exposed to the surrounding atmosphere during the production process will be called the air side. Chemical composition of the alloys enriched in ^{57}Fe was checked by optical emission spectrometry with inductively coupled plasma (Mo, B) and flame atomic absorption spectrometry (Fe, Co, Cu).

2.2 Methods

2.2.1 Synchrotron radiation and its diffraction. Synchrotrons represent unique sources of radiation that is characterised by outstanding properties.[31] The synchrotron radiation features tuneable energy, a high degree of polarization, a small

beam cross-section, negligible beam divergence, pulsed time structure, and above all extremely high brilliance (intensity).

The tremendous brilliance of synchrotron radiation enables such diffraction experiments that are not feasible with conventional X-ray sources. For example, it is possible to acquire diffractograms during continuous temperature increase of a heat treated investigated sample and thus to observe *in situ* the process of structural transformation.

DSR was performed at the KMC-2 experimental station at BESSY II, Berlin, with the energy of 7 keV (λ = 0.177121 nm) and a photon flux of $\sim 2 \times 10^{10}$ photons per s. The estimated heat load at the sample was $\sim$22 μW. The main (110) reflection maximum of a bcc-Fe lattice was registered using a 2-D Bruker HI-STAR detector. The data were acquired every 10 s with an angular resolution of 0.03° in a standard 2θ scattering geometry. Using grazing incidence arrangement, the penetration depth of the radiation is $\sim$3–4 μm. In this way, surface studies are possible and that is why the diffractograms were recorded from both sides of the ribbon-shaped samples.

About 2 cm long pieces of as-quenched alloys were positioned in an evacuated hemispherical dome made from beryllium. The samples were attached to a heated holder and exposed to continuous heating with a temperature increase of 10 K min^{-1} up to 800 °C.

2.2.2 Nuclear forward scattering of synchrotron radiation (NFS). Mössbauer spectroscopy (MS) is a method that directly correlates magnetic states of the studied materials with their structure through hyperfine interactions.[7–10,23] It is, however, quite time consuming and thus not suitable for observation of rapid dynamic processes. With the availability of the third generation synchrotron sources, the method of nuclear forward scattering (NFS) of synchrotron radiation[32] became feasible. NFS makes use of the ^{57}Fe resonant atoms as probes of the local magnetic and electronic properties in the investigated samples and provides information on hyperfine interactions similar to MS. Application of this technique is helpful in revealing the mutual relation between the magnetic arrangement and the structure of the studied materials and it can be used in dynamic *in situ* regimes.

The pulsed time structure of synchrotron radiation opens up new horizons for experiments in the time domain. The synchrotron radiation beam is tuned to the energy of the requested Mössbauer isotope and highly monochromatized with an energy bandpass of meV. The beam impinges on to the sample, where all energetic levels of every Mössbauer nucleus present in the sample are excited at the same time during the short pulse of the synchrotron radiation. In the time slot between two subsequent pulses, all excited nuclei coherently emit the excess energy in the form of resonance delayed photons that are registered with the fast detector.

The nuclear levels are often split due to hyperfine interactions as shown at the left-hand side of Fig. 1. Here, an example of magnetically split nuclear levels of ^{57}Fe is shown. Energy separation among the levels is of the order of μeV. Thus, the synchrotron radiation with a bandwidth of several meV excites all nuclear transitions simultaneously. The successive decay is characterized by an interference of the nuclear transitions from all excited levels giving rise to the delayed signal in the time domain, *viz.* NFS interferogram. The latter exhibits characteristic beating of intensities called quantum beats. An example of such a record is shown on the right-hand side of Fig. 1.

The resulting NFS interferogram of the characteristic quantum beats carries information on electric quadrupole and magnetic dipole hyperfine interactions that are unique for individual atomic sites of the resonant atoms. The counts of delayed photons are registered as a function of the time that has elapsed after the excitation. That is why NFS is sometimes referred to as Mössbauer spectrometry in the time domain. Several applications of this technique to different problems of condensed matter physics including NFS in glassy and nanoscale materials are reviewed in ref. 33.

NFS experiments were performed at the Nuclear Resonance side-station ID22N of the European Synchrotron Radiation Facility (ESRF), Grenoble. Excitation of the ^{57}Fe nuclear levels was accomplished by a photon beam with 14.413 keV energy, $\sim 10^9$ photons per s flux, and $\sim$3 meV bandwidth. The estimated heat load at the sample was $\sim$2 μW. Samples were placed in a vacuum furnace and heated up with a ramping rate of 10 K min^{-1} up to 670 °C. The maximum annealing temperature was limited by Kapton windows of the furnace. The total annealing time was 65 minutes. The NFS interferograms were continuously recorded every minute during the whole annealing process in transmission geometry. Thus, information for the bulk of the sample is obtained. Samples enriched in the stable ^{57}Fe isotope were used in order to enable faster data acquisition. They were $\sim$1–2 mm wide while the spot-size of the synchrotron beam was 0.7 × 0.3 mm^2. Evaluation of the experimental data was accomplished by the CONUSS software package.[34,35]

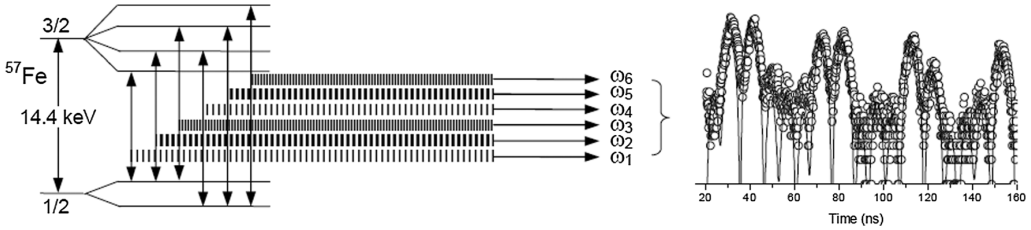

Fig. 1 Magnetically split nuclear levels of ^{57}Fe (left), photons from de-excitation transition decays that are characterized by the frequencies (energies) ω_1 to ω_6 (middle), and the resulting interferogram (right).

3. Results and discussion

3.1 Diffraction of synchrotron radiation

The process of structural transformation of originally amorphous metallic glasses was followed by DSR taken from both sides of the ribbon-shaped samples. In order to speed-up the acquisition of experimental data, the position of the 2-D detector was fixed. Taking into consideration the distance between the sample and the detector as well as the sensitive area of the latter, it was possible to acquire the scattered signal from about 14° of 2θ angles. That was enough for following the time evolution of the principal (110) reflection belonging to an expected bcc-Fe crystalline phase.

Diffractograms obtained for the $(Fe_{1-x}Co_x)_{76}Mo_8Cu_1B_{15}$ alloys are presented as contour plots in Fig. 2–4 for x = 0, 0.25, and 0.5, respectively. Vertical scales show the temperature

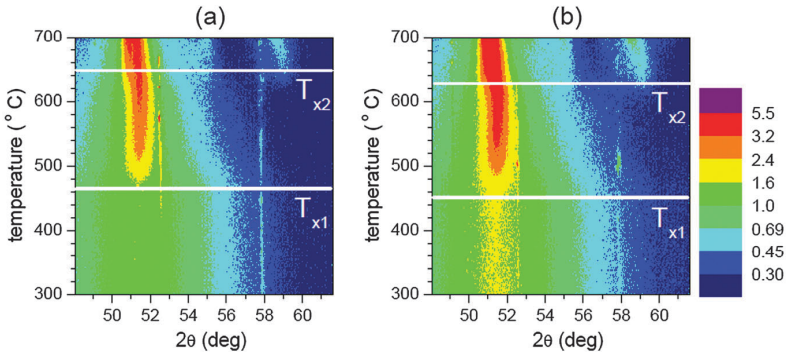

Fig. 2 Contour plots of diffractograms recorded by *in situ* DSR from the air (a) and the wheel (b) side of the $(Fe_{1-x}Co_x)_{76}Mo_8Cu_1B_{15}$ (x = 0) alloy. Crystallization temperatures T_{x1} and T_{x2} are indicated by the horizontal white lines.

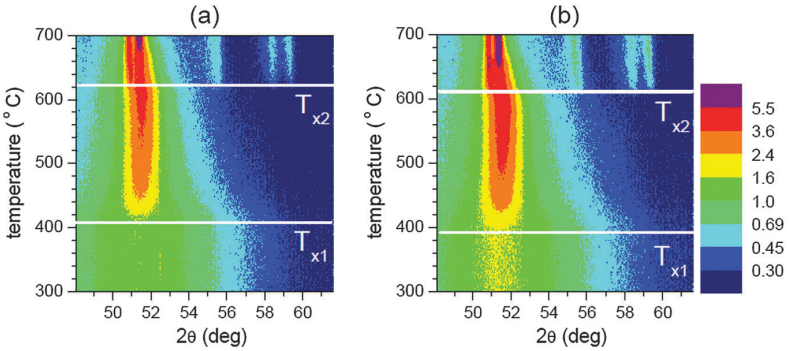

Fig. 3 Contour plots of diffractograms recorded by *in situ* DSR from the air (a) and the wheel (b) side of the $(Fe_{1-x}Co_x)_{76}Mo_8Cu_1B_{15}$ (x = 0.25) alloy. Crystallization temperatures T_{x1} and T_{x2} are indicated by the horizontal white lines.

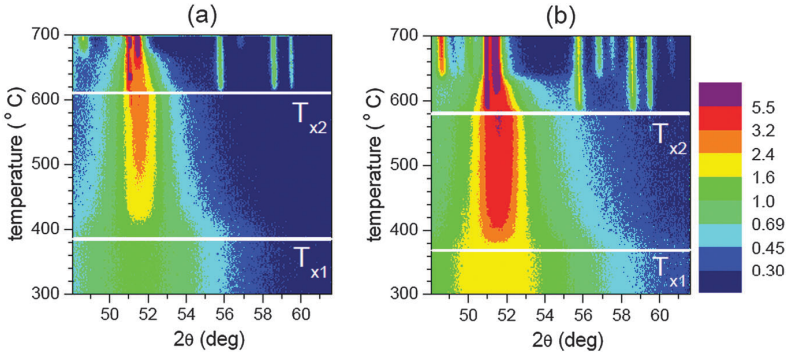

Fig. 4 Contour plots of diffractograms recorded by *in situ* DSR from the air (a) and the wheel (b) side of the $(Fe_{1-x}Co_x)_{76}Mo_8Cu_1B_{15}$ (x = 0.5) alloy. Crystallization temperatures T_{x1} and T_{x2} are indicated by the horizontal white lines.

of the sample and the horizontal ones represent 2θ angles from 48° to 62°. This range was covered by the fixed 2-D detector and coincides with the position of the main (110) reflection at ~52°. Intensities of the diffracted lines are colour coded as shown by the corresponding legends. The depicted temperatures T extend from 300 °C up to 700 °C where the structural transformations of interest take place within this temperature interval. The temperature of the onset of the first and the second crystallizations T_{x1} and T_{x2}, respectively, are marked in the figures with white lines.

The contour plots in Fig. 2–4 can be subdivided into three temperature regions. In the first region where $T < T_{x1}$, the investigated alloys are fully amorphous. The corresponding diffractograms exhibit broad reflections that are spread over a wide range of 2θ angles. The second temperature region with $T_{x1} < T < T_{x2}$ is characterized by the onset and formation of the first crystallization phase. This is identified by a single narrow reflection peak that progressively rises in intensity with annealing temperature. At the same time, a shift of the position of its maximum towards smaller 2θ-values is observed. This can be ascribed to a lattice expansion with increasing temperature of the sample. For $x = 0$ in Fig. 2, this crystalline phase belongs to bcc-Fe that is supersaturated with some Mo. The newly formed nanocrystals are only about 5–8 nm in size.[11] In the $x = 0.25$ (Fig. 3) and $x = 0.5$ (Fig. 4) alloys, the main diffraction peak corresponds to bcc-(Fe,Co) phase.

In the third temperature region where $T > T_{x2}$, additional crystalline phases have evolved. They were identified as fcc-$Fe_{23}B_6$ ($x = 0$) and $Fe(Co,Mo)_{23}B_6$ ($x = 0.25$, 0.5). In the early stages of the 2nd crystallization, a CoMoB crystalline phase was identified in the $x = 0.5$ alloy. Above the temperature of ~660 °C, formation of the tetrahedral B_2Mo_2Fe phase is observed for $x = 0$.[11]

Using the contour plots in Fig. 2–4, the T_{x1} and T_{x2} values were determined. They are plotted as a function of the cobalt concentration in Fig. 5. The estimated uncertainty in the determination of the crystallization temperatures is of ±3 °C. The corresponding error bars in Fig. 5 are almost equal to the size of the symbols.

The onset of the first (T_{x1}) and the second (T_{x2}) crystallization processes occurs earlier at the wheel side. Temperature differences in T_{x1} between the air and the wheel side are of 13 °C, 10 °C, and 23 °C as determined for $x = 0$, 0.25, and 0.5, respectively. In the case of T_{x2}, the values of 7 °C, 15 °C, and 30 °C were obtained. It is noteworthy that for the Co-containing alloys, variations in T_{x1} and T_{x2} observed for both sides scale with the Co content. Doubling the amount of Co from $x = 0.25$ to $x = 0.5$ has doubled also the temperature separation.

As seen in Fig. 5, both stages of crystallization start at lower temperatures in the alloys with higher Co contents. One can also compare the deviations between T_{x2} and T_{x1} for both sides of the ribbon-shaped samples. At the air side, they represent temperature separations of 177 °C, 216 °C, and 217 °C for $x = 0$, 0.25, and 0.5, respectively. At the wheel side, the crystallization temperatures differ between the second and the first structural transformation by 183 °C, 211 °C, and 210 °C, correspondingly. However, in contrast to the temperature deviations observed between both sides of the ribbon, the Co addition has practically no effect upon the temperature interval between the onsets of the second and the first crystallization stages.

We have performed quantitative analysis of all data obtained from *in situ* DSR experiments shown in Fig. 2–4. The crystalline contents and positions of the principal reflection peaks were derived from fits of the diffractograms with Gauss and Lorentz lines. They were assigned to the amorphous phase and newly formed nanocrystals, respectively.

The areas under the narrow lines can be considered to be proportional to the relative amounts of bcc-Fe and/or bcc-(Fe,Co) nanocrystals that have evolved from original amorphous precursors during the heat treatment. They are plotted against the annealing temperature in Fig. 6. In order to avoid any influence of crystalline phases that start appearing at the onset of the second crystallization step, the analyses were terminated well below T_{x2} of the particular alloys.

It should be noted that the data presented in Fig. 6 need not necessarily correspond to the actual contents of nanocrystals because the diffractograms were recorded only from a limited range of 2θ angles. A systematic error of about ±3% can be estimated due to truncation of some parts of the diffractograms mostly in the small 2θ angle region. An example of such fitting is demonstrated in Fig. 7 for the wheel side and $x = 0.5$ at the temperature of 450 °C. The error bars plotted in Fig. 6 were obtained from the fitting procedure. Despite the above

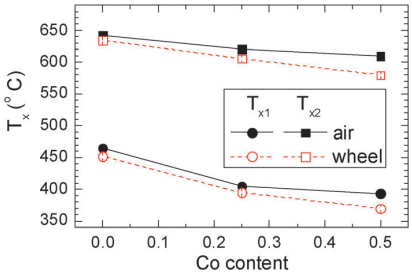

Fig. 5 Crystallization temperatures T_{x1} and T_{x2} plotted against the Co content in the $(Fe_{1-x}Co_x)_{76}Mo_8Cu_1B_{15}$ alloys as derived from *in situ* DSR taken from both the air and wheel sides of the ribbons. The lines are only guides to the eye.

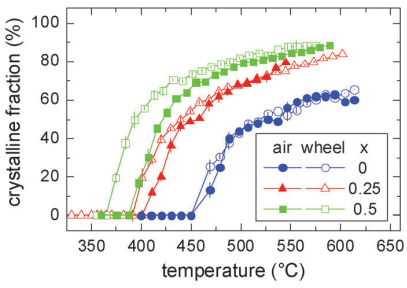

Fig. 6 Crystalline fractions plotted against the temperature of annealing as obtained from the deconvolution of *in situ* DSR data recorded from the air (full symbols) and the wheel (open symbols) sides of the $(Fe_{1-x}Co_x)_{76}Mo_8Cu_1B_{15}$ alloy. Solid lines are only guide to the eye.

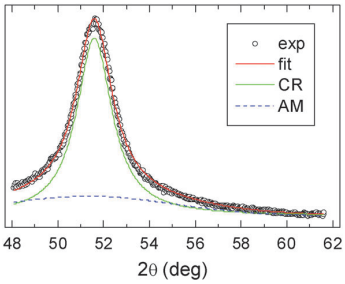

Fig. 7 Deconvolution of a diffractogram obtained from the wheel side of the $(Fe_{1-x}Co_x)_{76}Mo_8Cu_1B_{15}$, x = 0.5 alloy at 450 °C. The individual components correspond to the crystalline phase (CR) and to the residual amorphous matrix (AM).

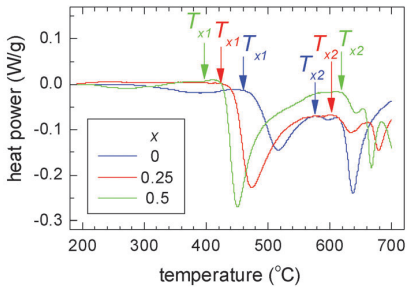

Fig. 8 Differential scanning calorimetry of the $(Fe_{1-x}Co_x)_{76}Mo_8Cu_1B_{15}$ alloy. Temperature of the onset of crystallization is marked with arrows.

mentioned restrictions, the overall trends in the temperature evolution of the crystalline contents are maintained. The temperatures of the onset of the first crystallization T_{x1} determined from Fig. 6 are in agreement with those presented in Fig. 5.

DSC records obtained from the investigated samples are plotted in Fig. 8. The onset of crystallization is marked with arrows. A reasonable agreement between DSR and DSC data is achieved. Small deviations observed might be caused by different annealing conditions. DSC was acquired under an inert atmosphere whereas DSR was performed in vacuum.

Positions of the reflections from DSR were used to calculate the lattice parameters of the bcc phases. They are shown in Fig. 9 as a function of temperature for all investigated samples.

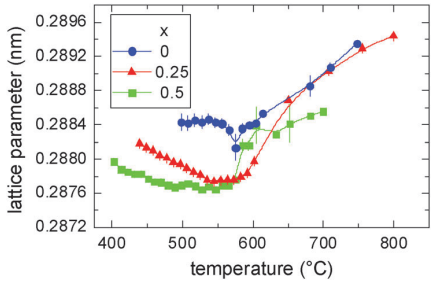

Fig. 9 Lattice parameter plotted against the annealing temperature for the $(Fe_{1-x}Co_x)_{76}Mo_8Cu_1B_{15}$ alloy. Solid lines are only guide to the eye.

The Co-free alloy (x = 0) shows rather high lattice parameters, which means that probably Mo is incorporated into the bcc lattice thus causing its expansion. In the x = 0.25 and 0.5 alloys, lower values are observed depending upon the Co content. This indicates that Co atoms apparently expel molybdenum from the bcc lattice. The initial decrease of the lattice parameter with temperature can be caused by two possible effects: (i) Mo that is incorporated into the nanograins diffuses out with increasing temperature and (ii) the lattice parameter at lower temperatures, *i.e.*, when the grains start to evolve, is influenced by an interface effect.[36] A rapid increase of the lattice parameter indicates temperature-induced lattice expansion.

3.2 Nuclear forward scattering of synchrotron radiation

The use of *in situ* DSR described above helped in the elucidation of the temperature induced structural transformations in the studied $(Fe_{1-x}Co_x)_{76}Mo_8Cu_1B_{15}$ MG. Because of the applied experimental geometry (see Section 2.2.1), the reported results were obtained from subsurface regions that extend only to a limited depth (~3–4 μm). On one hand, this approach has revealed structural differences between both sides of the investigated ribbon-shaped specimens. On the other hand, information related to areas far away from the surface (>4 μm) of the samples is not available. However, this can be gathered from another *in situ* synchrotron-based technique, namely with nuclear forward scattering (NFS) of synchrotron radiation. Some basic aspects of this less established method are briefly mentioned in Section 2.2.2. Let us emphasise that NFS scans hyperfine interactions of the ^{57}Fe resonant nuclei that are contained in the whole investigated material. As the hyperfine interactions are governed by local atomic order, information on both structural arrangement and magnetic ordering can be obtained simultaneously from NFS interferograms. The latter represent plots of the number of 'delayed' photons, which are emitted by the sample during the process of its de-excitation, as a function of time that has elapsed after the excitation with a synchrotron-radiation pulse.

In order to facilitate the NFS experiments, samples enriched in ^{57}Fe to about 50% have been used. Contour plots obtained from NFS interferograms recorded every minute during continuous temperature increase (with the ramping-rate of 10 K min^{-1}) are shown in Fig. 10 for x = 0 and x = 0.25 alloys. Vertical axes represent the temperature of the investigated samples while the elapsed time is given on the horizontal ones. The counts of the registered photons (intensities) are colour coded in a logarithmic scale. In total, about 90 interferograms were acquired during one experiment. Only those which exhibit pronounced development of hyperfine parameters with temperature are shown in Fig. 10.

Clear distinctions are seen in the character of the contour plots for x = 0 and x = 0.25. The as-quenched Co-free $Fe_{76}Mo_8Cu_1B_{15}$ MG shows close-to-room Curie temperature T_C = 40 °C.[37] That is why the obtained NFS records in Fig. 10a correspond to quadrupole electric interactions that are typical for paramagnetic materials. Consequently, the presented NFS interferograms can be described by the quantum beats that stem

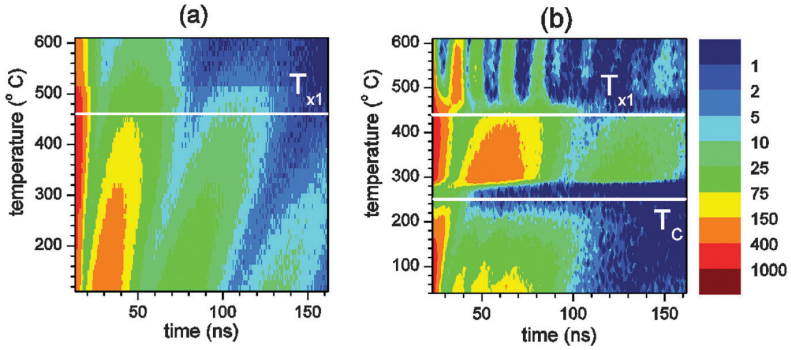

Fig. 10 Contour plot of 3-D nuclear forward scattering data of $(Fe_{1-x}Co_x)_{76}Mo_8Cu_1B_{15}$ for x = 0 (a) and x = 0.25 (b). Crystallization T_{x1} and Curie T_C temperatures are indicated by the horizontal white lines.

from distributed quadrupolar doublets. Their evolution with increasing annealing temperature does not show any qualitative changes. Even the onset of the first crystallization T_{x1} is quite difficult to unveil only from these data. This is partly also due to the fact that the produced bcc-Fe nanograins are small (~5–8 nm) and not very abundant (see Section 3.1). Consequently, the corresponding hyperfine interactions at $T > T_{x1}$ are considerably smeared out and their contribution to the NFS time records is hindered with the signal from the residual amorphous matrix. Because of these unfortunate difficulties, the x = 0 alloy is obviously an inappropriate candidate to demonstrate the diagnostic potential of the *in situ* NFS technique. On the other hand, the x = 0.5 sample exhibits stronger magnetic interactions[28] which give rise to higher T_C. At the same time, this composition features lower temperature of the first crystallization T_{x1} (Fig. 8) than the x = 0.25 alloy. Consequently, one can expect a narrower temperature region between T_C and T_{x1} in which pure paramagnetic amorphous phase exists and the evolution of NFS time records would be rather rapid. We have also considered technological limitations that are associated with the production of iron enriched alloys. That is why the main attention is paid merely to the results achieved from the x = 0.25 alloy in the following part.

The character of NFS interferograms in Fig. 10b changes abruptly at two distinct temperatures, *viz.* T_C and T_{x1}. They subdivide the inspected temperature interval into three diverse regions. In the first one where $T < T_C$, the studied alloy is completely amorphous and it undergoes the second order structural transition from the ferromagnetic to paramagnetic state at T_C. Addition of cobalt to the original NANOPERM-type Fe–Mo–Cu–B alloy modifies its chemical composition. In this way, a HITPERM-type Fe(Co)–Mo–Cu–B MG is produced. The latter is ferromagnetic at room temperature in the as-quenched amorphous state.

Evaluation of interferograms in this region was accomplished according to the physical model consisting of two distributions of hyperfine magnetic fields. They were assigned to short-range order (SRO) regions with high (~22 T) and low (~8 T) average hyperfine magnetic fields under ambient conditions (room temperature). They originate from deviations in chemical composition around the resonant iron atoms (chemical SRO) as well as from the influence of topological SRO.

In the intermediate temperature region where $T_C < T < T_{x1}$, the qualitative behaviour of NFS interferograms is similar to that observed in the x = 0 alloy. From a structural point of view, the sample is still amorphous. It is, however, already paramagnetic and that is why only relatively simple quantum beats of electric quadrupole interactions are observed. Consequently, the experimental data corresponding to this temperature interval were modelled with one distribution of quadrupole splitting.

Selected examples of interferograms from these two temperature regions are shown in Fig. 11a. After a moderate temperature increase to 107 °C, the sample exhibits amorphous structure with quantum beats assigned to hyperfine magnetic interactions. They are demonstrated by small periodic oscillations in the 35–65 ns time region. At 167 °C, minor traces of these beats are still visible but they vanish completely at T_C ~ 247 °C. Beyond this temperature (*e.g.*, at 307 °C), the interferograms demonstrate quantum beats that correspond to electric quadrupole hyperfine interactions. Here, the sample is still fully amorphous but already paramagnetic. This character of the quantum beats persists, from a qualitative point of view, till the onset of crystallization (see for example the interferogram at 427 °C in Fig. 11b).

The third temperature region $T > T_{x1}$ is characterized by continuous formation of nanocrystalline bcc-(Fe,Co) grains. They are identified by the corresponding quantum beats that appear in the time region 43–83 ns, and represent hyperfine magnetic fields. Fig. 11b shows, however, an interferogram at 447 °C in which the magnetic quantum beats are better visible. With increasing annealing temperature these rather narrow magnetic quantum beats gradually quickly evolve as the corresponding nanocrystalline phase does. This is demonstrated by an interferogram taken at 457 °C. Finally, at the end of the heating process at ~647 °C, the sample is already well crystallized and the resulting interferogram clearly shows magnetic structure.

Evaluation of the interferograms in this temperature region was accomplished with a model that took into consideration

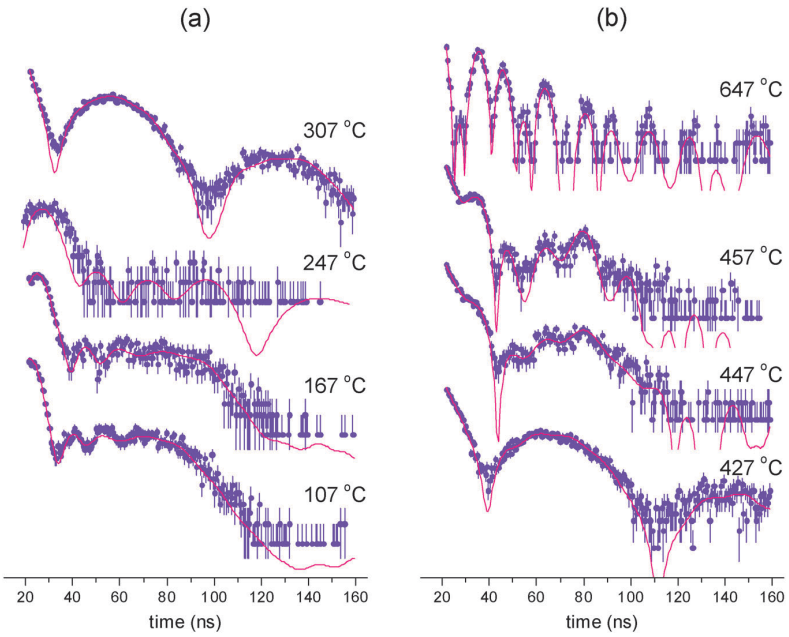

Fig. 11 Selected records obtained from NFS for the $(Fe_{1-x}Co_x)_{76}Mo_8Cu_1B_{15}$ (x = 0.25) at the indicated temperatures in the vicinity of T_C (a) and T_{x1} (b). Experimental data (symbols) are fitted (solid lines) according to the model described in the text.

both the presence of a residual amorphous matrix that was, however, in the paramagnetic state as well as the newly formed bcc-(Fe,Co) nanocrystals. The former was fitted with one distribution of quadrupole splitting that was applied actually already in the $T > T_C$ region. The latter were represented by four components with hyperfine magnetic fields (not distributed) whose relative fractions were derived from a binomial distribution of the Co nearest neighbours:

$$P(n) = \frac{8!}{n! \cdot (8-n)!} \cdot x^n \cdot (1-x)^{(8-n)} \qquad (1)$$

where n is the number of Co nearest neighbours and x is the Co concentration (x = 0.25). The number of sextets used was determined by a condition of a minimum contribution $P(n) > 5\%$ that could be unambiguously distinguished in the interferograms. Consequently, 0, 1, 2, and 3 Co nearest neighbours in the bcc-(Fe,Co) lattice were considered. In order to ensure a convergent fitting procedure, the relative fractions of the magnetic components were fixed to the values obtained from eqn (1). Their hyperfine magnetic fields were fitted without any restrictions. We have tried also more magnetic components, however the fit became unstable.

As can be seen from Fig. 11, the obtained fits (solid lines) satisfactorily represent the measured experimental data (full symbols). Some deviations are observed at the transition temperatures (T_C, T_{x1}) where the applied physical models change. This is well visible at T_C because of an abrupt transformation of the character of the hyperfine interactions from dipole magnetic into quadrupolar electric ones. In addition, the beat intensities are dramatically reduced for times higher than 60 ns due to the broad distribution of the hyperfine magnetic field. This is a nice demonstration of the second order phase transformation observed *in situ* that alters the magnetic microstructure while the structural arrangement is maintained.

The above mentioned physical models were used to fit all the measured interferograms. It should be noted that during acquisition of the NFS data, temperature was continuously increasing with the ramping-rate of 10 K min^{-1}. Evolution of the content of the bcc-(Fe,Co) nanocrystalline phase and the residual amorphous matrix is plotted in Fig. 12 against the annealing temperature. The onset of crystallization is determined at $T_{x1} \sim 435$ °C, which is slightly higher than those determined from DSR for the air and the wheel sides of the ribbon-shaped sample. This is due to the fact that the crystallization starts first on the surfaces and then progresses into the bulk that is scanned by NFS.

The evolution of relative fractions of the crystalline phase can be used to describe the kinetics of crystallization. Using isothermal annealing experiments, we have introduced a relatively simple model of the evolution of nanograins[29] and a satisfactory match between the experimental and theoretical data was achieved. Because one deals in this case with dynamical temperature regimes, more elaborate crystallization models should be employed that describe non-isothermal time evolution.[38,39] We would like to emphasise that the main aim of this study is to show how synchrotron-based techniques of DSR and NFS can be used in the description of structural transformations during dynamic annealing. The application of different kinetics models is beyond the scope of this study.

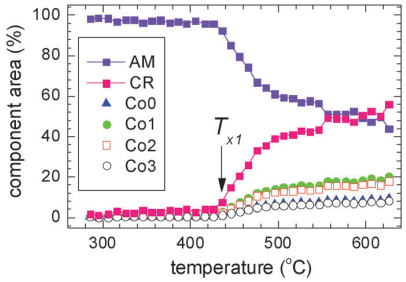

Fig. 12 Fraction of the residual amorphous matrix (AM) and bcc-(Fe,Co) crystalline phase (CR) plotted against the annealing temperature as obtained from the fitting of *in situ* NFS data of the $(Fe_{1-x}Co_x)_{76}Mo_8Cu_1B_{15}$ (x = 0.25) alloy. Fractions of crystalline sites with different amounts of Co nearest neighbours (Co0–Co3) are also given. Solid lines are only guide to the eye. The arrow indicates the onset of crystallization T_{x1}.

One more important point should be mentioned, however. While DSR experiments provide information on the total amount of bcc nanocrystalline grains, NFS can go even further. By the help of the fitting models described above, it is possible to distinguish among structurally different iron occupational sites within the bcc lattice. Through hyperfine interactions (*viz.* hyperfine magnetic fields) acting upon the ^{57}Fe resonant nuclei, the presence of varying number of their cobalt nearest neighbours is evidenced. Temperature development of relative contributions of iron sites with none (Co0), one (Co1), two (Co2), and three (Co3) cobalt nearest neighbours are plotted in Fig. 12, too. The sum of these four components constitutes the overall contents of nanograins (CR).

Average hyperfine magnetic fields of the amorphous and nanocrystalline phases are displayed in Fig. 13. In the temperature region $T < T_C$ in Fig. 13a, the fields represent different SRO arrangements of the resonant ^{57}Fe nuclei in the amorphous structure. The high-field component (~22 T at close-to-room temperature) represents Fe neighbours that are surrounded predominantly with Co while the low-field one (~8 T) reflects contributions from other constituent elements (Mo, B). Both average magnetic hyperfine fields decrease with temperature and they are supposed to vanish at T_C. It should be noted that the values of ~3–5 T for the low-field component in the vicinity of T_C are comparable in strength with the newly developing electric quadrupole interactions and can be hardly distinguished one from another. In this respect, small hyperfine magnetic fields can be treated as quadrupole splitting. On the other hand, the high-field component that attains ~11 T at T_C contributes only marginally at higher temperatures.

Here, a huge diagnostic potential of the NFS technique, which scans simultaneously both the local structural arrangement and hyperfine interactions, is nicely seen. Though the overall structure is amorphous, contributions from regions with different chemical SRO and their evolution can be followed *in situ* as a function of increasing temperature of measurement. Such data can be hardly obtained by any other technique. Majority of conventional analytical tools treat amorphous structures as structurally isotropic regions, which usually provide only a featureless (broadened and/or halo) signal.

Hyperfine magnetic fields in Fig. 13b belong to four narrow components that were used to reconstruct the contributions of the bcc-(Fe,Co) nanocrystals. Shortly after the onset of crystallization they show a growing trend with temperature. This is due to progressing formation of the bcc lattice that is still building-up. A similar effect is observed by DSR for the lattice parameter in Fig. 9. Eventually, the hyperfine fields arrived at their average values of ~27.2 T, ~29.2 T, ~30.5 T, and ~31.6 T and follow the expected temperature dependences. According to the obtained hyperfine magnetic field values, the particular components were assigned to iron atom sites with zero, one, two, and three cobalt nearest neighbours in the bcc-(Fe,Co) crystalline lattice.

Similarly to the case of the $T < T_C$ region, where the system is fully amorphous, the *in situ* NFS technique is also very exceptional here. The mutual relationship between the structural arrangement and the corresponding hyperfine interactions enables the formation of the bcc-(Fe,Co) lattice to be indirectly followed by making use of its hyperfine magnetic fields. The practical applicability of the method rests with the fact that even particular crystalline lattice sites, which have eventually different numbers of Co nearest neighbours, can be identified and, subsequently, their behaviour with continuously varying temperature can be also independently and separately studied.

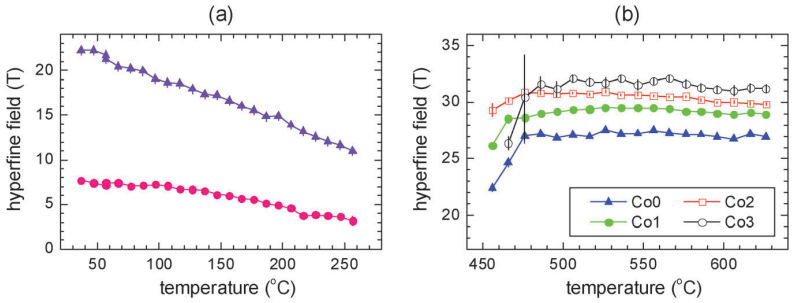

Fig. 13 Hyperfine magnetic fields of the fitted components in the amorphous state (a) and of the individual crystalline lattice sites with zero (Co0), one (Co1), two (Co2), and three (Co3) cobalt nearest neighbours (b) plotted against the annealing temperature as obtained from the fitting of *in situ* NFS data of the $(Fe_{1-x}Co_x)_{76}Mo_8Cu_1B_{15}$ (x = 0.25) alloy. Solid lines are only guide to the eye.

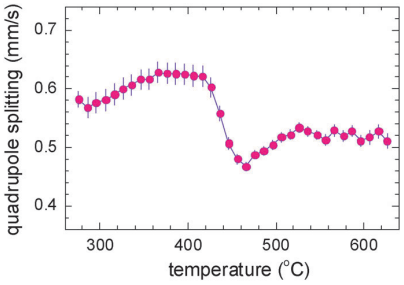

Fig. 14 Average values of quadrupole splitting of the amorphous residual matrix plotted against the annealing temperature as obtained from the fitting of *in situ* NFS data of the $(Fe_{1-x}Co_x)_{76}Mo_8Cu_1B_{15}$ (x = 0.25) alloy. Solid line is only guide to the eye.

As mentioned above, in the intermediate temperature region where $T_C < T < T_{x1}$, the experimental data were modelled with one distribution of quadrupole splitting. After the onset of crystallization ($T > T_{x1}$), the amorphous residual matrix still persists, and taking into consideration relatively high temperatures of the NFS experiments, it was reconstructed also by one distribution of quadrupole splitting (QS). The obtained average QS values are plotted against the temperature of annealing in Fig. 14.

Quadrupole splitting provides information about bond properties and local symmetry of the iron site. The quantitative change in QS values at $\sim$450 °C coincides with the onset of crystallization. In the temperature range $T >$ 500 °C where the crystalline phase is already quite well developed, stabilization of QS occurs. It should be noted that the physical model that we have used to describe the behaviour of the studied system comprises distributions of hyperfine parameters (*viz.*, amorphous residual matrix) and well defined values of the crystalline components. Consequently, the fitting procedure is very complex. From this perspective we should admit that the absolute values of QS could be debatable.

This situation is quite similar to that which the researchers were faced with about 30 years ago when the first attempts to refine broad Mössbauer spectra of amorphous metallic glasses have appeared. In order to ensure consistency of the obtained hyperfine parameters, we have checked their temperature evolution rather than to relay upon fitting of a single NFS interferogram. This approach is closely discussed in ref. 8 for the case of conventional Mössbauer spectra. As demonstrated by Fig. 13 and 14, we hope that we have succeeded in obtaining relevant temperature dependencies of the particular hyperfine parameters. To our best knowledge, similar data do not exist in the literature and we have introduced the obtained hyperfine parameters (namely QS) in order to provoke discussion on the ways how to fit NFS data of amorphous and/or nanocrystalline alloys. Nevertheless, the methodological aspects of NFS data evaluation are beyond the scope of the current work.

Here, we wanted to point at the particular features of the NFS technique which allows *in situ* transformation studies aimed at understanding the evolution of specific materials properties *during* these transient periods. The latter can be followed through the evolution of hyperfine parameters. More examples of such studies can be found in our most recent papers.[40,41]

4. Conclusions

The formation of nanocrystalline structure is decisive for macroscopic physical properties that in turn govern the practical applications of these materials. Under external conditions of prolonged elevated temperature, compositional-dependent structural transformations may occur. The influence of temperature was followed during *in situ* experiments using the techniques based upon synchrotron radiation.

Effects of cobalt substitution on kinetics of crystallization was investigated for $(Fe_{1-x}Co_x)_{76}Mo_8Cu_1B_{15}$ (x = 0, 0.25, 0.5) nanocrystalline alloy by *in situ* diffraction of synchrotron radiation. We observed a tendency of the first and the second crystallization temperature to decrease with increasing cobalt content. It was shown that the surface crystallization starts earlier at the wheel side than at the air side of ribbon-shaped samples. Structural characteristics comprising temperature evolution of the relative amount of newly formed crystalline phases as well as their lattice parameters were followed *in situ* during heat treatment of the original metallic glass. These parameters were obtained from analyses of the diffractograms taken during short time intervals.

Along with structural characteristics, also magnetic states of the studied system were inspected *via* temperature development of the associated hyperfine interactions. The latter were derived from time interferograms that were recorded by nuclear forward scattering of synchrotron radiation. This technique enables separate evaluation of the contributions that stem from structurally different regions within the investigated samples, including the newly formed nanocrystals and the residual amorphous matrix. In addition, their magnetic microstructures can be also assessed. We have shown that even minor Co content (x = 0.25) has a substantial effect not only upon the magnetic behaviour of the alloy but also upon its structure. Making use of hyperfine magnetic fields it was possible to unveil structurally diverse positions of Fe atoms that reside in a nanocrystalline lattice with different numbers of Co nearest neighbours.

Extremely high brilliance of the present sources of synchrotron radiation makes doable experiments that are capable of providing information on-fly during continuous variation of external conditions (*e.g.*, temperature). Such an approach is hardly affordable with other sources of radiation. In this way, the use of synchrotron-based techniques paves a completely new road to the understanding of technologically important details on the formation of nanocrystalline structures by heat treatment of the originally amorphous precursors.

Acknowledgements

The authors gratefully acknowledge the support by the project LO1305 of the Ministry of Education, Youth and Sports of the

Czech Republic and the projects, CZ.1.07/2.3.00/20.0155, and CZ.1.07/2.3.00/30.0041. Allocation of synchrotron beamtimes at Helmholtz-Zentrum Berlin and European Synchrotron Radiation Facility is also gratefully acknowledged.

References

1 M. E. McHenry and D. E. Laughlin, *Acta Mater.*, 2000, **48**, 223.
2 Y. Yoshizawa, A. Oguma and K. Yamauchi, *J. Appl. Phys.*, 1988, **64**, 6044.
3 K. Suzuki, N. Kataoka, A. Inoue, A. Makino and T. Masumoto, *Mater. Trans., JIM*, 1990, **31**, 743.
4 M. A. Willard, D. E. Laughlin, M. E. McHenry, D. Thoma, K. Sickafus, J. O. Cross and V. G. Harris, *J. Appl. Phys.*, 1998, **84**, 6773.
5 A. Hernando, *J. Phys.: Condens. Matter*, 1999, **11**, 9455.
6 G. Herzer, *Acta Mater.*, 2013, **61**, 718.
7 S. Stankov, B. Sepiol, T. Kaňuch, D. Scherjau, R. Würschum and M. Miglierini, *J. Phys.: Condens. Matter*, 2005, **17**, 3183.
8 M. Miglierini and J.-M. Grenèche, *J. Phys.: Condens. Matter*, 2003, **15**, 5637.
9 M. Miglierini, M. Kopcewicz, B. Idzikowski, Z. E. Horváth, A. Grabias, A. I. Škorvánek, P. Dluzewski and C. C. Daróczi, *J. Appl. Phys.*, 1999, **85**, 1014.
10 M. Pavuk, M. Miglierini, M. Vujtek, M. Mashlan, R. Zboril and Y. Jiraskova, *J. Phys.: Condens. Matter*, 2007, **19**, 216219.
11 M. Paluga, P. Švec, D. Janičkovič, D. Muller, P. Mrafko and M. Miglierini, *Rev. Adv. Mater. Sci.*, 2008, **18**, 481.
12 M. Miglierini, A. Lančok and J. Kohout, *Appl. Phys. Lett.*, 2010, **96**, 211902.
13 U. Köster, U. Schünemann, M. Blank-Bewersdorff, S. Brauer, M. Sutton and G. B. Stephenson, *Mater. Sci. Eng., A*, 1991, **133**, 611.
14 J. M. Borrego, C. F. Conde, M. Millán, A. Conde, M. J. Capitán and J. L. Joulaud, *Nanostruct. Mater.*, 1998, **10**, 575.
15 C. R. M. Afonso, C. Bolfarini, W. J. Botta Filho and C. S. Kiminamim, *J. Non-Cryst. Solids*, 2006, **352**, 3404.
16 J. Bednarčík, R. Nicula, M. Stir and E. Burkel, *J. Magn. Magn. Mater.*, 2007, **316**, 823.
17 A. R. Yavari, A. Le Moulec, A. Inoue, N. Nishiyama, N. Lupu, E. Matsubara, W. J. Botta, G. Vaughan, M. Di Michiel and Å. Kvick, *Acta Mater.*, 2005, **53**, 1611.
18 H. F. Poulsen, J. A. Wert, J. Neuefeind, V. Honkimäki and M. Daymond, *Nat. Mater.*, 2005, **4**, 33.
19 S. Mechler, G. Schumacher, I. Zizak, M. P. Macht and N. Wanderka, *Appl. Phys. Lett.*, 2007, **91**, 021907.
20 N. Mattern, M. Stoica, G. Vaughan and J. Eckert, *Acta Mater.*, 2012, **60**, 517.
21 G. Wang, N. Mattern, J. Bednarčík, R. Li, B. Zhang and J. Eckert, *Acta Mater.*, 2012, **60**, 3074.
22 S. Michalik, J. Michalikova, M. Pavlovic, P. Sovak, H.-P. Liermann and M. Miglierini, *Acta Mater.*, 2014, **80**, 309.
23 M. Miglierini, T. Kaňuch, M. Pavúk, P. Švec, G. Schumacher, I. Zizak and Y. Jirásková, *Hyperfine Interact.*, 2008, **183**, 31.
24 C. F. Conde, A. Conde, D. Janičkovič and P. Švec, *J. Magn. Magn. Mater.*, 2006, **304**, e739.
25 G. Vlasák, C. F. Conde, D. Janičkovič and P. Švec, *Mater. Sci. Eng., A*, 2007, **449–451**, 464.
26 C. F. Conde, J. M. Borrego, J. S. Blázquez, A. Conde, P. Švec and D. Janičkovič, *J. Alloys Compd.*, 2011, **509**, 1994.
27 T. Kaňuch, M. Miglierini, A. Lančok, P. Švec and E. Illeková, *Acta Phys. Pol.*, 2008, **113**, 63.
28 M. Miglierini, *J. Phys.: Conf. Ser.*, 2010, **217**, 012092.
29 M. Miglierini, V. Procházka, S. Stankov, P. Svec Sr., M. Zajac, J. Kohout, A. Lancok, D. Janickovic and P. Svec, *Phys. Rev. B: Condens. Matter Mater. Phys.*, 2013, **86**, 020202(R).
30 K. Suzuki, A. Makito, N. Kataika, A. Inoue and T. Masumoto, *Mater. Trans., JIM*, 1991, **32**, 93.
31 G. Mülhaupt and R. Rüffer, *Hyperfine Interact.*, 1999, **123/124**, 13.
32 G. V. Smirnov, *Hyperfine Interact.*, 1999, **123/124**, 31.
33 R. Rüffer, *C. R. Phys.*, 2008, **9**, 595.
34 W. Sturhahn and E. Gerdau, *Phys. Rev. B: Condens. Matter Mater. Phys.*, 1994, **49**, 9285.
35 W. Sturhahn, *Hyperfine Interact.*, 2000, **125**, 149.
36 M. Dittrich and G. Schumacher, *Mater. Sci. Eng., A*, 2014, **604**, 27.
37 M. Hasiak, M. Miglierini, J. Kaleta and M. Bujdoš, *Acta Phys. Pol., A*, 2015, **127**, 608.
38 F. Liu, F. Sommer and E. J. Mittemeijer, *J. Mater. Sci.*, 2004, **39**, 1621.
39 J. S. Blázquez, J. M. Borrego, C. F. Conde, A. Conde and S. Lozano-Pérez, *J. Alloys Compd.*, 2012, **544**, 73.
40 M. Miglierini, V. Procházka, R. Rüffer and R. Zbořil, *Acta Mater.*, 2015, **91**, 50.
41 V. Procházka, V. Vrba, D. Smrčka, R. Rüffer, P. Matúš, M. Mašláň and M. B. Miglierini, *J. Alloys Compd.*, 2015, **638**, 398.

PCCP

COMMUNICATION

Direct evidence of Fe(v) and Fe(iv) intermediates during reduction of Fe(vi) to Fe(iii): a nuclear forward scattering of synchrotron radiation approach†

Cite this: DOI: 10.1039/c5cp03784k

Received 30th June 2015,
Accepted 29th July 2015

DOI: 10.1039/c5cp03784k

www.rsc.org/pccp

Libor Machala,*[a] Vít Procházka,[a] Marcel Miglierini,[ab] Virender K. Sharma,[c] Zdeněk Marušák,[a] Hans-Christian Wille[d] and Radek Zbořil*[a]

Identification of unstable high-valent iron species in electron transfer reactions of ferrate(vi) ($Fe^{VI}O_4^{2-}$, Fe(vi)) has been an important challenge in advancing the understanding of the oxidative mechanisms of ferrates. This paper presents the first example of distinguishing various phases differing in the valence state of iron in the solid state reduction of Fe(vi) to Fe(iii) oxides at 235 °C using hyperfine parameters, isomer shift and hyperfine magnetic field, obtained from nuclear forward scattering of synchrotron radiation (NFS). The NFS technique enables a fast data accumulation resulting in high time resolution of *in situ* experiments. The results suggest a reaction mechanism, involving Fe(v) and Fe(iv) species, in the thermal decomposition of K_2FeO_4 to $KFeO_2$. The present study opens up an approach to exploring the unambiguous identification of Fe(vi), Fe(v), Fe(iv), and Fe(iii) in electron-transfer reaction mechanisms of ferrates in solid and aqueous phase systems.

Iron as an element exhibits a unique range of valence states (0, I, II, III, IV, V, and VI), which have applications in medicine, biocatalysis, energy, remediation, and nanotechnology.[1–5] High-valent-iron-oxo (Fe^{IV}=O and Fe^{V}=O) species have been frequently implicated in chemical and biological oxidation reactions.[6–8] During the past decade, several complexes of the high-valent iron have been synthesized and characterized to learn their roles in the catalytic activation of O_2 by iron-containing metalloenzymes.[8–14] In comparison, studies on high-valent tetra-oxy iron species (*e.g.* $Fe^{VI}O_4^{2-}$, ferrate(vi)) are very limited, although these species have been shown to be important in industrial and environmental reactions, including cleaner ("greener") synthesis of organic compounds and two-dimensional materials,[15] high energy density rechargeable batteries, and disinfection and purification of water.[3,16–20]

The reduction of $Fe^{VI}O_4^{2-}$ ions may occur through either 1-e^- or 2-e^- processes.[21,22] For example, thermal decomposition of solid K_2FeO_4 may yield both Fe(iv) ($K_2FeO_4 \rightarrow K_2FeO_3 + 1/2O_2$) and Fe(v) ($K_2FeO_4 \rightarrow KFeO_3 + 1/3K_2O + 1/3KO_2$).[22] Significantly, both $KFeO_3$ and K_2FeO_3 can form $KFeO_2$, the experimentally observed final product. In solution reactions, the correlation of rates with redox potentials of substrates also suggested the formation of both Fe(v) and Fe(iv) species as intermediates.[21,22] The oxygen atom transfer in the oxidation of the sulfur substrate can occur *via* Fe(iv) (direct oxygen atom transfer) and Fe(v) (electron transfer, followed by oxygen atom transfer).

During the past four decades, numerous studies have proposed Fe(iv) and Fe(v) as intermediate species in the reduction of Fe(vi),[2–3,23,24] but direct evidence of the formation of intermediates is still missing. There are various difficulties associated with the investigation of the intermediates, including instability of the intermediates in solid and solution phases, presence of intermediates at low concentrations, and limitations of the analytical techniques that can be used to probe *in situ* formation of intermediates with short half-lives.[25,26] Furthermore, the conventional analytical techniques do not allow *in situ* kinetic monitoring of the formation/transformation of intermediates. In the present paper, nuclear forward scattering (NFS) of synchrotron radiation was applied, which endowed the direct unambiguous identification of Fe(iii), Fe(iv), Fe(v), and Fe(vi) during the thermally induced solid state transformation of Fe(vi) to Fe(iii). Synchrotron radiation and the use of an ^{57}Fe-enriched K_2FeO_4 sample shortened the collection time of NFS time spectra to ~1 min, which allowed the study of the concomitant decay/growth of all four ferrate species. Therefore, the present study shows the very first direct experimental proof of intermediate states during Fe(vi) decay. The development of the method involving synchrotron radiation will allow

[a] *Regional Centre of Advanced Technologies and Materials, Departments of Experimental Physics and Physical Chemistry, Faculty of Science, Palacký University, Šlechtitelů 11, 783 71 Olomouc, Czech Republic. E-mail: libor.machala@upol.cz, radek.zboril@upol.cz*
[b] *Institute of Nuclear and Physical Engineering, Slovak University of Technology, Ilkovicova 3, 812 19 Bratislava, Slovakia*
[c] *Department of Environmental and Occupational Health, School of Public Health, Texas A&M University, 1266 TAMU, College Station, Texas 77843, USA*
[d] *DESY, Notkestraße 85, D-22607 Hamburg, Germany*

† Electronic supplementary information (ESI) available. See DOI: 10.1039/c5cp03784k

direct elucidation of a number of iron intermediates with low concentration and relatively short lifetimes in several other chemical and biological systems. This has been briefly discussed.

An ^{57}Fe enriched Fe(III) salt source was used as a precursor to synthesize the ^{57}Fe-enriched solid K_2FeO_4 sample (ESI†). The powdered K_2FeO_4 had a grain size in the range of 1–100 μm (Fig. S1a, ESI†). The purity of the sample was tested using ^{57}Fe NFS at room temperature (Fig. S1b, ESI†). The sample contained 98% Fe(VI) and the remaining 2% was Fe(III), corresponding to ferric hydroxide. The series of NFS time spectra of a powdered K_2FeO_4 were collected at the Dynamics Beam line at PETRAIII,[27] DESY, Hamburg, Germany. K_2FeO_4 was introduced into a glass capillary with a diameter of 1.2 mm before it was placed into the furnace (Linkam THMS600). The sample was heated up to 235 °C with a ramp rate of 50 °C min^{-1} and NFS data were collected every ~1 min for 205 min. A total of 173 time spectra was acquired during the study, and they were analyzed using the CONUSS software.[28,29]

A set of NFS time spectra is shown in Fig. 1 in the form of a contour plot. Here, the *x*-axis represents the time that has elapsed after the synchrotron excitation pulse, and the *y*-axis shows the thermal treatment from the beginning of the heating process. Logarithmic intensities of the NFS time spectra are color coded. Examples of typical time spectra that were recorded after 20, 70, and 140 min of heat treatment are separately displayed in Fig. 1a. In Fig. 1a, experimental data are overlaid with solid curves that correspond to fits according to the chosen theoretical model. The significance of the fits was checked using the chi square criterion. As seen from the selected NFS records in Fig. 1, very satisfactory fits were achieved. They were obtained using a thorough analysis of components, and the model that consists of five individual components (see detailed description in the ESI†). Basically models having less than five components are not justified statistically.

The first component (A) of the fitted model represents K_2FeO_4. The second component (E) exhibits isomer shift IS = 0.15 mm s^{-1}, quadrupole shift Q = 0.09 mm s^{-1} and hyperfine magnetic field B = 45 T which are typical for $KFeO_2$ with tetrahedrally coordinated Fe^{3+} atoms.[19] Component (C) has isomer shift, IS (0.30 mm s^{-1}) and quadrupole shift Q (0.15 mm s^{-1}) higher than those of $KFeO_2$, suggesting that Fe^{3+} may be in an octahedral coordination.[30] This component could be assigned to K_3FeO_3 based on the hyperfine parameters, obtained in our experiments, which did not match with any of those corresponding to other Fe(III) oxides. The isomer shifts of components (B) and (D) correspond to +4 and +5 oxidation states of Fe, respectively.[31,32] The obtained hyperfine parameters are listed in Table S1 (ESI†) together with the maximum observed relative amounts.

Fig. 2 presents the formation of components B, C, D, and E during the thermal decomposition of K_2FeO_4 (component A). Initially, the decomposition of K_2FeO_4 was relatively slow with the formation of $KFeO_2$ as the major species produced (Fig. 2a). In addition, coincident growth of a few percent of other ferrate species (B, C, D) was observed. The amount of component (B) increased to ~4% after 50 min, followed by a decrease to almost an insignificant amount after 100 min. Significantly,

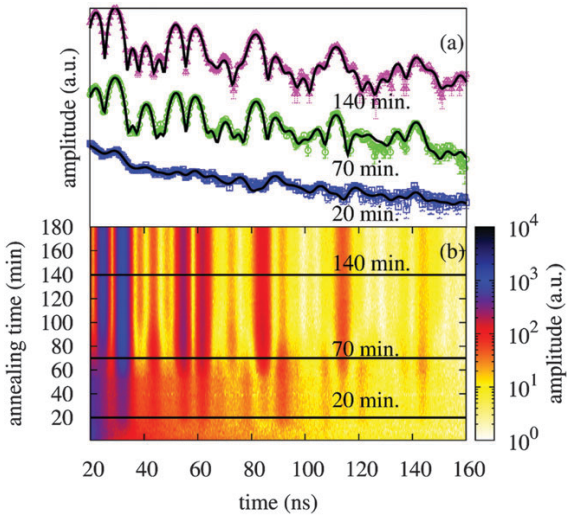

Fig. 1 (a) Selected NFS data (open symbols) with fits (solid lines) for 20, 70, and 140 min. (b) Contour plot of all NFS time spectra recorded during heat treatment at 235 °C.

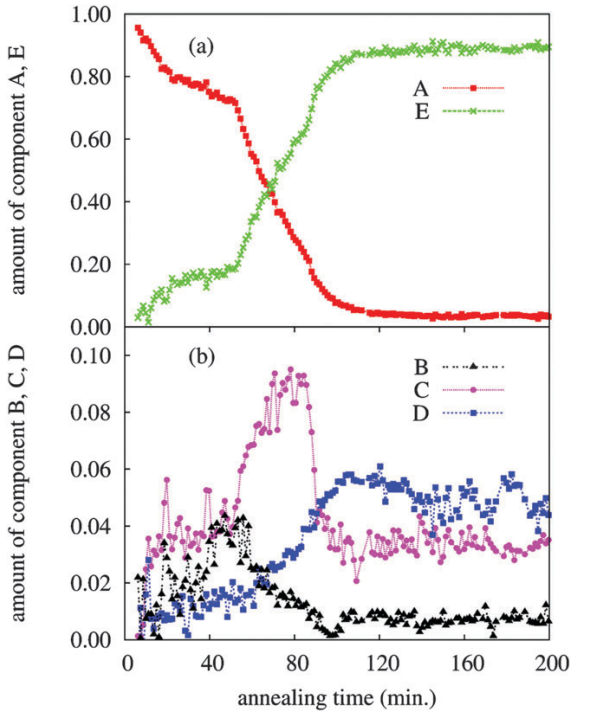

Fig. 2 Relative amounts of components (A) and (E) (a) and components (B), (C), and (D) (b) plotted as a function of time during annealing of K_2FeO_4 at 235 °C. Note different relative scales in (b).

when component (B) began to decrease (at 50 min), there were considerable changes in the rates of Fe(VI) decrease, $KFeO_2$ increase, and component (C) increase (Fig. 2). This indicates that after 50 min the decomposition of Fe(VI) becomes faster, with preferential formation of Fe(III) species.

The amount of component (C) rapidly increased even after the decrease of Fe(V), reaching a maximum of ~9% at 80 min. Therefore, component (C) could be formed directly from K_2FeO_4 as well. Component (C) rapidly decreased to ~3% after 100 min of the experiment. This decrease was accompanied by a faster formation of $KFeO_2$ (see the change of trend in component (E) in Fig. 2a at 80 min). A progressive growth of component (D) was observed from the beginning of the decomposition reaching a maximum of ~5% at 100 min. At this point, only a minor decrease of ~1% of component (D) was seen. It appeared that formation of component (D) took place independently of the formation of component (B). The decomposition process was essentially completed after 100 min when ~90% of $KFeO_2$, ~6% of component (D) and ~3% of component (C) were present (see all five nearly saturated curves in Fig. 2). Previously, $KFeO_2$ was determined to be the only final decomposition product of K_2FeO_4 using conventional Mössbauer spectroscopy.[22] It is worth noting that the high resonant intensity of an NFS experiment results in a good time resolution of the determination of the chemical constituents, which cannot be achieved by conventional Mössbauer spectroscopy. Other transformation products of K_2FeO_4 were K_2O, KO_2, and O_2.[22]

Based on the analysis of the curves shown in Fig. 2, eqn (1)–(3) are proposed for the reduction of Fe(VI). Transformation of Fe(VI) to Fe(III) through sequential 1-e^- reductions of Fe(VI) → Fe(V) → Fe(IV) → Fe(III) is another possibility. The reduction has to be accompanied by the corresponding electron transfers; numbers of evolved electrons are included in the equations. Suggested possible chemical equations describing the formation of intermediates during the decomposition are summarized in Table S1 (ESI†). Accordingly, the evolved electrons are consumed by the formation of oxygen molecules and/or potassium superoxide.

$$\mathrm{Fe(VI)} \rightarrow \mathrm{Fe(III)} + 3e^- \quad (1)$$

$$\mathrm{Fe(VI)} \rightarrow \mathrm{Fe(IV)} + 2e^- \rightarrow \mathrm{Fe(III)} + e^- \quad (2)$$

$$2\ \mathrm{Fe(VI)} \rightarrow \mathrm{Fe(V)} + \mathrm{Fe(III)} + 4e^- \quad (3a)$$

$$\mathrm{Fe(V)} \rightarrow \mathrm{Fe(III)} + 2e^- \quad (3b)$$

The possibility of the reactions, shown in eqn (1)–(3), may be understood thermodynamically by computational calculations[33,34] in future work. Significantly, some experimental evidences suggest the thermodynamic feasibility of the reactions. For example, the positive standard potential for reduction of Fe(VI) to Fe(III) (E^0 = +2.2 V and +0.8 V in acidic and basic medium, respectively).[35] Also, the estimated redox potential of Fe(VI) to Fe(V) was positive in basic medium (Fe^{VI}/Fe^{V} = 0. 76 V in basic medium).[21] Moreover, some direct experimental evidences of the formation of different intermediate iron species *via* 1-e^- and 2-e^- transfer steps involving ferrate species are known in the literature.[19–23,36–37]

The Fe(IV) phase could be presented by either K_4FeO_4 and K_2FeO_3. Since the precursor compound was K_2FeO_4, the compound of the Fe(IV) phase may be K_2FeO_3. As for the Fe(V) phase, there are also two possible chemical forms, that would be reasonable, K_3FeO_4 and $KFeO_3$. Since known quadrupole splitting of K_3FeO_4 (Q = 0.95 mm s^{-1}) is very far from that obtained for component (B) in the course of the NFS measurements (Q = 0.15 mm s^{-1}), $KFeO_3$ was finally ascribed to component (B). Overall, the components (C), (D), and (B) are proposed to be K_3FeO_3, K_2FeO_3, and $KFeO_3$, respectively. The proposed reactions, given in Table S2 (ESI†), represent a simple description of the observed formation and decay of iron species of different oxidation states during the thermal decomposition of K_2FeO_4. However, self-decomposition of high-valent iron intermediates, bimolecular reactions among ferrates intermediates, and reduction of high-valent iron compounds with reducing oxygen species may also occur.

Overall, the studied system of ferrates is of great interest due to renewed interest in synthesis of high-valent iron oxo species for various applications such as evolution of molecular oxygen from water and treatment of emerging toxins/contaminants.[2,37–39] The presented example using the NFS technique can be extended to many other systems (chemical or biological) for reliable detection of iron intermediates with low concentrations and relatively short lifetimes. Examples include generation of intermediate species in enzymatic reactions and in mechanism studies of Fe(IV)/Fe(V) model compounds.[6,8,40–43] Furthermore, an improvement in synchrotron radiation (FLASH XFEL) is in progress where a brilliance increase of 10^9 is planned for beam time structure suitable to NFS. This will lead to collection of NFS spectra faster several orders of magnitude more quickly than at PETRAIII. Significantly, this will allow *in situ* monitoring of reactions over a second time scale by the NFS technique demonstrated herein.

Conclusions

This study provides the first experimental evidence of the formation of Fe(IV) and Fe(V) intermediate phases of low concentrations during the reduction of Fe(VI) to Fe(III). This groundbreaking contribution of high-valent states of iron will advance knowledge on intermediate iron species in chemical and biological processes.

Acknowledgements

The authors gratefully acknowledge the financial support provided by Technology Agency of the Czech Republic "Competence Centres" (project TE01020218), by the project LO1305 of the Ministry of Education, Youth and Sports of the Czech Republic, and by Operational Program Education for Competitiveness – European Social Fund (projects CZ.1.07/2.3.00/30.0041, CZ.1.07/2.3.00/20.0155, CZ.1.07/2.3.00/20.0058). V.K.

Sharma acknowledges the support of the United States National Science Foundation (CBET-1439314). The authors further gratefully thank DESY (Hamburg, Germany) for the opportunity to carry out nuclear forward scattering experiments using synchrotron radiation. The authors would also like to thank Tomáš Hatala, Jiří Frydrych, Jozef Bednarčík, and Jakub Navařík for their help during measurements on the synchrotron in DESY, Hamburg. The authors thank Karolína Machalová Šišková for final reading of the manuscript.

Notes and references

1 L. Machala, J. Tuček and R. Zbořil, *Chem. Mater.*, 2011, **23**, 3255.
2 R. Sarma, A. M. Angeles-Boza, D. W. Brinkley and J. P. Roth, *J. Am. Chem. Soc.*, 2012, **134**, 15371.
3 Y. Lee, R. Kissner and U. von Gunten, *Environ. Sci. Technol.*, 2014, **48**, 5154.
4 L. Hu, M. A. Page, T. Sigstam, T. Kohn, B. J. Mariñas and J. T. Strathmann, *Environ. Sci. Technol.*, 2012, **46**, 12079.
5 S. A. Wilson, T. Kroll, R. A. Decreau, R. K. Hocking, M. Lundberg, B. Hedman, K. O. Hodgson and E. I. Solomon, *J. Am. Chem. Soc.*, 2013, **135**, 1124.
6 A. R. McDonald and L. Que, *Coord. Chem. Rev.*, 2013, **257**, 414.
7 J. J. Scepaniak, C. S. Vogel, M. M. Khusniyarov, F. W. Heinemann, K. Meyer and J. M. Smith, *Science*, 2011, **331**, 1049.
8 W. Nam, Y. M. Lee and S. Fukuzumi, *Acc. Chem. Res.*, 2014, **47**, 1146.
9 I. Prat, J. S. Mathieson, M. Guell, X. Ribas, J. M. Luis, L. Cronin and M. Costas, *Nat. Chem.*, 2011, **3**, 788.
10 J. Hohenberger, K. Ray and K. Meyer, *Nat. Commun.*, 2012, **3**, 720.
11 M. Ghosh, K. K. Singh, C. Panda, A. Weitz, M. P. Hendrich, T. J. Collins, B. B. Dhar and S. S. Gupta, *J. Am. Chem. Soc.*, 2014, **136**, 9524.
12 S. Shaik, D. Kumar, S. P. de Visser, A. Altun and W. Thiel, *Chem. Rev.*, **105**, 2279–2328.
13 S. Shaik, S. Cohen, Y. Wang, H. Chen, D. Kimar and W. Thiel, *Chem. Rev.*, 2010, **110**, 949–1017.
14 S. Kumar, A. S. Faponie, P. Sarman, A. K. Vardhaman, C. V. Sastry, D. Kumar and S. P. de Visser, 2014, **136**, 17102–17115.
15 L. Peng, Z. Xu, Z. Liu, Y. Wei, H. Sun, Z. Li, X. Zhao and C. Gao, *Nat. Commun.*, 2015, **6**, 5716.
16 L. Delaude and P. Laszlo, *J. Org. Chem.*, 1996, **61**, 6360.
17 S. Licht, *Energies*, 2010, **3**, 960.
18 S. M. Hightower, B. B. Lorenz, J. G. Bernard and M. D. Johnson, *Inorg. Chem.*, 2012, **51**, 6626.
19 V. K. Sharma, *Coord. Chem. Rev.*, 2013, **257**, 495.
20 J. Filip, R. A. Yngard, K. Siskova, Z. Marusak, V. Ettler, P. Sajdl, V. K. Sharma and R. Zboril, *Chem. – Eur. J.*, 2011, **17**, 10097.
21 V. K. Sharma, *Environ. Sci. Technol.*, 2010, **45**, 5148.
22 L. Machala, R. Zboril, V. K. Sharma, J. Filip, O. Schneeweiss and Z. Homonnay, *J. Phys. Chem. B*, 2007, **111**, 4280.
23 E. M. Casbeer, V. K. Sharma, Z. Zajickova and D. D. Dionysiou, *Environ. Sci. Technol.*, 2013, **47**, 4572.
24 S. M. Hightower, B. B. Lorenz, J. G. Bernard and M. D. Johnson, *Inorg. Chem.*, 2012, **51**, 6626.
25 J. D. Rush and B. H. Bielski, *J. Inorg. Chem.*, 1994, **33**, 5499.
26 L. Machala, R. Zboril, V. K. Sharma, J. Filip, D. Jancik and Z. Homonnay, *Eur. J. Inorg. Chem.*, 2009, 1060.
27 H.-C. Wille, H. Franz, R. Röhlsberger, W. A. Caliebe and F.-U. Dill, *J. Phys.: Conf. Ser.*, 2010, **217**, 012008.
28 W. Sturhahn and E. Gerdau, *Phys. Rev. B: Condens. Matter Mater. Phys.*, 1994, **49**, 9285.
29 W. Sturhahn, *Hyperfine Interact.*, 2000, **125**, 149.
30 In *Mössbauer Spectroscopy (Topics in Applied Physics; 5)*, ed. U. Gonser, Springer-Verlag, 1975.
31 Y. D. Perfiliev and V. K. Sharma, *ACS Symposium Series*, 2008, 985, Ferrates, pp. 112–123.
32 C. Jeannot, B. Malaman, R. Gerardin and B. Oulladiaf, *J. Solid State Chem.*, 2002, **165**, 266.
33 A. Ansari, A. Kaushik and G. Rajaraman, *J. Am. Chem. Soc.*, 2013, **135**, 4235–4249.
34 A. Ansari and G. Rajaraman, *Phys. Chem. Chem. Phys.*, 2014, **16**, 14601–14613.
35 R. H. Wood, *J. Am. Chem. Soc.*, 1958, **80**, 2038–2041.
36 D. E. Cabelli and V. K. Sharma, *ACS Symposium Series*, 2008, 985, Ferrates, pp. 158–166.
37 V. K. Sharma, R. Zboril and R. S. Varma, *Acc. Chem. Res.*, 2015, **48**(2), 182.
38 W. Jiang, L. Chen, S. R. Batchu, P. R. Gardinali, L. Jasa, B. Marsalek, R. Zboril, D. D. Dionysiou, K. O. O'Shea and V. K. Sharma, *Environ. Sci. Technol.*, 2014, **48**, 12164.
39 R. Prucek, J. Tucek, J. Kolarik, I. Huskova, J. Filip, R. S. Varma, V. K. Sharma and R. Zboril, *Environ. Sci. Technol.*, 2015, **49**(4), 2319.
40 I. Garcia-Bosch, S. K. Sharma and K. D. Karlin, *J. Am. Chem. Soc.*, 2013, **135**, 16248.
41 S. Kumar, A. S. Faponie, P. Barman, A. K. Vardhaman, C. V. Sastri, D. Kumar and S. P. de Visser, *J. Am. Chem. Soc.*, 2014, **136**, 17102.
42 L. R. Widger, C. G. Davis, T. Yang, M. A. Siegler, O. Troeppner, G. N. L. Jameson, I. I. Burmazovic and D. P. Goldberg, *J. Am. Chem. Soc.*, 2014, **136**, 2699.
43 D. Mitra, S. J. George, Y. Guo, S. Kamli, S. Keable, J. W. Peters, V. Pelmenschikov, D. A. Case and S. P. Cramer, *J. Am. Chem. Soc.*, 2013, **135**, 2530.

Electronic Supplementary Material (ESI) for Physical Chemistry Chemical Physics.

Supporting Information

Direct Evidence of Fe(V) and Fe(IV) Intermediates during Reduction of Fe(VI) to Fe(III): Nuclear Forward Scattering of Synchrotron Radiation Approach

Libor Machala,[1*] Vít Procházka,[1] Marcel Miglierini,[1,2] Virender K. Sharma,[3] Zdeněk Marušák,[1] Hans-Christian Wille,[4] Radek Zbořil[1*]

1 Regional Centre of Advanced Technologies and Materials, Departments of Experimental Physics and Physical Chemistry, Faculty of Science, Palacký University, Šlechtitelů 11, 783 71 Olomouc, Czech Republic

2 Institute of Nuclear and Physical Engineering, Slovak University of Technology, Ilkovicova 3, 812 19 Bratislava, Slovakia

3 Department of Environmental and Occupational Health, School of Public Health, Texas A&M University, 1266 TAMU, College Station, Texas 77843, USA

4 DESY, Notkestraße 85, D-22607 Hamburg, Germany

E-mail: libor.machala@upol.cz, radek.zboril@upol.cz

^{57}Fe-enriched solid K_2FeO_4 sample

A two-step process was used to prepare an aqueous solution of $Fe(NO_3)_3 \cdot 9H_2O$ enriched by ^{57}Fe isotope, which served as a precursor for the ferrate(VI) synthesis. The enrichment is labelled as ^{57}Fe in the following text. Firstly, ^{57}Fe ferric chloride was prepared by dissolution of ^{57}Fe hematite in a stoichiometric amount of hydrochloric acid. In the second step, ^{57}Fe ferric chloride was combined with silver nitrate in an aqueous metathesis reaction. The precipitate of silver chloride was filtered out from the solution. The excess liquid was evaporated by a dry nitrogen flow at room temperature due to the low thermal stability of ferric nitrate solution.

A powdered (^{57}Fe) K_2FeO_4 sample was prepared according to the method of Thompson et al.[1] Briefly, oxidation of (^{57}Fe) $Fe(NO_3)_3 \cdot 9H_2O$ by hypochlorite in a 14 M NaOH solution resulted in sodium ferrate(VI) (Na_2FeO_4), which was then precipitated as (^{57}Fe) K_2FeO_4 by adding solid KOH. The prepared crystals were then dried in ethanol and stored in a vacuum desiccator.

The powdered K_2FeO_4 had a grain size in the range of 1-100 μm (Fig. S1a). The purity of the sample was tested using ^{57}Fe NFS at room temperature (Fig. S1b). The sample contained 98 % Fe(VI) and the remaining 2 % was Fe(III), corresponding to ferric hydroxide. The series of NFS time spectra of a powdered K_2FeO_4 were collected at the Dynamics Beam line at PETRAIII,[2] DESY, Hamburg, Germany. The K_2FeO_4 was introduced into a glass capillary with a diameter of 1.2 mm before it was placed into the furnace (Linkam THMS600).

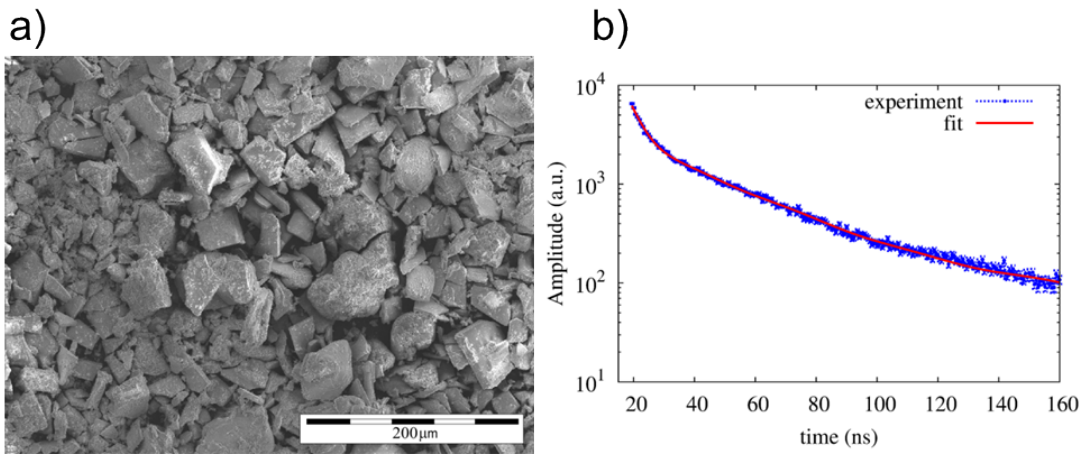

Fig. S1. a) Scanning electron microscope (SEM) image of (^{57}Fe) K_2FeO_4 powder; b) Nuclear forward scattering time spectrum of (^{57}Fe) K_2FeO_4 sample fitted by a major singlet component (98 % Fe) corresponding to K_2FeO_4 and a minor component (2 % Fe) related to ferric hydroxide.

Synchrotron experiments

Nuclear forward scattering (NFS) belongs to the family of hyperfine methods based on the nuclear level excitation and Mössbauer effect.[3] All resonant nuclei in the sample are coherently excited by a beam of synchrotron radiation and followed by a coherent deexcitation connected with gamma-quanta emission. This results in a time spectrum, where information about the hyperfine structure of the sample is encoded. Due to the high brilliancy of synchrotron radiation, which induces the excitation of the nuclei, together with the usage of samples enriched by ^{57}Fe isotope, the time needed for the detection of one relevant time spectrum[4] of a sufficient quality is reduced to approximately one minute. This makes the NFS an excellent tool with good time resolution of the chemical state for a thorough *in-situ* study of the mechanism and kinetics of the thermal decomposition process of potassium ferrate(VI). Monochromated linearly polarized radiation with energy of 14.4 keV and energy resolution of 1 meV was applied to the sample in a spot of 1×2 mm. The photon flux was $7 * 10^{13}$ ph s^{-1}.

Evaluation of NFS spectra

Each NFS time spectrum was accumulated and recorded within the time interval of one minute, with repeated NFS time spectra collected (a few seconds between two successive records were consumed follow for memory storing and software/hardware processing). Thus, in total 173 time spectra were acquired during a time period of 210 min including the heating from room temperature to 235 °C and isothermal heating at 235 °C. The acquired time spectra were analyzed by the CONUSS software. [5] The detection limit of the NFS technique is approximately one percent. Since contents of the intermediate species were only a few percent above this limit, special attention was paid to the data analysis procedure. A number of theoretical models for reconstruction of the time spectra were proposed and tested in order to identify the most relevant one. A model with initial values of hyperfine parameters already known for K_2FeO_4 and $KFeO_2$ was used to calculate the theoretical time spectrum, which was compared with the experimental one. Next, the hyperfine parameters were varied in order to obtain the best fit of the theoretical curve to the experimental data. The chi-square test was used as a criterion for fitting the curve. In some general cases, a reduced chi-square is reliable for comparing the applicability of different models. However, this was not relevant for our study because all points obtained in the time spectra were supposed to be independent and also experimental points in one time spectrum were high.

Initially, the simple two-component model was applied to analyze the data. The chi-square parameter exceeded certain values depending on the annealing time. This indicated the presence of other phases in the sample. This analysis was followed by testing of additional fitted models having three, four, and five different spectral components. The incorporation of additional components into the fitted

models significantly improved statistical quality of the fits. However, the improvements were hardly seen visually since the data were presented in a log scale and thus enhanced observations of lower intensities. This was in contrast to the fitting procedure which was more sensitive to higher intensities than lower intensities. Therefore, the quantum beats that exhibit proper oscillations in the log plots were controlled. Simultaneously, we monitored the decrease of the chi-square parameter, which quantitatively reflected the integral improvement of the fit. Fig. S2 compares the fits using models with two and five components.

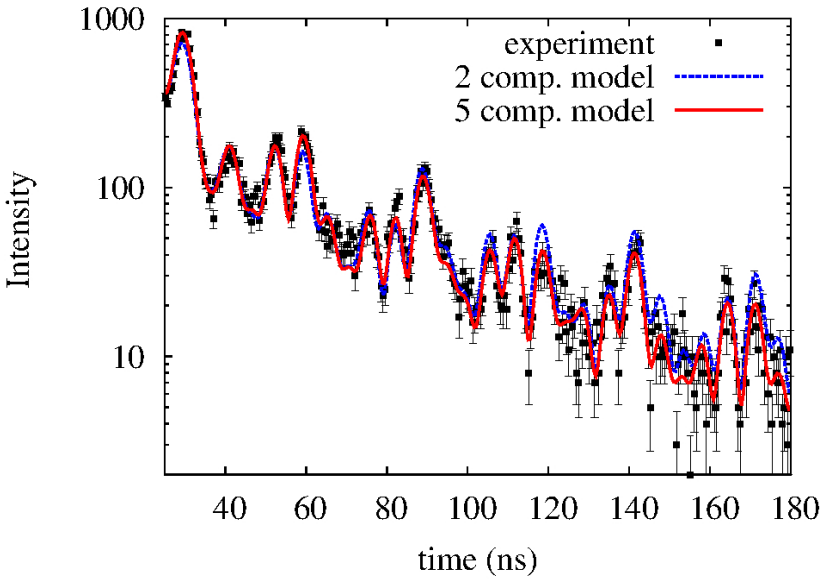

Fig. S2. Comparison of two-component and five-component fitted models for the experiment at the 50th minute of annealing.

Fig. S3 presents the evolution of the chi-square parameter for all the fitted models during the annealing process. The individual components are marked as A, B, C, D, and E. During the fitting of four components, we observed that there were two ranges: a higher amount of the fourth component, separated by a minimum where the amount of the component decreased below 1 %. The first maximum corresponded to an isomer shift of –0.55 mm/s; the second maximum exhibited an isomer shift of –0.3 mm/s. Because there was no significant overlap between these two entities, two ranges were interpreted as two separate components with fixed values of isomer shift, which were precisely determined from the corresponding NFS time spectra. Consequently, we present the two four-component models, where component (B) or (D) is missing. These models are labeled as \$4B and \$4D while other models are labeled by symbols \$2, \$3 and \$5 (Fig. S3).

Fig. S3 clearly shows that the five-component fitted model fit the experimental data better than the other tested models over the entire period of the annealing process. However, values of chi-square were strongly affected by the intensity of the synchrotron radiation, which oscillated due to monochromator instabilities. Higher intensity of the incident radiation caused higher intensity of the scattered radiation and consequently higher relative accuracy of the measurement. Therefore, the chi-square increased when the intensity of the beam increased. In order to avoid this effect in comparison of two models, it was better to calculate the ratios of the chi-squares corresponding to two given fitted models.

In Fig. S4, the chi-square values corresponding to the two-, three-, and four-component models are compared with the chi-square values obtained using the five-component model within the period between 20th and 100th minute of the experiment. In this time range, the majority of the transformations were observed. Fig. S4 shows that the models with three, four and five components satisfied the experimental data at the beginning of the decomposition. The chi-square for the two- component model \$2 is significantly 30% higher over the entire period of time. Up to minute 40 of the decomposition process, models \$3, \$4B, \$4D, and \$5 were in good agreement with the experimental data and the chi-square values differed less than by 10 %. Beginning minute at 40, the chi-square increased by approximately 20 % for models \$3 and \$4D in relation to the \$5 model. The chi-square for the \$4B model was still just 5 % above the chi-square for the \$5 model. In the period from the 40th to the 60th minute, component (B) ascribed to iron(V) was observed. When the (C) component occurred at ~ 50 min, the chi-square increased slightly. When the amount of component (D) increased after 70 minutes, the chi-square became higher with respect to the \$5 model. In contrast, the chi-square for the \$4D model decreased after 70 minutes. This occurred because component (B) was almost non-existent before the 70th minute, but increased after minute 70. Therefore, the \$4D model was selected over the \$4B model. The chi-square of the 4D\$ model approached the chi-square of the \$5 model after minute 90 because component (B) disappeared and therefore did not affect the fit of the model.

These data clearly demonstrate that the five-component model could be easily replaced by the model containing only four components since the overlap of the ranges with significant amounts of components (B) and (D) were rather small. It would be the most appropriate for the interpretation to use the five-components model which was physically equivalent with that containing four components. In order to exclude any correlations between the fitting parameters, a set of fittings was also performed where different parameters were fixed and released. All the results were compared and the best were selected, based on a satisfactory agreement in the quality and quantity of the parameter. Overall, the in-depth precise evaluation procedure used in this research was reasonable and the amounts of

intermediates slightly above the resolution limit were true representatives of the transformation reactions.

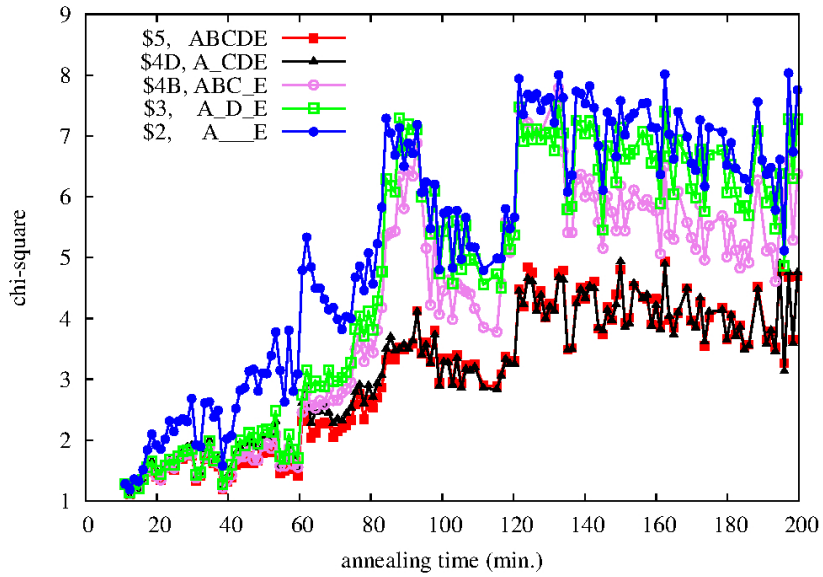

Fig. S3. The chi-square parameter for two, three four and five-component models for the full time span of the measurement.

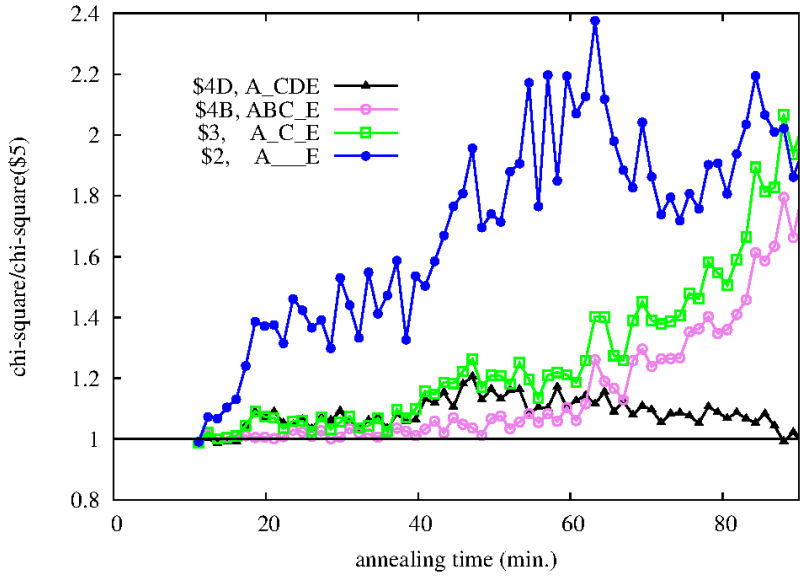

Fig. S4. The chi-square for different fitting models normalized to the 5-component model.

Tab. S1. Maximum relative amounts and hyperfine parameters of spectral components as derived from the NFS time spectra.

Component	Iron oxidation state	Max amount (%)	*IS* * (mm/s)	*Q* (mm/s)	*B* (T)
A	Fe(VI)	98 ± 1	–0.90 (fixed)	0	0
E	Fe(III)	90 ± 1	(0.10-0.15) ± 0.02	0.09 ± 0.01	(45.0-45.3) ± 0.3
C	Fe(III)	9 ± 2	0.30 ± 0.03	0.15 ± 0.05	(43.8-44.8) ± 0.5
D	Fe(IV)	5 ± 1	–0.30 ± 0.03	0.37 ± 0.03	0
B	Fe(V)	4 ± 1	–0.55 ± 0.04	0.15 ± 0.02	0

IS…isomer shift related to α-Fe at room temperature; Q…quadrupole splitting/shift; B…hyperfine magnetic field;
* Isomer shift values are related to room temperature, so they are not affected by the second order Doppler shift

Tab. S2. Proposed transformations from Fe(VI) to Fe(III) via Fe(V) and Fe(IV) in the thermal decomposition process at 235 °C.

Transformations	Time span (min)
$K_2Fe^{VI}O_4 \rightarrow KFe^{III}O_2 + 1/3(K_2O + KO_2) + 1/2\ O_2$	0 – 110
$2K_2Fe^{VI}O_4 \rightarrow KFe^{V}O_3 + K_3Fe^{III}O_3 + O_2$	0 – 110
$KFe^{V}O_3 \rightarrow KFe^{III}O_2 + 1/2\ O_2$	50 – 100*
$K_3Fe^{III}O_3 \rightarrow KFe^{III}O_2 + K_2O$	80 – 110**
$K_2Fe^{VI}O_4 \rightarrow K_2Fe^{IV}O_3 + 1/2\ O_2$	0 – 110
$K_2Fe^{IV}O_3 \rightarrow KFe^{III}O_2 + 1/3(K_2O + KO_2)$ ***	110 – 200
$K_2Fe^{VI}O_4 \rightarrow K_3Fe^{III}O_3 + KFe^{III}O_2 + 3/2\ O_2$	0 – 110
$K_3Fe^{III}O_3 \rightarrow KFe^{III}O_2 + K_2O$	80 – 110

* the beginning corresponds to the change of trend of (E) at 50 min

** the beginning corresponds to the change of trend of (E) at 80 min

*** this process is very slow (observable after 110 min)

References

(1) G. W. Thompson, G. W. Ockerman and J. M. Schreyer, *J. Am. Chem. Soc.,* 1951, **73**, 1379.

(2) H.-C. Wille, H. Franz, R. Röhlsberger, W. A. Caliebe and F.-U. Dill, *J. Phys.: Conf. Ser.*, 2010, **217**, 012008.

(3) J. B. Hastings, D. P. Siddons, U. Vanburck, R. Hollatz, U. Bergmann, *Phys. Rev. Let.,* 1991, **66(6)**, 770.

(4) Time spectrum: In fact, during a NFS experiment a time dependent intensity of the de-excited radiation, i.e. an interferogram, is detected. It consists of photons that are emitted by the system during its transition from the excited state into a ground state which occurs immediately after the synchrotron excitation pulse. Note that to get rid of the influence of the original excitation photons, the data acquisition starts with some time delay which is typically ~20 ns. Depending upon the number of nuclear energy levels governed by hyperfine interactions, usually photons of several energies (frequencies) sum up and construct a time-dependent signal. For the sake of simplicity, we will refer to these experimentally recorded data as 'time spectra'; though, strictly speaking, they are only a representation of nuclear level transitions in time domain.

(5) W. Sturhahn, E. Gerdau, *Phys. Rev. B,* 1994, **49**, 9285.